

PROGRESS TOWARDS A NEW PARITY NON-CONSERVATION
MEASUREMENT IN CESIUM-133

A Dissertation

Submitted to the Faculty

of

Purdue University

by

Yao De George Toh

In Partial Fulfillment of the

Requirements for the Degree

of

Doctor of Philosophy

August 2019

Purdue University

West Lafayette, Indiana

THE PURDUE UNIVERSITY GRADUATE SCHOOL
STATEMENT OF DISSERTATION APPROVAL

Dr. Daniel S. Elliott, Chair

School of Electrical and Computer Engineering

Dr. Yong P. Chen

School of Electrical and Computer Engineering

Dr. Francis Robicheaux

Department of Physics and Astronomy

Dr. Ephraim Fischbach

Department of Physics and Astronomy

Approved by:

Dr. Dimitrios Peroulis

Head of the School of Electrical and Computer Engineering

To my family.

ACKNOWLEDGMENTS

Having been at Purdue for 8 years, there are so many people I need to thank and acknowledge. I am most grateful for Professor Elliott's patience and encouragement, which were both necessary for the completion of this PhD. I am also thankful for the many wonderful students from our group, both past and present. Dionysis, John and Adeel for teaching me what I know. Ian, Amy and Jungu whom I worked and bounced ideas around with. Also the many undergrads who came through our lab, Jonah, Nathan G, Eric and most recently Nathan C.

I also want to acknowledge Prof. Weiner, whom I did a semester of reading with. Although I ultimately moved to a different lab, I still collaborated with his group, especially Jose who introduced us to the use single photon detectors. Dan Leaird is also always available when we needed some extra expertise, or equipment to borrow!

I taught electrical engineering senior design (ECE477) for 5 years as a teaching assistant. It was a joy working with Prof. Meyer, Prof. Mithuna and Dr. Johnson as we supervised students through what was the final semester for most. There were many crazy and silly projects, which were only made possible with the technical expertise of Chuck Barnett and Joe Bougher, the all-knowing lab engineers. I wish Prof. Meyer all the best in retirement!

All of this would not be possible without the help of the various Purdue staff members. The first people from Purdue I communicated with were the staff members of the ECE graduate office: Michelle Wagner and Matt Golden. Later on Elisheba would join the team at the grad office. Viki, Laura and Christy must have been sick of dealing with my purchase orders, but nevertheless helped me place them. Bob, Cathy and Steve at the EE mailroom made sure I got all my packages, including those with no name! Dee Dee was always there to make sure I got my travel claims

sorted out. Jim Corwin at the machine shop, and Tom Miller from the PRIME lab were always helpful when I needed advice with machinery or vacuum pumps.

Then there were the friends I made along the way from the various labs at Purdue. Chuan Hsun must be the longest of them, having enrolled the same time I did, and who is also graduating this semester. May and Cheng-An from Prof. Chen-Lung Hung's lab have given me so much good advice. Jungu's brother Honggu has also been a good friend. I wish them all the best.

Finally, this PhD would not have been possible without the support of friends and family. Mum and dad, I am forever grateful.

TABLE OF CONTENTS

	Page
LIST OF TABLES	x
LIST OF FIGURES	xii
ABSTRACT	xxi
1 INTRODUCTION	1
1.1 History of Parity Violation	1
1.2 Weak charge and Physics beyond the Standard Model	3
1.3 PNC in atomic systems	4
1.4 Nuclear spin independent and dependent components	6
1.5 1997 Measurement of E_{PNC} in cesium $6S \rightarrow 7S$ transition	8
1.6 Measurement of weak transition moments with two-pathway coherent control	10
1.7 Summary of my contributions towards a new PNC measurement	12
2 THEORY	14
2.1 Cesium atomic structure	14
2.2 Electric dipole matrix elements	16
2.3 Transition amplitudes	17
2.3.1 Stark amplitude	18
2.3.2 Magnetic dipole amplitude	18
2.3.3 PNC amplitude	19
2.3.4 Two-photon amplitude	20
2.4 Scalar and vector transition polarizabilities, α, β	20
2.5 Two pathway coherent control amplitude	23
3 EXPERIMENTAL APPARATUS	26
3.1 Overview of the experimental setup for the PNC measurement	26

	Page	
3.2	852 nm lasers for optical pumping and detection	28
3.3	Laser locking scheme - saturated absorption	31
3.4	Laser locking transitions	35
3.4.1	Optical pumping lasers	36
3.4.2	Detection laser	41
3.5	Heterodyning of 852 nm ECDLs for laser linewidth estimation . . .	43
3.6	The 1079 nm laser system	46
3.6.1	Second harmonic generation to obtain the 540 nm laser . . .	46
3.6.2	Frequency locking scheme for the 1079 nm laser system . . .	50
3.7	Raman laser for spin polarization optimization	51
3.8	Vacuum chamber and cesium oven heating	55
3.8.1	Vacuum chamber	55
3.8.2	Turbopump and vibration damping	57
3.8.3	Liquid nitrogen cooled baffles	57
3.8.4	Cesium oven	58
4	PROGRESS TOWARDS THE PNC MEASUREMENT	62
4.1	Detection laser	62
4.2	Detection system photodiode TIA circuit (Ver. 1)	63
4.3	Newer detection system TIA circuit (Ver. 2)	66
4.4	Improving spin polarization of the atomic beam	67
4.5	Pound-Drever-Hall laser frequency stabilization	70
4.5.1	Introduction to PDH	70
4.5.2	PDH theory	72
4.5.3	Implementation of PDH	78
4.5.4	PDH progress to date	86
4.6	Power build-up cavity	89
4.6.1	Purpose of the PBC	89
4.6.2	Progress so far	90

	Page	
4.6.3	Locking scheme for the power build-up cavity	92
4.6.4	Future upgrades to PBC	94
5	SYSTEMATIC EFFECTS	96
5.1	Stark induced contributions	96
5.2	Magnetic dipole induced contribution	98
5.3	Zeeman mixing between magnetic components	98
5.4	Systematic effects conclusion	99
6	LIFETIME MEASUREMENT OF CESIUM $7S_{1/2}$ EXCITED STATE . .	100
6.1	Introduction	100
6.2	Theory	102
6.2.1	Spontaneous decay from the $7S_{1/2}$ excited state	102
6.2.2	Time-correlated single photon counting (TCSPC)	103
6.2.3	Asynchronous detection technique	104
6.3	Lifetime measurement experimental details	107
6.3.1	Experimental setup	107
6.3.2	Data acquisition	110
6.3.3	Analysis of results	112
6.3.4	Comparison of results	120
7	MEASUREMENT OF CESIUM $7S_{1/2}$ BRANCHING RATIO	121
7.1	Introduction	121
7.2	Theory	121
7.2.1	S_{\parallel}/S_{\perp} ratio	122
7.2.2	P_L ratio	126
7.3	Branching ratio experimental details	128
7.3.1	Earlier attempts (2015-2017)	128
7.3.2	Final experimental setup	129
7.3.3	Results and analysis	138
7.3.4	Comparison of result with theory	145

	Page
7.4 Calculation of matrix elements	146
8 NEW DETERMINATION OF CS $6S \rightarrow 7S$ VECTOR POLARIZABILITY	
β	148
8.1 Summary of 6S-7P measurement	148
8.2 Revisiting the 7S-7P matrix elements	150
8.3 Review of E1 matrix elements	153
8.4 Determination of α and β by sum over states	155
8.5 A new determination of Q_w	160
9 CONCLUSION	163
9.1 Contributions towards atomic parity violation	163
9.2 Future work	164
LIST OF REFERENCES	165
A $6S \rightarrow 7S$ ENERGY LEVEL DIAGRAM	175
B IMPORTANT CESIUM FACTS	176
C $C_{FM}^{F'M'}$ COEFFICIENTS	178
D CORRECTIONS TO DATA FOR BRANCHING RATIO MEASUREMENT	179
D.1 Imperfect extinction ratio	179
D.2 Manual rotation of half-wave plate	180

LIST OF TABLES

Table	Page
1.1 Best measurements of E_{PNC} in various atomic systems.	5
5.1 Estimated magnitudes of potential systematic contributions to the E_{PNC} measurement. ^a The Clebsch-Gordon coefficient has been abbreviated to [C], see text for long form.	97
6.1 Sources of error and the percentage uncertainty resulting from each. The total uncertainty is dominated primarily by statistical error.	118
6.2 Experimental and theoretical results for the lifetime τ_{7S} of the cesium $7S^2S_{1/2}$ state. We derived theory values marked with an asterisk (*) from matrix elements $\langle 7S r 6P_{1/2}\rangle$ and $\langle 7S r 6P_{3/2}\rangle$ reported there. In the theoretical works marked with a dagger ([†]), the authors only reported values of $\langle 7S r 6P_{1/2}\rangle$, so we estimated $\langle 7S r 6P_{3/2}\rangle$ from $1.528 \times \langle 7S r 6P_{1/2}\rangle$ in order to derive τ_{7S}	119
7.1 Sources of error and the correction applied to $S_{ }/S_{\perp}$ and uncertainty for each. We compute the uncertainty for each data point in Fig. 7.9 as the quadrature sum of these contributions. The final uncertainty is dominated by statistical uncertainty.	140
7.2 State energies and electric dipole $E1$ transition moments $\langle 7S_{1/2} r nP_J\rangle$ and $\langle nP_J r 6S_{1/2}\rangle$ used to determine R . Transition moments are given in terms of a_0 . ^a State energies as found in NIST tables [118]. ^b Weighted average of several independent determinations from Refs. [66–68, 103–106, 108]. ^c Ref. [64], including the Supplemental Information. ^d Ref. [119]. ^e Ref. [96].	142
7.3 A list of the absolute values of the most recent precise measurements of the $\langle 6P_J r 6S_{1/2}\rangle$ matrix elements. For our calculations, we use the weighted average of these measurements, as listed in Table 7.2. ^a Zhang reports slightly different lifetimes in the abstract from the text, I have used the number from the text to calculate these matrix elements.	144
7.4 Absolute values of the $7S_{1/2} - 6P_J$ reduced dipole matrix elements (in a_0) and their ratio calculated in different approximations (see text for more details). This data is from references [64] and [57].	146

Table	Page	
7.5	Experimental and theoretical results for the ratio and absolute values of reduced dipole matrix elements for the cesium $6p\ ^2P_J \rightarrow 7s\ ^2S_{1/2}$ transitions. We compute the ratio R_{7S6P} from the values of $\langle 7s_{1/2} r 6p_{1/2} \rangle$ and $\langle 7s_{1/2} r 6p_{3/2} \rangle$ reported in Refs. [21, 63, 64, 71, 115, 121].	147
8.1	We show in this table the calculated contributions to α_{7S} from the $\langle 7S_{1/2} r nP_J \rangle$ matrix elements for $n = 6, 8 - 12$ using Equation (8.3). We deduct from α_{7S} the other contributions listed, to calculate the contributions from the $\langle 7S_{1/2} r 7P_J \rangle$ matrix elements.	152
8.2	This table lists the newest values of matrix elements for the lowest cesium transitions and their present uncertainties. See text for more information. ^a Weighted mean of multiple measurements, see Table 7.3. ^b Most recent theory determination from [64]. ^c Ref. [123]. ^d Ref. [63].	155
8.3	E1 dipole moments, eigenstate energies, and contributions to the scalar polarizability α . See text for a full description. $n = 6, 7$ matrix elements as discussed earlier, theory values from Ref. [64].	158
8.4	This table lists several determinations of α and β since 1992. We have listed our direct calculations of both α and β through sum over states, but the sum for beta has large uncertainty due to cancellation of terms. The determinations labeled "Sum over states (α)" combine a calculation of α and the high precision measurement of α/β by [77] to determine β . β with the best precision (before this work) combines the measurement in 1999 by [73] of M_{hf}/β and the calculation in 2000 of M_{hf} [76]. I have bolded the two highest precision determinations of β in the Table.	159
8.5	This table lists the various determinations of Q_w for cesium since 1992. I have listed our determinations using both theory values of k_{PNC} . Where publications list multiple values, I have included the 'recommended' values. Some papers report separate experimental and theoretical uncertainties, I have added them in quadrature.	162

LIST OF FIGURES

Figure	Page
1.1 Image of the Wu experimental setup in 1957. In the mirror-reversed arrangement, we expect beta emission to be preferentially up (direction of current flow) if parity is conserved. It was found experimentally that the opposite was true, that beta emission was preferentially down, indicating that parity is not conserved for beta emission. Image from Wikipedia. .	2
1.2 Running of the effective weak mixing angle with energy scale Q . The black curve is the SM prediction. The colored curves are predictions for a dark Z for mass (a) 50 MeV (green), (b) 100 MeV (blue) and 200 MeV (red). Image from [20].	4
1.3 Experimental setup for the measurement of E_{PNC} in cesium by [28]. The atomic beam passes through three regions of interest: optical pumping, interaction and detection. PBC - power build-up cavity.	9
1.4 Experimental setup for the measurement of the magnetic dipole moment in cesium [55]. The phase between the green 539.5 nm laser and the infrared 1079 nm laser is varied by turning an optical flat in the path of the green beam.	11
1.5 Measured signal from the M1 magnetic dipole experiment. Left: The modulating part of the measured waveform as the phase difference $\Delta\phi_{scan}$ is scanned for (a) $E_y = 0$ V/cm and (b) $E_y = 75.09$ V/cm . Right: A plot of $K(E_y)/K(0)$ against E_y . The circles represent data points while the solid line is the curve of best fit. Images from [55].	12
2.1 This figure shows the Zeeman splitting of the cesium $6S_{1/2}$ ground states in the presence of an applied dc magnetic field.	15
2.2 Beam and field orientation for measurement of E_{PNC}/α . The Cs atomic beam travels along x, the 540/1079 nm beams are along y while the static electric and magnetic fields are along z.	24
2.3 Amplitude (left) and phase (right) of modulation in the transition rate as a function of the Stark field E_z	25
3.1 Experimental setup for the PNC measurement. EOM - electro-optic modulator, FA - fiber amplifier, PPLN - frequency doubling crystal, PBC - power build-up cavity.	26

Figure	Page
3.2 This image from [78] shows an external cavity diode laser in: (a) Littrow configuration (b) Littman-Metcalf configuration. The Littrow configuration uses fewer components, but the Littman-Metcalf laser beam output direction remains constant as we tune the laser frequency.	29
3.3 The base plate where the laser diode holder and grating mirror mount are mounted. Image from [53].	30
3.4 Home-made external cavity diode laser showing the collimation tube within the tube-holder, optical grating attached to a mirror mount and base-plate.	31
3.5 (a) Doppler broadened absorption profile. (b) Doppler-free probe transmission profile.	33
3.6 An oscilloscope sweep showing the Doppler-free saturated absorption peaks of the Cesium 6S $F=3$ to $6P_{3/2}$ (F' as labelled) transition. The peaks labeled c.o. are the crossover peaks that occur halfway between two transitions. The lower curve shows the error signal extracted from this saturated absorption signal.	34
3.7 The gradient of the (a) absorption peak gives us a (b) dispersion shaped curve which we can use as an error signal.	35
3.8 Set-up for saturated absorption. The pump beam overlaps one of the probe beams to saturate the atoms. The BPD removes the Doppler broadened profile from the electronic signal through the use of a second probe beam. BPD - balanced photodetector, ECDL - external cavity diode laser. . .	36
3.9 Diagram showing the Cesium 6S, $6P_{1/2}$, $6P_{3/2}$ and 7S energy levels. Labeled are the laser wavelengths to excite the 1-photon transitions, but the 6S to 7S transition is electric dipole forbidden. Hyperfine splittings for the $6P_{3/2}$ energy level are shown in Figure 3.10.	37
3.10 This diagram shows the pumping scheme to populate the $(4, \pm 4)$ and $(3, \pm 3)$ magnetic sublevels of the ground 6S level. HF - hyperfine, ZM - Zeeman.	39
3.11 This figure shows the Zeeman pumping to the cesium $6S_{1/2}$ $(4, 4)$ magnetic sublevel. Because the laser is right circularly polarised, only $\Delta m = +1$ transitions are driven.	40
3.12 The large photodiode is placed under an interference filter to block photons at 540 nm and 1079 nm. A concave mirror above the detection region reflects photons emitted upwards back down onto the photodiode. Image from [53].	42

Figure	Page
3.13 The hyperfine laser and Detection laser are separately locked to different cesium hyperfine transitions using saturated absorption spectroscopy. The two lasers are combined using a beamsplitter and sent to a fast photodiode. The beatnote between the two lasers is observed using a Siglent SSA3021X 2 GHz spectrum analyzer.	44
3.14 This screenshot of the rf spectrum analyzer shows the beat signal between the two 852 nm lasers. FWHM as measured by the delta markers is about 1.5 MHz.	45
3.15 Drawing of the PPLN crystal. The image shows the five periodically poled grating channels through the crystal. Image from the MSHG1064-1.0-20 datasheet.	47
3.16 Wavelength-temperature dependence of the 5 different periodically poled gratings of the PPLN crystal. Image from the MSHG1064-1.0-20 PPLN crystal datasheet.	48
3.17 This figure shows the focus of the 1079 nm laser into the PPLN crystal. An $f = 12.5$ cm lens focuses the 1079 nm laser beam into the PPLN crystal, while on the output, an $f = 15$ cm achromatic lens collimates both beams. EOM - electro-optic modulator, PBS - polarizing beamsplitter, FC - fiber coupler.	49
3.18 Block diagram of the 3-stage locking scheme for the 1079 nm laser. The PDH lock of the laser to the power build-up cavity has the highest servo bandwidth, while the next two lock stages need not be as fast.	50
3.19 Photos of the PMT enclosure, showing the internal components. (a) The whole PMT setup; (b) The enclosure containing the PMT and shroud around it; (c) Interference filter located in front of the PMT active area; (d) 1-in. imaging lens located halfway between the PMT and the vapor cell; (e) Vapor cell enclosed in aluminum for heating.	52
3.20 Setup of the home-made Raman laser in Littrow configuration. An additional Invar bar keeps the cavity length constant. Image from [53].	54
3.21 Scan of the Raman laser by a scanning Fabry-Perot interferometer with 300 MHz FSR. The larger peaks correspond to the center frequency while the moderately sized peaks are the modulated sidebands. Roughly 50% of laser power goes into the Raman laser sidebands. Image from [53].	54
3.22 Side-view of the vacuum chamber for the experiment.	56
3.23 Photo of the vacuum chamber in our laboratory. The turbopump and gate valve can be seen attached to the bottom of the vacuum chamber.	56

Figure	Page
3.24 These plots from the manufacturer of the turbopump (Edwards) show the benefit of installing a vibration damper between the turbopump and the gate valve. Vibrations at 800 Hz, the turbopump operating RPM, are reduced by about two orders of magnitude.	58
3.25 Drawing of the cesium oven, used to produce our atomic beam of cesium atoms.	59
4.1 Circuit diagram of the transimpedance amplifier (TIA) and subsequent amplifier stages. The op-amp used for the TIA is the OPA827, chosen for its JFET inputs and low bias current and voltage offset. The OPA4227 was used for the gain stages because we have experience with this op-amp in our lab.	64
4.2 Photograph of the tiny PCB holding the OPA827 TIA and OPA4227 quad op-amp. The PCB is only 1.4×1.1 in ²	65
4.3 Photos of the improved TIA circuit. On the left, we show a top-down view of the PCB. On the right, the photo shows how the PCB directly connects to the vacuum chamber feedthrough.	66
4.4 Experimental setup for the Raman laser. The portion of the Raman laser up-shifted by 160 MHz in the AOM is locked to the $6S_{1/2}$ F=3 to $6P_{3/2}$ F=2 transition by saturated absorption. VCO - voltage controlled oscillator, AOM - acousto-optic modulator, DC - dc component of the diode current from the current controller. Image from [53].	68
4.5 Energy level diagram showing off-resonant Raman transitions between two cesium magnetic sublevels due to the Raman laser. The ground state magnetic sublevels degeneracy is broken by a ~ 7 G magnetic field. Image from [53].	69
4.6 Oscilloscope sweeps showing the detection photodiode signal as the Raman laser modulation frequency is scanned with: (a) only hyperfine pumping and (b) hyperfine and Zeeman pumping. The far right peak in both scans is due to the ramp return and not a part of the scan.	71
4.7 Transmission spectrum of a Fabry-Perot optical cavity versus frequency of the incident laser. The cavity finesse here is 12. Image from [92].	73
4.8 Reflected spectrum of a Fabry-Perot optical cavity versus frequency of the incident laser. On resonance, the reflected intensity is zero. Modulating the laser frequency tells us which side of the resonance we are on. Image from [92].	74

Figure	Page
4.9 Transmission spectrum of a Fabry-Perot optical cavity versus frequency of the incident laser, when the incident laser has strong sidebands due to phase modulation. Image from [93].	76
4.10 This diagram shows the major components of our Pound-Drever-Hall setup. EOM - electro-optic modulator, PBS - polarizing beamsplitter, $\lambda/4$ - Quarter wave-plate, PD - photodetector.	79
4.11 Plot of error signal versus frequency normalized to the free spectral range for low modulation frequency. When the modulation frequency is low, the error signal is a broad dispersion shaped curve. Image from [92].	82
4.12 Plot of error signal versus frequency normalized to the free spectral range for PDH. When the modulation frequency is high, the PDH error signal has this shape. Notice the much larger frequency span where the error signal is large ($0.96 - 1.04$) compared to that of Figure 4.11 ($0.997 - 1.003$). The slope of the error signal close to resonance is also much steeper. Image from [92].	82
4.13 Bode plot for an ideal P-I op-amp, otherwise known as a limited integrator. Very high gains can be obtained at very low frequencies where $f \ll f_0$	83
4.14 Schematic of an inverting op-amp. Z_{input} and $Z_{feedback}$ are resistive or capacitive elements.	85
4.15 Bode plot for op-amp with very high gain (80 dB) at dc, and a low pass filter at f_0	86
4.16 10 MHz span of the laser noise spectrum, centered at the modulation frequency, 13.5 MHz. Resolution bandwidth is 1 kHz. The blue line shows the noise on the laser with only slow (PZT) feedback. The green line shows the noise on the laser when fast (laser current) feedback is turned on. We see that small servo bumps 2 MHz from the center are present. At low frequencies, noise is reduced by at least 30 dBm.	88
4.17 2 kHz span of the laser noise spectrum, centered at the modulation frequency of 13.5 MHz. The blue line shows the noise on the laser with only slow (PZT) feedback. The green line shows the noise on the laser when fast(laser current) feedback is turned on. We clearly see that most of the noise in this span of 2 kHz is reduced by 50 dBm! The small peaks on the green curve reveal the presence of 60 Hz harmonics.	89

Figure	Page
4.18 Experimental setup for the 3-stage lock of the 1079 nm laser. The laser is locked via PDH to the PBC using reflected light from the cavity. The PBC is then stabilized to the Invar cavity. Finally, the Invar cavity is locked to the peak of the cesium Doppler-free two-photon resonance in a vapor cell. $\lambda/4$ - quarter wave-plate, PBS - polarizing beamsplitter, PD - photodetector, EOM - electro-optic modulator, FA - fiber amplifier, PBC - power build-up cavity, PMT - photomultiplier tube.	93
4.19 A sketch of the power build-up cavity. The input mirror has a tube PZT for adjusting the length of the cavity. The output mirror has picomotors for re-alignment of the mirrors. Electric field plates will have to be mounted on the same granite block. The granite block provides a stable base for the optics and is suspended from the vacuum chamber floor by springs.	95
6.1 Energy level diagram for the cesium $7S_{1/2}$ lifetime measurement. We excite the $7S_{1/2}$ upper state by 2-photon excitation with a 1079 nm laser. Of the 4 different decay wavelengths, we choose to detect the direct decay from $7S_{1/2}$ to $6P_{3/2}$ at $1.47 \mu m$	101
6.2 This figure shows the basis behind the time correlated single photon counting technique. A short laser pulse excites the sample of atoms. We precisely keep track of time and record the time delay between the arrival of the laser pulse at the sample, and arrival time of the photon at the detector. This figure is from a Picoquant application note.	103
6.3 A figure from the test results of the Aurea Technology gated-SPD showing the signal-to-noise ratio (SNR) of the detector as a function of gate width. We observe that when we increase the gate width, we have to sacrifice SNR. The different lines denote the SNR when operating the gated-SPD at different quantum efficiency.	105
6.4 Timing diagram of the experiment. The dashed line represents the start time for the TCSPC module, and t the arrival time of the first photon detected within the gate pulse. $f_1 = 1.25$ MHz is the laser repetition rate and f_2 is the SPD gate repetition rate. The difference in frequencies ($f_2 \neq f_1$) causes the SPD to gate during a different part of the measurement window every cycle. This gate-free method of capturing data allows us to utilize the SPD with a 40 ns gate, while capturing a 800 ns measurement window of photon fluorescence.	106

Figure	Page
6.5 A test of the SPD background photon count while the 1079 nm laser is pulsed through the vapor cell but tuned off-resonance. The SPD is running in gated mode, and triggered asynchronously from the laser pulses. This screen capture of the TCSPC software shows the data from three different runs, each of length 10 minutes. We conclude that the number of background photon counts is very uniform while using the gated-SPD in asynchronous mode.	107
6.6 Experimental setup for the lifetime measurement. Abbreviations in this figure are: (PBS) polarizing beam splitter cube; (AOM1) and (AOM2) acousto-optic modulators; (VC1) and (VC2) cesium vapor cells; (PMT) photomultiplier; (FC) fiber coupling optics; (AWG) arbitrary waveform generator; (SPD) single photon detector; and (TCSPC) time-correlated single photon counter.	108
6.7 (Color) This is a sample of data from 6 different 1-hour long runs of photon counts versus time. The purple line that runs across the bottom is a laser off-resonance background counts test, where we accidentally left the computer running for slightly longer than 1-hour. The different peak photon counts are due to differences in cell temperature or laser alignment.	111
6.8 Decay curve of the Cs $7S_{1/2}$ level. (a) The main figure consists of 1 hour of recorded data and shows the excitation of atoms and exponential decay of fluorescence. (b) The same data for 350 – 800 ns with the background deducted, shown on a logarithmic scale in green and the best-fit line in black. We see that by ~ 600 ns, the decay signal has fallen below the shot noise level, $\approx \sqrt{1200} = 35$ photons.	113
6.9 This plot shows the variation of fitted lifetime τ as we change the truncation point T_0 . Each of the 16 colored lines represents a single data set. The horizontal line marks our final reported lifetime of $\tau_{7S} = 48.28$ ns. The two vertical lines denote 360 – 380 ns, the range of values we chose to average for our final result (see text for discussion).	115
6.10 A plot showing the 16 individual measurement results used to calculate the final value. Data sets 9 and 10 were 10 hours long, while the rest were for 1 hour. The total of 34 hours of data was captured over a period of three days. The final data point T and the red horizontal line is the weighted mean of the 16 data sets, with error bars inclusive of statistical and systematic uncertainties.	117

Figure	Page
7.1 Energy level diagram of atomic cesium, showing the states relevant to this measurement. Atoms are excited from the $6S_{1/2}$ ground state to the $7S_{1/2}$ excited state by two-color, two-photon excitation. We collect fluorescence photons at 852 nm from the second step of the spontaneous decay of atoms from the $7S$ state to the ground state by way of the $6P_{3/2}$ state.	122
7.2 S_{\parallel}/S_{\perp} theory curve for detuning $0 < \Delta < 550 \text{ cm}^{-1}$. The blue curve is for the $6S_{1/2} \text{ F}=3 \rightarrow 7S_{1/2} \text{ F}=3$ transition, while the red curve is for $4 \rightarrow 4$. This theory curve of S_{\parallel}/S_{\perp} was calculated using our final result of $R_{7S6P} = 1.5272$	127
7.3 P_L theory curve for detuning $0 < \Delta < 550 \text{ cm}^{-1}$. The blue curve is for the $6S_{1/2} \text{ F}=3 \rightarrow 7S_{1/2} \text{ F}=3$ transition, while the red curve is for $4 \rightarrow 4$. This theory curve of P_L was calculated using our final result of $R_{7S6P} = 1.5272$	127
7.4 Sample peak captured in 2015, with parallel laser polarizations in the vacuum chamber, with detuning $\Delta \approx 3 \text{ cm}^{-1}$	129
7.5 Final experimental setup for the measurement of the relative peak amplitudes with perpendicular and parallel laser polarizations. We keep the polarization of the Ti:sapphire (Ti:Sa) laser beam constant and change the polarization of the external cavity diode laser (ECDL) beam. Other abbreviations in this figure are: (AOM) acousto-optic modulator; (BS) beam sampler; (ChW) beam chopper wheel; (DAQ) data acquisition system; (IF) interference filter; (Iso) optical isolator; (L) lens; (LIA) lock-in amplifier; (PC) personal computer; (PD) photodetector; (PMT) photomultiplier tube; (Pol) polarizer; (SMF) single-mode optical fiber; (VC) vapor cell; ($\lambda/2$) half-wave plate in a rotation stage.	130
7.6 Optical table setup for Ti:sapphire beam. The Ti:sapphire is located in SB50, and we send it through $\sim 30 \text{ m}$ of single mode fiber to the optical table in SB1. Abbreviations in this figure are: (AOM) acousto-optic modulator; (BS) beam sampler; (FC) fiber collimator; (L) lens; (PD) photodetector; (Pol) polarizer; (SMF) single-mode optical fiber; (VC) vapor cell; ($\lambda/2$) half-wave plate; ($\lambda/4$) quarter-wave plate.	131
7.7 Optics for polarization control of the 1450 nm ECDL. Abbreviations in this figure are: (BS) beam sampler; (ChW) beam chopper wheel; (IF) interference filter; (Iso) optical isolator; (L) lens; (PD) photodetector; (Pol) polarizer; (VC) vapor cell; ($\lambda/2$) half-wave plate in a rotation stage.	133

Figure	Page
7.8 Absorption spectra for (a) parallel polarization and (b) perpendicular polarization, at a detuning of $\Delta/2\pi = 107.5 \text{ cm}^{-1}$. The black dots are experimental data while the red curve is the least-squares Gaussian fit to the data. With a laser frequency scan rate of $\sim 2.0 \text{ GHz/sec}$, the total frequency width of these plots is $\sim 1.0 \text{ GHz}$. The ratio of peak heights at this detuning is $S_{\parallel}/S_{\perp} \approx 5.35$	136
7.9 (a) The ratio of peak heights S_{\parallel}/S_{\perp} as a function of detuning $\Delta/2\pi$. The lower (red) curve is for the $4 \rightarrow 4$ transition while the upper (blue) curve is for the $3 \rightarrow 3$ transition. The data points are the experimental data, with error bars showing 1σ uncertainties. (In many cases, the uncertainties are smaller than the data point size.) The smooth lines show the best fit plots of Equations (7.13)-(7.14), with $R = 1.5272$ the only adjustable parameter. (b) Residuals, showing the difference between data points and the fitted curve in (a). $4 \rightarrow 4$ residuals are shown with an \times , while $3 \rightarrow 3$ residuals are shown with an open circle (\circ). This figure is reproduced from [57].	143
8.1 Figure summarizing the uncertainties in the reduced dipole matrix elements between the lowest four cesium states. With our recent efforts measuring the $6S_{1/2} \rightarrow 6P_J$ and $6P_J \rightarrow 7S_{1/2}$ matrix elements, all uncertainties have been reduced under 0.2%. Combined, these matrix elements comprise 98.5% of the sum over states contributions to α	154
A.1 This figure shows the $6S \rightarrow 7S$ energy levels. The 6S hyperfine splitting is exact, 7S hyperfine splitting is from [60], while the energy level difference is from [132].	175
B.1 This diagram shows the lowest energy levels (for S, P and D orbitals) of Cs-133. Data for the energy levels is from the NIST database, while hyperfine splitting data is from a variety of sources. I have listed the hyperfine splitting of the $6P_j$ and $7P_j$ states are in the lower right corner.	177

ABSTRACT

Toh, George Ph.D., Purdue University, August 2019. Progress Towards a New Parity Non-Conservation Measurement in Cesium-133. Major Professor: Daniel S. Elliott.

Atomic parity violation measurements provide a way to probe physics beyond the Standard Model. They can provide constraints on conjectures of a massive Z' boson or a light boson, or searches of dark energy. Using the two-pathway coherent control technique, our group plans to make a new measurement of the weak interaction induced parity non-conservation (PNC) transition moment (E_{PNC}) on the cesium $6S \rightarrow 7S$ transition. We will coherently interfere a 2-photon transition with the Stark and PNC transitions to amplify and extract the PNC amplitude. Previously, our lab has measured the magnetic dipole transition moment on the same $6S \rightarrow 7S$ transition to about 0.4% uncertainty using this technique. In this dissertation, I discuss improvements made to the system, and review what future upgrades are needed for a new E_{PNC} measurement. Key systematics are also described. For an accurate determination of E_{PNC} , properties of cesium such as the scalar (α) and vector (β) transition polarizabilities are needed. I present improved determinations of key electric dipole matrix elements, and calculate new high precision determinations of α and β . Finally, using β and the previously measured value of E_{PNC}/β , I calculate new values for the weak charge of the cesium nucleus Q_w .

1. INTRODUCTION

1.1 History of Parity Violation

Parity non-conservation (PNC) or parity violation (PV) was first proposed in the mid-1950s by Tsung-Dao Lee and Chen-Ning Yang [1]. Previously, experiments had shown that parity was conserved for the strong interaction and the electromagnetic interaction. While examining meson decays, Lee and Yang realized that parity non-conservation could explain a strange puzzle in particle physics [1]. They brought their ideas for an experiment to Madam Chien-Shiung Wu, who in 1957 [2] confirmed using Cobalt-60 that parity is not conserved for beta decay. Madam Wu found that the directionality of electron emission was different in the mirror-reversed arrangement. This is contrasted against the predicted direction of beta emission if parity were conserved, shown in Figure 1.1.

PNC in atoms is due to the exchange of the Z^0 boson between an electron and a quark and is due to the weak interaction [3–6]. This is analogous to the exchange of a photon between a quark and an electron due to the electromagnetic force.

The weak interaction between the nucleus and electrons causes perturbations to atomic eigenstates, weakly mixing electronic states of opposite parity. Thus, the weak interaction results in optical transitions between atomic states of the same parity. For example, the $6S \rightarrow 7S$ 1-photon optical transition in Cs is typically forbidden by selection rules, but becomes weakly allowed due to this weak interaction.

We propose to use the two-color coherent control techniques pioneered in our lab [7–11] for a new more precise measurement of the PNC transition amplitude in cesium. In this dissertation, I discuss progress made towards this goal, and my contributions toward more precise determinations of cesium properties necessary for PNC measurements.

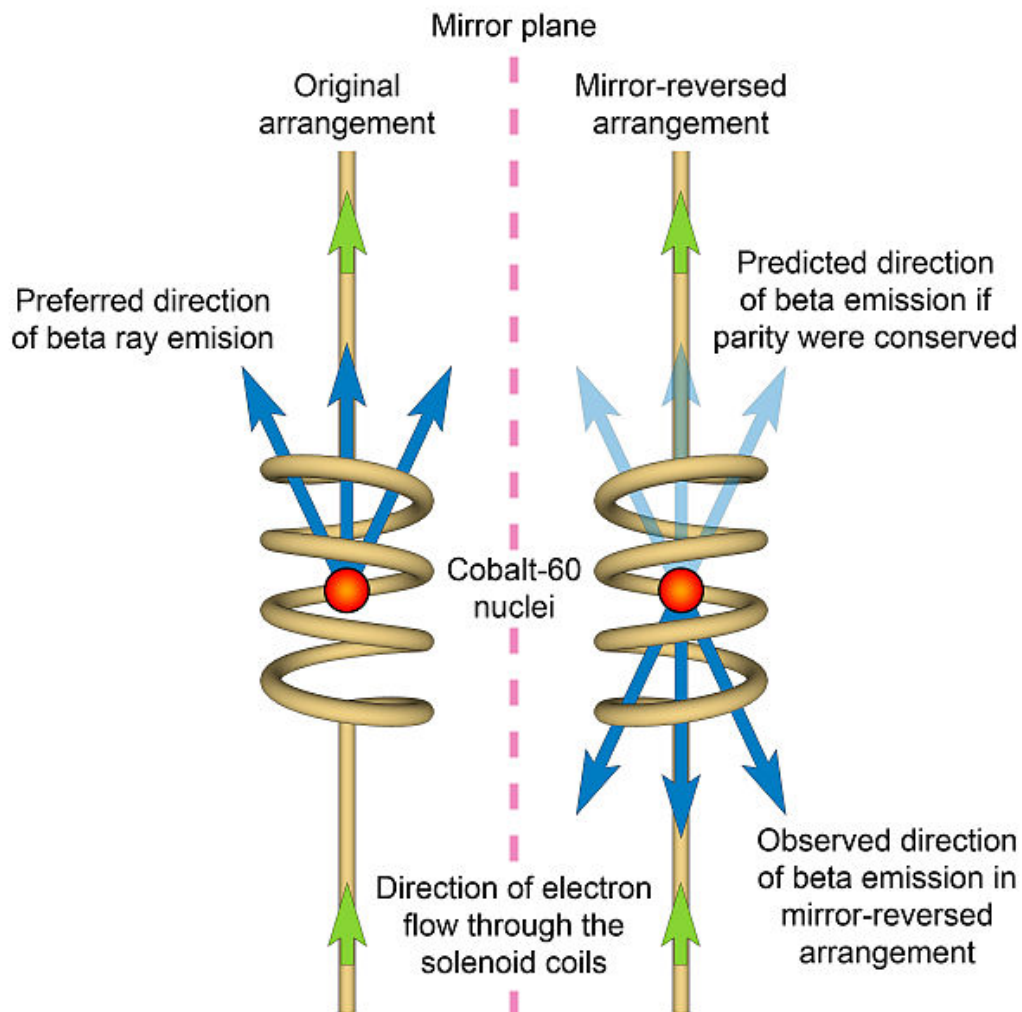


Fig. 1.1. Image of the Wu experimental setup in 1957. In the mirror-reversed arrangement, we expect beta emission to be preferentially up (direction of current flow) if parity is conserved. It was found experimentally that the opposite was true, that beta emission was preferentially down, indicating that parity is not conserved for beta emission. Image from Wikipedia.

1.2 Weak charge and Physics beyond the Standard Model

Parity violating (PV) transitions in atomic systems play a role defining constraints on new frontiers of physics beyond the Standard Model [3–6]. Atomic parity violation (APV) measurements can place constraints on conjectures of a massive Z' boson [12–16], a light boson [17,18] or in the search of dark energy [17,19,20]. PV measurements have also yielded determinations of the weak charge Q_w in various atoms, been used to find the anapole moment of the nucleus of an atom and to determine the weak mixing angle θ_w . Ref. [6] is a great review of the various approaches being undertaken in atoms and molecules to search for new physics, and has a nice chapter about current generation atomic parity violation experiments.

The weak mixing angle (or Weinberg angle) θ_w of the nucleus is related to the weak charge through the following equation [3,21]:

$$Q_w \approx -N + Z(1 - 4\sin^2\theta_w) \quad (1.1)$$

where N denotes the number of neutrons in the nucleus and Z the number of protons. For the cesium atom, $Z = 55$ and $N = 78$. Recent theoretical searches [19,20,22] for dark matter posit the existence of a light dark boson Z_d that decays mainly into dark matter, but weakly interacts with standard model matter. The existence of this light dark boson would affect the weak mixing angle θ_w at low collision energies.

Figure 1.2 from [20] shows the variation of $\sin^2\theta_w$ with collision energy. The solid black curve shows the Standard Model (SM) prediction, and the data points show several experimental measurements at various collision energies. The shaded areas in the figure show the range of $\sin^2\theta_w$ for the mass of the dark boson $m_{z_d} = 50$ MeV (green), 100 MeV (blue) and 200 MeV (red). The datapoints labeled in the figure are: APV(Cs) - Atomic parity violation in cesium, E158 - polarized electron-electron scattering asymmetry, Q_w - measurement of the weak charge of the proton by electron-proton deep inelastic scattering, $\nu - DIS$ - neutrino-nucleon scattering, LEP - forward-backward asymmetry in Z boson decay, and SLAC - electron-positron scattering asymmetry. As we can see from the figure, the most precise atomic parity

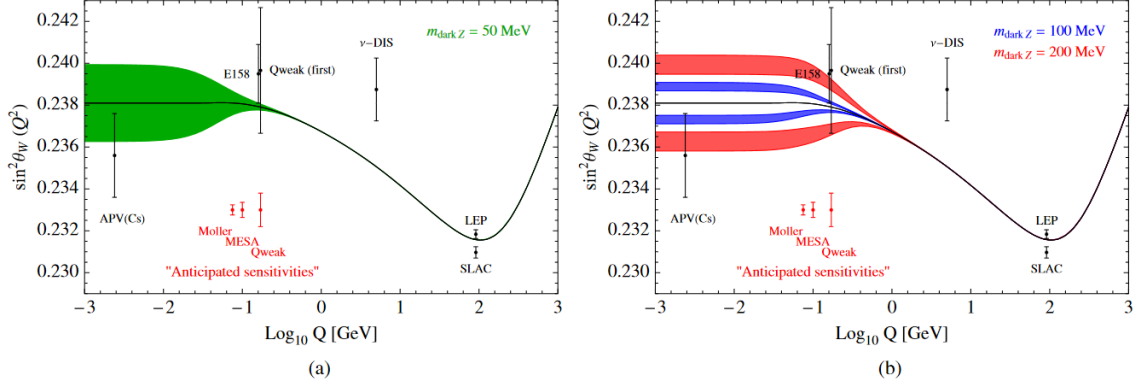


Fig. 1.2. Running of the effective weak mixing angle with energy scale Q . The black curve is the SM prediction. The colored curves are predictions for a dark Z for mass (a) 50 MeV (green), (b) 100 MeV (blue) and 200 MeV (red). Image from [20].

violation measurement to date (APV(Cs)) is not sufficient to verify a shift in $\sin^2\theta_w$ or to differentiate between the various possibilities of the mass of the Z_d boson.

1.3 PNC in atomic systems

The PNC effect has been measured in several atomic systems including cesium [23–29], bismuth [30], lead [31, 32], thallium [33, 34] and ytterbium [35–40]. We also know of efforts to measure the effect in francium [41] and dysprosium [42]. Efforts have also been made to measure the PNC effect in ions of Ba^+ [43–45], Ra^+ [46, 47] and Yb^+ [48]. The PNC amplitude is quantified by the parity nonconserving matrix element E_{PNC} , and more details are in Section 2.3.3. In Table 1.1, we have included the most precise measurements of E_{PNC} for some of these systems.

Because the amplitude of E_{PNC} is so small, it is difficult to make a direct measurement of the PNC amplitude. Instead, experimentalists have mainly used two different techniques to measure this weak transition amplitude. The first technique is an interference technique, where E_{PNC} is interfered with the Stark or magnetic dipole

transition to amplify the signal. This method was used to great success with cesium in 1997 and later on in ytterbium in 2019 (see Table 1.1). In these two cases, E_{PNC} was measured relative to β the vector transition polarizability. β characterizes the transition amplitude when a static electric field is applied, and is a parameter that has to be accurately measured to determine E_{PNC} .

The other commonly used technique for measurement of E_{PNC} is optical rotation (labeled ‘Optical Rotation’ in Table 1.1). In this scheme, the rotation in polarization of a laser beam propagating through the atomic medium is measured. For bismuth, lead and thallium, E_{PNC} was measured relative to M , the magnetic dipole transition moment. Like β , M has to be accurately measured for an accurate determination of E_{PNC} . For these, other measurements to determine the value of M or β are needed in conjunction with a ratio measurement of E_{PNC} . We discuss measurements made to improve the precision of β later in this thesis.

After we determine a value of E_{PNC} , we must know the dependence of E_{PNC} on Q_w . They have the relationship:

$$E_{PNC} = k_{PNC} \cdot Q_w \quad (1.2)$$

where k_{PNC} is a proportionality factor which has to be determined by precise atomic theory calculations. Fortunately, the atomic structure of cesium is extremely well

Table 1.1
Best measurements of E_{PNC} in various atomic systems.

Atom	Year	Uncertainty	Technique	Ref.
Cs	1997	0.35%	Stark Interference	[28]
Yb	2019	0.5%	Stark Interference	[40]
Bi	1991	2%	Optical Rotation	[30]
Pb	1995	1.1%	Optical Rotation	[31]
Th	1995	1.1%	Optical Rotation	[34]

known due to it being an alkali atom with a single valence electron around a tightly bound inner core. This is one advantage cesium has over other atomic systems such as Yb. Theoretical modeling of the cesium atomic system has improved by a lot over the years, encouraged by the precise E_{PNC} measurements of [28, 29] in cesium. However, the two most recent determinations of k_{PNC} [13–15] do not quite agree with one another, differing by 0.8%. In [13, 14], Porsev *et al.* reported the results of their coupled-cluster method calculations, including correlations up to valence triple excitations and published a result of $k_{PNC} = -0.8906 (24) iea_0/N \cdot 10^{-11}$ with precision of 0.27%. However, a subsequent 2012 analysis by Dzuba *et al.* [15] reported corrections by the core and highly-excited states, publishing a new result of $k_{PNC} = -0.8977 (40) iea_0/N \cdot 10^{-11}$ with precision of 0.45%. We have heard from A. Derevianko that he is submitting a grant proposal to conduct new calculations which would take into account these corrections, and potentially resolve the 0.8% difference.

1.4 Nuclear spin independent and dependent components

The primary weak interaction in atomic systems is due to the neutral current vector (V_n) coupling to the nucleus and the electron axial vector coupling (A_e) mediated through the exchange of the neutral Z^0 boson [3]. It was first suggested in 1974 that parity violating transitions could be observed in atoms [23, 24]. When the weak force interaction is not present, eigenfunctions of atoms are purely even or purely odd. Transitions between atomic states due to optical fields must obey selection rules depending on the symmetry of the transition (electric dipole transition (E1), magnetic dipole transition (M1) or the electric quadrupole transition (E2) for example). The weak interaction causes the mixing of atomic states of opposite parity. This means that transitions forbidden in the absence of the weak force interaction can become weakly allowed. Measuring the weak force induced transition amplitude E_{PNC} thus gives us a way to determine the weak force using laser techniques in a table-top laboratory setting.

The Hamiltonian for the parity violation interaction has a large contribution that is nuclear spin-independent (NSI) and is characterized by the weak charge of the nucleus Q_w . A smaller contribution that depends on the nuclear spin \vec{I} is largely due to the nuclear anapole moment (κ) [3]. We term this other contribution the nuclear spin-dependent (NSD) component of the PV interaction. The PV Hamiltonian is of the form [3]:

$$H_w = \frac{G}{\sqrt{8}} \rho(r) \left\{ \kappa \vec{\alpha} \cdot \vec{I} - Q_w \gamma_5 \right\} \quad (1.3)$$

where G is the Fermi constant, $\rho(r)$ is the nuclear density, κ is the nuclear anapole moment, $\vec{\alpha}$ is a product of Dirac matrices, \vec{I} is the nuclear spin, Q_w is the weak charge, and γ_5 is a Dirac matrix. As we can see, equation (1.3) has a nuclear spin-dependent term, and a negative nuclear spin-independent term.

The NSD component of the PV interaction has three main components, the largest being due to the nuclear anapole moment. The vector electron (V_e) and axial nucleus (A_n) Z^0 boson exchange, and combined effects due to the hyperfine interaction and (V_n, A_e) current also contribute [3]. The nuclear anapole moment is due to parity violating interactions within the nucleus. It was measured in [28], but with poor precision, and theoretical efforts to understand the result have not been successful [3, 49–51]. The measurement of E_{PNC} on various hyperfine lines could reveal the anapole moment, and comparisons between different isotopes of the same species could remove the dependence of this determination on precise atomic theory. The authors of reference [40] were successful in measuring E_{PNC} in four even isotopes of Yb-170 – 176 to precisions of $\sim 0.5\%$. Their results confirm the “isotopic variation of the weak force between the nucleus and valence electrons,” and electroweak theory prediction regarding “weak charge scaling with number of neutrons,” see Equation (1.1). Efforts are also underway in a multitude of other atomic systems including Tl [34], Fr [41], Ba⁺ [43–45], Ra⁺ [46, 47] and Yb⁺ [48]. In parallel with the experiment being discussed in this dissertation, Jungu Choi from our group is working on a more precise measurement of the anapole moment on the cesium ground hyperfine states.

The NSI component of the PV interaction, which is the majority contributing factor to the interaction, is due to the so-called weak charge Q_w of the atom. A precise measurement of the NSI component allows us to determine the value of Q_w , and extract the weak mixing angle θ_w . To date, the best measurement of the NSI component of the PV interaction is by [28]. They measured the E_{PNC}/β ratio on two hyperfine transitions: the 6S $F=3 \rightarrow 7S F=4$ (3-4) and the 6S $F=4 \rightarrow 7S F=3$ (4-3) transitions. A weighted average of the ratios for the 3–4 and 4–3 transitions resulted in a precision of E_{PNC}/β of 0.35%. We discuss the details from that experiment in Section 1.5.

1.5 1997 Measurement of E_{PNC} in cesium 6S \rightarrow 7S transition

The best measurement to date of E_{PNC} in an atomic system is by the Boulder group [28, 29]. An astonishing effort over two decades by Carl E. Wieman’s group [25–29], the ratio $E_{PNC}/\beta = -1.5935(56)$ mV/cm was measured to an impressive precision of 0.35%. In our experiment, which is conducted on the same 6S \rightarrow 7S transition in atomic cesium, we borrow many of the same experimental techniques the Boulder group pioneered. In this section, we summarize the experimental details of their measurement, which in addition to [28, 29], come from the PhD. thesis of Christopher S. Wood [52].

Figure 1.3 shows the experimental setup for the E_{PNC} measurement in cesium of the Boulder group [28]. An atomic beam of cesium atoms passes through three regions of interaction. The first region is the optical pumping region, where the atoms are prepared in a specific (F, m) state, and one of the two ground hyperfine levels of cesium is emptied of atoms. The second region is the interaction region where the power build-up cavity (PBC) amplifies the intensity of the 540 nm laser beam. Segmented electric field plates give a static electric field along the x direction. The parity violating transitions occur within this interaction region, and a fraction of atoms that undergo a transition will decay to the previously empty ground hyperfine

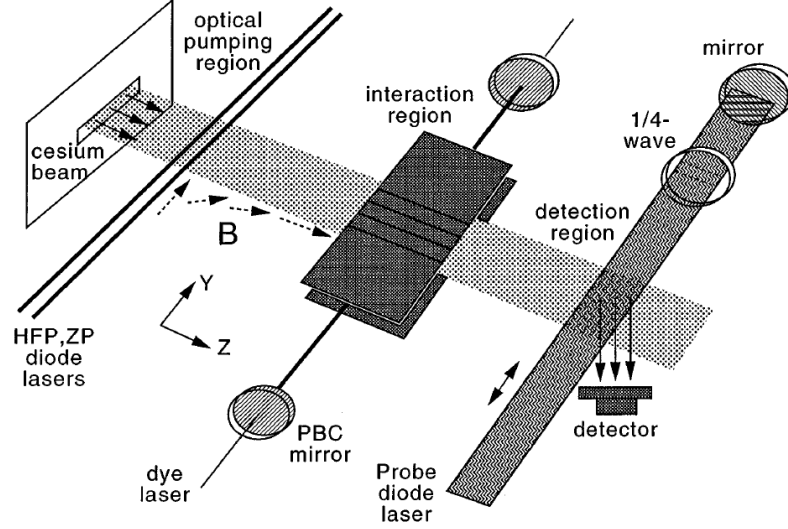


Fig. 1.3. Experimental setup for the measurement of E_{PNC} in cesium by [28]. The atomic beam passes through three regions of interest: optical pumping, interaction and detection. PBC - power build-up cavity.

state. Finally, the atomic beam passes through the detection region where the number of atoms in the initially empty ground hyperfine state now tell us the number of atoms that underwent a transition in the interaction region.

The E_{PNC} amplitude is very weak, and extremely difficult to measure directly. In [28], the E_{PNC} amplitude is interfered with a Stark amplitude 10^5 times larger which amplifies the signal. By using multiple different parity reversals, they were able to detect and eliminate potential systematic errors and isolate the parity violating effect. The result was E_{PNC}/β measured on two different hyperfine transitions:

$$\frac{Im(E_{PNC})}{\beta} = \begin{array}{ll} -1.5576(77) \text{ mV/cm} & 6S \ F = 3 \rightarrow 7S \ F' = 4 \\ -1.6349(80) \text{ mV/cm} & 6S \ F = 4 \rightarrow 7S \ F' = 3 \end{array} \quad (1.4)$$

By averaging the two, the nuclear spin-independent result was $E_{PNC}/\beta = -1.5935(56)$ mV/cm, a precision of 0.35%. Taking the difference resulted in 0.077(11) mV/cm which is the nuclear spin-dependent component. The uncertainties they reported were dominated by statistical uncertainty (versus systematic uncertainties).

As mentioned earlier, in the experiment discussed in this dissertation, we use many of the same techniques developed by the Boulder group. Dionysios Antypas [53] has put together much of the equipment for our lab, and in 2013 successfully measured the magnetic dipole transition in cesium [54]. This will be discussed in Section 1.6.

1.6 Measurement of weak transition moments with two-pathway coherent control

We plan to measure the PNC amplitude in atomic cesium using the two color two pathway coherent control techniques pioneered by our lab [7–11]. In this subsection, we discuss some of the earlier work that has been done by M. Gunawardena and D. Antypas to demonstrate the effectiveness of this technique for measuring weak transition moments.

In 2007, M. Gunawardena and Elliott demonstrated the use of coherent control with CW lasers by using it to measure the strength of the Stark-induced transition on the $6S \rightarrow 8S$ transition in atomic cesium [10,11]. A pair of phase coherent laser fields at 822 nm (fundamental) and 411 nm (second harmonic) drive the cesium $6S \rightarrow 8S$ transition through a strong two-photon transition and a much weaker Stark-induced transition. By varying the phase difference $\Delta\phi$ of the two laser fields, they amplified the Stark induced transition by greater than two orders of magnitude.

In 2013, our group made a second demonstration of the effectiveness of two-pathway coherent control by measuring the magnetic dipole transition amplitude (A_{M1}) on the cesium $6S \rightarrow 7S$ transition [54,55]. In that experiment, a 1079 nm laser driving a strong two-photon transition was interfered with a 540 nm laser driving the weak magnetic dipole M1 transition. The experimental setup is shown in Figure 1.4

The atomic beam is first prepared into a specific (F, m) state, before passing through the interaction region, and finally the detection laser is used to measure the number of atoms making the transition in the interaction region. Many of the techniques including atomic state preparation and detection are the same for the PNC

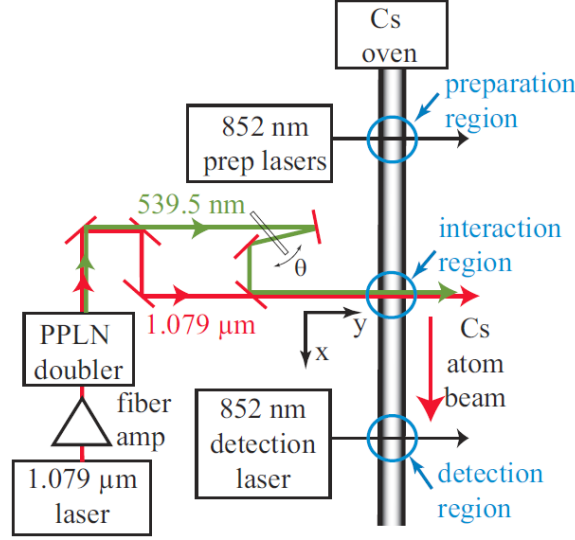


Fig. 1.4. Experimental setup for the measurement of the magnetic dipole moment in cesium [55]. The phase between the green 539.5 nm laser and the infrared 1079 nm laser is varied by turning an optical flat in the path of the green beam.

experiment and their details will be discussed in the next chapter. The phase between the two lasers $\Delta\phi_{scan}$ is scanned by turning an optical flat in the path of the green beam, changing its path length. Changing the phase difference modulates the total transition rate, resulting in a detected signal like shown in Figure 1.5(a) (with large dc offset due to the two-photon transition removed). As the applied static electric field is increased, the amplitude $K(E_y)$ of the modulation increases, as shown in Figure 1.5(b) where $E_y = 75.09$ V/cm. Finally, by plotting the curve of $K(E_y)/K(0)$ for multiple values of E_y , we get the hyperbola shown in Figure 1.5(c). Fitting the hyperbola to the data, we can extract the value of the magnetic dipole transition moment A_M .

The weak magnetic dipole transition amplitude A_M was measured to a precision of 0.37% [54], demonstrating that the two-color two pathway coherent control technique is good for measuring weak transition amplitudes. In the rest of this report, we go

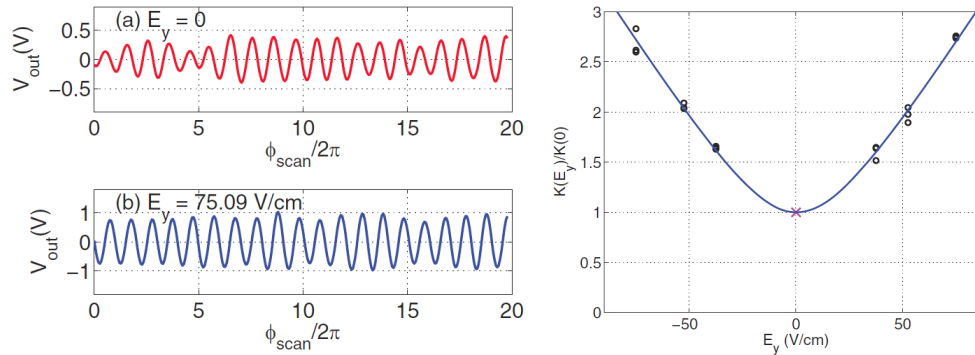


Fig. 1.5. Measured signal from the M1 magnetic dipole experiment. Left: The modulating part of the measured waveform as the phase difference $\Delta\phi_{scan}$ is scanned for (a) $E_y = 0$ V/cm and (b) $E_y = 75.09$ V/cm. Right: A plot of $K(E_y)/K(0)$ against E_y . The circles represent data points while the solid line is the curve of best fit. Images from [55].

over the details for a measurement of the parity non-conserving transition amplitude in the same $6S \rightarrow 7S$ transition in atomic cesium.

1.7 Summary of my contributions towards a new PNC measurement

In this dissertation, I discuss my contributions towards a new PNC measurement in cesium on the $6S_{1/2} \rightarrow 7S_{1/2}$ transition. Roughly, these contributions can be split into two broad categories: (a) improvements made to the PNC experimental apparatus; (b) measurements and more precise determinations of cesium properties. These will be covered in more detail later in this dissertation.

(a) Improvements to PNC apparatus I discussed in Section 1.6 how our group measured the magnetic dipole transition amplitude on the $6S_{1/2} \rightarrow 7S_{1/2}$ transition. To measure the PNC amplitude, many changes will have to be made, most critically the implementation of a laser power build-up cavity (PBC) to increase the intensity of laser light within the interaction region. I discuss the progress made towards building a PBC in Section 4.6.

Next, we will need to be able to lock the 1079 nm laser to the PBC via Pound-Drever-Hall (PDH) frequency stabilization. In Section 4.5, I discuss the success I have had locking the laser to a stable invar cavity, and progress made locking the 1079 nm laser to a prototype PBC.

Finally, I discuss improvements to the detection laser in Section 4.1, and noise reductions of the detection photodiode and gain stage in Sections 4.2 and 4.3.

(b) Atomic properties A measurement of E_{PNC} by itself is not sufficient to determine a value for the weak charge Q_w . Precise determinations of the transition polarizabilities α and β , and atomic theory calculations are necessary as well. We have undertaken a series of measurements of polarizabilities and reduced dipole matrix elements of critical cesium transitions.

In Chapter 6, we discuss a precise measurement of the lifetime of the $7S_{1/2}$ state [56]. Combined with a measurement of the $7S_{1/2}$ branching ratio [57], discussed in Chapter 7, we can determine precise reduced electric dipole matrix elements for $\langle 7S_{1/2} || r || 6P_J \rangle$ and $\langle 7S_{1/2} || r || 7P_j \rangle$. I have also measured the static polarizability of the $7P_J$ states [58], but this measurement is not discussed in this dissertation.

We tie up our contributions to cesium properties in Chapter 8, where we report newly calculated values for α and β in Section 8.4. Using our more precise determination of β , combined with the measurement of E_{PNC}/β , we can then calculate a new value of Q_w , which we report in Section 8.5.

2. THEORY

In this chapter, theory necessary to understand the PNC experiment is discussed. We begin with a discussion of cesium atomic structure and go over the hyperfine and Zeeman splitting of the energy levels relevant to the experiment. This is followed by a discussion of the various transition amplitudes that are possible for the $6S \rightarrow 7S$ transition. Finally, we discuss how the interference of the various transition amplitudes affects the total excitation rate of cesium atoms.

2.1 Cesium atomic structure

Cesium-133 (^{133}Cs) contains one valence electron and is the heaviest stable alkali atom. The PNC amplitude is roughly proportional to Z^3 , where Z is the atomic number [23, 24]. Because of previous PNC measurements in cesium and due to the simple electronic structure, cesium has been well studied by theorists, and calculations have reached the 0.3% level [13, 14]. The ^{133}Cs atom is thus well suited for probing weak interactions via atomic parity violation measurements.

For the PNC measurement, we are interested in the $6S \rightarrow 7S$ transition in cesium. The cesium $6S \rightarrow 7S$ transition has a one-photon resonant frequency of 555 682 GHz, corresponding to a laser wavelength of 539.5 nm. The 7S excited state natural lifetime was previously measured to be approximately 48.5 ns [59], leading to a 3.3 MHz natural transition linewidth. In this thesis, we report a more precise measurement of the lifetime $\tau_{7S} = 48.28(7)$ ns. ^{133}Cs has a nuclear spin of $I=7/2$ resulting in each of the cesium nS states having $F=3$ and $F=4$ hyperfine levels. The ground 6S hyperfine levels are split by exactly 9.192 631 770 GHz while the excited 7S hyperfine levels have a splitting of 2.18 GHz [60], see Figure A.1 in Appendix A for a detailed energy level diagram. Each of the hyperfine levels is $2F + 1$ degenerate, where $F = I + L + S$

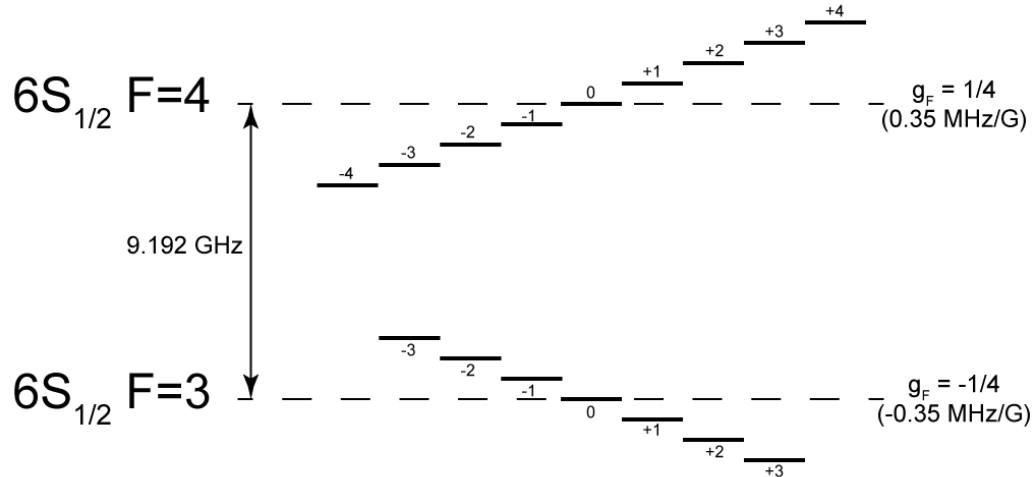


Fig. 2.1. This figure shows the Zeeman splitting of the cesium $6S_{1/2}$ ground states in the presence of an applied dc magnetic field.

is the total angular momentum of the atom (L being the orbital angular momentum, S is the spin angular momentum). Thus, the $F=3$ hyperfine level has $2F + 1 = 7$ Zeeman sublevels (Figure 2.1), while the $F = 4$ hyperfine level has $2F + 1 = 9$ Zeeman sublevels. We denote the Zeeman sublevels by m .

To lift the degeneracy of the Zeeman sublevels, we can apply a magnetic field, which will cause the states to shift by:

$$\Delta E = mg_F \mu_B B_z$$

where g_F is the Lande g-factor, μ_B is the Bohr Magnetron and B_z is the magnetic field applied. This results in a -0.35 MHz/G splitting between consecutive Zeeman levels for the $F=3$ hyperfine level and $+0.35 \text{ MHz/G}$ for $F=4$.

2.2 Electric dipole matrix elements

Dipole matrix elements characterize the strength of interaction between cesium and nearly-resonant optical radiation [61]. For example, the matrix element coupling the $|6S_{1/2} F m\rangle$ ground state to the $|6P_{1/2} F' m'\rangle$ excited state will be written as

$$\langle 6S_{1/2} F m | r | 6P_{1/2} F' m' \rangle.$$

As described in the previous section, F and m here stand for the hyperfine level and Zeeman sublevel of the initial $6S_{1/2}$ state respectively. The primed variables denote the excited state.

It is convenient to factor out the angular dependence and re-write the dipole matrix element as the multiplication of a Clebsch-Gordan coefficient and a reduced matrix element. For a matrix element between two atomic states $|\gamma F m\rangle$ and $|\gamma' F' m'\rangle$, we use the Wigner-Eckart theorem to obtain

$$\langle \gamma J F m | r | \gamma' J' F' m' \rangle = (-1)^{F'-m'} \begin{pmatrix} F' & 1 & F \\ -m' & q & m \end{pmatrix} \langle \gamma J F || r || \gamma' J' F' \rangle, \quad (2.1)$$

which shows how the moments vary with projection quantum number m [62]. The 3 by 2 matrix within the parentheses is the Wigner $3-j$ symbol. Since r acts only on the electronic angular momentum, we can further reduce this using

$$\begin{aligned} \langle \gamma J F || r || \gamma' J' F' \rangle &= (-1)^{J+I+F'+1} [(2F+1)(2F'+1)]^{1/2} \\ &\times \begin{Bmatrix} J & F & I \\ F' & J' & 1 \end{Bmatrix} \langle \gamma J || r || \gamma' J' \rangle. \end{aligned} \quad (2.2)$$

Here, $I = 7/2$ is the nuclear spin, and the array inside the brackets is the Wigner $6-j$ symbol. Now, the reduced dipole matrix element $\langle \gamma J || r || \gamma' J' \rangle$ is independent of F and m , which can be easily calculated for any particular transition. An example is $\langle 6P_{1/2} || r || 6S_{1/2} \rangle$ which is the reduced dipole matrix element for the D1 transition $6S_{1/2} \rightarrow 6P_{1/2}$.

Depending on the normalization conventions, the magnitudes of reported reduced dipole matrix elements can be different. The convention we present here is the same

as used by many theorists [21, 62–64] and experimentalists [65–68]. The cesium D line data paper by Steck [61] uses a different convention. To convert the reduced matrix elements in that paper to match those reported here, we need to multiply his listed numbers by $\sqrt{2}$. The Flambaum group at the University of New South Wales (UNSW) reports radial integrals $\langle s|r|p_J \rangle$ instead of reduced matrix elements [69–72]. The conversions, Equations (4) and (5) of Ref. [70], are

$$\langle s||r||p_{1/2} \rangle = \langle p_{1/2}||r||s \rangle = \sqrt{2/3} \langle s|r|p_{1/2} \rangle, \quad (2.3)$$

$$\langle s||r||p_{3/2} \rangle = -\langle p_{3/2}||r||s \rangle = \sqrt{4/3} \langle s|r|p_{3/2} \rangle. \quad (2.4)$$

Finally, we discuss the relative sign convention for our reduced dipole matrix elements. We use the usual convention where the $\langle 6S_{1/2}||r||6P_J \rangle$ matrix elements are positive. This results in positive matrix elements for $\langle 6S_{1/2}||r||nP_J \rangle$, and positive $\langle 7S_{1/2}||r||nP_J \rangle$ except $\langle 7S_{1/2}||r||6P_J \rangle$ which are negative. In Equations (2.3) and (2.4), the reader may have noticed that switching the order of initial and final states leads to a change in sign when $J = 3/2$, but not when $J = 1/2$. Re-writing these reduced matrix elements in our notation, we obtain the relations

$$\langle mS_{1/2}||r||nP_{1/2} \rangle = \langle nP_{1/2}||r||mS_{1/2} \rangle, \quad (2.5)$$

$$\langle mS_{1/2}||r||nP_{3/2} \rangle = -\langle nP_{3/2}||r||mS_{1/2} \rangle. \quad (2.6)$$

In our collaboration with Prof. Safronova, she used lowest-order Dirac-Hartree-Fock (DHF) calculations to verify these signs discussed here.

2.3 Transition amplitudes

We are interested in the same $6S \rightarrow 7S$ transition in cesium as the Boulder group [26, 28, 29]. The 6S and 7S energy levels have the same parity, and therefore the transition between these states is electric dipole forbidden. However, in the presence of static electric and magnetic fields, several weaker interactions are allowed:

1. A_{ST} – Stark-induced transition amplitude

2. A_{M1} —Magnetic dipole transition amplitude
3. A_{E2} —Electric quadrupole transition amplitude
4. A_{PNC} —Weak-induced parity non-conserving transition amplitude
5. A_{2P} —Two-photon interaction transition amplitude

In particular, the A_{M1} , A_{E2} and A_{PNC} transition amplitudes are very small, and are particularly difficult to measure directly. In this section, we discuss these transition amplitudes, and follow up with a discussion of the math behind the two-pathway coherent control technique to be used.

2.3.1 Stark amplitude

The Stark transition becomes allowed when an electric field is applied to the atomic system, causing a mixing of states of opposite parity through the dipole interaction. The Stark amplitude for the cesium $|6S_{1/2} F m\rangle$ to $|7S_{1/2} F' m'\rangle$ transition has the form:

$$\begin{aligned}
 A_{ST} &= \langle \overline{7S_{1/2}, F', m'} | -d \cdot \varepsilon | \overline{6S_{1/2}, F, m} \rangle \\
 &= [\alpha E \cdot \varepsilon \delta_{F,F'} + i\beta(E \times \varepsilon)_z C_{Fm}^{F'm'}] \delta_{m,m'} \\
 &\quad + [\pm i\beta(E \times \varepsilon)_x - \beta(E \times \varepsilon)_y] C_{Fm}^{F'm'} \delta_{m,m' \pm 1}
 \end{aligned} \tag{2.7}$$

where α and β represent the scalar and vector transition polarizabilities (discussed in more detail in Section 2.4), ε represents the electric field of the laser and E represents the static electric field applied to the system. The coefficients $C_{Fm}^{F'm'}$ are related to the normal Clebsch-Gordon coefficients, were calculated by [26] and have been reproduced in Appendix C.

2.3.2 Magnetic dipole amplitude

The magnetic dipole transition amplitude between the 6S and 7S states is:

$$A_{M1} = \{(\hat{k} \times \varepsilon)_z \delta_{m,m'} + [\pm(\hat{k} \times \varepsilon)_x + i(\hat{k} \times \varepsilon)_y] \delta_{m,m' \pm 1}\} M C_{Fm}^{F'm'} \quad (2.8)$$

where \hat{k} is the laser propagation unit vector and M is the magnetic dipole (M1) matrix element. The M1 transition is extremely weak, and is defined as:

$$M = \left\langle 7S \left| \frac{\mu_z}{c} \right| 6S \right\rangle \quad (2.9)$$

where μ_z is the z component of the magnetic dipole operator. The value of M was measured by our group in 2013 using the two-pathway coherent control technique as a stepping stone towards the measurement of E_{PNC} . The result we obtained was $M = -4.251(16) \cdot 10^{-5} \mu_B$ [53, 54] which agreed with the earlier measurement of $M = -4.241(10) \cdot 10^{-5} \mu_B$ by [73, 74], approximately $1.5474(37) \cdot 10^{-7} e a_0$.

2.3.3 PNC amplitude

The parity non-conserving (PNC) transition amplitude has the form:

$$A_{PNC} = [\varepsilon_z \delta_{m,m'} + (\pm \varepsilon_x + i \varepsilon_y) \delta_{m,m' \pm 1}] i \text{Im}(E_{PNC}) C_{Fm}^{F'm'} \quad (2.10)$$

where E_{PNC} is the purely imaginary PNC matrix element, defined by Bouchiat and Bouchiat in [23, 24] as:

$$E_{PNC} = \sum_{n,J} \left(\frac{\langle 7S | H_W | nP_J \rangle \langle nP_J | D | 6S \rangle}{E_{7S} - E_{nP_J}} + \frac{\langle 7S | D | nP_J \rangle \langle nP_J | H_W | 6S \rangle}{E_{6S} - E_{nP_J}} \right). \quad (2.11)$$

In later publications (see for example [13–15, 21, 72, 75]), it was noted that only the $J = 1/2$ terms contribute to E_{PNC} , so the summation is reduced to

$$E_{PNC} = \sum_n \left(\frac{\langle 7S | H_W | nP_{1/2} \rangle \langle nP_{1/2} | D | 6S \rangle}{E_{7S} - E_{nP_{1/2}}} + \frac{\langle 7S | D | nP_{1/2} \rangle \langle nP_{1/2} | H_W | 6S \rangle}{E_{6S} - E_{nP_{1/2}}} \right). \quad (2.12)$$

Here, $\langle a | D | b \rangle$ are electric-dipole matrix elements. $\langle a | H_W | b \rangle$ represent the weak interaction matrix elements, which mixes S and P states. It is this mixing of odd and even parity eigenstates of the atoms that gives rise to the transition amplitude A_{PNC} .

The most accurate measurement of the transition amplitude $Im(E_{PNC})/\beta = 1.5935(56)$ mV/cm was done by the Boulder group in 1998 [28, 29, 52]. Note that because the E_{PNC} amplitude is so tiny, it was measured as a ratio of β , the vector polarizability of the transition. The most precise determination of $\beta = 26.957(51) a_0^3$ comes from a measurement of M_{hf}/β [73] and a calculation of M_{hf} by [76]. This leads to the determination $Im(E_{PNC}) = 8.387(38) \cdot 10^{-12} ea_0$, more than 18,000 times smaller than the magnitude of $M = 1.5474 \cdot 10^{-7} ea_0$.

2.3.4 Two-photon amplitude

A two photon transition amplitude has the general form:

$$A_{2P} = \left[\tilde{\alpha} \varepsilon^{\omega_1} \cdot \varepsilon^{\omega_2} \delta_{F,F'} + i \tilde{\beta} (\varepsilon^{\omega_1} \times \varepsilon^{\omega_2})_z C_{Fm}^{F'm'} \right] \delta_{m,m'} + \left[\pm i \tilde{\beta} (\varepsilon^{\omega_1} \times \varepsilon^{\omega_2})_x - \tilde{\beta} (\varepsilon^{\omega_1} \times \varepsilon^{\omega_2})_y \right] C_{Fm}^{F'm'} \delta_{m,m' \pm 1} \quad (2.13)$$

where ε^{ω_1} and ε^{ω_2} are the laser electric field amplitudes, where ω_1 and ω_2 denote the frequencies of the two optical waves. The scalar term $\tilde{\alpha}$ and vector term $\tilde{\beta}$ characterize the two-photon amplitude for polarizations of ε^{ω_1} and ε^{ω_2} parallel and perpendicular to each other, respectively. We save the discussion of $\tilde{\alpha}$ and $\tilde{\beta}$ to the next section. When the laser field driving the two photon transition consists of only a single component of frequency $\omega_1 = \omega_2 = \omega/2$ (where ω is the frequency of the forbidden one photon transition), the two photon transition amplitude is reduced to the form:

$$A_{2P} = \tilde{\alpha} (\varepsilon^{\omega_1})^2 \delta_{F,F'} \delta_{m,m'} \quad (2.14)$$

The one-color two-photon transition only drives $\Delta F = 0$ and $\Delta m = 0$ transitions, so we can safely ignore transitions where $\Delta F \neq 0$ and $\Delta m \neq 0$.

2.4 Scalar and vector transition polarizabilities, α , β

We have discussed in earlier sections that E_{PNC} is measured as a ratio of the scalar transition polarizability α or the vector transition polarizability β . α and β

are analogous to the Stark polarizability α_γ , which is the energy shift of state γ in the presence of a dc electric field. For example, we can write the Stark polarizability of the $7S_{1/2}$ state as a sum over intermediate states [63]

$$\alpha_{7S} = \frac{1}{3} \sum_n \left[\frac{|\langle 7S_{1/2} || r || nP_{1/2} \rangle|^2}{E_{nP_{1/2}} - E_{7S}} + \frac{|\langle 7S_{1/2} || r || nP_{3/2} \rangle|^2}{E_{nP_{3/2}} - E_{7S}} \right]. \quad (2.15)$$

Here, E_γ is the energy level of the labelled γ state, and we sum over all nP_J states, where the largest contributions come from $n = 6, 7$.

Similarly, the scalar transition polarizability for the $6S \rightarrow 7S$ transition can also be written as a sum over intermediate states

$$\begin{aligned} \alpha = & -\frac{1}{6} \sum_n \left[\langle 7S_{1/2} || r || nP_{1/2} \rangle \langle nP_{1/2} || r || 6S_{1/2} \rangle \right. \\ & \times \left(\frac{1}{E_{nP_{1/2}} - E_{7S}} + \frac{1}{E_{nP_{1/2}} - E_{6S}} \right) \\ & - \langle 7S_{1/2} || r || nP_{3/2} \rangle \langle nP_{3/2} || r || 6S_{1/2} \rangle \\ & \left. \times \left(\frac{1}{E_{nP_{3/2}} - E_{7S}} + \frac{1}{E_{nP_{3/2}} - E_{6S}} \right) \right] \end{aligned} \quad (2.16)$$

from [21], where we have swapped the signs of the energy denominators to keep them consistent with Equation (2.15). Considering the different signs of the reduced matrix elements as described in Section 2.2, we find that all the terms contributing to α add constructively, and its value is $\alpha \approx -270 a_0^3$. In Chapter 8, we calculate a new value of α using Equation 2.16. The result is shown in Table 8.3.

In Section 2.3.4 we first saw $\tilde{\alpha}$, which is the two-photon transition polarizability. Functionally, $\tilde{\alpha}$ is the same as α , as we shall show. We re-write the energies E_γ as frequencies ω_γ (while omitting \hbar) for convenience, and obtain

$$\begin{aligned} \tilde{\alpha} = & \frac{1}{6} \sum_n \left[\langle 7S_{1/2} || r || nP_{1/2} \rangle \langle nP_{1/2} || r || 6S_{1/2} \rangle \right. \\ & \times \left\{ \frac{1}{\omega_2 - \omega_{nP_{1/2}}} + \frac{1}{\omega_1 - \omega_{nP_{1/2}}} \right\} \\ & - \langle 7S_{1/2} || r || nP_{3/2} \rangle \langle nP_{3/2} || r || 6S_{1/2} \rangle \\ & \left. \times \left\{ \frac{1}{\omega_2 - \omega_{nP_{3/2}}} + \frac{1}{\omega_1 - \omega_{nP_{3/2}}} \right\} \right]. \end{aligned} \quad (2.17)$$

In this equation, ω_{nP_J} is the angular frequency of the denoted nP_J energy level from the 6S ground state. Compared with Equation 2.16, we have replaced the 6S and 7S energies E_γ with ω_1 and ω_2 . These denote the frequencies of the two photons exciting the atom from the 6S ground state to the 7S excited state. We use $\tilde{\alpha}$ to determine the two-photon amplitude A_{2P} , and α to determine the Stark-induced transition amplitude A_{ST} .

Next, the vector transition polarizability β , which has magnitude relative to α $|\frac{\alpha}{\beta}| \approx 10$, can be written in the following form [21]

$$\begin{aligned} \beta = & -\frac{1}{6} \sum_n \left[\langle 7S_{1/2} || r || nP_{1/2} \rangle \langle nP_{1/2} || r || 6S_{1/2} \rangle \right. \\ & \times \left(\frac{1}{E_{nP_{1/2}} - E_{7S}} - \frac{1}{E_{nP_{1/2}} - E_{6S}} \right) \\ & + \frac{1}{2} \langle 7S_{1/2} || r || nP_{3/2} \rangle \langle nP_{3/2} || r || 6S_{1/2} \rangle \\ & \left. \times \left(\frac{1}{E_{nP_{3/2}} - E_{7S}} - \frac{1}{E_{nP_{3/2}} - E_{6S}} \right) \right]. \end{aligned} \quad (2.18)$$

Note the change in signs, and the additional term of $\frac{1}{2}$ in the second half of the equation. Because of these differences from α , there is a large amount of cancellation between the various terms contributing to β . It is calculated to be $\beta \approx 27 a_0^3$. The ratio $\alpha/\beta \approx 10$ has been precisely measured in 1997 by Cho *et al.* [77] to be

$$\frac{\alpha}{\beta} = -9.905(11).$$

Precise determinations of α and β are important because measurements of E_{PNC} are always made as a ratio to either α or β . The Wieman experiment [28] as described in Section 1.5, measured E_{PNC} as the ratio E_{PNC}/β . To extract a precise value of E_{PNC} using their result, we need to know β precisely. Similarly, to determine E_{PNC} using our coherent control technique, we will measure it as a ratio of α , i.e. E_{PNC}/α . Since the ratio $\frac{\alpha}{\beta}$ is precisely known, a high precision determination of either α or β leads to precisely knowing the other. We have discussed one determination of β earlier in Section 2.3.3 from M_{hf}/β .

Finally, because α and β can be calculated as a sum of reduced matrix elements over intermediate states (Equations (2.16) and (2.18)), precise determinations of $mS \rightarrow nP_J$ matrix elements for $6 \leq m, n \leq 7$ are needed. Here $J = 1/2, 3/2$, which means we need to know 8 reduced dipole matrix elements precisely to calculate α to high precision. Combined, these 8 matrix elements contribute to $> 98\%$ of α , which is why the precision of all other terms are not as critical. In Chapter 8, we round-up the progress our group has made towards more precise determinations of these reduced matrix elements, and calculate new recommended values for α and β .

2.5 Two pathway coherent control amplitude

To measure E_{PNC} with our two pathway coherent control method, we choose an experimental geometry (Figure 2.2) that minimizes the M1 (magnetic dipole) and E2 (electric quadrupole) transition rates. The remaining two-photon, Stark and PNC amplitudes are coherently interfered. The 1079 nm and 539.5 nm optical fields propagate in the y-direction, and are linearly polarized along the z-axis. The static electric and magnetic fields also point in the z-direction. Careful control of the various field orientations and uniformity is critical as the E_{PNC} amplitude is 20,000 times smaller than A_{M1} . Small imperfections in the orientation of the fields can introduce large systematic contributions to the overall one-photon transition rate.

With the beam and field orientation in Figure 2.2, the earlier equations for A_{2P} , A_{ST} and A_{PNC} get reduced to:

$$\begin{aligned} A_{ST} &= \alpha E_z \cdot \varepsilon_z \delta_{F,F'} \delta_{m,m'} \\ A_{PNC} &= iIm E_{PNC} \varepsilon_z C_{Fm}^{F'm'} \delta_{m,m'} \\ A_{2P} &= \tilde{\alpha} (\varepsilon^{\omega_1})^2 \delta_{F,F'} \delta_{m,m'} \end{aligned}$$

In the interaction region, the sum of transition amplitudes becomes:

$$\begin{aligned} \sum A &= A_{2P} + A_{ST} + A_{PNC} \\ \sum A &= A_{2P} + \left\{ \alpha E \cdot \varepsilon_z \delta_{F,F'} + iIm(E_{PNC}) \varepsilon_z C_{Fm}^{F'm'} \right\} \delta_{m,m'} \end{aligned} \tag{2.19}$$

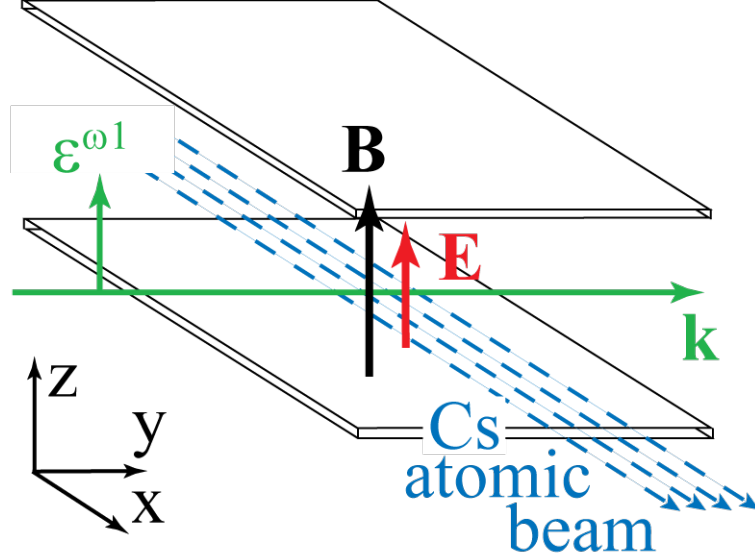


Fig. 2.2. Beam and field orientation for measurement of E_{PNC}/α . The Cs atomic beam travels along x, the 540/1079 nm beams are along y while the static electric and magnetic fields are along z.

With $m = m'$ and $F = F'$, this results in the following cesium transition rate equation:

$$W = |A_{2P}|^2 + \left(2 |A_{2P}| \varepsilon_z \sqrt{(\alpha E_z)^2 + (\text{Im}(E_{PNC}) C_{Fm}^{Fm})^2} \right) \sin(\Delta\phi + \delta\phi(E_z)) \quad (2.20)$$

$$\approx |A_{2P}|^2 + K(E_z) \sin(\Delta\phi + \delta\phi(E_z))$$

where $\Delta\phi$ is the controllable phase difference between the optical fields ω and ω_1 :

$$\Delta\phi = 2\phi^{\omega_1} - \phi^\omega$$

The overall transition rate (Eqn. 2.20) has two parts, a dc component ($|A_{2P}|^2$) and an ac component $K(E_z) \sin(\Delta\phi + \delta\phi(E_z))$. The amplitude and phase of the modulating part of the transition rate are given by:

$$K(E_z) = 2 |A_{2P}| \varepsilon_z \sqrt{(\alpha E_z)^2 + (\text{Im}(E_{PNC}) C_{Fm}^{Fm})^2} \quad (2.21)$$

$$\delta\phi(E_z) = \tan^{-1} \left(\frac{\alpha E_z}{\text{Im}(E_{PNC}) C_{Fm}^{Fm}} \right) \quad (2.22)$$

From equations (2.21) and (2.22), we see that measurements of $K(E_z)$ for various electric field strength E_z can yield the ratio $\text{Im}(E_{PNC}) C_{Fm}^{Fm}/\alpha$ and measurements

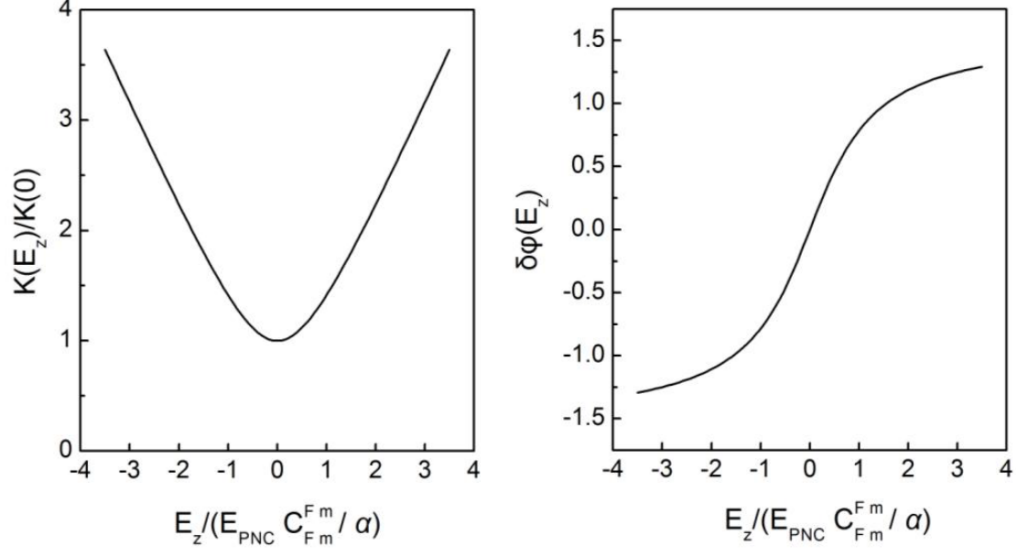


Fig. 2.3. Amplitude (left) and phase (right) of modulation in the transition rate as a function of the Stark field E_z .

of the phase shift $\delta\phi(E_z)$ for various E_z yields the sign of $Im(E_{PNC})/\alpha$. This is similar to the technique applied in Section 1.6 by [54] to measure the magnetic dipole moment.

Figure 2.3 shows the expected plots of $K(E_z)$ and $\delta\phi(E_z)$ versus E_z . In the figure, $K(E_z)$ has been re-scaled by dividing $K(E_z)$ by $K(E_z = 0)$, to obtain the ratio $K(E_z)/K(0)$. On the x-axis, we have re-scaled the electric field E_z by $Im(E_{PNC}) C_{Fm}^{Fm} / \alpha$.

3. EXPERIMENTAL APPARATUS

3.1 Overview of the experimental setup for the PNC measurement

In this chapter, we discuss the apparatus of the PNC measurement. In this overview section, we give a high-level look at how all of the equipment goes together. Each of these components is discussed in more detail in the following sections.

Figure 3.1 shows the experimental setup for the PNC measurement. On one end of the vacuum chamber, we have a cesium oven which generates a collimated beam of cesium atoms. The atoms pass through three regions of interaction with various laser beams. The first region we term the preparation region. Here, the atoms are

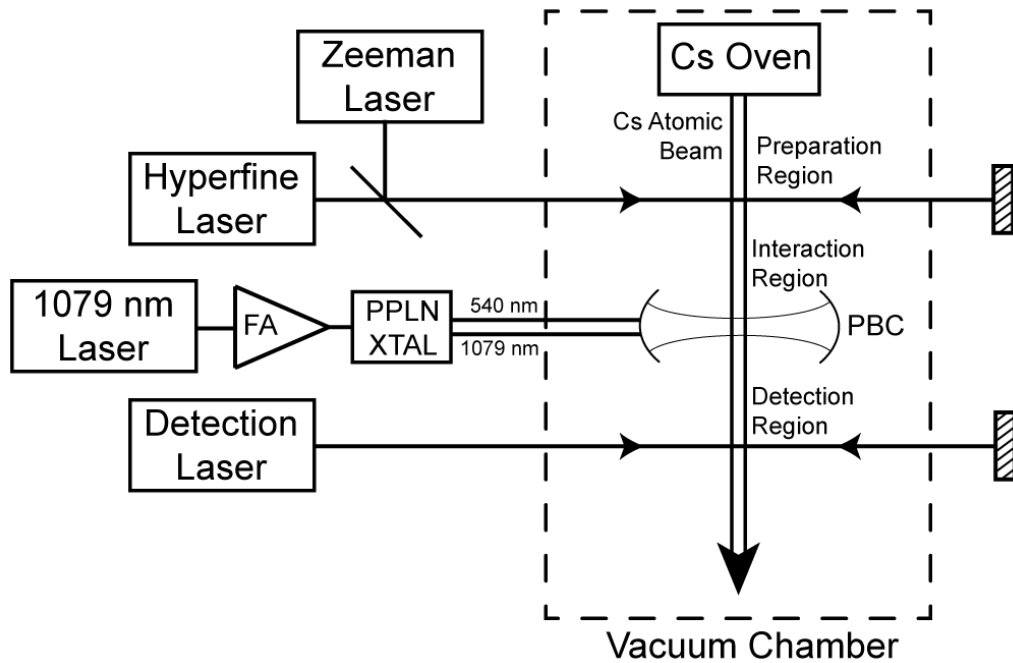


Fig. 3.1. Experimental setup for the PNC measurement. EOM - electro-optic modulator, FA - fiber amplifier, PPLN - frequency doubling crystal, PBC - power build-up cavity.

optically pumped into a specific magnetic sublevel (m state) of the cesium ground states by two lasers, the hyperfine laser, and the Zeeman laser. The linearly polarized hyperfine laser empties out one of the two hyperfine levels of the cesium ground states ($6S$ $F = 3$ or $F = 4$), while the circularly polarized Zeeman laser pumps the atoms towards the m state we target.

After passing through the preparation region, ideally all of the atoms would be in just one Zeeman m sublevel of cesium. The realities of the experiment mean we can only pump $\sim 92\%$ of the atoms into the right m sublevel. The atoms then go into the interaction region. Here, we use a power build-up cavity (PBC) to amplify the intensity of the 540¹ nm and 1079 nm laser beams. The 1079 nm laser drives a 2-photon transition on the cesium $6S \rightarrow 7S$ transition. The 1-photon transition $6S \rightarrow 7S$ is highly forbidden except due to Stark, magnetic dipole and PNC contributions, as discussed earlier in Section 2.3. We apply a small electric field to weakly allow the Stark amplitude. The interaction of the 2-photon, Stark and PNC amplitudes causes atoms to undergo a $6S \rightarrow 7S$ transition, where they then have a chance to decay down to the previously empty hyperfine ground level. To extract the PNC contribution, we modulate the phase between the 540 nm and 1079 nm lasers using a simple technique described later.

Finally, to detect our signal, the atoms fly through the detection region, where the detection laser beam is double-passed. The detection laser is an 852 nm laser tuned to one of the cesium D2 lines. Locked to a cycling transition, the laser causes atoms in the previously empty hyperfine level to fluoresce multiple times. A large area photodiode directly under the detection region picks up this fluorescence and a transimpedance amplifier outside of the vacuum chamber amplifies the output. Using a lock-in amplifier, we mix the amplified signal with the modulation frequency of the phase between the 540/1079 nm lasers to extract our final detected signal.

Since the 540 nm laser is the one driving the PNC interaction, we will have to improve the locking system from the one used by Antypas in his measurement of the

¹The actual laser wavelength is close to 539.5 nm, I round it to 540 nm for brevity.

Cs M1 amplitude [55]. We will introduce a new two-color PBC, which will hugely amplify the intensity of both the 540 nm and 1079 nm lasers. We aim for the finesse of the 540 nm cavity to be $\sim 100,000$, while the requirements for the 1079 nm laser are less stringent (only finesse ≈ 1000). With a doubly-resonant cavity, the nodes and anti-nodes of the two colors will align more precisely, a detail that is necessary for the PNC amplitude to not be attenuated.

As I mentioned at the beginning of this section, this is only a high-level overview of the experimental setup. More details can be found in the following sections and chapters.

3.2 852 nm lasers for optical pumping and detection

We have three home-made external cavity diode lasers (ECDL) at 852 nm. The hyperfine and Zeeman lasers are almost identical and are used for optical pumping. They each contain a ThorLabs L850P030 Fabry Perot laser diode which can put out up to 30 mW of laser power at a maximum current of 95 mA. Typically, we operate the laser diodes at around 55 – 70 mA, which gives about 15 – 20 mW of output laser power. The detection laser diode is a ThorLabs L852P050 50 mW Fabry Perot laser diode, which we typically drive with 50 mA of diode current. We used to drive these laser diodes with ThorLabs current controllers, the LDC202C. We have built homemade current controllers with lower noise and larger modulation bandwidth than the LDC202C. Currently, the hyperfine and Zeeman lasers are driven by these homemade current controllers. The plan going forward is to build more of these homemade controllers and replace the Thorlabs current controller for the detection laser as well.

The laser system is setup in a Littrow ECDL configuration, shown in Figure 3.2(a). Laser light from a laser diode is directed onto a diffraction grating, aligned such that some light reflected from the grating (first order diffracted beam) goes directly back into the laser chip. This optical feedback allows the user to force the frequency of the

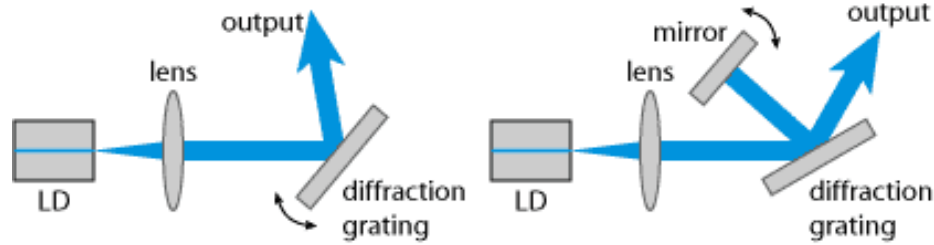


Fig. 3.2. This image from [78] shows an external cavity diode laser in: (a) Littrow configuration (b) Littman-Metcalf configuration. The Littrow configuration uses fewer components, but the Littman-Metcalf laser beam output direction remains constant as we tune the laser frequency.

laser (by tuning the angle of the diffraction grating, the user chooses what frequency of light is reflected back into the laser) to the frequency we need. Further, the linewidth of the laser diode, typically on the order of several MHz, is reduced to ~ 1 MHz. An alternative configuration is the Littman-Metcalf configuration shown in Figure 3.2(b), which provides better frequency stabilization and linewidth narrowing, but has a more complicated setup. The inclusion of an additional optical component (the mirror) adds another degree of tuning that is needed within the ECDL box, which is why we usually choose to use the simpler Littrow configuration. However, one advantage of the Littman-Metcalf configuration is that the output beam direction does not change as we tune the laser frequency. This can be important in certain scenarios.

The laser diodes are housed within a ThorLabs collimation tube which is then held in place by a rectangular aluminum holder. The holder is mounted onto a wide aluminum base plate, where a diffraction grating also sits (Figure 3.3). The diffraction grating (1800 lines/mm) is mounted on a small kinematic mirror mount, which allows the user to do coarse frequency tuning. A piezoelectric stack inserted into one of the three contact points of the mirror mount (typically the lower side tuning screw) allows micrometer-scale adjustment of the position of the grating, resulting in fine tuning of the ECDL output frequency.

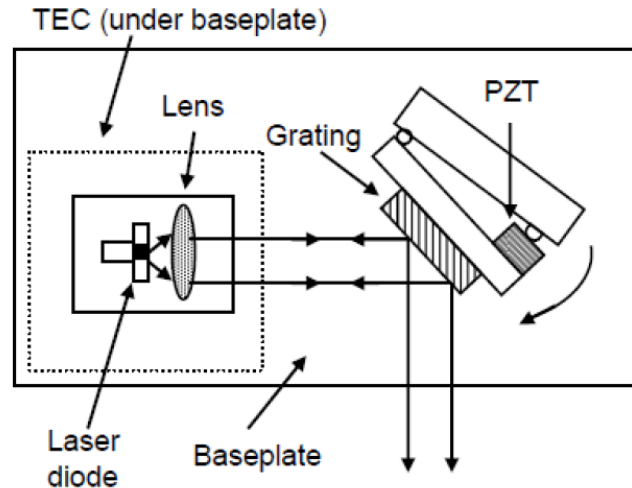


Fig. 3.3. The base plate where the laser diode holder and grating mirror mount are mounted. Image from [53].

The wide aluminum base sits on a thermoelectric cooler (TEC). The temperature of the baseplate is kept stabilized, ensuring that the laser diode temperature is kept constant, and the length of the external cavity is stabilized. Temperature feedback is given by a AD590 temperature sensor mounted on the laser diode holder, and the TEC is powered by a THORLABS temperature control module (TED8020). This setup is effective at keeping the frequency of the laser diode stable even as the temperature in the lab fluctuates.

To protect the ECDLs from air currents, mechanical and acoustic vibrations and noise, the aluminum base plate (and TEC) are then mounted on a thick aluminum block, greatly increasing the mass of the whole system and providing a good temperature sink for the TEC. The block rests on a thin layer of Sorbothane which serves to further isolate any vibrations of the optical table. All of this is then housed within a 1/2-in thick aluminum box for acoustic isolation and shields the ECDL from any air currents in the lab (Figure 3.4). Overall, this results in a very stable laser system that will stay locked to a cesium saturated absorption transition for many hours at once.

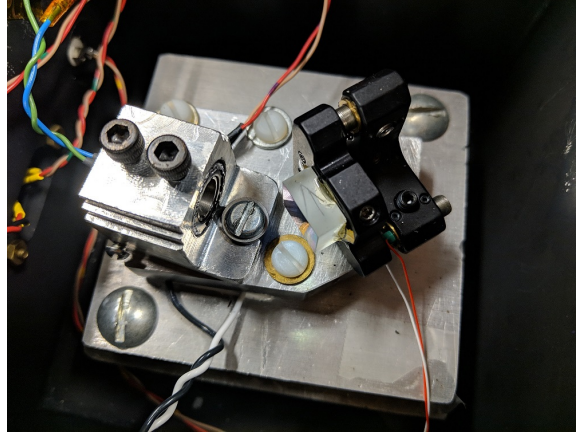


Fig. 3.4. Home-made external cavity diode laser showing the collimation tube within the tube-holder, optical grating attached to a mirror mount and base-plate.

The cavity length chosen for the ECDL is approximately 2.5 cm, which corresponds to an FSR of 6 GHz. This is a convenient choice as it is far from 9.2 GHz (Cs ground state hyperfine separation) and 4.6 GHz (half of 9.2 GHz). This is important because an ECDL operating at a particular external cavity mode may have some power present in adjacent modes. By staying away from these frequencies, we avoid having unwanted transitions in the Cs atoms due to laser power in adjacent modes. This could result in noise or a higher background signal.

3.3 Laser locking scheme - saturated absorption

The three 852 nm laser diodes are frequency locked using saturated absorption to specific hyperfine lines of the Cs D2 transition lines. The specific choice of ground state hyperfine or excited state hyperfine line used depends on the pumping and detection scheme of the day, but the technique is the same.

Saturated absorption spectroscopy is a fairly simple technique commonly used to lock or stabilize the frequency of a laser to an atomic transition resonance. The technique removes most of the Doppler broadening, resulting in a peak with narrow

linewidth that allows us to accurately lock our lasers to the center of the atomic transition. A thorough discussion can be found in [79]; important details have been included in this section.

When a probe beam is passed through a cesium vapor cell, the Doppler broadened transition results in a probe transmission profile as shown in Figure 3.5(a). The full width at half maximum (FWHM) of the resonance peak is increased many hundred times and can be calculated by

$$\Delta\nu_D = \nu \sqrt{\frac{8k_B T \ln 2}{mc^2}}. \quad (3.1)$$

ν is the frequency of the resonance, k_B is the Boltzmann constant, m the mass of the cesium atom and c the speed of light. At $T = 300$ K, $\Delta\nu_D \approx 1.2$ GHz for the D2 line. This Doppler broadening makes it difficult to lock to the center of the peak, and also obscures any hyperfine structure that is present.

Figure 3.5(b) shows what happens when we include a strong pump beam co-linear with and opposite in direction to the probe beam. The pump beam depletes all the atoms from the ground state. Thus, when precisely on resonance, there are much fewer atoms in the ground state to absorb the probe beam, and its transmission increases. Off-resonance, because the pump and probe beam are opposite in direction but of the same frequency, they interact with different sets of Doppler-shifted atoms, which is why the probe beam is not affected. This simple pump-probe technique allows us to more precisely extract the center frequency of the resonance.

In practice, two probe beams are typically used to get rid of the Doppler broadened dip. They are incident onto a balanced photodetector with two photodiodes, which outputs the difference in signal between the two photodiodes. The pump beam is made to cross with only one of the two probe beams, and the result is the difference between Figure 3.5(a) and (b), a sharp peak on resonance! Figure 3.6 shows the balanced photodetector output as the ECDL PZT voltage is tuned. Tuning the PZT of the ECDL scans the laser frequency so it crosses the cesium $6S \rightarrow 6P_{3/2}$ hyperfine transitions. There are three atomic transitions ($F - F'$: 3-2, 3-3, 3-4) possible by

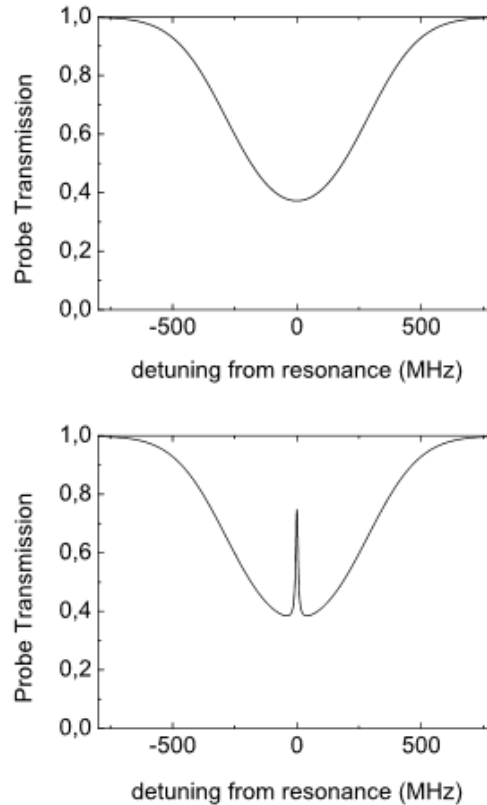


Fig. 3.5. (a) Doppler broadened absorption profile. (b) Doppler-free probe transmission profile.

selection rules (3-5 is not allowed), but 6 peaks are detected. The additional 3 peaks marked in Figure 3.6 are crossover peaks that occur halfway between two transitions due to the counter-propagating laser beams. More information about crossover peaks can be found in [79].

After obtaining the transition peaks, there is one more problem to solve. Because our signal (see Figure 3.7(a)) decreases for both a decrease and increase in laser frequency, the control loop would not be able to differentiate between the two. To lock to the transition resonance, we need to generate an error signal that is asymmetric about its center such as the dispersion shaped curve shown in Figure 3.7(b). To do this, we apply a dither of $\omega \approx 25$ kHz to the laser current controller modulation input. This modulates the laser current and hence frequency at 25 kHz. I show

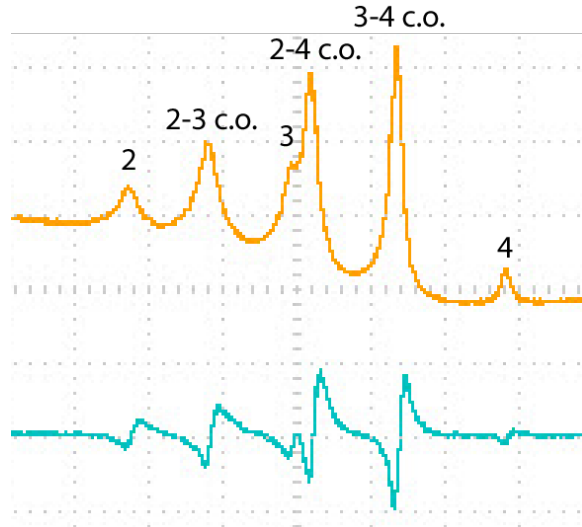


Fig. 3.6. An oscilloscope sweep showing the Doppler-free saturated absorption peaks of the Cesium 6S $F=3$ to $6P_{3/2}$ (F' as labelled) transition. The peaks labeled c.o. are the crossover peaks that occur halfway between two transitions. The lower curve shows the error signal extracted from this saturated absorption signal.

the experimental setup for saturated absorption in Figure 3.8. The output from the balanced photodetectors will contain this 25 kHz modulation which we mix in an analog multiplier with the $\omega' \approx 25$ kHz signal.

The resulting components at $\omega - \omega'$ and $\omega + \omega'$ are low pass filtered to keep only the $\omega - \omega'$ dc component, resulting in the error signal we want. The error signal is now a frequency differentiator for a small decrease or increase in laser frequency. We feed this error signal to the laser diode through a loop filter which adjusts the laser current and laser PZT position to keep the laser locked to the resonance peak.

A low frequency home built loop filter designed by Dionysios Antypas [53] is used to keep the laser locked. Low noise OPA4227 op-amps and a 10 MHz analog multiplier the AD734 are used for filtering, driving the PZT and generating an appropriate voltage for laser current modulation. More details about the locking circuit can be found in the thesis of Dionysios Antypas [53] or reference [80].

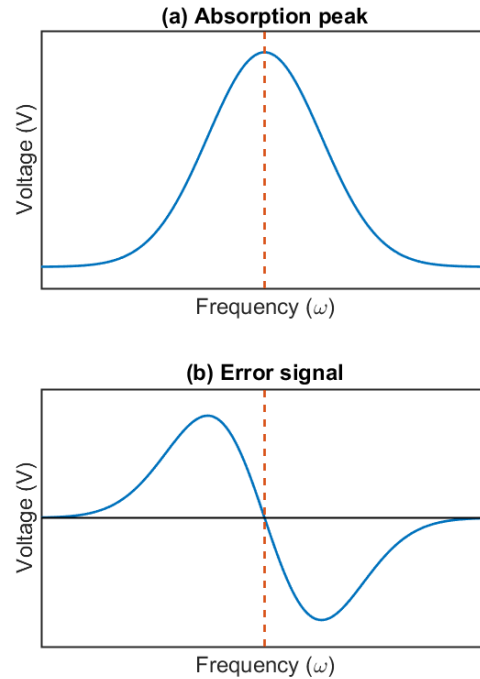


Fig. 3.7. The gradient of the (a) absorption peak gives us a (b) dispersion shaped curve which we can use as an error signal.

3.4 Laser locking transitions

From the $6S$ ground state of cesium, there are two strong transitions with roughly equal transition strength we can use for pumping or detection, the D1 and D2 lines. These correspond to the $6P_{1/2}$ and the $6P_{3/2}$ states, respectively (see Figure 3.9). The D1 transition is at 894 nm and the D2 transition is at 852 nm, both wavelengths where laser diodes are readily available from suppliers such as ThorLabs and QPhotonics.

The $6P_{3/2}$ state, having 4 hyperfine levels ($F = 2, 3, 4, 5$) has inherent advantages over the $6P_{1/2}$ having only 2 hyperfine levels ($F = 3, 4$). These advantages will be discussed later in the discussion of atomic pumping or state preparation. Thus we chose the D2 transition at 852 nm over the D1 transition.

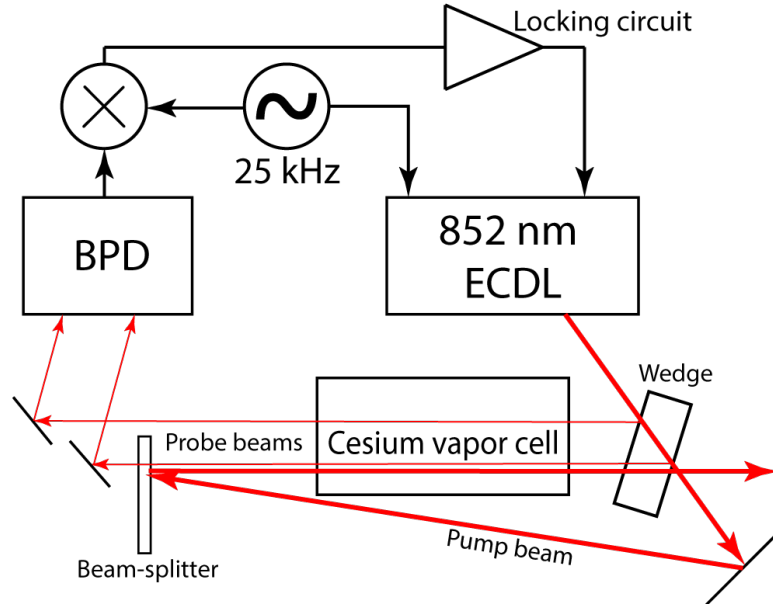


Fig. 3.8. Set-up for saturated absorption. The pump beam overlaps one of the probe beams to saturate the atoms. The BPD removes the Doppler broadened profile from the electronic signal through the use of a second probe beam. BPD - balanced photodetector, ECDL - external cavity diode laser.

3.4.1 Optical pumping lasers

We have two pump lasers we use for atom state preparation. The first of these lasers, which we call the hyperfine laser, empties out one of the $6S_{1/2}$ $F = 3$ or 4 hyperfine levels, pushing almost all of the atoms into the other hyperfine state. The second laser, the Zeeman laser, pushes all the atoms towards the $+m$ or $-m$ Zeeman sublevel of the particular F hyperfine level. After optical pumping, $>90\%$ of the atoms in the atomic beam are thus prepared into the specific $6S_{1/2}$ $F, m = \pm F$ state (or $(F, m = \pm F)$ state) we choose. In the following sub-sections, the steps for pumping to the $F = 4, m = +4$ state $(4, 4)$ are described.

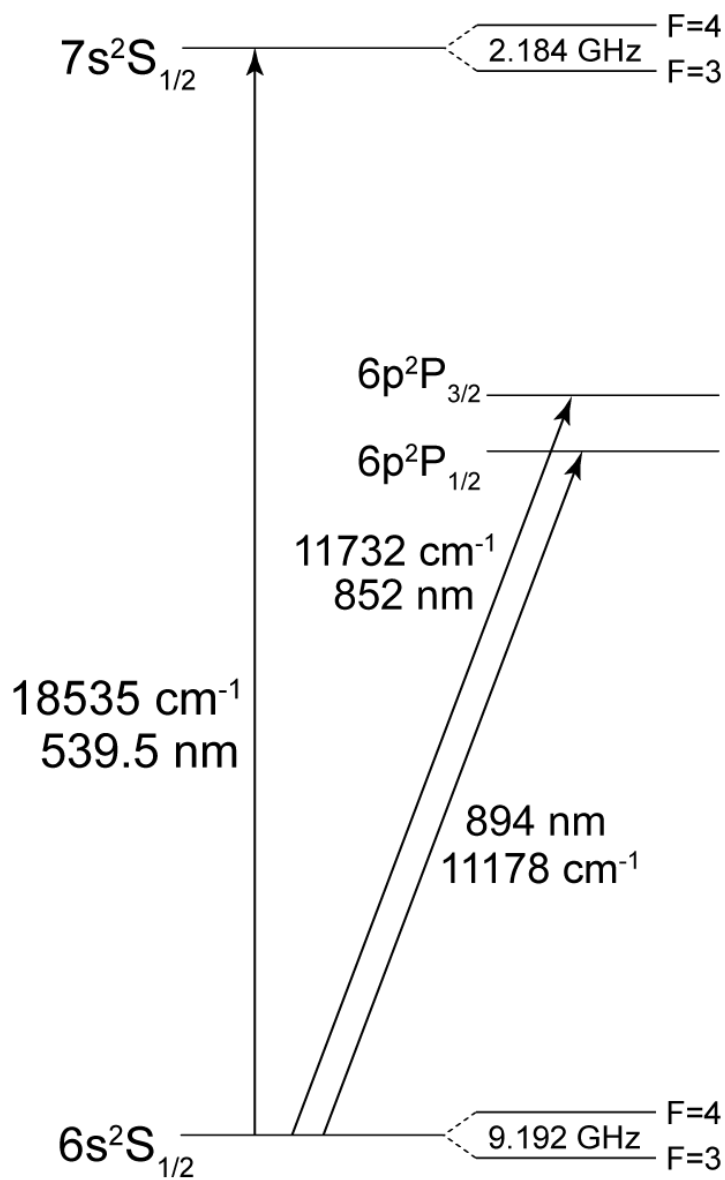


Fig. 3.9. Diagram showing the Cesium $6S$, $6P_{1/2}$, $6P_{3/2}$ and $7S$ energy levels. Labeled are the laser wavelengths to excite the 1-photon transitions, but the $6S$ to $7S$ transition is electric dipole forbidden. Hyperfine splittings for the $6P_{3/2}$ energy level are shown in Figure 3.10.

Hyperfine laser

The hyperfine laser has to pump all the atoms into the $F=4$ hyperfine level. We tune the laser to the $6S_{1/2} F=3$ to $6P_{3/2} F=4$ transition (see Figure 3.10). Thus, atoms that are already in the $F=4$ state are not affected by the laser, while atoms in the $F=3$ state get pumped to the $6P_{3/2} F=4$ state. From the $6P_{3/2} F=4$ excited state, the atoms have roughly 58% chance to decay down to the ground state $F=4$ hyperfine level, and approximately 42% chance to decay back to the $F=3$ ground state [52,61]. After a few transition cycles with a hyperfine laser (5 mW/cm^2) that saturates the transition ($\sim 1.5 \text{ mW/cm}^2$), better than 97% of the atoms can be put into the $6S_{1/2} F=4$ hyperfine level, with only a tiny percentage of population of the atoms remaining in the $F=3$ level. Pumping on the $F=4$ to $F=3$ transition is more efficient, with 75% of atoms decaying back to $6S F=3$ ground state, due to favorable branching ratios.

For each transition of the atom from ground state to excited state, a photon will be emitted when the atom decays back down to one of the ground states. The random direction of photon emission causes light to be scattered throughout the vacuum chamber by the optical pumping process. This can cause some pumped atoms past the pumping region to get excited, and decay into the empty hyperfine level, resulting in a higher background signal voltage level.

Zeeman laser

While the hyperfine laser pumps most of the atoms into the selected hyperfine level ($F=4$ in this example), the Zeeman laser ($\sim 1 \text{ mW/cm}^2$) is used to pump all the atoms into the target magnetic sub-level. In this case, it is the $m=+4$ Zeeman level. A small ~ 2 Gauss magnetic field is applied to the atoms in the interaction region, which breaks the degeneracy of the Zeeman levels ($m: -4$ to $+4$). The ground state $6S$ and excited $6P_{3/2}$ Zeeman sublevels are split by different amounts, but the splitting is small compared to the power broadening of the transition due to the intense laser

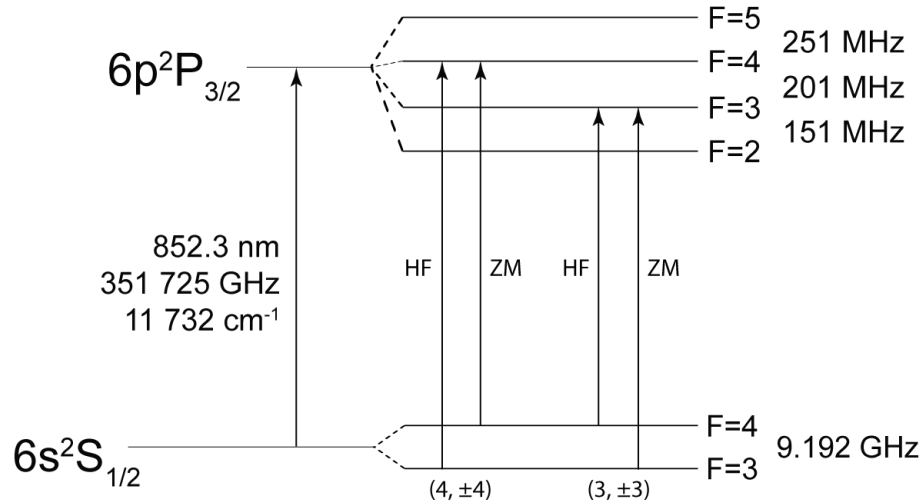


Fig. 3.10. This diagram shows the pumping scheme to populate the $(4, \pm 4)$ and $(3, \pm 3)$ magnetic sublevels of the ground $6S$ level. HF - hyperfine, ZM - Zeeman.

beam, so we are still able to hit all the transitions at once. We circularly polarize the Zeeman laser, which according to selection rules, permits only $\Delta m = +1$ transitions. The laser thus excites all the $(F = 4, m = n) \rightarrow (F = 4, m = n + 1)$ transitions at once, and through several transition cycles, pushes all the atoms towards the $6S_{1/2}(4, +4)$ edge state, as shown in Figure 3.11.

The $6S_{1/2}(4, +4)$ edge state has no upper state to transit to and the cycle stops. This is one advantage of pumping from $F=4 \rightarrow 4$ instead of using the $F=4 \rightarrow 5$ transition. Pumping $F=4 \rightarrow 5$ has advantages in that atoms from the $F=5$ excited state can only decay down to the $F=4$ hyperfine level. Using the $F=4 \rightarrow 4$ pumping transition, atoms from the excited state can decay down to the (previously empty) $6S$ $F=3$ ground state where they are lost until they undergo a hyperfine laser transition once again. However, the disadvantage of the $F=4 \rightarrow 5$ transition is that once the atoms are successfully pumped to the $6S$ $(4, +4)$ state, they can still undergo the $(4, 4) \rightarrow (4, 5)$ cycling transition (which is later used for detection). The continuous pumping and decay of atoms on this cycling transition results in lots of fluorescence being generated within the vacuum chamber. This light, which is emitted in random

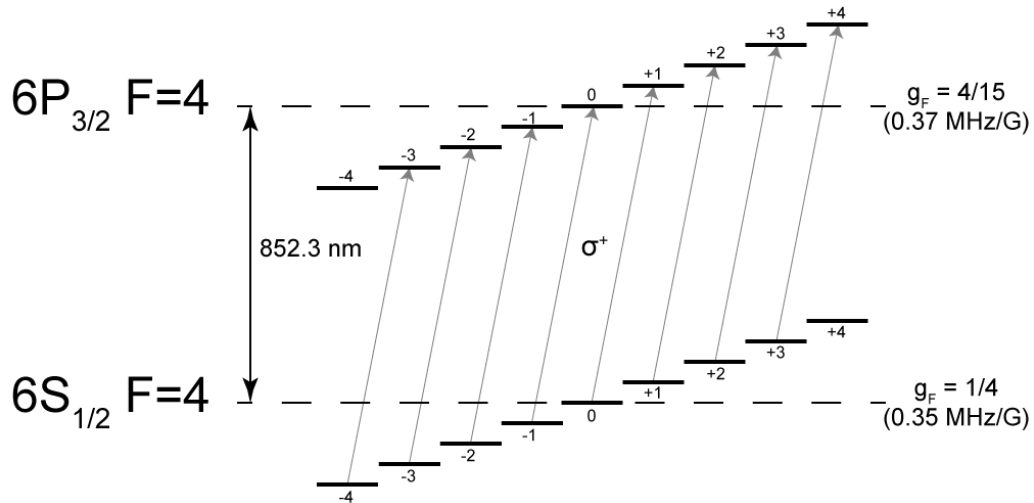


Fig. 3.11. This figure shows the Zeeman pumping to the cesium $6S_{1/2}$ (4, 4) magnetic sublevel. Because the laser is right circularly polarised, only $\Delta m = +1$ transitions are driven.

directions, reflects throughout the vacuum chamber until: (a) It is absorbed by another cesium atom in the pumping region, knocking it out of the $F=4$ state into the $F=3$ empty state, resulting in additional background signal; (b) It gets absorbed by an atom further along in the beam that did not undergo a transition, resulting in a false signal; (c) It gets picked up by the photodiode in the detection region. All of these result in additional noise on the signal we detect, which we avoid by pumping on the $F=4 \rightarrow 4$ transition instead.

Optical pumping - conclusion

In practice, we align the HF and ZM beam so that they are collinear and interact with the atomic beam at the same time. Both beams are 6 mm in diameter and fully overlap the roughly 3 mm tall atomic beam. As previously discussed, fluorescence from the optical pumping region can cause unwanted excitations and result in more atoms in the $6S F=3$ empty state, causing an increase in the background dc level of our detected signal.

To mitigate the increase in background signal due to scattered light, a hyperfine clean-up beam is employed to empty out the chosen hyperfine level (6S $F=3$ in this example). A tiny portion of the hyperfine beam is picked off with a glass slide and double-passed through the vacuum chamber roughly 7 cm downstream from the optical pumping region. It passes once through the atom beam, and is then retro-reflected, retracing its original path. This weak HF clean-up beam aims to empty out the 6S $F=3$ hyperfine level, resulting in an almost completely empty $F=3$ state.

At the end of the optical pumping region, we estimate that less than 0.2% of atoms remain in the empty $F=3$ state after clean-up, while >92% of atoms are in the target (4,+4) state.

3.4.2 Detection laser

The atoms first pass through the optical pumping region, then fly through the interaction region, and finally end up in the detection region. The detection laser is tuned to detect the number of atoms in the previously empty hyperfine ground state. In this example, it is the 6S $F=3$ state. The laser is linearly polarized and tuned to the cycling transition between the 6S $F=3$ state and the $6P_{3/2}$ $F=2$ state. In this way, all the atoms that undergo the transition up to the $6P_{3/2}$ $F=2$ hyperfine state must decay back down to the $F=3$ hyperfine level of the ground state. Selection rules forbid a 1-photon transition where angular momentum changes by 2. This means that for the time the atom takes to fly through the detection region, the atoms can interact and fluoresce multiple times.

We shape the detection laser beam intersecting the atomic beam to be wider than tall, which extends the region the atoms interact with the laser. The laser is linearly polarized and double-passed by a retro-reflection at the opposite end of the vacuum chamber. This increases the intensity of light interacting with the laser, increasing the amount of photons emitted by the atomic beam. Considering the time of flight, natural lifetime of the excited state and region of interaction, we estimate that each

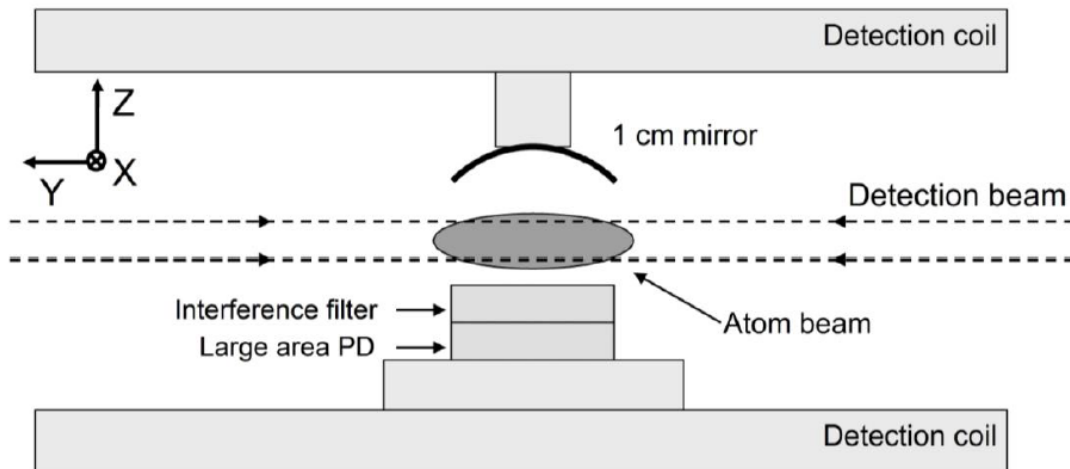


Fig. 3.12. The large photodiode is placed under an interference filter to block photons at 540 nm and 1079 nm. A concave mirror above the detection region reflects photons emitted upwards back down onto the photodiode. Image from [53].

atom in the previously empty hyperfine state emits 1000 photons in the detection region. However, the majority of these 1000 photons do not get picked up by the photodiode.

To maximize the number of photons picked up by the photodetector in the detection region we use a large surface area photodiode (Hamamatsu #S3204-08, 18×18 mm²) placed directly under the interaction region (see Figure 3.12). Directly on top of this photodiode, an interference filter is placed which allows only the 852 nm photons through and blocks out unwanted photons at 540 nm and 1079 nm. About 1 cm above the interaction region, a concave mirror with $f = 10$ mm is placed to reflect the photons emitted upwards back down onto the photodiode, maximizing the photon capture rate.

3.5 Heterodyning of 852 nm ECDLs for laser linewidth estimation

The fundamental frequency of a laser beam is very high, making it extremely difficult to directly measure the linewidth of a laser. The first demonstration of optical heterodyne to estimate laser linewidth was in 1980 by [81]. In the optical heterodyne technique, two lasers are incident on a photodiode, which mixes the inputs and outputs the beat signal (frequency difference) of the two lasers. If one of the two lasers is known to have much narrower linewidth than the second, sending this beat signal to a spectrum analyzer would allow us to estimate the linewidth of the second laser. However, if the two lasers have the same linewidth, such as in optical homodyne, the beatnote full width at half maximum (FWHM) will be much larger. Assuming purely frequency noise on each of the two lasers, a Lorentzian noise spectrum results in a beatnote FWHM twice as large, while a Gaussian spectrum results in one that is $\sqrt{2}$ as large [81].

Since the optical pumping and detection lasers are all at 852 nm, and of similar design, we estimate that they have similar linewidth. By beating any two of them together, they would generate a beat note with FWHM between $\sqrt{2}$ to $2\times$ linewidth.

Out of convenience, the detection laser and hyperfine laser were selected for this measurement. A figure of the setup for this short test is shown in Figure 3.13. The lasers were combined using a 50/50 beamsplitter (EBS1) from Thorlabs. The combined laser beam is then directed onto a fast photodiode (150 MHz B/W, Thorlabs PDA10A). The dc-coupled output is monitored to maximize optical power incident on the photodiode while ensuring the output is not saturated. The ac-coupled output from the photodiode is sent to a spectrum analyzer where we can observe the beat note.

The two lasers are individually locked using saturated absorption to the Cesium D2 line. When both lasers are locked to the same hyperfine transition (so that they are at the same frequency), the beat note is centered at 0 Hz and $1/f$ (pink) noise makes it difficult to measure the FWHM of the beat note peak. Hence, the lasers are

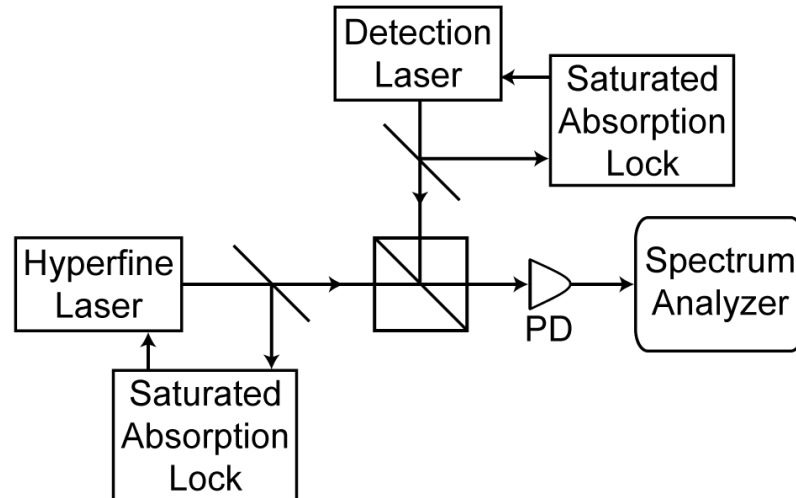


Fig. 3.13. The hyperfine laser and Detection laser are separately locked to different cesium hyperfine transitions using saturated absorption spectroscopy. The two lasers are combined using a beam-splitter and sent to a fast photodiode. The beatnote between the two lasers is observed using a Siglent SSA3021X 2 GHz spectrum analyzer.

locked to different hyperfine transitions instead (e.g. $4 \rightarrow 4$ and $4 \rightarrow 5$). The frequency difference of the hyperfine splitting pushes the beat note center out to that frequency, where there is less noise.

In Figure 3.14, the HF laser is locked $4 \rightarrow 4$, while the detection laser is locked to the $4 \rightarrow 4&5$ crossover peak, so that the frequency difference is ~ 126 MHz. We see the beat note centered at ~ 126 MHz with a full width half maximum (-3dB point) of ~ 1.5 MHz. Multiple measurements were done with the lasers locked to several other hyperfine transition combinations (resulting in frequency differences of 75, 150, 175 and 200 MHz) but they all resulted in the same ~ 1.5 MHz FWHM.

The measurement of the beat note having FWHM ~ 1.5 MHz suggests that either one or both of the 852 nm ECDLs has a linewidth on the order of ≥ 1 MHz, instead of the often suggested several hundred kilohertz. We have a third 852 nm ECDL (the Zeeman laser). The three lasers have similar design, so we expect that the three of them have similar linewidth. We plan to beat the hyperfine and detection lasers

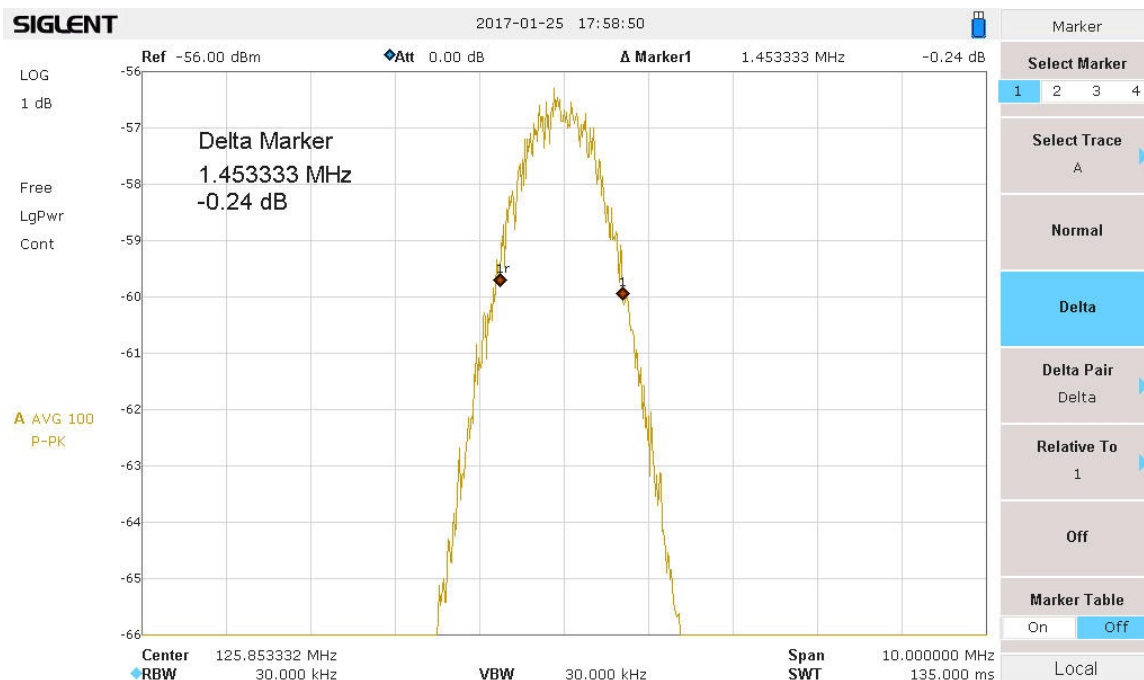


Fig. 3.14. This screenshot of the rf spectrum analyzer shows the beat signal between the two 852 nm lasers. FWHM as measured by the delta markers is about 1.5 MHz.

against the Zeeman laser in pairs, and measure the beat note of these two new pairs. This will allow us to determine if just one of the lasers has a larger linewidth, or if more than one of the lasers have linewidth ≥ 1 MHz.

Because a narrow linewidth is not necessary for the PNC experiment, the result of this short experiment does not invalidate or affect the main experiment in any way. But it suggests that the diodes and gratings used to build the ECDL are not performing at the level expected. For a higher precision measurement of the laser linewidth, we could potentially beat the laser against the frequency comb laser in Prof. Weiner's lab.

3.6 The 1079 nm laser system

The 1079 nm laser which drives the two-photon $6S \rightarrow 7S$ transition is a critical component of the PNC measurement. We need a lot of 1079 nm laser power in order to generate the 540 nm laser (by second harmonic generation in a frequency doubling crystal), which drives the one-photon $6S \rightarrow 7S$ electric dipole forbidden transition. To generate this, we have a Keopsys fiber amplifier which can generate up to 12 W of laser power at 1079 nm with less than 5 mW² of input power.

To seed the fiber amplifier, we have built a 1079 nm external cavity diode laser (ECDL) in the Littrow configuration. The laser diode is a single mode AR-coated diode bought from QPhotonics, and can put out up to 80 mW of 1079 nm laser light. The grating we use is a visible reflective holographic grating (GH13-12V) from ThorLabs with 1200 grooves/mm. Higher groove density is better for frequency resolution but has poor efficiency at 1079 nm. The cavity length is 4 cm, which corresponds to an external cavity free spectral range of 3.5 GHz. According to [53], a longer cavity reduces tunability but also results in lower ECDL linewidth.

In 2018-2019, we have started building a new 1079 nm seed laser using a different optical feedback configuration. The new laser design is known as an interference-filter based external-cavity diode laser (IFECDL) [82]. Instead of using a grating, the IFECDL uses an interference filter (typically very narrow-band) and a cat-eye reflector for optical feedback and wavelength selectivity. The new design promises to be less susceptible to vibrations and other noise sources, with linewidths on the order of 50 kHz. This could reduce the requirements for locking the 1079 nm laser to the power build-up cavity.

3.6.1 Second harmonic generation to obtain the 540 nm laser

The 1079 nm laser drives the cesium $6S \rightarrow 7S$ two-photon transition while the 540 nm laser drives the same one-photon transition. Our coherent control mea-

²The Keopsys fiber amplifier can operate with as little as 1 mW of seed laser light.

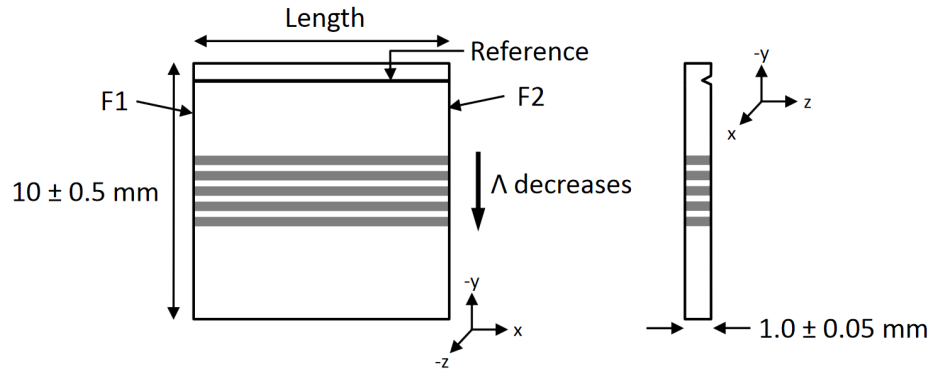


Fig. 3.15. Drawing of the PPLN crystal. The image shows the five periodically poled grating channels through the crystal. Image from the MSHG1064-1.0-20 datasheet.

surement scheme depends on interference between these two lasers, so it is necessary that the two lasers are phase coherent. To generate the 540 nm laser, we use a Magnesium-doped periodically poled Lithium Niobate (MgO:PPLN) crystal from Covesion (MSHG1064-1.0-20). The crystal comes with five periodically poled gratings with different periods (see Figure 3.15). This results in a wavelength-temperature dependence as shown in Figure 3.16. I have shown only the curves for the higher temperature range, but the crystal works at lower temperatures too, for a total wavelength range of 1060 – 1080 nm. To heat the PPLN crystal, we use a commercial oven assembly sold by Covesion, and achieve quasi phase-matching at a temperature of $\sim 190^\circ\text{C}$ while using the poled grating with $6.96\ \mu\text{m}$ period.

Precisely aligning the laser through the correct poled grating is critical for efficient second harmonic generation (SHG). We mount the crystal oven on a rotation stage, which is then mounted to a mirror mount, which is itself mounted to a 3-axis (X-Y-Z) translation stage. With 6 degrees of freedom, alignment is quite easy, but extreme care has to be taken when adjusting the alignment while running the 1079 nm laser at high power. The poled gratings are extremely fragile and uneven heating can easily cause the crystal to crack and become irreversibly destroyed. We previously had a crystal with $0.5 \times 0.5\ \text{mm}^2$ cross section area which broke during high-power laser

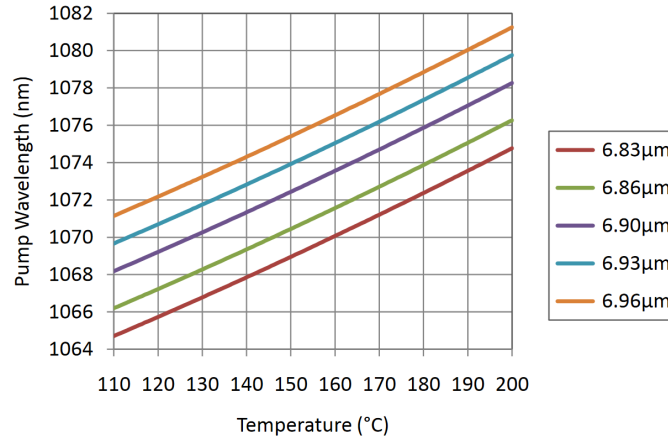


Fig. 3.16. Wavelength-temperature dependence of the 5 different periodically poled gratings of the PPLN crystal. Image from the MSHG1064-1.0-20 PPLN crystal datasheet.

alignment. The current crystal we have has poled gratings of cross sectional area $1 \times 1 \text{ mm}^2$.

Figure 3.17 shows the setup for passing the beam through the PPLN crystal. A 12.5 cm lens focuses the 1079 nm laser into the PPLN crystal, and the output beams are collimated by an achromatic lens of focal length $f = 15 \text{ cm}$. Previously, we used a curved silver-coated mirror of focal length 15 cm for collimation, but damage to the silver coating affected proper beam collimation³. With the achromatic lens, we have not yet noticed any deterioration in collimation quality. A tighter focus within the PPLN crystal can yield higher second harmonic generation conversion efficiency, but Antypas in [53] suggests that heating in the crystal may be causing slight instabilities in the $6S \rightarrow 7S$ modulation rate.

Careful alignment of the 1079 nm laser through the PPLN crystal is critical for efficient SHG conversion efficiency, and for retaining a nice circular beam shape (Gaussian (0,0) mode) for both the green (540 nm) and infrared (1079 nm) lasers. For alignment, we initially set the temperature of the crystal lower by 10 – 20°C and put

³This manifested as a ‘donut’-shaped laser mode, see for example the Laguerre-Gaussian (1,0) or (0,1) modes.

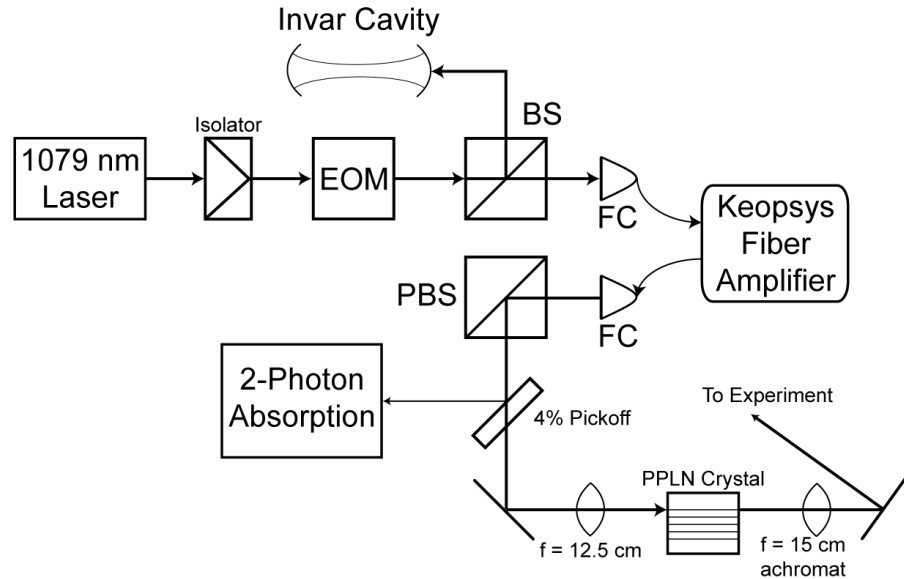


Fig. 3.17. This figure shows the focus of the 1079 nm laser into the PPLN crystal. An $f = 12.5$ cm lens focuses the 1079 nm laser beam into the PPLN crystal, while on the output, an $f = 15$ cm achromatic lens collimates both beams. EOM - electro-optic modulator, PBS - polarizing beamsplitter, FC - fiber coupler.

only 1 W of infrared light through the crystal. A weak green beam at 540 nm will be generated and we use this spot to direct the beam in a safe direction. Slowly, the temperature is increased and the laser power out of the fiber amplifier increased to 3 – 4 W. At this lower laser intensity, we can clearly see the shape of the green laser on any dark surface. While watching this image, we move the PPLN oven using the translation stage and can count as we go through the different poled gratings and un-poled material. The new crystal has a much larger cross-section at 1×1 mm² and so alignment is much less stringent. By determining the edges of the poled grating channel, we try to pass the beam close to the center of the channel we choose. Then, the temperature is raised to the optimum temperature for SHG, and the fiber amplifier output increased.

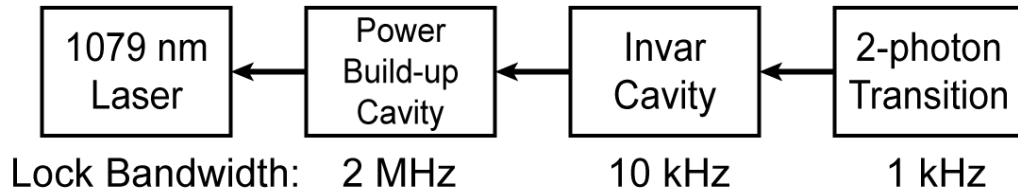


Fig. 3.18. Block diagram of the 3-stage locking scheme for the 1079 nm laser. The PDH lock of the laser to the power build-up cavity has the highest servo bandwidth, while the next two lock stages need not be as fast.

3.6.2 Frequency locking scheme for the 1079 nm laser system

Finally, we briefly discuss the locking scheme for the 1079 nm laser system in this section. A block diagram of the scheme is shown in Figure 3.18. Further details can be found in Section 4.6.3, after the discussion about the power build-up cavity.

The 1079 nm laser is first locked using Pound-Drever-Hall to the high finesse power build-up cavity (PBC) which will be installed within the vacuum chamber. The PBC resonance frequency tends to be unstable on a timescale longer than several milliseconds and will be locked to a stable Invar cavity. The Invar cavity is a more traditional cavity made of two mirrors, a piezoelectric (PZT) tube and a 15 cm long Invar tube, reducing its susceptibility to vibrations. Finally, the Invar cavity resonance is locked to a cesium two-photon resonance using the 1079 nm laser. Low frequency locking of the 1079 nm laser directly to the two-photon resonance has been achieved [53], and I discuss here the details of this lock and how it will carry over to lock the Invar cavity instead.

We have two options for locking the 1079 nm laser to the cesium $6S \rightarrow 7S$ transition. To generate an error signal, we could use the atomic beam in the vacuum chamber or we could use a cesium vapor cell outside the vacuum chamber. In [52], Wood describes how the Boulder group used their green (540 nm) laser to generate an error signal within the PBC. However, a limitation they faced was the 1 ms it takes for atoms to get from the interaction region to the detection region, and this

limited the locking frequency to less than 1 kHz. With our experimental setup, we would face the same 1 ms delay and the same 1 kHz bandwidth limitation.

Instead, we double-pass a portion of the 1079 nm laser through a cesium vapor cell to do Doppler-free two-photon spectroscopy of cesium. We use a 15 cm lens to focus the beam to a 120 μm beam diameter at the center of a 8 cm long cesium vapor cell. Upon exiting the cesium cell, the beam is collimated with another lens and retro-reflected, retracing the same path back through the vapor cell. Because the two-photon transition is weak (relative to a Cs D1 or D2 transition), we have to heat the vapor cell. The cesium vapor cell is housed in a heated aluminum enclosure ($\sim 70^\circ$), and we show in Figure 3.19 several photos of the PMT enclosure and its internals. A 1-in. focal length lens focuses fluorescence from the vapor cell onto a Hamamatsu R928 photomultiplier tube (PMT). An 850 ± 5 nm interference filter placed in front of the PMT blocks any unwanted 1079 nm light from entering the PMT.

Antypas measured the linewidth of the Doppler-free $6S, F = 3 \rightarrow 7S, F = 3$ transition from this locking setup to be approximately 7 MHz [53]. This is much smaller than the linewidth measured while using the atomic beam of ~ 14 MHz. For the M1 measurement, the 1079 nm laser was dithered at approximately 30 kHz to generate the error signal from the two-photon transition in the vapor cell, and lock the laser to the peak of the resonance. For the PNC measurement, we will phase modulate the infrared 1079 nm laser using an EOM. This modulation will let us extract an error signal from the two-photon transition in the cesium vapor cell.

3.7 Raman laser for spin polarization optimization

In earlier sections, we discussed how the hyperfine and Zeeman lasers optically prepare the atoms into a specific (F, m) state for the PNC experiment. We need to measure the population distribution of the atoms among the various magnetic (m) sublevels. We use off-resonant Raman spectroscopy, discussed by Wood in [52]

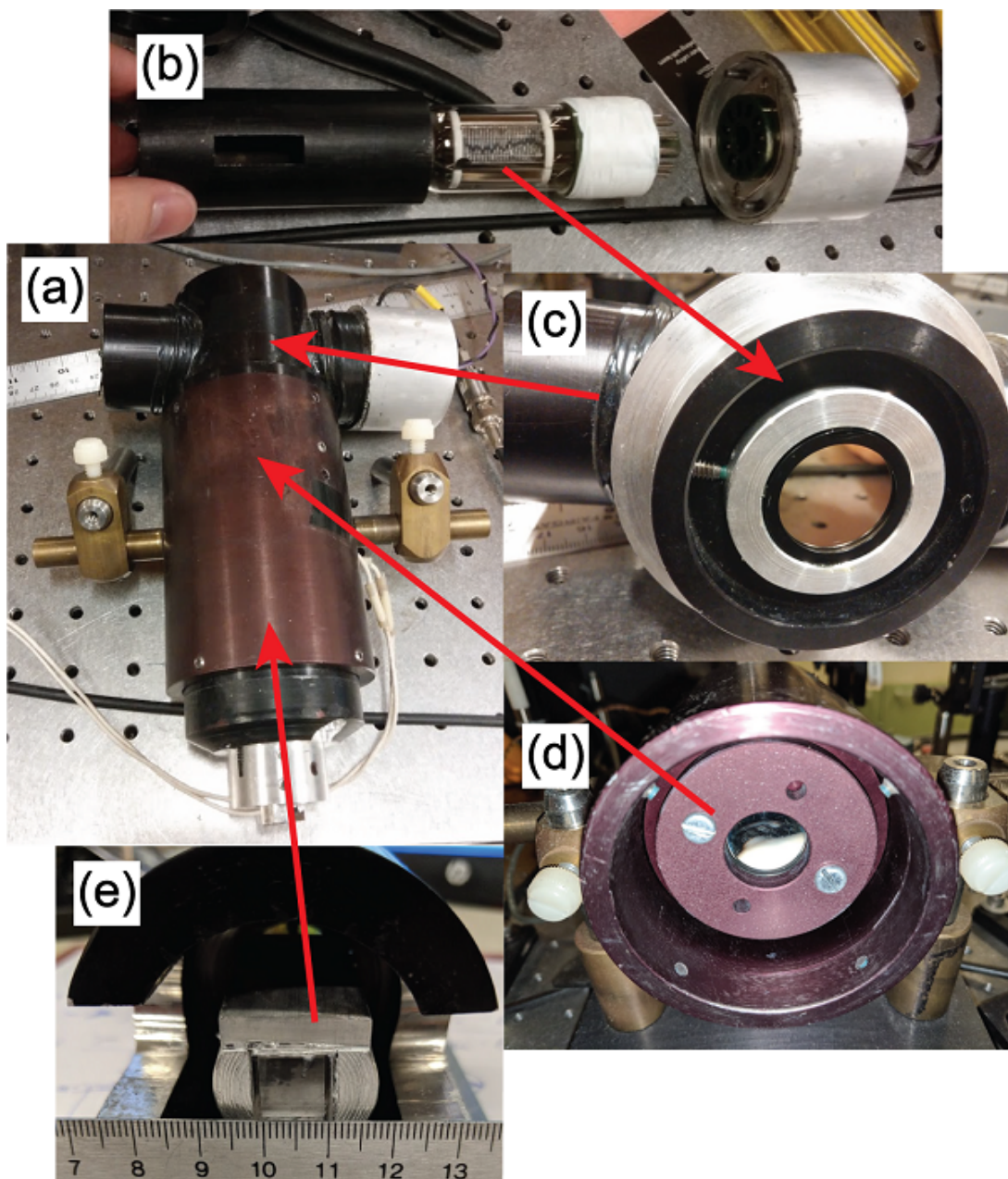


Fig. 3.19. Photos of the PMT enclosure, showing the internal components. (a) The whole PMT setup; (b) The enclosure containing the PMT and shroud around it; (c) Interference filter located in front of the PMT active area; (d) 1-in. imaging lens located halfway between the PMT and the vapor cell; (e) Vapor cell enclosed in aluminum for heating.

in great detail, to measure the relative m populations. In this section, we discuss the details of the Raman laser, while a discussion of spin polarization and atomic population distribution is left for section 4.4.

For Raman spectroscopy on the cesium ground states, which are ~ 9.2 GHz apart, we need two optical frequencies at 9.2 GHz apart. There are multiple ways to obtain two lasers with 9.2 GHz frequency difference, such as passing one through an electro-optic modulator (EOM) at 9.2 GHz and phase-locking the two lasers. However, EOMs that operate at such high frequencies are expensive to obtain, and the setup is complicated.

Instead, we use the same technique as Wood [52] and injection current modulate a single diode at 4.6 GHz. This has the effect of placing sidebands 4.6 GHz apart on the laser, resulting in a tunable frequency difference of 9.2 GHz between the laser sidebands. The gain profile of a laser diode typically falls off sharply after $\sim 2 - 3$ GHz, so we have to do something to increase the gain at ± 4.6 GHz. We place the laser diode in an external cavity (like all our other lasers), but calibrate the length of the external cavity to give a free spectral range (FSR) of ~ 4.6 GHz. This provides additional gain for the laser at its sideband frequencies and we can think of the diode as lasing in three consecutive/adjacent external cavity modes.

Figure 3.20 shows the key components of the Raman ECDL. The length of the external cavity is ~ 3.3 cm which corresponds to a FSR of 4.6 GHz. To better temperature stabilize the laser diode, we place the TEC directly under the diode holder. Injection current modulation at such high frequencies has a tendency to cause temperature fluctuations [53], so better temperature stabilization in this manner is required. To keep the cavity length constant, the grating is mounted to a short block of Invar and attached close to the diode holder. Invar is an iron-nickel alloy known for its extremely low coefficient of thermal expansion (CTE), and the name comes from the word “invariable.”

We obtain the 4.6 GHz frequency from a Mini-Circuits voltage-controlled oscillator (VCO). The tiny microwave signal is passed through 3 amplifiers, then combined with

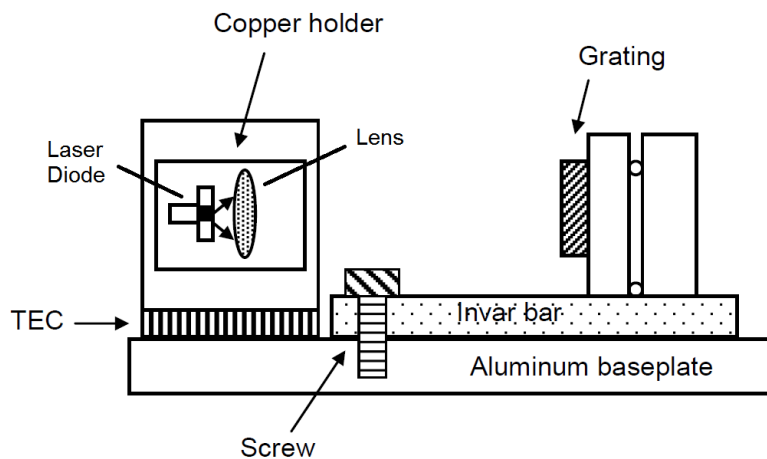


Fig. 3.20. Setup of the home-made Raman laser in Littrow configuration. An additional Invar bar keeps the cavity length constant. Image from [53].

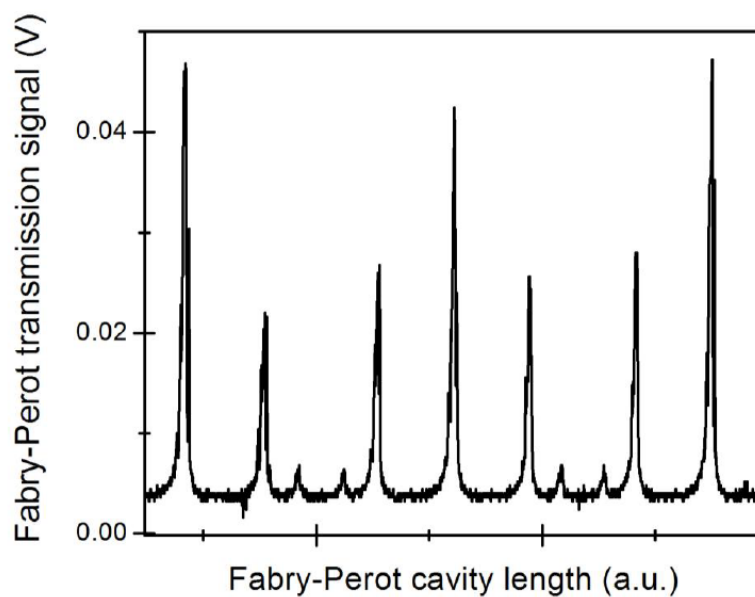


Fig. 3.21. Scan of the Raman laser by a scanning Fabry-Perot interferometer with 300 MHz FSR. The larger peaks correspond to the center frequency while the moderately sized peaks are the modulated sidebands. Roughly 50% of laser power goes into the Raman laser sidebands. Image from [53].

the dc component of the laser diode current in a bias-tee. The microwave amplitude at the output of the bias-tee is ~ 16 dBm, but we are not sure how much actually gets coupled into the laser diode. In any case, as Figure 3.21 shows, about half the laser power ends up in the laser sidebands, which is more than sufficient for Raman spectroscopy.

Because we generate side-bands on the Raman laser by modulating the diode current at high frequency, this laser is very unstable. It requires frequent tweaking to operate at the correct wavelength. Jungu Choi has built a pair of Raman lasers which will be optically phase-locked, and should be much more stable than this Raman laser. With small adjustments, we will be able to use Jungu's lasers instead to probe the atomic spin polarization.

We lock the laser using saturated absorption spectroscopy, just as in section 3.3, but with slight complications due to the laser being 3 frequency components instead of being monochromatic. We discuss this difference and more in section 4.4, where spin polarization efficiency of the atomic beam is explored.

3.8 Vacuum chamber and cesium oven heating

3.8.1 Vacuum chamber

The vacuum chamber containing the Cs beam is a large rectangular aluminum box (see Figure 3.22). It is welded tight on 5 sides and access is through the top, where a heavy 20 kg lid rests. More details can be found in the thesis of Dionysios Antypas [53]. The vacuum chamber is $55 \times 50 \times 40$ cm³, and was made out of aluminum to keep any stray magnetic fields at a minimum. It was designed to be sufficiently large to contain multiple magnetic field coils, electric field plates, nitrogen cryo-baffles and an optical build-up cavity. Several pairs of optical windows are included on the sides, allowing the pump, interaction and detection laser beams through the chamber. The four pairs of 2-in windows have 852 nm anti-reflection (AR-)coatings while the interaction region pair of 1-in windows have dual wavelength 540/1080 nm AR-coatings.

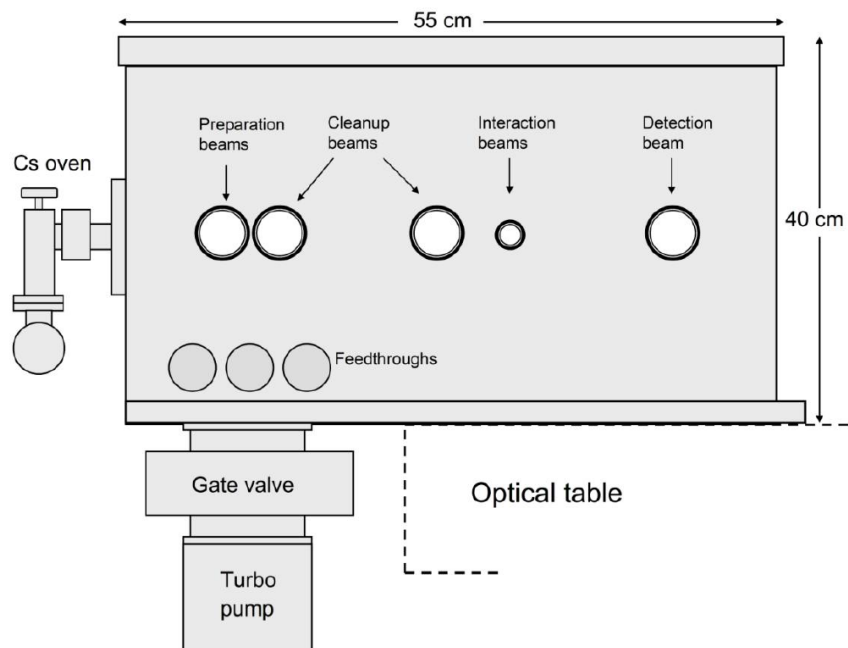


Fig. 3.22. Side-view of the vacuum chamber for the experiment.



Fig. 3.23. Photo of the vacuum chamber in our laboratory. The turbopump and gate valve can be seen attached to the bottom of the vacuum chamber.

3.8.2 Turbopump and vibration damping

The chamber is pumped through a gate valve (see Figure 3.23) by a Edwards STP-451 turbopump (480 L/s) which is magnetically levitated. The turbopump is backed by a roughing pump (200 L/s) which sits on the lab floor. The gate valve shown in the figure allows venting of the vacuum chamber to atmospheric pressure without having to stop the turbopump. This avoids unnecessary starting/stopping of the turbopump which can decrease its lifetime. The chamber pumps down to a base pressure of roughly $3 \cdot 10^{-6}$ Torr, which is low enough that the fraction of atoms in the Cs beam colliding with background gas is small (2%). It takes roughly a day to pump the system back down to base pressure after each time we open the vacuum chamber to make changes or load new cesium.

Despite having very low levels of vibrations, the optics on the optical table pick up the vibrations of the turbopump at 800 Hz. In order to suppress this source of noise, we have purchased and installed a vibration damper between the gate valve and the turbopump. This device consists of a bellows wrapped by a thick layer of vibration absorbing rubber. The resulting vibration at 800 Hz (according to measurements by Edwards) will be reduced by two orders of magnitude (see Figure 3.24). We have not done any experiments to measure the effect of the vibration damper, but recently we have not noticed any oscillations at 800 Hz.

3.8.3 Liquid nitrogen cooled baffles

A pair of liquid nitrogen cooled baffles were installed within the vacuum chamber to reduce Cs clouding in the vacuum chamber. Without cooling these baffles and while running the atomic beam, a cloud of Cs atoms builds up within the chamber. This affects the pumping efficiency and also increases the detected signal background noise. Cooling these plates down with liquid nitrogen causes any Cs atoms colliding with the baffles to stick instead of continuing to bounce around the vacuum chamber. One of these baffles is placed close to the Cs oven with a 10 mm wide x 3 mm tall

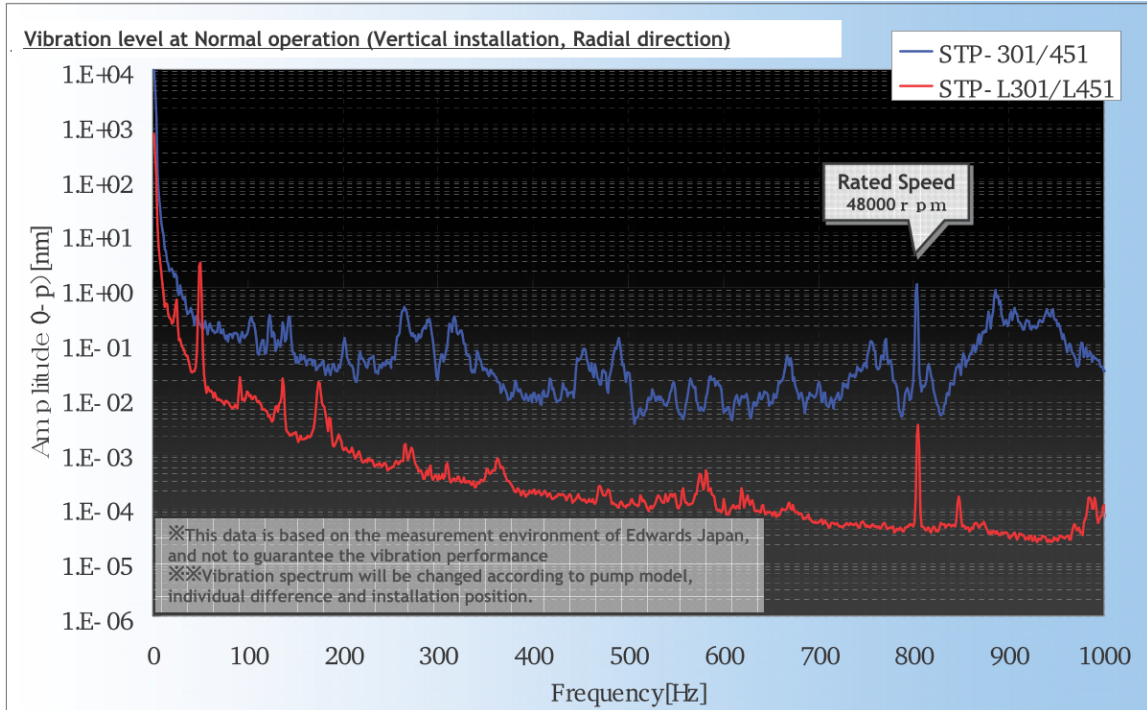


Fig. 3.24. These plots from the manufacturer of the turbopump (Edwards) show the benefit of installing a vibration damper between the turbopump and the gate valve. Vibrations at 800 Hz, the turbopump operating RPM, are reduced by about two orders of magnitude.

aperture which allows the atom beam through. The second baffle is placed on the opposite wall at the end of the Cs beam path, which should capture all the Cs atoms after they travel across the vacuum chamber.

3.8.4 Cesium oven

To generate the cesium atomic beam, we built an oven adapted from [83]. The oven constructed by us has a similar nozzle design and size, and we operate at the same oven temperature. The authors of [83] report an atomic beam density of roughly 10^{10} cm^{-3} , while a shot noise measurement by Dionysis in [53] estimates our beam density to be $3 \times 10^9 \text{ cm}^{-3}$.

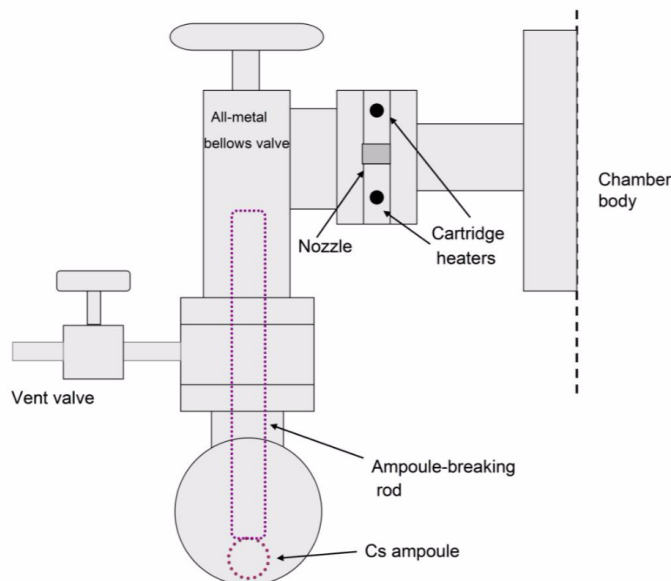


Fig. 3.25. Drawing of the cesium oven, used to produce our atomic beam of cesium atoms.

The cesium atomic beam is generated from a cesium oven connected to one end of the vacuum chamber. A sketch of the various components of the oven is shown in Figure 3.25. With the exception of the nozzle, it is constructed out of off-the-shelf vacuum components and is mounted to the vacuum chamber by several screws. This means it is easy for us to take apart for cleaning or necessary modifications. The density of the atomic beam that effuses is controlled by the temperature of the oven, which we adjust by heating.

There are two main components to our home-made cesium oven. The bellows valve portion of the oven holds the cesium metal and gives us a way to close off the source of cesium. The nozzle collimates and limits the size of the cesium atomic beam effusing from the oven into the vacuum chamber. A vacuum vent valve was included so that the oven can be sealed and kept under rough vacuum when we have to open the main vacuum chamber. Under the bellows valve, there is a small space which

can hold a small cesium ampoule⁴. We load 5 g cesium ampoules into the oven by gently placing them under the ampoule-breaking rod. This way, we can pump down the vacuum chamber and cesium oven before pressing the rod against the ampoule to break it. This means the cesium would not be exposed to air except when we open up the oven for cleaning or loading. Each 5 g cesium ampoule lets us run the system for 3-6 months before we have to re-load a new cesium ampoule.

The second key component in the vacuum chamber is the nozzle, fitted between the bellows valve and the vacuum chamber. The nozzle is made up of roughly 100 stainless steel hypodermic needle tubes, each 1 cm in length, 0.8 mm inner diameter, a design adapted from [83]. They are concentrated in the center of a CF blank flange and have roughly $12 \times 8 \text{ mm}^2$ in total cross section. To ensure that the nozzle does not get clogged, two heater cartridges are placed very close to the nozzle. We run these heaters all the time, even while the system is not in operation. During operation, the heaters are run at higher current to keep them at a higher temperature than the rest of the cesium oven.

For heating the cesium oven, roughly 1 m of heat rope is wrapped around it. Aluminum foil layers cover the heat rope to allow for more uniform heating of the cesium oven. Two thermocouples, one near to the cesium ampoule, and a second close to the nozzle, are used to keep track of the temperature of our cesium oven. The section of the oven containing the cesium ampoule is held at $\sim 100^\circ\text{C}$, while the nozzle is kept at a higher temperature of $\sim 120^\circ\text{C}$ when the system is in operation. Current to the oven heaters is from a pair of benchtop DC power supplies. After turning them on, it takes roughly 2 hours for the temperature to stabilize. We estimate that atomic density drift is stable to $1 - 2\%$ /hour, which is sufficiently low that active temperature feedback is not required.

Proper maintenance of the cesium oven is important for cesium beam operation, and some cleaning and inspection is necessary whenever we open up the oven. Cesium

⁴Typically, we use 99.8% purity cesium ampoules which have a length of ~ 10 cm. High-purity cesium (99.98%) comes in breakseal ampoules which are about 17 cm in length and are too long to fit in the space.

reacts violently with water, so when flushing out the oven, we should always use isopropanol and never water. If there is remaining cesium in the oven, be prepared for the alcohol to catch on fire during cleaning, and have a plan to extinguish the flames. Another downside of using water is that it can cause rust to develop within the oven. This is a huge problem for the nozzle, which should only be flushed with isopropanol and should always be kept dry. Because of the constant heating and cooling, the heat rope and heater cartridge wires are brittle. They should be inspected occasionally to ensure they are still electrically connected. Finally, whenever the oven is disconnected from the chamber body, it is important to inspect the bellows valve. When shut, the valve should hold a 10^9 Torr pressure differential. When recently tested after a long period of use, it would only hold a vacuum of 0.5 Torr. After cleaning with isopropanol and cotton swabs, the valve would comfortably hold a vacuum of $1 \mu\text{Torr}$.

4. PROGRESS TOWARDS THE PNC MEASUREMENT

In this chapter, we discuss the progress that has been made towards completing this measurement and what has to be done to measure the PNC amplitude. Reducing sources of noise in our measurement detection system is the first topic, and in his PhD thesis, Dionysis Antypas [53] measured the contributions of several sources of noise to the M1 measurement. We then go over some improvements made to the detection photodiode electronics. Efficient spin polarization of the cesium atomic beam is critical to maximizing our signal. We detail the workings of the Raman laser that we use to probe the atomic beam population. Following that, we discuss the Pound-Drever-Hall technique, used by some to frequency stabilize lasers to better than sub-Hertz level [84]! We do not go the full extent of frequency stabilization, but use it to reduce fluctuations in the frequency of the 1079 nm and 540 nm lasers. Finally, we discuss the power-build-up cavity, used to increase the intensity of the 540 nm laser power within the interaction region. We discuss the necessity and practicality of having a two-color optical cavity at both 1079 nm and 540 nm.

4.1 Detection laser

In his thesis [53], Dionysios Antypas noted that detection laser frequency noise was a significant source of noise in the M1 measurement. We have identified a couple of ideas to work on to improve the frequency noise on that laser.

Previously, the laser was driven by a commercial ThorLabs current controller. We have now replaced the commercial ThorLabs current drivers with one of our new home-made Libbrecht-Hall [85] current drivers. Recent papers [86–88] examine the current driver in more detail and propose a number of improvements that we have also implemented. We have begun to phase out the ThorLabs current controllers

in exchange for these home-made current controllers. From using them in other measurements, we find that these home-made controllers out-perform the ThorLabs current driver in terms of laser frequency noise.

Other ideas we have to reduce detection laser noise are to optimize the current low frequency servo loop used for saturated absorption frequency locking, or alternatively to implement PDH frequency stabilization of the detection laser.

4.2 Detection system photodiode TIA circuit (Ver. 1)

The photodiode (Hamamatsu #S3204-08, 18×18 mm²) located directly under the detection region is connected to a transimpedance amplifier (TIA) outside the vacuum chamber. The simple circuit consists of an operational amplifier (op-amp) in the transimpedance amplifier configuration to convert the current output from the photodiode into a voltage output. This output is connected to 3 separate op-amps for ac-coupled and dc-coupled outputs.

The initial circuit was hastily built, used through-hole components and a perforated protoboard which is sub-optimal for minimizing signal noise. To reduce noise on the detection signal and improve measurement signal to noise ratio (SNR), the circuit was replaced. The electrical design was laid out using printed circuit board (PCB) software (EAGLE PCB) and sent off for PCBs to be professionally fabricated. Components continue to be hand soldered to the PCB. The schematic for the PCB is shown in figure 4.1.

The new PCB is tiny at only 1×1.4 in.² and utilizes only surface mount (SMD) resistors and capacitors of 1206 (3216 metric or 3.2×1.6 mm²) footprint. The smaller 0805 footprint was considered but was ultimately rejected due to the extra space savings not contributing significantly. The DIP package op-amps were replaced by op-amps in the SOIC surface mount footprint.

For the transimpedance amplifier, the OPA132 was replaced by the newer Texas Instruments (TI) junction field effect transistor (JFET) OPA827. Modern JFET op-

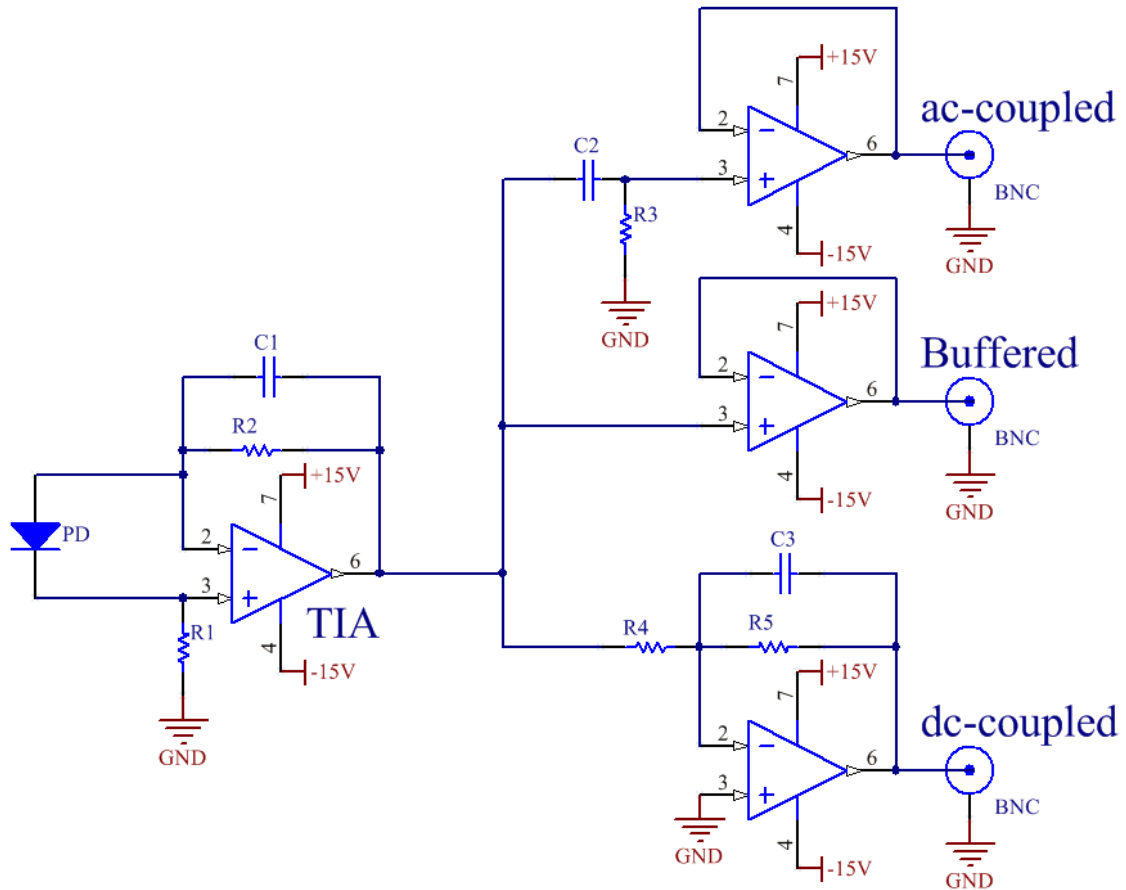


Fig. 4.1. Circuit diagram of the transimpedance amplifier (TIA) and subsequent amplifier stages. The op-amp used for the TIA is the OPA827, chosen for its JFET inputs and low bias current and voltage offset. The OPA4227 was used for the gain stages because we have experience with this op-amp in our lab.

amps such as the OPA827 have extremely low bias current ($3 - 10 \text{ pA}$) and voltage offset ($>150 \mu\text{V}$). The OPA827 also has lower current noise ($2.2 \text{ pA}/\sqrt{\text{Hz}}$) and voltage noise ($4 \text{ nV}/\sqrt{\text{Hz}}$) than the older OPA132.

We choose to use the same second stage quad op-amp the OPA4227 due to its stability and low noise characteristics. Of the three outputs, the first is ac-coupled to get rid of the dc offset in the signal caused by the 1079 nm 2-photon transition



Fig. 4.2. Photograph of the tiny PCB holding the OPA827 TIA and OPA4227 quad op-amp. The PCB is only 1.4×1.1 in².

when the laser is locked in resonance. The second output is a buffer stage only and typically feeds into an oscilloscope for us to monitor the detection signal. The third output is an op-amp in the inverting configuration. If more gain is needed, the ratio of $R5/R4$ can be increased above 1.

Currently, there are sockets on the PCB for connecting the inputs and outputs from panel-mounted BNCs to the circuit board. We have found that these connectors introduce noise when used at higher frequencies (>100 kHz). A future improvement to the PCB could be to replace these on-board sockets with PCB-mounted BNC connectors, and move to smaller footprint op-amps and resistors/capacitors. Temporarily, we have soldered wires directly to the PCB from panel mounted BNC connectors.

With the new circuit (see Figure 4.2), we observe a reduction in background noise of the detection signal by approximately half, when viewed on an oscilloscope. However, a measurement of a weak atomic transition is necessary to accurately estimate the improvement in detected signal signal-to-noise ratio (SNR).

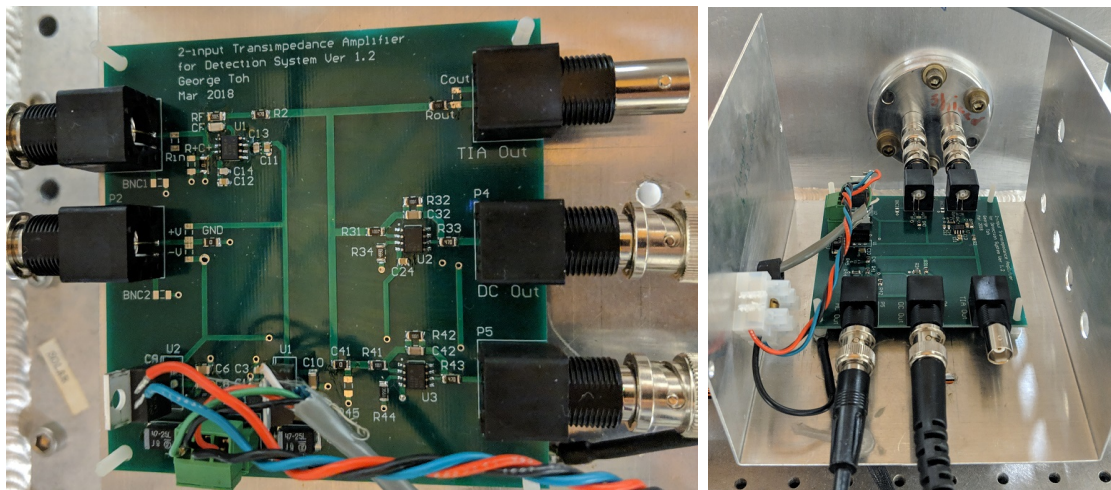


Fig. 4.3. Photos of the improved TIA circuit. On the left, we show a top-down view of the PCB. On the right, the photo shows how the PCB directly connects to the vacuum chamber feedthrough.

4.3 Newer detection system TIA circuit (Ver. 2)

In 2018, we re-built the detection system TIA circuit again. We found that a major source of electronic noise was being picked up by the coaxial cables connecting the vacuum feedthrough to the PCB. We also improved on some of the other design decisions made from Version 1.

Version 2 of the TIA circuit, seen in Figure 4.3, at $3.5 \times 3.5 \text{ in}^2$, is much larger than Version 1 (seen in Figure 4.2), having almost 8 times as much surface area. For the first stage of gain, we use the same low bias current and low offset voltage op-amp, the OPA827. However, on the output, we replaced the quad op-amp (OPA4227) with two single OPA140 op-amps. In Version 1, we found that sometimes there was cross-talk between the different channels of the OPA4227. We also added a direct output from the OPA827 for de-bugging purposes. We show the layout of the op-amps on the PCB in the left photo of Figure 4.3. There are empty component spaces on the PCB so that the circuit can be customized for different configurations in the future.

Most of the space on the PCB was left unused, but we intentionally made it larger than needed in order to space out the components and reduce the effects of

cross-talk. The other reason for the much larger PCB was size of the board-mounted BNC connectors, visible in Figure 4.3. In Version 1, we used panel-mounted BNC connectors, which connect to the PCB via a pair of twisted wires and sockets on the board. We replaced all the signal connectors with board-mounted BNC connectors, so that there are no wires between the connectors and the PCB. This results in less opportunity for noise pick-up. On the input side, we designed the distance between the connectors to be the same as the connectors on the vacuum feedthrough. As can be seen in the right photo of Figure 4.3, we can now directly connect the PCB to the vacuum feedthrough, removing the need for connector cables. We found that this greatly reduced the amount of electronic noise picked up and amplified by the TIA op-amp, especially 60 Hz and 120 Hz electrical noise.

With Version 2 of the TIA circuit, we find very much reduced noise and dark current. While the background voltage (op-amp bias current $I_{\text{bias}} \times 50 \text{ M}\Omega$ feedback resistance) used to be 10 – 20 mV, this has now been improved to $V_{\text{bg}} < 1 \text{ mV}$. In addition, high frequency noise or fuzziness of the line when seen on a high-frequency oscilloscope has been reduced to $V_{\text{noise}} < 1 \text{ mV}$.

Finally, to estimate the bandwidth of the transimpedance amplifier, we use Equation (2) from the OPA827 datasheet [89]:

$$f_{-3dB} = \sqrt{\frac{\text{UGBW}}{2\pi R_F C_{\text{total}}}} \text{ Hz} \quad (4.1)$$

where UGBW is the unity gain bandwidth of the op-amp (22 MHz), R_F is the feedback resistance of the TIA (50 M Ω) and C_{total} is the total capacitance, dominated here by the photodiode capacitance (2 nF at $V_R = 0 \text{ V}$). The -3dB bandwidth is thus calculated to be $f_{-3dB} \approx 5.9 \text{ kHz}$.

4.4 Improving spin polarization of the atomic beam

Currently, only $\sim 90\%$ of the atoms in the cesium atomic beam are pumped into the target m state, while minimal population (less than 0.5%) of atoms remain in the empty hyperfine level. With more tweaking of the overlap and power of the hyperfine

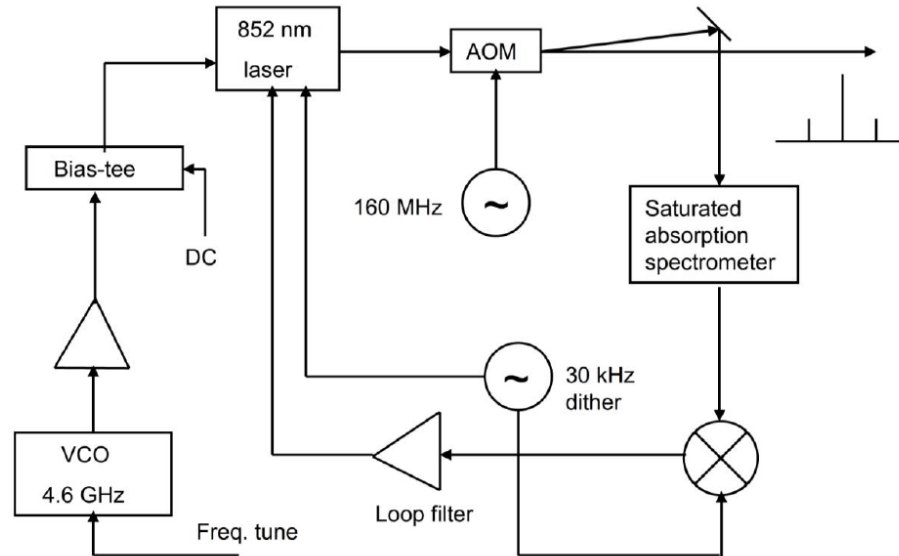


Fig. 4.4. Experimental setup for the Raman laser. The portion of the Raman laser up-shifted by 160 MHz in the AOM is locked to the $6S_{1/2} F=3$ to $6P_{3/2} F=2$ transition by saturated absorption. VCO - voltage controlled oscillator, AOM - acousto-optic modulator, DC - dc component of the diode current from the current controller. Image from [53].

and Zeeman pump lasers, we expect to be able to improve the pumping efficiency. In this section, we discuss the Raman spectroscopy technique and how it allows us to determine the population density of the cesium ground state.

In section 3.7, we discussed the Raman laser and how we put together an ECDL to generate frequency components 9.2 GHz apart. Recall that the laser current is modulated at 4.6 GHz so three frequency components are present on the laser output: ω , $\omega + 4.6$ GHz and $\omega - 4.6$ GHz. Figure 4.4 shows the experimental setup for the Raman laser. We use an acousto-optic modulator (AOM) driven at 160 MHz to split the laser output into two sets. The un-shifted frequency trio is sent to the vacuum chamber for spectroscopy, while the trio that is up-shifted by 160 MHz is sent to a Cs vapor cell for saturated absorption locking.

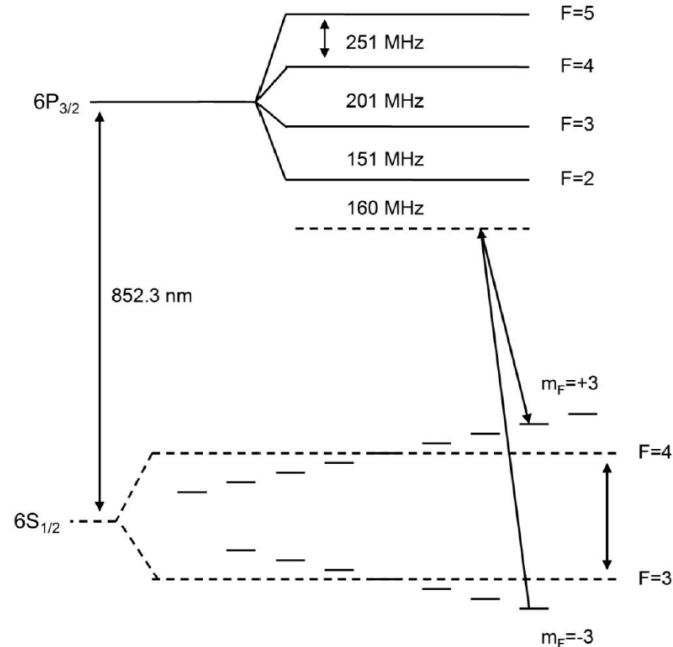


Fig. 4.5. Energy level diagram showing off-resonant Raman transitions between two cesium magnetic sublevels due to the Raman laser. The ground state magnetic sublevels degeneracy is broken by a ~ 7 G magnetic field. Image from [53].

The locking procedure for the Raman laser is the same as in section 3.3. However, due to the components at $\omega \pm 4.6$ GHz, the saturated absorption signal will look weird. This is because the 3 frequency components of the laser cause the system to become a 3-level system, instead of a 2-level system [52]. For the edge transitions ($F = 4 \rightarrow 5$ and $3 \rightarrow 2$), only one frequency component is resonant so we can safely lock to the $F = 3 \rightarrow 2$ transition with the upper frequency component ($\omega + 4.6$ GHz).

Since we used the frequency up-shifted set for saturated absorption, the un-shifted trio of frequencies ends up being off-resonant. Figure 4.5 shows the energy level diagram of our off-resonant Raman spectroscopy scheme. Here, $\Delta m = 0$ transitions are used to probe the 6S $F=4$ ground states of the atoms. We optically pump all of the atoms into the $F=3$ ground hyperfine state, and detect the number of atoms in the previously empty $F=4$ ground state. As the modulation frequency of the Raman

laser is slowly scanned around 4.6 GHz, each of the individual $(F = 3, m) \rightarrow (F = 4, m)$ transitions is sequentially resonantly driven by the sidebands of the Raman laser. We set the detection laser to detect $F = 4$ ground state atoms. Functionally, when the scan rate is slow enough, this allows us to measure the population in each of the Zeeman sublevels of the 6S $F = 3$ ground state. Figure 4.6(a) shows the oscilloscope scan when we sweep across the $m = -1 \rightarrow +3$ Zeeman levels, while the Zeeman laser is turned off. The atoms are approximately evenly spread across the various Zeeman sublevels.

When the Zeeman laser is operated at the same time as the hyperfine laser, the atoms in the 6S $F=3$ tend to get pushed to one of the edge magnetic levels ($m = \pm 3$), depending on the handedness of circular polarization of the Zeeman laser. In Figure 4.6(b), right circularly polarized light from the Zeeman level pumps the atoms toward the far right $m=+3$ sublevel. We see that there is still significant population of atoms in the $m=+2$ magnetic sublevel, and trace population in $m=-1,0,+1$ sublevels.

It is clear from Figure 4.6 that we have to optimize the optical pumping of the atomic beam to place more of the atoms into the edge $m=+3$ magnetic sublevel. In [53], Antypas reports that he achieved pumping of 92% of atoms into the extreme $m=\pm 3$ sublevels while using the same experimental setup, while Wood in [52] was able to get 97-98% into the same sublevels. This tells me that there is much work to be done optimizing the spin polarization of the cesium atomic beam, before we proceed with the PNC measurement.

4.5 Pound-Drever-Hall laser frequency stabilization

4.5.1 Introduction to PDH

Pound-Drever-Hall (PDH) laser frequency stabilization is a frequency modulation (FM) technique first proposed for masers by Pound [90] and later demonstrated in lasers by Drever and Hall *et al.* [91]. For more recent guides to PDH, see [80,92–94]. It

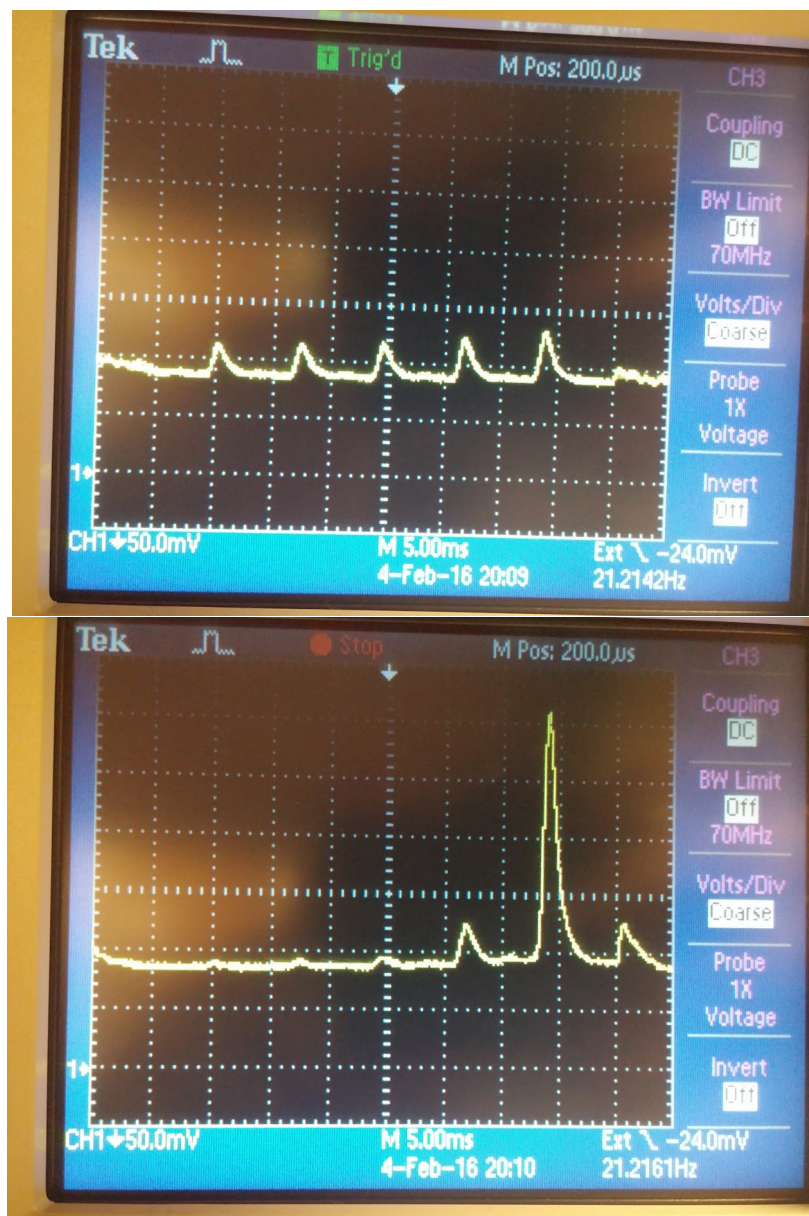


Fig. 4.6. Oscilloscope sweeps showing the detection photodiode signal as the Raman laser modulation frequency is scanned with: (a) only hyperfine pumping and (b) hyperfine and Zeeman pumping. The far right peak in both scans is due to the ramp return and not a part of the scan.

is an important part of the technology behind the Laser Interferometer Gravitational-Wave Observatory (LIGO) experiment which first detected gravity waves in 2015.

The technique involves modulating a laser at high frequency (typically >10 MHz) to impose frequency sidebands on the laser beam [92]. The laser is then coupled into a stable optical cavity, where the reflection off the cavity input mirror allows us to make a measurement of the laser frequency. This measurement is fed back into the laser to suppress frequency fluctuations of the laser against the optical cavity. One benefit of this locking scheme is that the system can respond to fluctuations faster than the response time of the cavity (cavity ring-down time), where the cavity acts as a phase discriminator rather than a frequency discriminator.

As mentioned earlier, the articles [80,92] offer an excellent explanation and tutorial to PDH frequency stabilization. New students intending to implement PDH in their setup should read both papers carefully. While [92] offers a good theoretical overview behind the technique, [80] is a good tutorial for experimentalists wanting to setup PDH for one of their lasers. I have distilled the bare minimum from these two papers for a good qualitative understanding of the Pound-Drever-Hall technique and included that in this chapter.

4.5.2 PDH theory

PDH scheme

A key component of the Pound-Drever-Hall (PDH) technique is the stable optical cavity. When the incoming laser light is resonant with the length of the optical cavity, light will be transmitted through the cavity. This occurs when the frequency of light is equal to an integer number of the free spectral range of the cavity $FSR = c/2nL$ where L is the length of the cavity, c is the speed of light in vacuum and n is index of refraction of the medium (typically air or vacuum). When the laser is off resonance, we get no transmitted beam. Figure 4.7 shows the transmission profile of a laser that is scanned in frequency across >2 free spectral ranges with a cavity of finesse 12.

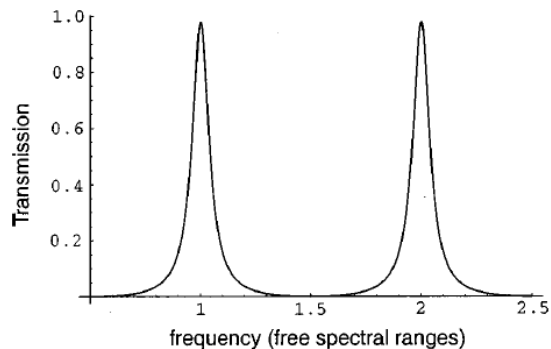


Fig. 4.7. Transmission spectrum of a Fabry-Perot optical cavity versus frequency of the incident laser. The cavity finesse here is 12. Image from [92].

If we naively attempt to use this transmission profile as an error signal to lock the laser to the maximum point of the transmission peak, we quickly run into a problem. The intensity is symmetric about the resonance, so we cannot tell whether we should increase or decrease the frequency of the laser to correct for the fluctuation.

The way around this problem is to find the derivative of the intensity, which we obtain by modulating the frequency of the input beam. This is shown in Figure 4.8. Here we show the reflected power, rather than the transmitted power as was shown in Figure 4.7. The frequency of the input laser is modulated slowly, and we observe how the reflected beam responds. When perfectly on resonance, a small variation in the frequency of the laser causes no change in reflected intensity. However, when the laser frequency is slightly higher than the cavity resonance, an increase in frequency of the laser causes an increase in detected intensity, a positive derivative relationship. When the laser frequency is slightly lower than the cavity resonance, an increase in laser frequency leads to a decrease in detected intensity (a negative derivative). We showed a similar derivative curve earlier for saturated absorption in Figure 3.7.

The 180° phase difference of the derivative when above and below resonance allows us to tell which side of the resonance we are on! If we extract this derivative signal

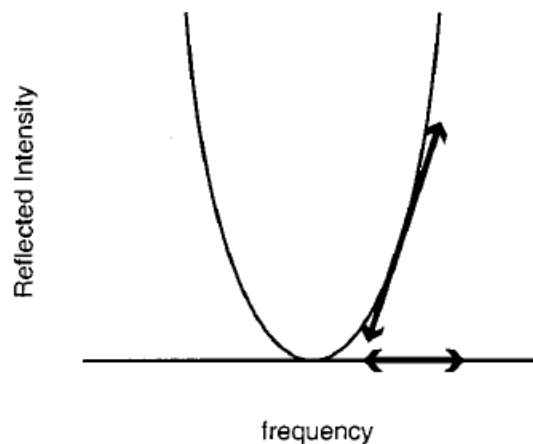


Fig. 4.8. Reflected spectrum of a Fabry-Perot optical cavity versus frequency of the incident laser. On resonance, the reflected intensity is zero. Modulating the laser frequency tells us which side of the resonance we are on. Image from [92].

and feed it back to the laser as an error signal, we can electronically compensate for any frequency fluctuations in the laser.

Reflected beam

The beam being reflected from the optical cavity input mirror is actually the coherent sum of two components. The first component is the part of the input beam that does not enter the cavity, and is reflected from the surface of the mirror. The second component, which we term the leakage beam, is due to the build-up of optical power within the cavity leaking out of the cavity through the input mirror due to reflectivity not being perfectly 100%.

When the input beam is on resonance with the optical cavity, the reflection component is 180° out of phase with the leakage component, and thus they interfere destructively. This results in there being no reflected beam from the cavity when the laser is exactly on resonance, as shown in Figure 4.8.

When the laser frequency is not an integer multiple of the cavity free spectral range (off resonance condition), the resultant phase difference between these two components is no longer 180° . This means that the two beams do not cancel, and so there will be a reflected beam from the cavity. The phase of the reflected beam then tells you which side of the resonance (above or below resonance condition) you are on.

Modulating the beam: Sidebands

While the discussion thus far has talked about modulating the frequency of the input laser, it is easier to do phase modulation in practice. By passing the beam through a Pockels cell or an electro-optic modulator (EOM), we can easily phase modulate the input beam, and the result is the same as frequency modulation.

The electric field of the input beam can be written as:

$$E_{inc} = E_0 e^{i\omega t} \quad (4.2)$$

where E_0 is the amplitude of the electric field, ω is the frequency of the laser, and t is time. After phase modulation at frequency Ω , the electric field of the beam becomes:

$$E_{inc} = E_0 e^{i[\omega t + \beta \sin(\Omega t)]} \quad (4.3)$$

Using Bessel functions, we expand equation (4.3) into the following form:

$$\begin{aligned} E_{inc} &\approx [J_0(\beta) + 2iJ_1(\beta) \sin(\Omega t)] e^{i\omega t} \\ E_{inc} &\approx E_0 [J_0(\beta) e^{i\omega t} + J_1(\beta) e^{i(\omega+\Omega)t} - J_1(\beta) e^{i(\omega-\Omega)t}] \end{aligned} \quad (4.4)$$

Notice that the beam is the sum of three components at frequencies ω , $\omega + \Omega$ and $\omega - \Omega$. These represent the carrier frequency (ω) and the two sidebands at $\omega \pm \Omega$. Thus, phase modulating a laser beam has the effect of imposing sidebands (see Figure 4.9) at the carrier frequency \pm the modulation frequency.

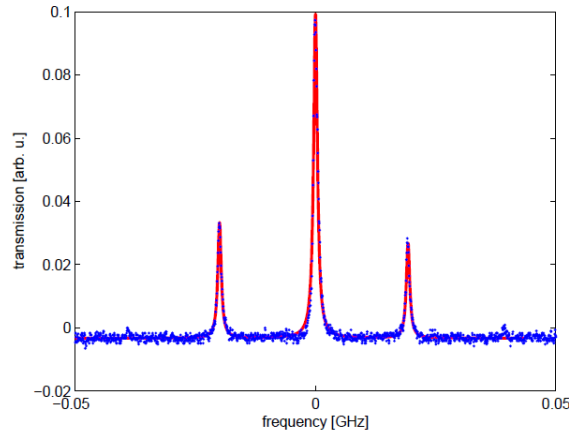


Fig. 4.9. Transmission spectrum of a Fabry-Perot optical cavity versus frequency of the incident laser, when the incident laser has strong sidebands due to phase modulation. Image from [93].

Measuring the phase of the reflected beam

We do not yet know how to directly measure the phase of a laser beam electronically. PDH gives us a method to indirectly measure the phase. First, we phase modulate the laser beam as described in the previous sub-section. This effectively imposes sidebands on the laser beam. Interfering the sidebands with the reflected beam at the carrier frequency, we obtain a beat pattern at the modulation frequency which we pick up using a fast photodiode. From the phase of the beat pattern, we then have information about the phase of the reflected beam.

Reflection of modulated beam

After phase modulation, the beam has been split into three distinct frequencies, but the analysis is still simple. We treat the three frequencies as separate incident beams, and multiply each by the reflection coefficient of the cavity at its frequency. If the cavity reflection coefficient at frequency ω is:

$$F(\omega) = \frac{E_{ref}}{E_{inc}} \quad (4.5)$$

then the electric field of the reflected beam is the sum of the three components:

$$E_{ref} = E_0 \left[F(\omega) J_0(\beta) e^{i\omega t} \right. \quad (4.6)$$

$$+ F(\omega + \Omega) J_1(\beta) e^{i(\omega + \Omega)t} \quad (4.7)$$

$$\left. - F(\omega - \Omega) J_1(\beta) e^{i(\omega - \Omega)t} \right] \quad (4.8)$$

and the reflected power is the square of the electric field:

$$P_{ref} = |E_{ref}|^2 \quad (4.9)$$

An expansion of terms for the square of the electric field can be found in reference [92]. There will be terms at the carrier frequency ω , and at $\omega \pm \Omega$. It is the interference of these two terms that results in a beat pattern at Ω which lets you sample the phase of the reflected carrier.

Measuring the error signal

Now that we have the beat signal at frequency Ω , we input this to an RF mixer, and mix it with a local oscillator (LO) at frequency Ω' . We denote these two signals as pure sinusoidal frequencies, and mathematically the mixer output can be written:

$$\sin(\Omega t) \sin(\Omega' t) = \frac{1}{2} [\cos([\Omega - \Omega']t) - \cos([\Omega + \Omega']t)] \quad (4.10)$$

Mixing the beat signal with the LO results in two outputs, one at twice the modulation frequency ($\Omega + \Omega'$) which we do not want, and another term at dc ($\Omega - \Omega'$) which has the phase and frequency information we want. This is the error signal that we wanted to extract. All we have to do now is to feedback this error signal into the laser! Setting up the circuit and optical components to implement PDH will be discussed in section 4.5.3.

Note that I have assumed the beat signal and the LO are in phase. If the phase difference between them is 90° such that the LO input is now a cosine instead of sine, we get the following situation:

$$\sin(\Omega t) \cos(\Omega' t) = \frac{1}{2} [\sin([\Omega - \Omega']t) - \sin([\Omega + \Omega']t)] \quad (4.11)$$

In this case, since $(\sin(\Omega - \Omega') \approx 0)$, the DC signal vanishes! This is why all PDH guides will point out the need for a phase shifter on either the beat signal input, or LO input. We have chosen to leave out the phase shifter and instead vary the modulation frequency to tune the phase difference, as will be discussed in the next section.

4.5.3 Implementation of PDH

As discussed in the previous section, PDH frequency stabilization is quite well understood, and relatively easy to setup. Besides the optical cavity, all the optical table components to PDH are easily found in laser labs or can be bought off the shelf. An optical cavity at the right frequency is more difficult to obtain, and in our case, we constructed an Invar cavity with finesse ~ 1000 . In addition, the electronics such as laser controllers with a fast modulation input (Thorlabs laser controllers have a modulation input bandwidth of 250 KHz which is too slow) and an analog controller for the servo loop can be purchased from vendors such as Toptica and Vescent Photonics, but these cost quite a bit of money. We have built our own laser controllers (based on the Libbrecht-Hall design), and our own high frequency analog controller (inspired by the Toptica and Vescent controllers). Finally, the photodetector used for signal detection needs to have bandwidth greater than the modulation frequency. These are readily available off-the-shelf from places such as ThorLabs.

Optical table setup

We use a home-made optical cavity with a finesse of roughly 1000, and a FSR of 1 GHz. The cavity tube is made out of Invar due to its low coefficient of thermal expansion, and mounted within an aluminum shell with Sorbothane vibration damping material. The aluminum shell shields the Invar cavity from most air currents, but we

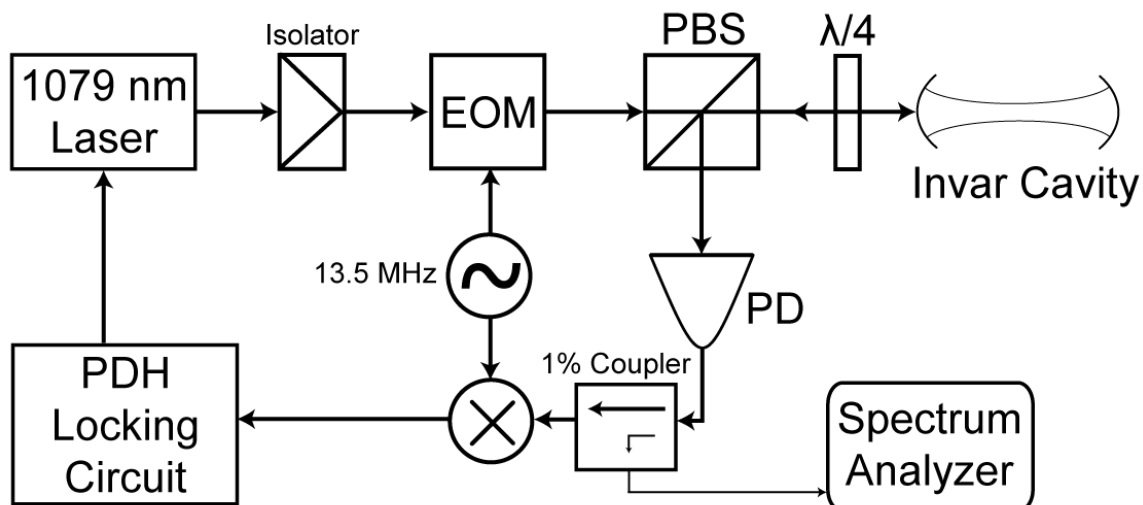


Fig. 4.10. This diagram shows the major components of our Pound-Drever-Hall setup. EOM - electro-optic modulator, PBS - polarizing beamsplitter, $\lambda/4$ - Quarter wave-plate, PD - photodetector.

have found that having an external box around the cavity significantly improves the frequency stability of the cavity.

To isolate the cavity from vibrations of the optical table, we mount the cavity, focusing telescope and final mirror on a 0.25 in thick aluminum plate. This aluminum plate rests on several strips of Sorbothane and is gently clamped to the optical table using 1/4-20 nylon screws. This ensures that the cavity is well isolated from vibrations on the optical table.

The 1079 nm laser is an ECDL, described in more detail in an earlier section. The various optical components for the PDH setup are shown in Figure 4.10. The output laser from the ECDL passes through an optical isolator, then through anamorphic prisms to round the beam shape. The beam is then passed through a non-polarizing beam splitter (BS), where half the power is used for PDH frequency stabilization, and half the power goes to the 10 W fiber amplifier for the experiment.

Because back-reflections have been an issue (causing instabilities in the laser), the portion of the beam sent to the optical cavity for PDH is passed through another optical isolator. It is then sent through an EOM where the laser is phase modulated. The linearly polarized beam then passes straight through a polarizing beam splitter (PBS) and a quarter wave plate. To maximize the coupling efficiency, a telescope gently focuses the beam into the cavity. The reflected beam from the optical cavity passes back through the quarter wave plate. This results in a 90° rotation of the polarization with respect to the input polarization, so the reflection is directed towards the fast photodiode shown in the Figure 4.10.

The photodiode we use is a ThorLabs FGA01, chosen due to its tiny surface area (low capacitance, fast response) and extremely low noise equivalent power (NEP) of $4.5 \times 10^{-15} \text{ W}/\sqrt{\text{Hz}}$. The photodiode is soldered onto a custom PCB, where the op-amp OPA657 (gain bandwidth of 3.9 GHz) is used as a transimpedance amplifier (TIA). The transimpedance resistance is 20 kohm, resulting in a 3 dB bandwidth of approximately 40 MHz. The TIA output feeds into a dual op-amp, the LMP8672. One of the outputs is ac-coupled, while the other is dc-coupled. The dc-coupled output is low-pass filtered, and sent to an oscilloscope for monitoring the error signal line shape and adjusting the laser alignment into the cavity. The ac-coupled output from the LMP8672 is sent to an RF directional coupler which picks off -20 dB of the input to send to a spectrum analyzer which we use for monitoring the lock. More details on the use of the spectrum analyzer are included in the following sections. The majority of the power ($>99\%$) goes into the RF port of our RF mixer (ZAD-8+ from Mini-Circuits). The modulation frequency, which is also fed to the EOM to phase modulate the laser, is fed into the LO port of the same RF mixer. Finally, we obtain an output from the intermediate frequency (IF) port. This signal is the error signal that we want, and will tell us which way to adjust the laser to keep it locked to the cavity resonance. We pass this error signal through the servo loop filter (or locking circuit) which feeds the filtered error signal to the laser diode and piezoelectric element.

Pound-Drever-Hall error signal

Depending on the frequency of the modulation, the error signal we obtain has two distinct regimes. In the low frequency regime, where $\Omega \ll$ linewidth of the cavity, the sidebands of the laser are not distinct from the carrier frequency and thus we obtain an error signal that looks like figure 4.11. This is akin to what we do in Section 3.3 to do saturated absorption locking. In the high modulation frequency regime, where the modulation frequency $\Omega \gg$ linewidth of the cavity, the sidebands of the laser are far from the carrier frequency (like in Figure 4.9) and each component can be distinguished from the other two. The result is the PDH error signal, an example which is shown in figure 4.12. From comparing the two figures, the two key advantages of the PDH error signal (fast modulation) is apparent: (1) the error signal is the correct sign for a larger frequency range in the fast modulation regime; (2) the slope of the error signal close to resonance is much steeper for fast modulation. For example, we see in Figure 4.11 that the error signal is significant (> 0.1) for normalized frequency range $0.997 - 1.003$. For PDH shown in Figure 4.12, the error signal is > 0.1 for the normalized frequency range $0.96 - 1.04$, a much larger range than when we have low frequency modulation! This means that the servo can correct for frequency excursions in a much larger range, and that any small fluctuations would be aggressively corrected for. Qualitatively, this is why the PDH technique works so well.

Servo loop filter

The servo loop filter (or locking circuit) comprises the electronics used to filter the error signal before it is fed back to the laser. As our laser is an ECDL with two adjustable inputs (the PZT for low frequency corrections, and the laser current for fast corrections), the loop filter has the important task of splitting the error signal into a slow and fast component. The slow component is fed to the PZT to correct

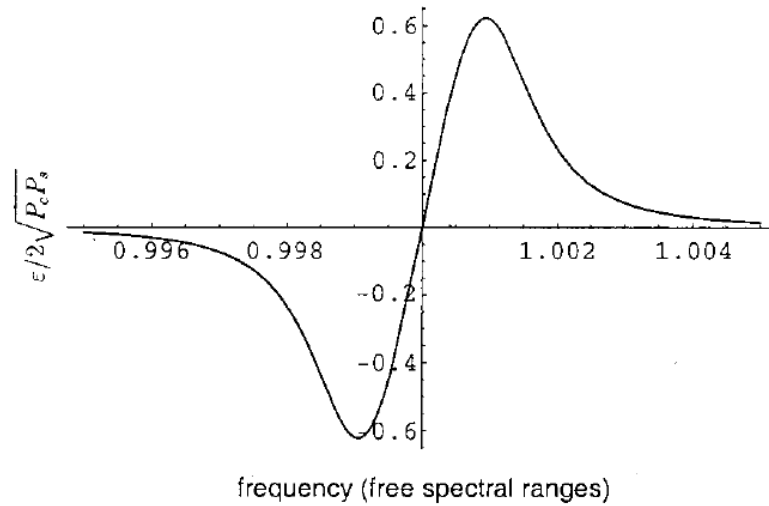


Fig. 4.11. Plot of error signal versus frequency normalized to the free spectral range for low modulation frequency. When the modulation frequency is low, the error signal is a broad dispersion shaped curve. Image from [92].

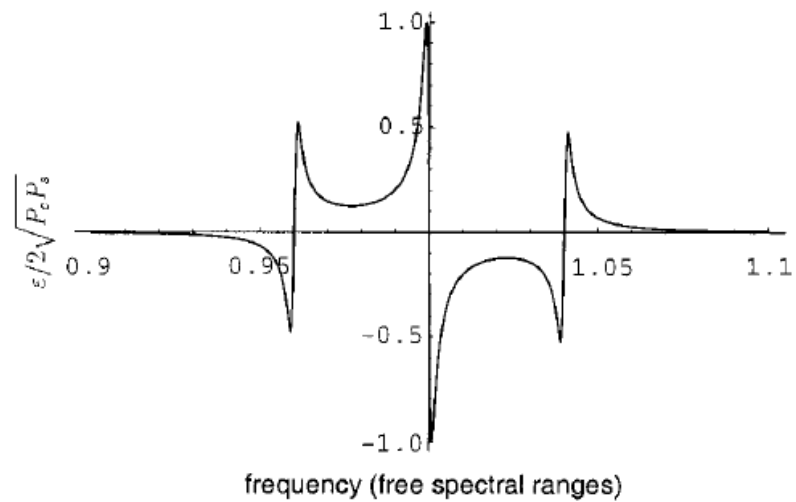


Fig. 4.12. Plot of error signal versus frequency normalized to the free spectral range for PDH. When the modulation frequency is high, the PDH error signal has this shape. Notice the much larger frequency span where the error signal is large (0.96 – 1.04) compared to that of Figure 4.11 (0.997 – 1.003). The slope of the error signal close to resonance is also much steeper. Image from [92].

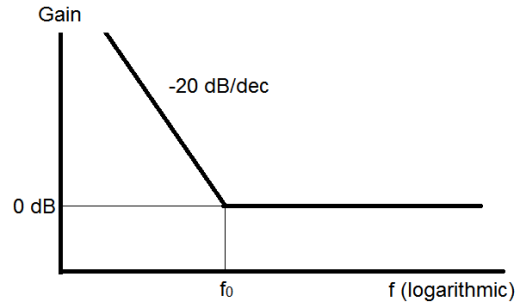


Fig. 4.13. Bode plot for an ideal P-I op-amp, otherwise known as a limited integrator. Very high gains can be obtained at very low frequencies where $f \ll f_0$.

any low frequency fluctuations, while the fast component is fed to the laser current controller to tune the laser current to correct for fast frequency fluctuations.

Slow The low frequency component of the error signal is sent to an integrating op-amp with a low cut-off frequency of ~ 1 kHz. The integrating op-amp boosts the gain of the error signal at low frequencies, correcting for frequency fluctuations in the laser for $f < 1$ kHz. Integrating op-amps have gain-frequency gradient of -20 dB/dec. Figure 4.13 shows the Bode plot of an integrating op-amp with a cut-off frequency at f_0 . When $f_0 \approx 1$ kHz, gain at very low frequencies (< 1 Hz) can be in excess of 60 dB! We use the PZT of the ECDL to correct for any long-term drifts in the laser frequency because the PZT has a wide dynamic range compared to the current controller feedback.

Fast The high frequency component of the error signal is sent to the laser current controller to correct for fast frequency fluctuations in the laser. The filtering electronics for the fast leg of the error signal comprises the majority of the locking circuit and will be discussed in the next few sections. We note here that the current feedback has a narrow dynamic range and the electronics gets easily saturated. This makes it necessary to high-pass the fast component of the error signal, which we filter at ~ 10 Hz. Without this high pass filter, we find that the fast feedback component of the

error signal will try to correct for slow drifts in the laser frequency against the slow feedback component and cause itself to saturate.

Hardware Leo Hollberg and John Hall recommend directly connecting this fast feedback component to the laser diode [80, 95]. We have not done this, and have instead connected it to the modulation input of our Libbrecht and Hall laser current controller board. This reduces the maximum performance we can get out of the locking circuit, but we get some electrical protection for our laser diode. We compensate for this difference by placing the current controller right next to the external cavity diode laser to shorten the feedback loop delay.

Another important thing to note is the necessity to use a fast laser current controller for PDH frequency stabilization. We initially used a ThorLabs LDC202C benchtop current controller, but soon realized that the modulation input is limited to 250 kHz. The Libbrecht-Hall current controller design utilizes 8 MHz op-amps for voltage matching on the modulation input, but it has been found by [87] that the modulation input is not dependent on the bandwidth of the input voltage stabilizing op-amps, and the modulation frequency cut-off is higher than 8 MHz.

Filter stages for fast feedback

We have designed and built our own printed circuit boards (PCBs) for filtering the fast component of the error signal. This has been an iterative process over a couple of months, starting from modified designs of an Antypas [53] locking circuit we use in our lab for saturated absorption locking. Thanks to low-cost quick-turn PCB manufacturers in China (such as PCBWay), we are able to quickly modify the circuit and re-spin the PCB. In the latest two versions, we were inspired by the FALC (Fast Analog Locking Circuit by Toptica) and added DIP switches to the PCB so that we can change the op-amp frequency cut-offs without re-soldering components. This has greatly reduced optimization time.

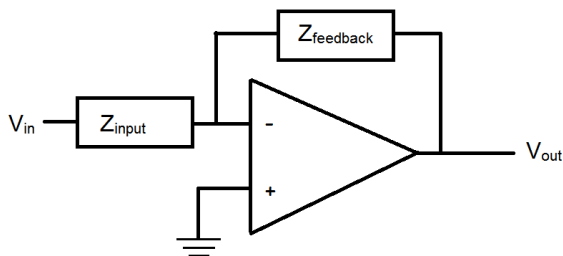


Fig. 4.14. Schematic of an inverting op-amp. Z_{input} and $Z_{feedback}$ are resistive or capacitive elements.

In the current version of the PDH locking circuit PCB, the key components are a string of four fast op-amps, laid out in the inverting configuration. Figure 4.14 shows the generic form of an inverting op-amp. In our case, we adjust the values for Z_{input} and $Z_{feedback}$, the input impedance and feedback impedance respectively, to change the gain profile of the op-amp. We use DIP switches with an assortment of resistors and capacitors for adjusting these frequency cut-off values. In figure 4.13, I showed a Bode plot of a proportional-integral op-amp setup, also known as a limited integrator. In the limited integrator setup, there is unity gain above the cut-off frequency f_0 , and increasing gain below f_0 . For $f_0 = 100$ kHz, this means that gain at $f = 1$ Hz can be up to 100 dB! This high amount of gain is necessary to counter the low frequency fluctuations of the laser, which we will see in the next section.

During my tests, I experimented with the unlimited integrator and limited integrator. However, it was found that an op-amp with very high dc gain and a low pass filter at low frequency (~ 100 Hz) gives the same effect and tends to be more stable. Figure 4.15 shows the Bode plot for an op-amp with such a configuration.

To analyze the effectiveness of the locking circuit (or servo loop), there are two key parameters that we look for. We want high gain at the Fourier frequencies near dc, and high servo bandwidth. High gain at low frequencies means that small deviations of the error signal are greatly amplified, to push the laser frequency back to the cavity resonance condition. Servo bandwidth is a little more complex to understand. Servo

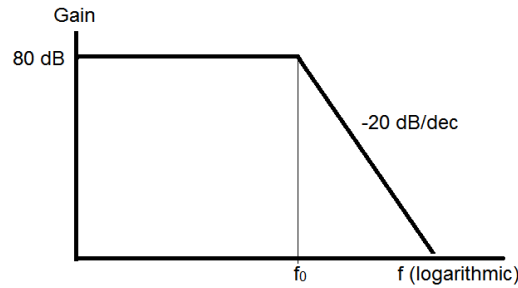


Fig. 4.15. Bode plot for op-amp with very high gain (80 dB) at dc, and a low pass filter at f_0 .

bandwidth can be explained as the frequency where the phase shift due to the servo loop is at 180° . When this happens, the correction signal fed to the laser is inverted, meaning that any small perturbations cause a build up in error, and the system will begin to oscillate. Servo designers thus design their servo loops to have < 0 dB gain where the phase shift approaches 180° . The servo bandwidth is also known as the unity gain point of the system. [80] has a good chapter talking about maximizing servo bandwidth, and good rules of thumb to follow when designing servo loops.

The second thing the filter has to correct for is the additional poles introduced by various components of the locking system. For instance, typical laser diodes have reduced response at ~ 300 kHz, while the Invar cavity introduces a pole at the frequency of its linewidth [80], in this case ~ 1 MHz. These poles act like a low pass filter, introduce phase shifts and reduce gain at higher frequencies, reducing our total servo bandwidth. The loop filter thus has to compensate for these poles by introducing zeros at the appropriate frequency. Unfortunately, choosing the right frequency for compensation of zeros is mostly an iterative process, and very time-consuming.

4.5.4 PDH progress to date

Significant progress has been made towards PDH frequency stabilization. We are now able to lock the laser to the Invar cavity and have it stay locked for hours at a time. We monitor the residual error signal from an output of the locking circuit

box, and we notice that this shrinks in amplitude by several times. From the locked error signal, we estimate that the 1079 nm laser has a residual frequency linewidth of about 50 kHz.

The second method we use to quantify the effectiveness of the locking circuit, is by looking at the error signal on a spectrum analyzer, a method suggested in [80]. We mentioned earlier that a -20 dB directional coupler picks off a portion (1%) of the ac-coupled photodiode signal and sends it to a spectrum analyzer (Siglent SSA3021X). This allows us to monitor the noise spectrum of the laser while locked. Because we are monitoring the photodiode signal here and not the output from the RF mixer (see Figure 4.10), the noise spectrum is centered at 13.5 MHz, the PDH modulation frequency. Mixing this signal with the local oscillator (LO) at 13.5 MHz in the RF mixer is what gives us the error signal centered at dc which we feedback to the laser.

Figure 4.16 shows a 10 MHz span (1 kHz resolution) of the laser noise spectrum. In the figure, the blue line shows the noise on the laser when only slow (PZT) feedback is applied. The green line shows the noise on the laser after we turn on the fast (laser current) servo loop. We see that at low Fourier frequencies < 1 MHz, we have a reduction in noise from the PZT-only lock. Close to the center, at the very low frequencies $\ll 1$ MHz, noise power on the laser is reduced by more than 30 dBm! At roughly ± 2 MHz from the center of the span, we notice two gentle bumps before a sharp fall off in noise intensity. When we increase the amplitude of the feedback to the laser current controller, these bumps become extremely sharp peaks, indicating oscillations at ~ 2 MHz. These are the servo bumps we have mentioned earlier, indicating positive feedback by the locking circuit (instead of negative feedback). According to [80,95], these servo bumps define the bandwidth of the locking circuit, and in this case, we have obtained roughly 2 MHz servo bandwidth.

In Figure 4.16, the spectrum analyzer resolution bandwidth was 1 kHz, which is not good for analyzing the noise reduction at low frequencies. In Figure 4.17, we show the noise spectrum of the same laser, locked with the same settings as in Figure 4.16. However, in 4.17, the span is only 2 kHz and the resolution bandwidth is 10 Hz.

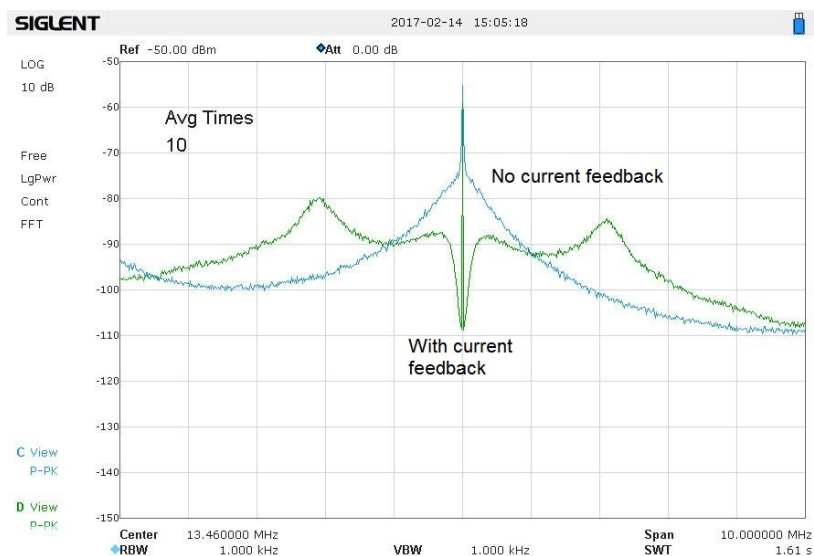


Fig. 4.16. 10 MHz span of the laser noise spectrum, centered at the modulation frequency, 13.5 MHz. Resolution bandwidth is 1 kHz. The blue line shows the noise on the laser with only slow (PZT) feedback. The green line shows the noise on the laser when fast (laser current) feedback is turned on. We see that small servo bumps 2 MHz from the center are present. At low frequencies, noise is reduced by at least 30 dBm.

The blue trace shows the noise spectrum of the laser when the laser is locked using only slow (PZT) feedback. The green trace shows the noise spectrum when fast (laser current) feedback is turned on. In this figure, it is quite obvious that noise at the \sim kHz level is reduced by more than 50 dBm in power, suggesting we have achieved more than 100 dB of (voltage) gain of the error signal.

With better than 2 MHz of servo bandwidth and 50 dBm reduction in noise power at low frequencies, the PDH circuit is off to a good start. We have made a new printed circuit board incorporating lessons from old designs that allowed us to achieve this. We expect only small incremental improvements to the servo loop and will seek a good balance between low frequency noise attenuation and high servo bandwidth.

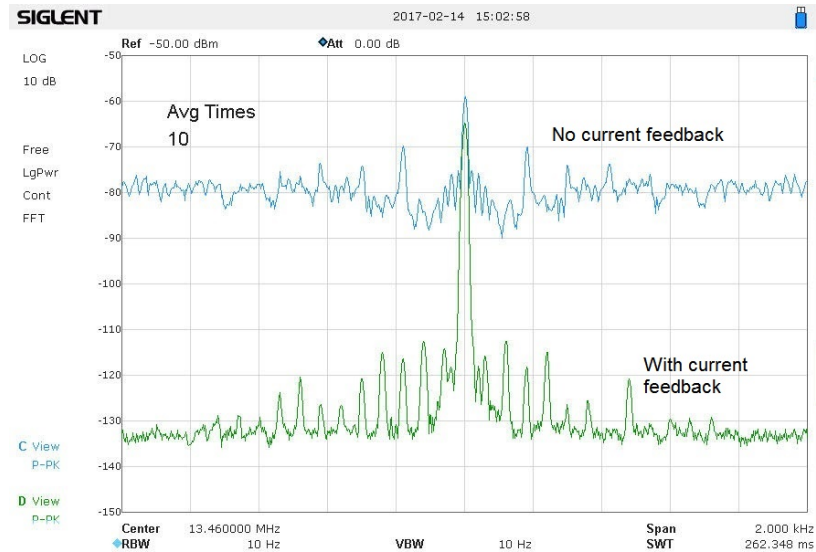


Fig. 4.17. 2 kHz span of the laser noise spectrum, centered at the modulation frequency of 13.5 MHz. The blue line shows the noise on the laser with only slow (PZT) feedback. The green line shows the noise on the laser when fast(laser current) feedback is turned on. We clearly see that most of the noise in this span of 2 kHz is reduced by 50 dBm! The small peaks on the green curve reveal the presence of 60 Hz harmonics.

4.6 Power build-up cavity

4.6.1 Purpose of the PBC

The power build-up cavity (PBC) is an essential component for the measurement of E_{PNC} . It is essentially a Fabry-Perot optical cavity with extremely high finesse, and used to greatly increase the intensity of laser light within the cavity. This increase in intensity is essential because while we were able to measure the ratio of M/β to 0.37% (see Section 1.6), E_{PNC} is about 20,000 smaller in amplitude than M !

With a pair of cavity mirrors of reflectivity $>99.995\%$, we estimate that we will be able to build a PBC with finesse $F \approx 30,000$. The power build-up factor (PBF) of an optical cavity can be estimated to be

$$PBF \approx F/\pi$$

The PBF can be thought of as the number of times a photon bounces within the cavity before exiting or lost through scattering. Thus the intensity of light within the PBC is approximately

$$I = I_{in} \cdot PBF$$

where I_{in} is the input intensity of light to the cavity. Since the PNC amplitude A_{PNC} is proportional to the laser field amplitude ϵ_z , the PBC amplifies the PNC amplitude by a factor of $\sqrt{PBF} = \sqrt{10,000} \approx 100$. Increasing the PNC signal in size by 100 times is a critical first step to precisely measuring $E_{PNC}/\alpha!$

To complicate matters further, the cavity will be a two-color resonant optical cavity. Above, we have discussed the PBF of the cavity at 540 nm to amplify the PNC amplitude. In addition, the PBC will also have to be resonant at 1079 nm. The magnetic dipole amplitude is dependent on the \hat{k} vector of the laser and a perfect standing wave zeros out this contribution. In practice, the mirrors are never 100% reflective, which leads to a systematic contribution discussed in section 5.2. Also, Prof. Elliott has made calculations that indicate we need the anti-nodes for the 540 nm beam to overlap the anti-nodes of the 1079 nm beam. Any small offset (y_0) between the anti-nodes will cause a reduction of the PNC signal. Having a cavity resonant at both wavelengths significantly reduces these two contributions.

In the next two sections, we discuss progress towards putting together the PBC, and future work that is needed to complete the PBC.

4.6.2 Progress so far

With a high finesse power build-up cavity, there are multiple challenges to overcome. Typically, a high finesse cavity will be constructed out of a low coefficient of thermal expansion (CTE) material such as Invar or ultra low expansion glass (ULE). However, we have an atomic beam passing through the center of our cavity so neither of these options will work. We have opted to construct an optical cavity like described in [52]. Two ultra-stable mirror mounts are mounted to a block of low CTE stone

(granite or marble). The block will be suspended using multiple springs to damp any vibrations.

We will have no access to the PBC once it is placed in the vacuum chamber. Thus, the input mirror will be mounted to a tube PZT, which will let us tweak the length of the cavity to be resonant with the incoming laser. In case of mis-alignments during installation of the cavity, the rear cavity will have picomotors, PZT controlled gears to tweak the cavity alignment. Currently we are testing the PBC outside the vacuum chamber, using a set of high reflectivity ($> 99.99\%$) 540 nm mirrors donated to us from the Boulder group when they shut down their lab. Despite being almost 20 years old, these mirrors have been well preserved and the coatings have retained their high reflectivity.

To maximize the radius of the laser beam within the interaction region, instead of a concentric or confocal cavity configuration, we choose to use mirrors with large radius of curvature. A cavity with large radius of curvature (2-10 m) results in there being minimal focusing of intensity within the PBC. [52] notes that with 800 kW/cm^2 of laser intensity within the cavity, increasing the size of the laser more efficiently increases the PNC signal, compared with increasing laser intensity. Currently, I have tested a 2 m and 5 m radius of curvature cavity configuration. The cavity is close to a flat-flat resonator and the laser beam diameter is pretty much constant across the entire cavity.

Testing the PBC outside the vacuum chamber has introduced new problems. Because the finesse of the cavity is so high, air currents in the lab are a great disturbance to the stability of the cavity resonance frequency. Over the period of several seconds, the resonance frequency will hop over a range of over $\sim 100 \text{ MHz}$, and the PDH feedback circuit cannot keep the laser locked. Placing an enclosure around the cavity shields it from most air currents and greatly stabilizes the resonant frequency, allowing us to lock the laser to the PBC. After we place the PBC into the vacuum chamber, it will not be affected by air currents so this will not be an issue.

To efficiently couple light into the cavity, we have to mode-match the incoming beam to the profile of the beam within the cavity. From the radius of curvature of the input and output mirrors of the PBC, we can calculate the beam profile of the Gaussian $(0, 0)$ mode within the cavity. Working the math beyond the input cavity mirror yields the profile of the input beam required for perfect coupling into the cavity. Because we need efficient coupling, a typical 1-lens focusing solution will not do the job. Other measurements with a PBC use a 2-lens telescope to mode-match the input laser to their cavities [29, 38].

A good amount of progress has been made towards constructing the power build-up cavity, but there is much work to be done. Practicing with the cavity outside the vacuum chamber has provided good lessons towards designing a better final PBC. In addition we have learned valuable lessons about how to align the two mirrors of the cavity, and how to couple light into the cavity. Without easy instant access to the PBC mirror mounts, this would have been a nearly impossible task.

4.6.3 Locking scheme for the power build-up cavity

The locking scheme for the power build-up cavity (PBC) and the 1079 nm laser system will be pretty complex. I describe here our current plan to keep the laser stabilized to the PBC and resonant with the cesium $6S \rightarrow 7S$ transition.

For the M1 measurement [55], Antypas only had 1 stage of locking. A small portion of the 1079 nm beam was picked off and double passed through a cesium vapor cell. The laser was then locked to the peak of the resulting Doppler-free two-photon transition peak [53]. We have since added the Invar cavity and PBC, which will make a 3-stage lock. Figure 4.18 shows a sketch of the experimental setup for the 3-stage lock.

Currently, the 1079 nm laser is Pound-Drever-Hall (PDH) locked to the Invar cavity (see Section 4.5). For the PNC measurement, we plan to follow the same strategy as laid out in [29, 52]. Recall that the 1079 nm laser is frequency doubled

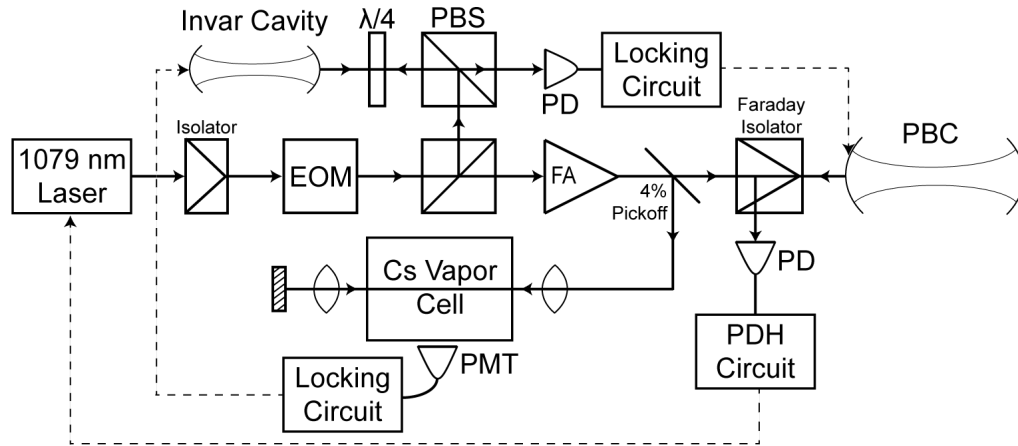


Fig. 4.18. Experimental setup for the 3-stage lock of the 1079 nm laser. The laser is locked via PDH to the PBC using reflected light from the cavity. The PBC is then stabilized to the Invar cavity. Finally, the Invar cavity is locked to the peak of the cesium Doppler-free two-photon resonance in a vapor cell. $\lambda/4$ - quarter wave-plate, PBS - polarizing beamsplitter, PD - photodetector, EOM - electro-optic modulator, FA - fiber amplifier, PBC - power build-up cavity, PMT - photomultiplier tube.

to generate the 540 nm beam. Using the reflection of the 540 nm beam off the PBC, we will lock the 1079 nm laser to the PBC using PDH. The high finesse of the PBC allows significant linewidth reduction [52] of the laser, but is unsuitable as a frequency reference because the narrow resonance peak tends to bounce around. Therefore, we will lock the PBC to the Invar cavity we currently use for PDH locking practice by sending a portion of the 1079 nm laser to it.

The Invar cavity as the name suggests, is made of a single piece of Invar, two laser mirrors and a PZT tube. The minimal amount of working parts reduces the amount of relative vibrations of the cavity mirrors, keeping the resonance frequency much more stable. Because the PDH lock to the PBC is doing most of the linewidth narrowing, a low frequency lock of the PBC to the Invar cavity is sufficient.

Finally, the Invar cavity will be locked to the cesium $6S \rightarrow 7S$ transition. Unlike the Boulder group which used the atomic beam within the vacuum chamber for the

transition lock [25, 28, 29, 96], we have access to the 1079 nm two-photon transition. Hence we will do the same thing as in the M1 measurement and lock the Invar cavity to the two-photon $6S \rightarrow 7S$ resonance in a cesium vapor cell.

4.6.4 Future upgrades to PBC

There is still much to be done to complete the PBC for the PNC measurement. In this section, I go over the known tasks to complete to get the PBC ready.

For the PDH lock of the laser to the PBC, a fast photodiode will be required. The current photodiode we use for locking the laser to the Invar cavity is a InGaAs (FGA10 from ThorLabs) and has a operating wavelength range of 900 - 1700 nm. We have selected a new Si photodiode (S5973 from Hamamatsu) to use at 540 nm. A similar transimpedance amplifier circuit has been put together to amplify the output of this new photodiode.

While we have a good idea about the locking scheme order, the details of the multiple locking circuits will have to be worked out. Currently, most of the circuits we use for locking are custom-built. Two more such circuits with differing servo loop bandwidths will have to be constructed for the multi-stage locking system. Getting them to play nice and stay stable will definitely be a challenge.

Once the PBC is placed within the vacuum chamber, there will be no access for adjusting the cavity mirror mounts. We have purchased and will install electronic PZT actuators for cavity re-alignment while under vacuum. Figure 4.19 shows a sketch of how we plan to setup the PBC.

We have ordered custom-made mirrors with high-reflectivity at both 540/1080 nm from a company (Five Nine Optics). The next step is to use these mirrors to replace the ones we are currently working with, and see how high a finesse we can achieve with both laser wavelengths at once. This will be quite a challenging task.

The PNC measurement will require that we apply a tiny electric field ($\sim 200 - 800 \mu\text{V}/\text{cm}$) within the interaction region. This will require extremely precise voltages

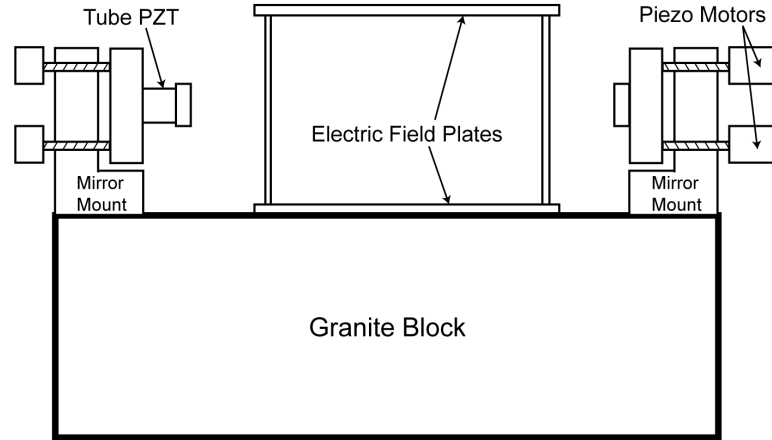


Fig. 4.19. A sketch of the power build-up cavity. The input mirror has a tube PZT for adjusting the length of the cavity. The output mirror has picomotors for re-alignment of the mirrors. Electric field plates will have to be mounted on the same granite block. The granite block provides a stable base for the optics and is suspended from the vacuum chamber floor by springs.

applied to electric field plates that have to be carefully constructed, to prevent the build-up of stray electric fields. Further, the electric field plates will have to be mounted to the PBC block for the best stability. These details will need to be worked out before we can put everything together.

The PBC in [52] was balanced on four beryllium-copper spring supports. We plan to use the same technique to balance the cavity in order to vibration isolate it from vibrations of the optical table (such as from the turbopump). Also, Christopher Wood [52] talks about the effects of birefringence in the mirror coatings. This required them to occasionally rotate the output cavity mirror. We will only use linear polarization in the experiment and thus do not believe this to be an issue for our experimental scheme. Modifications will have to be made to the PBC if regular rotation of one of the mirrors is required.

5. SYSTEMATIC EFFECTS

In this chapter, we discuss the primary systematic contributions we expect to encounter during our measurement of E_{PNC}/α . In Section 2.3, we had assumed perfect polarization of the laser fields, and perfect orientation of electric and magnetic fields. In reality, field misalignments, stray fields resulting from imperfect fields plates and misaligned laser field polarization components can all contribute to our measurement [97, 98]. In Table 5.1 we list the primary contributing systematics and their estimated magnitudes. We discuss these 5 contributions in the following sections.

5.1 Stark induced contributions

The first $\Delta E_x (\varepsilon_x''/\varepsilon_z')$ and second terms $(\beta/\alpha) \Delta E_y (\varepsilon_x'/\varepsilon_z') C_{Fm}^{Fm}$ of Table 5.1 arise from stray electric fields (ΔE_i) coupled with the off axis components of the laser field. ΔE_i is the i-component (x or y) of the stray, uncontrolled electric field, where the primary electric field is E_z . Stray fields could be caused by surface impurities or patch effects, and earlier PNC experiments placed limits on the magnitude of these stray fields. In [52], stray fields were estimated to have magnitude of 100 mV/cm, but they used much larger electric field strengths. In our experiment, we will only need a weak electric field $\sim 200 \mu\text{V}/\text{cm}$ for the amplitude $A_{ST} \approx A_{PNC}$, so we can use field plates with a large spacing. The RMS amplitude of stray electric fields goes as $1/d^2$ where d is the distance between the electric field plates. The Boulder experiment [52] used field plates that were ~ 1 cm apart. Because we apply much weaker electric fields, we will be able to position our field plates 5-10 cm apart, which will greatly reduce the amplitude of these stray field effects. We estimate that ΔE_x and ΔE_y will be kept below 1 mV/cm.

Table 5.1

Estimated magnitudes of potential systematic contributions to the E_{PNC} measurement. ^aThe Clebsch-Gordon coefficient has been abbreviated to [C], see text for long form.

Contribution	Components	Magnitude
$E_{PNC} (C_{Fm}^{Fm}/\alpha)$		160 $\mu\text{V}/\text{cm}$
$\Delta E_x (\varepsilon_x''/\varepsilon_z')$	$(1 \text{ mV}/\text{cm}) \times (10^{-3})$	1 $\mu\text{V}/\text{cm}$
$(\beta/\alpha) \Delta E_y (\varepsilon_x'/\varepsilon_z') C_{Fm}^{Fm}$	$(1/10) \times (1 \text{ mV}/\text{cm}) \times (10^{-3})$	0.1 $\mu\text{V}/\text{cm}$
$(1 - \Gamma_G \Gamma_{IR}^2) (M/\alpha) (\varepsilon_x''/\varepsilon_z') C_{Fm}^{Fm}$	$(10^{-4}) \times (3 \text{ V}/\text{cm}) \times (10^{-3})$	0.3 $\mu\text{V}/\text{cm}$
$(1 - \Gamma_G \Gamma_{IR}^2) (M/\alpha) (B_y/B_z) C_{Fm}^{Fm}$	$(10^{-4}) \times (3 \text{ V}/\text{cm}) \times (10^{-4})$	0.03 $\mu\text{V}/\text{cm}$
$(\beta/\alpha) \Delta E_y \times (B_x/B_z) \times 8 [C]^a$	$(1/10) \times (1 \text{ mV}/\text{cm}) \times (10^{-4})$	0.01 $\mu\text{V}/\text{cm}$

The $(\varepsilon_x''/\varepsilon_z')$ and $(\varepsilon_x'/\varepsilon_z')$ factors are related to the polarization purity of the primary 540 nm laser field. ε_z' represents the primary laser field component, while ε_x'' represents the out-of-phase x-component and ε_x' the in-phase x-component of the laser field. $(\varepsilon_x''/\varepsilon_z')$ represents an elliptical impurity of the laser field. To ensure linear polarization of the laser field, we will pass the beam through a calcite polarizer with (intensity) extinction ratio $\sim 10^{-6}$, which keeps this ratio $(\varepsilon_x''/\varepsilon_z') < 10^{-3}$. $(\varepsilon_x'/\varepsilon_z')$ denotes a mis-alignment of the laser field polarization from the z-axis. We estimate that we can reduce this ratio to $< 10^{-2}$ by routine alignment procedures, while alignment procedures outlined in [52] will help us reduce it to 10^{-3} .

Finally, β/α is a known ratio of $\approx 1/10$. When these factors are taken together, we estimate that Stark induced contributions will be reduced to below 1 $\mu\text{V}/\text{cm}$. This is greater than 0.6% of the amplitude of E_{PNC}/α . We will have to develop a good way to quantify ΔE_i and keep stray electric fields at a minimum ($< 1 \text{ mV}/\text{cm}$).

5.2 Magnetic dipole induced contribution

The third term of Table 5.1, $(1 - \Gamma_G \Gamma_{IR}^2) (M/\alpha) (\varepsilon_x''/\varepsilon_z')$ C_{Fm}^{Fm} , is due to the magnetic dipole contribution. The magnetic dipole contribution is reduced by the standing-wave PBC, since the M contributions from the forward and backward propagating terms cancel out, up to a factor of $(1 - \Gamma_G \Gamma_{IR}^2)$. Here, Γ_G and Γ_{IR} are the reflection coefficients of the back reflector of the PBC for the 540 nm green and 1079 nm infrared beams respectively. With the high reflectivities of the PBC mirrors, we conservatively estimate the factor to be $(1 - \Gamma_G \Gamma_{IR}^2) \approx 10^{-4}$. (M/α) is a known ratio, and has magnitude ≈ 3 V/cm. Finally, $(\varepsilon_x''/\varepsilon_z')$ represents an elliptical impurity of the laser field, and in section 5.1, the factor was estimated to be $< 10^{-3}$.

When these factors are taken together, the third term of Table 5.1 is estimated to be reduced to under $0.3 \mu\text{V}/\text{cm}$. This is greater than 0.1% of E_{PNC}/α so more work will have to be done to reduce the contribution of this systematic error.

5.3 Zeeman mixing between magnetic components

The fourth $(1 - \Gamma_G \Gamma_{IR}^2) (M/\alpha) \times (B_y/B_z) C_{Fm}^{Fm}$ and fifth $(\beta/\alpha) \Delta E_y \times (B_x/B_z) \times 8 \left[(C_{Fm+1}^{Fm})^2 + (C_{Fm-1}^{Fm})^2 \right]$ terms of Table 5.1 are due to Zeeman mixing between magnetic components (m). The magnetic field is primarily in the z-direction B_z , while the tranverse components B_y and B_x are due to imperfect alignment. With routine alignment, the ratios B_i/B_z (where $i = x$ or y) can be reduced to 10^{-3} . Procedures for further reduction have been outlined in [52], and we expect to reduce the ratio B_i/B_z to better than 10^{-4} .

Using some of the same factors from sections 5.1 and 5.2, we obtain magnitudes of $0.03 \mu\text{V}/\text{cm}$ and $0.01 \mu\text{V}/\text{cm}$ for the fourth and fifth terms respectively, better than 0.1%.

5.4 Systematic effects conclusion

Looking again at Table 5.1, most of the terms are under 0.1% of E_{PNC}/α . The third term is at the 0.2% level and more experimental care will have to be taken to minimize its contribution. Currently, conservative estimates of the mirror reflection coefficients Γ have been used. We will have to re-visit this systematic contribution when we fabricate our cavity mirrors. The first term is at $\sim 0.6\%$, and is potentially the biggest issue at the moment. We will have to be extremely careful when constructing our electric field plates, and develop methods to measure and estimate the amplitude of stray electric fields.

We will test for all these contributions using reversals of B_z , E_z and m , as is commonly done for these sorts of measurements [28, 29, 37]. We will also investigate other good methods and techniques to measure or isolate these systematic effects.

6. LIFETIME MEASUREMENT OF CESIUM $7S_{1/2}$ EXCITED STATE

6.1 Introduction

In this chapter, we discuss a measurement of the lifetime of the Cs $7S_{1/2}$ excited state, which we use to determine the $6P_J \rightarrow 7S_{1/2}$ matrix elements. There are different methods to experimentally determine atomic reduced dipole matrix elements, especially for transitions from the ground state. However, for matrix elements between two excited states, the situation is usually more complicated. There are no easy ways to directly measure the $\langle 7S_{1/2} || r || 6P_{1/2} \rangle$ and $\langle 7S_{1/2} || r || 6P_{3/2} \rangle$ reduced dipole matrix elements. Thus, we have chosen a method where two separate measurements are needed: a lifetime measurement and a branching ratio measurement. In this chapter, we discuss our measurement of the cesium $7S_{1/2}$ lifetime, while in Chapter 7 we discuss our measurement of the necessary branching ratio. With these two measurements, we are then able to determine the individual matrix elements.

The $7S_{1/2}$ state in cesium decays spontaneously to two lower states, the $6P_{1/2}$ and $6P_{3/2}$ states (see Figure 6.1). The lifetime of the $7S_{1/2}$ state is therefore related to the two reduced dipole matrix elements by the following equation:

$$\frac{1}{\tau_{7S}} = \sum_{J=1/2,3/2} \frac{4 \omega_J^3 \alpha}{3 c^2} \frac{|\langle 7S_{1/2} || r || 6P_J \rangle|^2}{2J' + 1} \quad (6.1)$$

where $J' = 1/2$ is the angular momentum of the excited $7S_{1/2}$ state, ω_J is the frequency of the $7S_{1/2} \rightarrow 6P_J$ transition, α is the fine-structure constant, and c is the speed of light. Using $J' = 1/2$, we can re-write Equation 6.1 into the following form:

$$\frac{1}{\tau_{7S}} = \sum_{J=1/2,3/2} \frac{2 \omega_J^3 \alpha}{3 c^2} |\langle 7S_{1/2} || r || 6P_J \rangle|^2 \quad (6.2)$$

$$\frac{1}{\tau_{7S}} = \frac{2 \alpha}{3 c^2} \left(\omega_{1/2}^3 |\langle 7S_{1/2} || r || 6P_{1/2} \rangle|^2 + \omega_{3/2}^3 |\langle 7S_{1/2} || r || 6P_{3/2} \rangle|^2 \right) \quad (6.3)$$

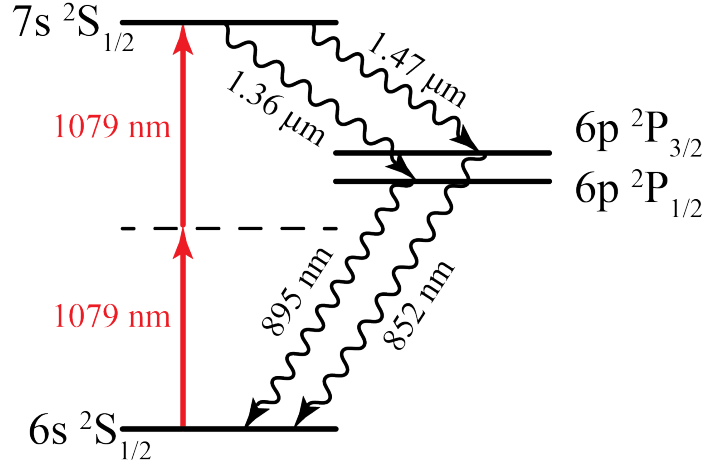


Fig. 6.1. Energy level diagram for the cesium $7S_{1/2}$ lifetime measurement. We excite the $7S_{1/2}$ upper state by 2-photon excitation with a 1079 nm laser. Of the 4 different decay wavelengths, we choose to detect the direct decay from $7S_{1/2}$ to $6P_{3/2}$ at $1.47 \mu m$.

where $\omega_{1/2}$ ($\omega_{3/2}$) is the frequency of the $7S_{1/2} \rightarrow 6P_{1/2}$ ($6P_{3/2}$) transition. To simplify the equation, we then introduce the ratio between matrix elements R_{7S6P}

$$R_{7S6P} = \frac{\langle 7S_{1/2} || r || 6P_{3/2} \rangle}{\langle 7S_{1/2} || r || 6P_{1/2} \rangle} \quad (6.4)$$

to obtain

$$\frac{1}{\tau_{7S}} = \frac{2}{3} \frac{\alpha}{c^2} |\langle 7S_{1/2} || r || 6P_{1/2} \rangle|^2 \left(\omega_{1/2}^3 + \omega_{3/2}^3 R_{7S6P}^2 \right). \quad (6.5)$$

In this chapter, I discuss our measurement of τ_{7S} , while we leave the measurement of the ratio R_{7S6P} to Chapter 7. This work is a collaboration between our group and Jose Jaramillo-Villegas from Professor A. M. Weiner's group. Two REU undergrads, Nathan Glotzbach and Jonah Quirk also helped with the measurement. It has been published in Phys. Rev. A [56].

6.2 Theory

6.2.1 Spontaneous decay from the $7S_{1/2}$ excited state

The cesium $7S_{1/2}$ state can spontaneously decay to the $6P_{1/2}$ and $6P_{3/2}$ states. From the $6P_J$ states, the atom can then decay back down to the $6S_{1/2}$ ground state with different lifetimes. Hence, as seen in Figure 6.1, there are 4 possible photons we can observe after exciting our atom to the $7S_{1/2}$ state. If we start with a sample of excited atoms at time $t = 0$, the number of atoms remaining in the $7S_{1/2}$ state after time t will be

$$N_{7S}(t) = A \exp\left(-\frac{t}{\tau_{7S}}\right) \quad (6.6)$$

where A is the number of excited atoms at time $t = 0$ and τ_{7S} the lifetime of the $7S_{1/2}$ state.

The intensity of fluorescence emitted by the sample is directly proportional to the number of excited atoms in the excited state. Thus by recording the number of photons emitted as a function of time, we can extract the lifetime of the relevant excited state. If we choose to detect and count the number of photons at 1360 nm or 1470 nm from the direct decay of the $7S_{1/2}$ state to the $6P_J$ state, we would fit the recorded data to an equation of the form

$$N_i = A \exp\left(-\frac{t}{\tau_{7S}}\right) + y_0 \quad (6.7)$$

where N_i is the number of photon counts at time t , A the maximum photon count at time $t = 0$, τ_{7S} is the fitted lifetime, and y_0 a term for background photon counts due to scattered light and detector dark current.

If instead we choose to record the cascaded fluorescence at 852 nm or 894 nm, our photon counts will be in the form of a double exponential decay curve [99–102] such as

$$N_i = A_{7S} \exp\left(-\frac{t}{\tau_{7S}}\right) + A_{6P_J} \exp\left(-\frac{t}{\tau_{6P_J}}\right) + y_0 \quad (6.8)$$

where τ_{6P_J} is the lifetime of the $6P_{1/2}$ state (for 894 nm) or $6P_{3/2}$ state (for 852 nm), and A_{6P_J} is the amplitude of the decay curve from the $6P_J$ state. Hence, if we choose

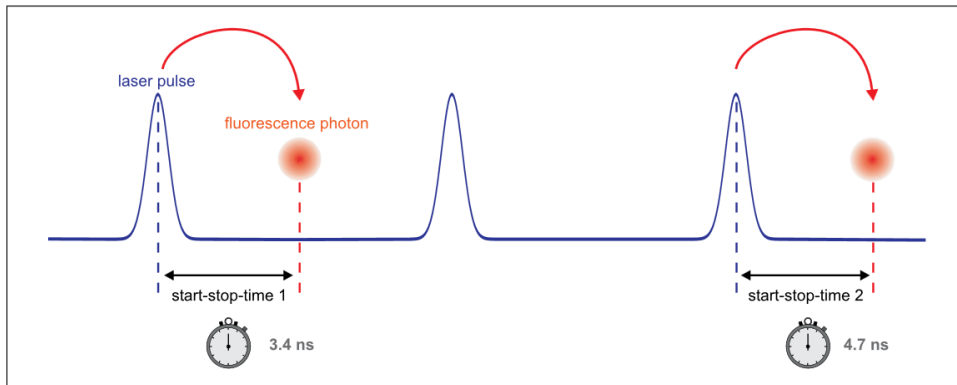


Fig. 6.2. This figure shows the basis behind the time correlated single photon counting technique. A short laser pulse excites the sample of atoms. We precisely keep track of time and record the time delay between the arrival of the laser pulse at the sample, and arrival time of the photon at the detector. This figure is from a Picoquant application note.

to detect photons at 852 nm or 894 nm, we will also need to precisely know the lifetime of the relevant $6P_{1/2}$ or $6P_{3/2}$ intermediate state to obtain a measurement of τ_{7S} . These lifetimes have been previously measured to a (weighted average) precision of $< 0.04\%$ by [66, 68, 103–108]. More importantly, the 852 nm and 894 nm light can be reabsorbed by ground state cesium atoms before it gets out of the vapor cell. This makes the measured lifetime appear to be longer, and is known as radiation trapping.

6.2.2 Time-correlated single photon counting (TCSPC)

Time-correlated single photon counting (TCSPC) is a well established measurement technique, used commonly in biology, chemistry and physics as a spectroscopic tool. TCSPC has been used previously to precisely measure excited state lifetimes in atoms such as cesium [101, 103, 109], francium [100, 110, 111] and rubidium [99, 102].

The key technologies that allow for TCSPC to work are fast, accurate timing electronics and single photon detectors (SPDs). In the simplest TCSPC configuration, we first hit the sample of atoms with a short pulse of laser light to prepare some atoms

into the excited state (see Figure 6.2). A trigger (or start) pulse is also sent to the TCSPC module, where a timer is started to keep track of time. When the SPD detects a photon, it sends a stop pulse to the TCSPC module, which records the time delay between the start and stop pulses. If no photon is detected during a preset waiting period, the cycle restarts with a new laser excitation pulse. In the lab, this process of excitation-detection is then repeated as many times as necessary to obtain sufficient photon counting statistics. Each photon detection is placed into a time bin of finite width, dependent on cycle length and electronic hardware limitations. (In our measurements described below, we used 256 ps time bins, 800 ns cycle length (1.25 MHz repetition rate) and typically collected data for 1 hour.) Finally, we fit the recorded data to an appropriate exponential decay function (Equations (6.7, 6.8)) to extract the excited state lifetime.

There are several types of SPDs commercially available today. Photomultiplier tubes have been used for many years as single photon detection devices, but most are designed to work in the visible or near-infrared (NIR) regime. They are cheap and can be purchased for \sim \$1000. More recently, avalanche photodiodes operating in Geiger-mode, also known as single-photon avalanche diodes (SPAD), have become fairly common. These detectors have detection efficiencies dependent on their p-n junction materials, and hence are available in different wavelength absorption ranges. Prices for these modules are also a lot higher, at \$20,000 – 50,000. Most recently, advances in the development of superconducting nanowire single photon detectors (SSPD) have brought broadband, high detection efficiency and high speed devices to the market. SSPDs also have extremely low dark counts and very short ‘dead’ time. Unfortunately, they come at extremely high cost $>$ \$50,000.

6.2.3 Asynchronous detection technique

The SPD we had available to us from Prof. Weiner’s group, was a gated single-photon detector. Compared to a free-running SPD which can remain ready until a

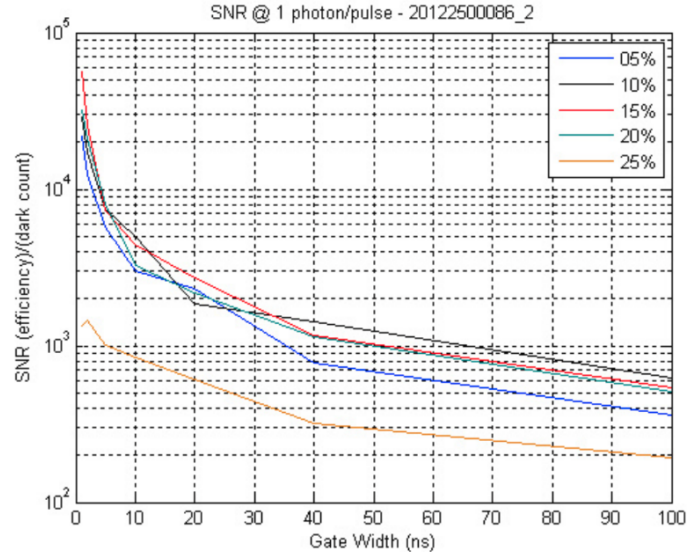


Fig. 6.3. A figure from the test results of the Aurea Technology gated-SPD showing the signal-to-noise ratio (SNR) of the detector as a function of gate width. We observe that when we increase the gate width, we have to sacrifice SNR. The different lines denote the SNR when operating the gated-SPD at different quantum efficiency.

photon is detected, our gated-SPD could only be active and ready for a maximum gate time of 100 ns, before needing to be cycled. Annoyingly, the longer the ‘gate time’ used, the higher the dark counts of the detector, and hence the poorer the signal-to-noise ratio (see Figure 6.3). Hence, we would want to use the shortest practical gate time to maximize the signal-to-noise ratio. The previous best measurement of the lifetime $\tau_{7S} = 48.5(5)$ ns means that at a maximum gate time of 100 ns, we would only be able to observe a period of time twice the atomic lifetime. For a good fit to the exponential decay and background, we should ideally record data for at least 5 – 10 times the decay lifetime.

In a typical synchronous configuration, we would synchronize the arrival of the laser pulse, with the start of the gated-SPD gate time. The gated-SPD would then be active for the preset length of time < 100 ns, then deactivate and wait for the next laser pulse. To get around the issue of the limited gate time, we adopted an asynchronous detection technique discussed previously in [112]. This 2013 paper

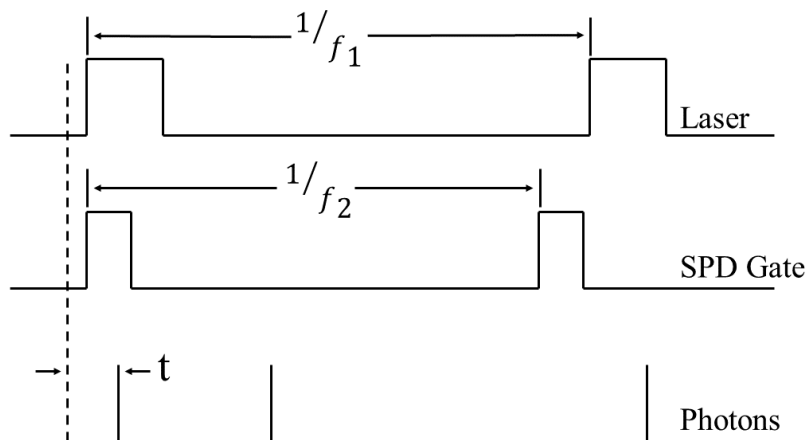


Fig. 6.4. Timing diagram of the experiment. The dashed line represents the start time for the TCSPC module, and t the arrival time of the first photon detected within the gate pulse. $f_1 = 1.25$ MHz is the laser repetition rate and f_2 is the SPD gate repetition rate. The difference in frequencies ($f_2 \neq f_1$) causes the SPD to gate during a different part of the measurement window every cycle. This gate-free method of capturing data allows us to utilize the SPD with a 40 ns gate, while capturing a 800 ns measurement window of photon fluorescence.

suggests triggering the gated-SPD using a different frequency from the laser pulse frequency. The two frequencies are not synchronized or locked (see Figure 6.4), and [112] demonstrated that this asynchronous technique results in an output equivalent to using a SPD in free-running configuration. We tested this idea in the lab by unlocking the repetition rate of the 1079 nm laser pulses from the gate frequency of our gated-SPD. Experimentally, we ran them off separate clocks (at similar frequencies) instead of using the same clock to trigger both.

The result of three 10 minute laser off-resonant tests is shown in Figure 6.5. We intentionally detune the 1079 nm laser from the two-photon resonance in order to suppress atomic excitation to the $7S_{1/2}$ state, but continue to pass it through the vapor cell so that photons due to scattered light would be recorded. As we accrue photon counts, the TCSPC program on the computer plots them onto a histogram. In Figure 6.5, we have a laser pulse every 800 ns, 256 ps time bins, and for the three



Fig. 6.5. A test of the SPD background photon count while the 1079 nm laser is pulsed through the vapor cell but tuned off-resonance. The SPD is running in gated mode, and triggered asynchronously from the laser pulses. This screen capture of the TCSPC software shows the data from three different runs, each of length 10 minutes. We conclude that the number of background photon counts is very uniform while using the gated-SPD in asynchronous mode.

tests displayed we integrated over 10 mins. We cycled the gated-SPD at ~ 1.25 MHz, with a gate window of 40 ns. A timing diagram is shown in Figure 6.4. We observe that with asynchronous detection, we can obtain uniform detection probability over a 800 ns time window. This is important because the measurement would not work if the detection probability was not uniform over the time window. We also confirm with the data that we are not sensitive to scattered light from the excitation pulse, which would manifest as an increase in photons counted around $t = 300$ ns.

6.3 Lifetime measurement experimental details

6.3.1 Experimental setup

We show a figure of the experimental setup for the $7S_{1/2}$ lifetime measurement in Figure 6.6. To excite the atoms from the ground $6S_{1/2}$ state to the excited $7S_{1/2}$ state,

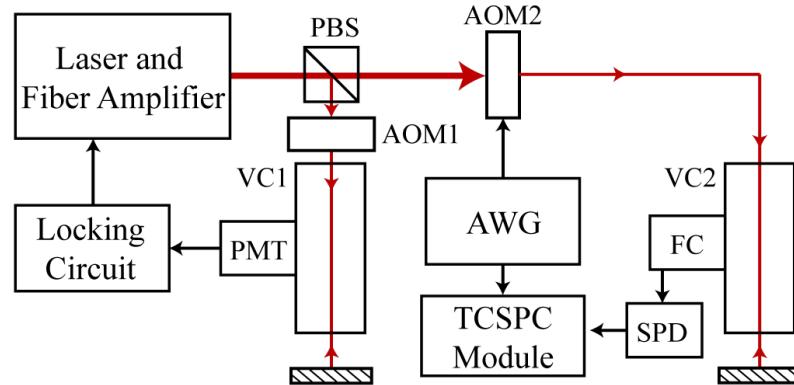


Fig. 6.6. Experimental setup for the lifetime measurement. Abbreviations in this figure are: (PBS) polarizing beam splitter cube; (AOM1) and (AOM2) acousto-optic modulators; (VC1) and (VC2) cesium vapor cells; (PMT) photomultiplier; (FC) fiber coupling optics; (AWG) arbitrary waveform generator; (SPD) single photon detector; and (TCSPC) time-correlated single photon counter.

we use the same 1079 nm laser from the PNC experiment. In brief, this is an external cavity diode laser in the Littrow configuration with ~ 20 mW of output laser power. We fiber couple the laser beam into a fiber amplifier, and obtain about 4 W of optical power. The 4 W beam is passed through a polarizing beam-splitter cube (PBS), where some of the laser power is picked off and used for frequency locking. This portion of the beam is passed through an acousto-optic modulator (AOM1) driven at 90 MHz, which shifts the optical frequency to $\omega + 90$ MHz. We counter-propagate this beam through a heated vapor cell and use it to lock the laser to the peak of the two-photon $6S_{1/2} \rightarrow 7S_{1/2}$ transition. The reason we shift the frequency by 90 MHz, is that we generate the pulsed laser output with another AOM, also driven at 90 MHz, which shifts the pulsed output in frequency by the same amount. More details about this two-photon frequency locking scheme is available in Section 3.6.2.

The majority of the 4 W laser output passes through the PBS and goes through a separate AOM2. We drive this AOM2 with a 90 MHz pulsed rf amplitude for 250 ns at a repetition rate of $f_1 = 1.25$ MHz. Initially, we used a black metal plate to dump the un-diffracted beam power, but noticed that it was scattering light into the photon-

counting setup. Therefore, the un-diffracted beam is directed to a Thorlabs LB2 beam dump (highly absorbing at 1079 nm), and the result is a diffracted pulsed output at f_1 repetition rate. We focus this pulsed output laser beam into a heated vapor cell in a counter-propagating configuration, for Doppler-free two-photon excitation of the cesium atoms. We found that the enhancement due to Doppler-free excitation was necessary to obtain sufficient photon counts for a precise measurement.

For this measurement, we chose to detect fluorescence at 1470 nm from $7S_{1/2} \rightarrow 6P_{3/2}$ spontaneous decay for several experimental reasons. Most importantly, the upper decay photon is less susceptible to radiation trapping effects, compared to the 852 or 894 nm photons, due to the much larger number of ground state atoms in the vapor cell. Radiation trapping effects could add a systematic error to our measurements, and we discuss them in more detail later. Secondly, detecting the 1470 nm photons would allow us to directly fit the data to a single exponential decay function (Equation (6.7)), instead of a double exponential for detecting the cascaded decay at 852 or 894 nm. This removes one factor of uncertainty from our measurement. Third, 1470 nm is away from all other wavelengths of light present in the vapor cell (852, 894, 1079, 1360 nm). We can easily filter out all other photons with a single long-pass filter at 1450 nm. Finally, between the two SPDs we had available to us, the SPD quantum efficiency was best at 1470 nm.

We couple the 1470 nm photons into a 10 μm core single-mode fiber, and send it to the gated-SPD. We calculate that this allows us to image an area of diameter 500 μm within the vapor cell. This area is much larger than the $\sim 10 \mu\text{m}$ distance travelled by an average velocity atom within one lifetime. The SPD we use is an Aurea Technology InGaAs avalanche single-photon detector. Upon detection of a photon, it sends an electrical pulse to the TCSPC module (HydraHarp 400) which time-tags the photon and puts it into one of the 256 ps time bins.

Timing precision is extremely important for this sort of measurement. We keep the majority of the electronics synchronized using an Arbitrary Waveform Generator (AWG), the Tektronix AWG7122C. This is a 12 GHz AWG with a timing resolution

of ~ 8 ps, more than accurate enough for our measurement. We use the AWG for timing of the 800 ns cycle window. The cycle begins with the AWG putting out a ~ 240 ns pulse of 90 MHz rf output. This rf output is amplified to ~ 1 W of rf power before being sent to AOM2. This produces a pulsed 1079 nm laser beam on the output, frequency shifted by 90 MHz. At the same time, the AWG also sends an electrical pulse to trigger “start” on the TCSPC module. This tells the HydraHarp 400 TCSPC module to begin expecting a “stop” pulse on its input from the SPD. The HydraHarp 400 module has timing resolution of 1 ps, and its specifications claim an error of < 10 ps. We choose to use a time bin length of 256 ps, well within its timing capabilities. The SPD has a timing jitter of 200 ps, which contributes a little to the uncertainty in this measurement.

Since we use an asynchronous detection technique, the gate timing of the gated-SPD is not synchronized or triggered by the AWG. We set the repetition rate of the gated-SPD (f_2) to a different frequency from the repetition rate of the AWG cycle ($f_1 = 1.25$ MHz). In this manner, the result is that the gated-SPD “gates” during a different portion of the cycle window every cycle. With sufficiently long data acquisition length, the gating probability is uniform across the cycle window. We showed this earlier using dark counts for acquisition times of 10 mins in Figure 6.5. For the actual measurements, we acquired data for at least 1-hour in each data run.

6.3.2 Data acquisition

In the last section, I have described what goes on within each 800 ns cycle. We show in Figure 6.7 a screen capture of the TCSPC software used to record data. The histogram is updated live as the TCSPC module accrues photon counts. Each photon is time-tagged and binned into one of the 256 ps time bins. In Figure 6.7, the data from 6 different 1-hour long runs is displayed, all with the same excitation, saturation and decay profiles, showing us that our measurement is consistent and

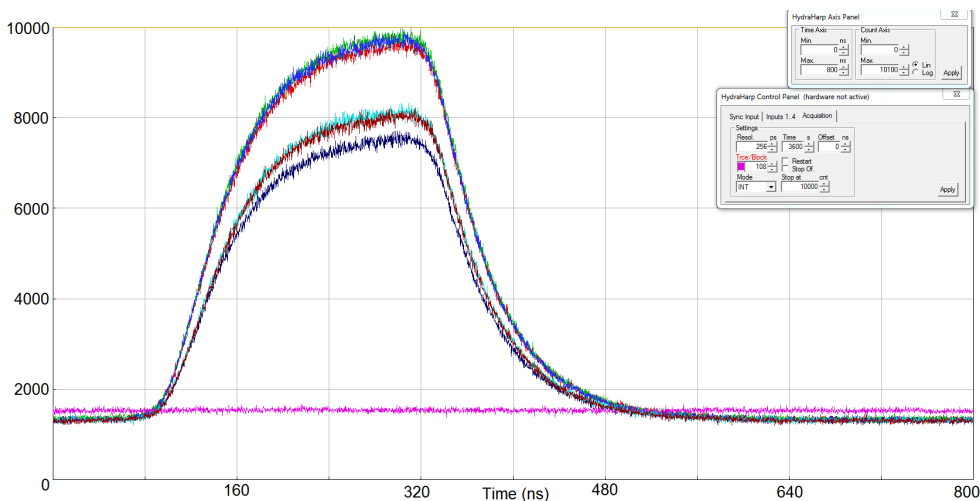


Fig. 6.7. (Color) This is a sample of data from 6 different 1-hour long runs of photon counts versus time. The purple line that runs across the bottom is a laser off-resonance background counts test, where we accidentally left the computer running for slightly longer than 1-hour. The different peak photon counts are due to differences in cell temperature or laser alignment.

repeatable. The purple line that runs horizontally across the bottom of Figure 6.7 is a laser off-resonance background photon count test where we accidentally let the system integrate for > 60 mins.

We see that the other 6 data curves have the same lineshape, but different amplitude. The different photon count amplitudes are due to differences in the cell temperature and laser beam alignment when we recorded the data. At approximately 80 ns into the cycle, the pulsed laser beam passes into the vapor cell, and we see an exponential increase in photon counts, as atoms are excited from the ground state to the $7S_{1/2}$ state, where they can then decay to the $6P_{3/2}$ state. The photon count begins to saturate at about 200 ns, and reach an equilibrium level as the atoms in the detection region are saturated. At about the 300 ns mark, we see the photon count start to fall off. This is the point where the laser pulse exits the vapor cell, and no more new atoms are excited from the $6S_{1/2}$ state. Due to the rise and fall time of AOM2, the initial 30 – 40 ns of this decay will not be a single exponential function.

Using a fast photodiode and oscilloscope, we estimate that our laser has ~ 20 ns fall time (90 – 10%) and we need to avoid using the data from those affected times.

While 20 ns (90 – 10%) sounds like a pretty slow turn-off time, recall that we excite the atoms using a two-photon process. The excitation rate of atoms from ground to excited $7S_{1/2}$ state goes as the square of the 1079 nm laser intensity. Hence, within ~ 40 ns of the laser beginning to turn off, the excitation rate of atoms has fallen to near-negligible levels.

6.3.3 Analysis of results

We show in Figure 6.8(a) a linear plot of photon counts against cycle time for one data run, and in Figure 6.8(b) a logarithmic plot of the same data from 350 – 800 ns. In Figure 6.8(b), the data are in green, and the best fit line to Equation 6.7 is in black.

Before we can proceed to curve fitting our data to an exponential decay function, we have to apply two corrections to our data. The first correction is for what is known in TCSPC as ‘pile-up’ error, and is unavoidable. Pile-up error arises from an assumption we made in our earlier TCSPC descriptions, that only 0 or 1 photons arrives at the SPD every cycle. The photons arrive at the detector with Poissonian distribution, and as the photon counting rate increases, the probability of 2 photons arriving within the same cycle increases. Because the detector only registers that at least one photon was detected, the second photon is not counted by our TCSPC system. Hence, it is important in TCSPC measurements for the count rate to be sufficiently low, such that the probability of a photon arriving in any cycle is $< 5\%$.

For our asynchronous detection technique, the probability of detecting a photon within a 40 ns window centered on the i th bin of the data set can be written as

$$P_i = \frac{N_i}{N_E} \times \frac{T_{gate}}{T_{bin}} \times \frac{1}{T_{gate} f_1} \quad (6.9)$$

where N_i is the number of photons in the i -th bin, N_E is the total number of laser pulse repetitions (typically $f_1 \times 1h = 4.5 \times 10^9$), T_{gate} and T_{bin} are the gate and bin

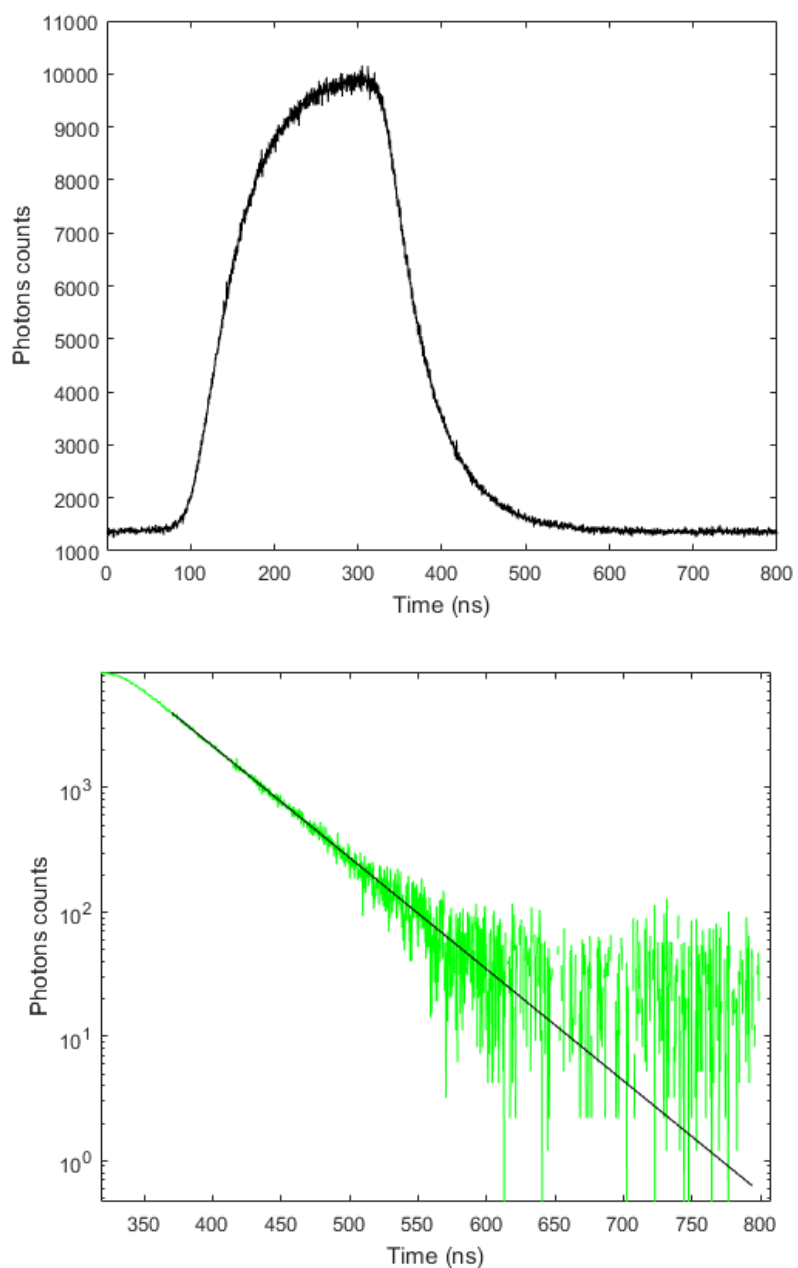


Fig. 6.8. Decay curve of the Cs $7S_{1/2}$ level. **(a)** The main figure consists of 1 hour of recorded data and shows the excitation of atoms and exponential decay of fluorescence. **(b)** The same data for 350 – 800 ns with the background deducted, shown on a logarithmic scale in green and the best-fit line in black. We see that by ~ 600 ns, the decay signal has fallen below the shot noise level, $\approx \sqrt{1200} = 35$ photons.

times respectively. T_{gate}/T_{bin} is the number of bins in each gate window and $T_{gate}f_1$ is the duty cycle of the SPD gate. In Equation (6.9), we multiply N_i by the total number of time bins, and divide the total by N_E to calculate the probability of detecting a photon during any excitation laser pulse. This equation simplifies to

$$P_i = \frac{N_i}{N_E T_{bin} f_1}. \quad (6.10)$$

To keep the correction small for a high precision lifetime measurement, we limit the 1079 nm laser intensity to keep the peak photon probability $P_i < 0.01$. This is much less than the 0.05 typically recommended for TCSPC measurements. The probability of there being a second photon within a cycle is $P_i/2$. The factor of 1/2 comes about because the photons arrive at the detector with a Poisson distribution. The probability of there being k photons in the same cycle $P(k)$ for a Poisson distribution is

$$P(k) = \exp^{-\lambda} \frac{\lambda^k}{k!},$$

where $\lambda \approx P_i$ is the average number of counts per cycle. The probability is different for the different time bins, and we apply a correction to the data by multiplying the number of counts in each time bin by $1 + P_i/2$.

The second correction we have to apply is to account for the gated-SPD dead time. After detecting a photon, the gated-SPD needs to ‘rest’ for a period of time and is unable to count photons. This is known in TCSPC as a dead time. Our SPD dead time of 1 μs is longer than the cycle window of 0.8 μs , which means that after detecting a photon, the SPD is not ready to count photons for part of the next cycle. We chose the excitation pulse repetition rate f_1 as a compromise between a sufficiently long cycle window, and fast data acquisition, omitting to consider the dead time of the detector. This results in us needing to apply an additional correction of $1 + P_i$ to the raw data. In combination with the previously discussed pile-up error correction, these two corrections change the fitted lifetime by $\sim 0.2\%$.

We discussed in the last section that the laser pulse has some turn off time ~ 20 ns. Once we have recorded the data as shown, one of the biggest challenges is to determine

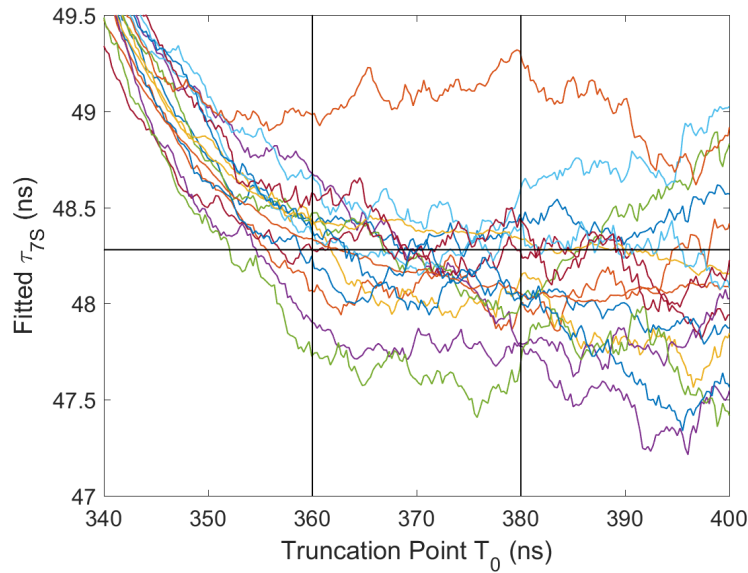


Fig. 6.9. This plot shows the variation of fitted lifetime τ as we change the truncation point T_0 . Each of the 16 colored lines represents a single data set. The horizontal line marks our final reported lifetime of $\tau_{7S} = 48.28$ ns. The two vertical lines denote 360 – 380 ns, the range of values we chose to average for our final result (see text for discussion).

the right ‘truncation point.’ We always fit the data to the end of the 800 ns cycle window, and define the ‘truncation point’ T_0 as the point in the cycle window where we start fitting our data to the exponential function, Equation 6.7:

$$N_i = A \exp\left(-\frac{t}{\tau}\right) + y_0$$

In this equation, N_i is the number of photon counts in the i -th time bin of the measurement after correcting for pile-up error and dead-time error. We fit the truncated data to three parameters, an amplitude A which represents the number of photon counts at $t = 0$, a decay lifetime τ and a constant term y_0 to represent the background photon counts.

To determine the correct truncation point T_0 for all the data, we tried a number of different things. For any single data run, we can easily fit the data using a range of values for T_0 , and plot the range of values of fitted τ versus T_0 . We show this for all

our data in Figure 6.9. We found that for values of $T_0 < 350$ ns, fitted τ increases with decreasing T_0 . This is expected because the number of atoms in the excited state are being replenished by the remaining small amount of laser power, and is quite clearly seen in Figure 6.9. For $T_0 > 400$, fitted A falls off exponentially and the variance in fitted τ increases dramatically. This is also expected behavior because the photon counts for $t > 400$ ns are dominated by background photons.

Eventually, after looking at many data sets, we decided that a truncation point in the range $360 \leq T_0 \leq 380$ ns would be most appropriate. Between 360 – 380 ns, the fitted lifetime suffers minimally from either of the two effects mentioned. In addition, the fitted lifetime for a truncation point in that range had the least variance (see Figure 6.9). However, we did not have a good reason to pick any specific number within that range.

We decided to take an average of the 82 fitted lifetime values ($(20+1)$ ns/256 ps = 82) from fits with truncation points $360 \leq T_0 \leq 380$ ns and the same end point $t = 800$ ns. We report this average as the fitted lifetime for each data run. To estimate the uncertainty in the lifetime due to truncation error, we calculate the standard deviation of this range of lifetimes. This standard deviation is added in quadrature with the statistical uncertainty coming from the curve fit, for a reported error which includes both statistical and truncation error.

In Figure 6.10, we noticed a larger variance in the results of data sets 11 – 16. We suspect that this may have been due to instability in the 1079 nm ECDL laser lock, resulting in lower peak photon counts for these data sets. During the data recording for that day, we noticed several times that the laser would lose lock and go off-resonance. We were present to monitor the data acquisition, and were able to quickly re-lock the 1079 nm laser. When the laser is off-resonance, atoms are not excited from the ground state to the excited $7S_{1/2}$ state. This results in higher background photon counts, but does not affect the recorded decay profile. For this reason, we decided to keep these data sets in our final determination.

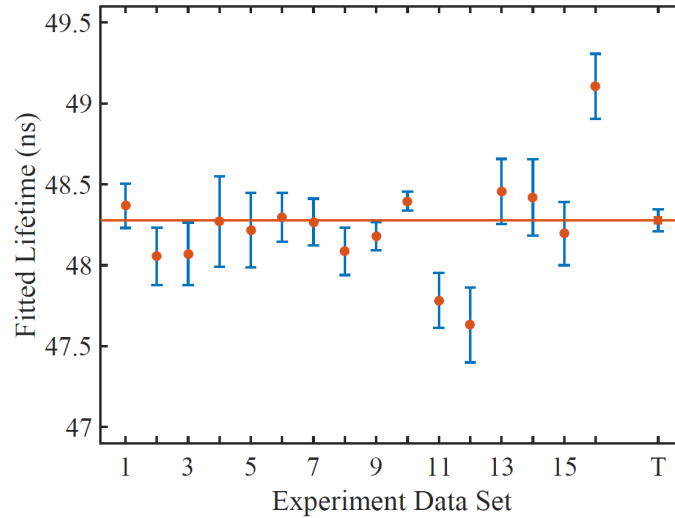


Fig. 6.10. A plot showing the 16 individual measurement results used to calculate the final value. Data sets 9 and 10 were 10 hours long, while the rest were for 1 hour. The total of 34 hours of data was captured over a period of three days. The final data point T and the red horizontal line is the weighted mean of the 16 data sets, with error bars inclusive of statistical and systematic uncertainties.

Calculating the weighted mean of fitted lifetimes across these 16 data sets, we obtain $\tau_{mean} = 48.28(3)$ ns, with $\chi_r^2 = 2.98$. To adjust for $\chi_r^2 > 1$, we chose to increase the statistical uncertainty by $\sqrt{2.98}$.

To rule out the effects of temperature effects, we recorded data at several different temperatures. We noticed no effect of the temperature on the measured lifetime from 117°C to 127°C, but measured a slightly higher lifetime at 134°C. At temperatures lower than 117°C, our photon counts begin to be dominated by background noise, making precise measurements difficult. In our final analysis, we did not include data runs recorded at 134°C and used only the ones recorded at lower temperatures.

While we expect magnetic field variations to have no effect on the lifetime, we also conducted tests to confirm this. In Figure 6.10, data sets 3, 4 and 5 were recorded with an applied magnetic field of 3 Gauss in each of three orthogonal directions. We

Table 6.1
Sources of error and the percentage uncertainty resulting from each.
The total uncertainty is dominated primarily by statistical error.

Error	% uncertainty
Statistical and truncation	0.12
Detection sensitivity	0.05
Radiation trapping	0.03
Time calibration	0.03
Pile-up correction	0.02
SPD timing jitter	0.01
Total uncertainty	0.14

observed no change in the measured lifetime and recorded the rest of the data sets with no applied magnetic field.

We considered many different systematic effects that could affect our measurement. A list of these errors is shown in Table 6.1. The first error listed, detection sensitivity, refers to any non-uniformity in the sensitivity of the detection system with delay time. We fit a straight line to the data from our background tests (shown in Figure 6.5) to estimate the maximum size of the non-uniformity. We calculate that this could affect our result by $< 0.05\%$. Temperature or vapor density effects could lead to radiation trapping effects for detection of photons at 852 or 894 nm, but are relatively insignificant at 1470 nm. We include an uncertainty of 0.03% for radiation trapping effects. The TCSPC module has some timing calibration uncertainty. We estimate that this leads to 0.03% uncertainty in the lifetime. Earlier, we made a correction to the data for pile-up error, we estimate an error of 0.02% resulting from this correction. Finally, the SPD timing jitter of 200 ps also contributes some uncertainty to our measurement. We modelled this effect as a convolution of a 200 ps peak with our recorded data, and calculate that it has an effect $< 0.01\%$.

Table 6.2

Experimental and theoretical results for the lifetime τ_{7S} of the cesium $7S^2S_{1/2}$ state. We derived theory values marked with an asterisk (*) from matrix elements $\langle 7S||r||6P_{1/2}\rangle$ and $\langle 7S||r||6P_{3/2}\rangle$ reported there. In the theoretical works marked with a dagger (\dagger), the authors only reported values of $\langle 7S||r||6P_{1/2}\rangle$, so we estimated $\langle 7S||r||6P_{3/2}\rangle$ from $1.528 \times \langle 7S||r||6P_{1/2}\rangle$ in order to derive τ_{7S} .

Group	τ_{7s} (ns)
<u><i>Experimental</i></u>	
This work, time-resolved fluorescence	48.28(7)
M. Bouchiat <i>et al.</i> , Hanle effect, 1984 [59]	48.5(5)
Hoffnagle <i>et al.</i> , Hanle effect, 1981 [113]	53.6(12)
Marek, time-resolved fluorescence, 1977 [114]	49(4)
<u><i>Theoretical</i></u>	
Porsev <i>et al.</i> , \dagger 2010 [14]	48.33
Dzuba <i>et al.</i> , \dagger 2002 [72]	48.24
Safronova <i>et al.</i> ,* 1999 [63]	48.42
Dzuba <i>et al.</i> ,* 1997 [70]	48.07
Blundell <i>et al.</i> ,* 1992 [21]	48.56
Dzuba <i>et al.</i> ,* 1989 [115]	48.07
C. Bouchiat <i>et al.</i> , 1983 [116]	48.35

Combining statistical and systematic errors, we add them in quadrature to obtain an uncertainty of 0.14%, for a final result of $\tau_{7S} = 48.28(7)$ ns. This result is shown in Figure 6.10 as the final data point labelled ‘T’.

6.3.4 Comparison of results

We show in Table 6.2 our new result of $\tau_{7S} = 48.28(7)$ ns in comparison to past experimental measurements and theoretical calculations. Our result is in good agreement with the most recent experimental measurement by Bouchiat [59], where her group used the Hanle effect to measure $\tau_{7S} = 48.5(5)$ ns. Our result is also in good agreement (within $1\text{-}\sigma$) with the most recent theoretical results of [14] and [72]. These theoretical calculations report reduced dipole matrix elements, which we use with Equation 6.3 to calculate τ_{7S} . For some of these theory papers which only report the value of $\langle 7S||r||6P_{1/2}\rangle$, we also use the theoretical ratio of $R_{7S6P} = 1.528$ to calculate the lifetime.

With this new measurement of τ_{7S} , we have reduced the experimental uncertainty of the lifetime from 1% to 0.14%, a improvement of 7 times. With a precise measurement of the branching ratio R_{7S6P} , we will be able to report high precision, experimentally determined values of the $\langle 7S||r||6P_{1/2}\rangle$ and $\langle 7S||r||6P_{3/2}\rangle$ reduced dipole matrix elements. We discuss our measurement of this branching ratio in Chapter 7.

7. MEASUREMENT OF CESIUM $7S_{1/2}$ BRANCHING RATIO

7.1 Introduction

In Chapter 6, we described our measurement of the lifetime of the cesium $7S_{1/2}$ state. As discussed earlier, this state has two decay pathways to the $6S_{1/2}$ ground state, via the intermediate $6P_{1/2}$ or $6P_{3/2}$ states, shown in Fig. 6.1. Hence, in order to determine the individual matrix elements $\langle 7S_{1/2} || r || 6P_{3/2} \rangle$ and $\langle 7S_{1/2} || r || 6P_{1/2} \rangle$, in addition to the measurement of the lifetime of the $7S_{1/2}$ state, we also need to measure the ratio of matrix elements

$$R_{7S6P} = \frac{\langle 7S_{1/2} || r || 6P_{3/2} \rangle}{\langle 7S_{1/2} || r || 6P_{1/2} \rangle}. \quad (7.1)$$

In this chapter, we describe a measurement of the $7S_{1/2}$ branching ratio R_{7S6P} using an interference technique. The work discussed in this chapter has been published in Phys. Rev. A [57].

7.2 Theory

The experiment to measure the $7S_{1/2}$ branching ratio is a two-color two-photon interference technique. This technique has previously been used to measure the branching ratio of the cesium $8S_{1/2}$ state in [117]. We excite atoms from the $6S_{1/2}$ ground state to the $7S_{1/2}$ excited state using two photons of different wavelength (see Figure 7.1). The first photon of wavelength λ_1 (or frequency ω_1) is detuned from the $6S_{1/2} \rightarrow 6P_{3/2}$ (D2 line, $\omega_{6P_{3/2}}$) by detuning Δ . For maximum sensitivity, we want the photon to have lower energy than that of the D2 resonance ($\omega_1 < \omega_{6P_{3/2}}$), and we define Δ to be this frequency difference $\Delta = \omega_{6P_{3/2}} - \omega_1$. The second photon of wavelength λ_2 (or frequency ω_2) completes the two-photon transition from $6S_{1/2} \rightarrow 7S_{1/2}$.

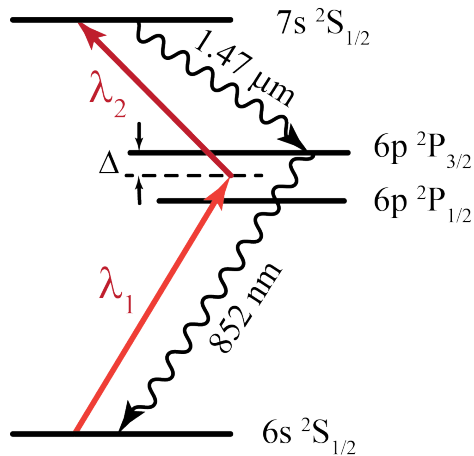


Fig. 7.1. Energy level diagram of atomic cesium, showing the states relevant to this measurement. Atoms are excited from the $6S_{1/2}$ ground state to the $7S_{1/2}$ excited state by two-color, two-photon excitation. We collect fluorescence photons at 852 nm from the second step of the spontaneous decay of atoms from the $7S$ state to the ground state by way of the $6P_{3/2}$ state.

As we change Δ , the intermediate virtual energy level is tuned between the $6P_{3/2}$ and $6P_{1/2}$ states, where the difference $\omega_{P_{3/2}} - \omega_{P_{1/2}} \approx 550\ \text{cm}^{-1}$. Interference effects due to the two photon amplitudes via the two states adding constructively or destructively causes the two-photon excitation rate to change as a function of Δ . This interference is strongly dependent on the relative polarization of the laser beams. By measuring the relative magnitudes of the signal with parallel laser polarization S_{\parallel} and with perpendicular laser polarization S_{\perp} , we are able to determine the $7S_{1/2}$ decay branching ratio.

7.2.1 S_{\parallel}/S_{\perp} ratio

We begin by deriving the two-photon transition rates for parallel and perpendicular polarization. From the Fermi golden rule, we begin with

$$S = \frac{2\pi}{\hbar} |A_{2P}|^2 \rho_{7S}(E), \quad (7.2)$$

where $\rho_{7S}(E)$ is the energy density of the 7S excited state. A_{2P} is the 2-photon transition amplitude and can be written with the expression

$$A_{2P} = \sum_{n,J} \left\{ \frac{\langle 7S_{1/2} | \hat{\epsilon}_1 E_1 \cdot e\mathbf{r} | nP_J \rangle \langle nP_J | \hat{\epsilon}_2 E_2 \cdot e\mathbf{r} | 6S_{1/2} \rangle}{\omega_2 - \omega_{nP_J} - i\Gamma_{nP_J}/2} + \frac{\langle 7S_{1/2} | \hat{\epsilon}_2 E_2 \cdot e\mathbf{r} | nP_J \rangle \langle nP_J | \hat{\epsilon}_1 E_1 \cdot e\mathbf{r} | 6S_{1/2} \rangle}{\omega_1 - \omega_{nP_J} - i\Gamma_{nP_J}/2} \right\}$$

where $\tilde{\epsilon}_k$, E_k and ω_k where $k = 1, 2$ are the laser polarization, amplitude and frequency of the laser k respectively. ω_{nP_J} are the transition frequencies of the intermediate nP_J states from the ground state. $\Gamma_{nP_J}/2$ represents the radiative linewidths of the intermediate states, but $\Gamma_{nP_J}/2 \ll \Delta$ so we can safely ignore this term for the rest of our analysis.

Next, using the Wigner-Eckart theorem, we factor out the F and m dependences from the electric dipole matrix element, to leave only the reduced matrix elements. We have shown how to do this earlier in Equations (2.1)-(2.2) of Section 2.2 so I will not repeat it here. The initial atomic population is evenly distributed over the 16 ground state Zeeman sublevels m (see Figure 2.1), and we have sufficient resolution to resolve the hyperfine energy levels F for both ground and excited states. Then, we average over initial m states and sum over final m' states to obtain the signal strengths S_{\parallel} and S_{\perp} .

When both lasers have the same linear polarization (parallel), the two-photon signal strength for the $6S_{1/2} F=4 \rightarrow 7S_{1/2} F=4$ transition can be shown to be

$$S_{\parallel,4 \rightarrow 4} = \frac{2\pi}{\hbar^2} \frac{9}{16} |\tilde{\alpha}|^2 E_1^2 E_2^2, \quad (7.3)$$

where E_1 and E_2 represent the electric field amplitudes of λ_1 and λ_2 respectively. $\tilde{\alpha}$ is the detuning dependent polarizability term and can be written in the following form

$$\begin{aligned} \tilde{\alpha} = & \frac{e^2}{6} \sum_n \left[\langle 7S_{1/2} || r || nP_{1/2} \rangle \langle nP_{1/2} || r || 6S_{1/2} \rangle \right. \\ & \times \left\{ \frac{1}{\omega_2 - \omega_{nP_{1/2}}} + \frac{1}{\omega_1 - \omega_{nP_{1/2}}} \right\} \\ & - \langle 7S_{1/2} || r || nP_{3/2} \rangle \langle nP_{3/2} || r || 6S_{1/2} \rangle \\ & \left. \times \left\{ \frac{1}{\omega_2 - \omega_{nP_{3/2}}} + \frac{1}{\omega_1 - \omega_{nP_{3/2}}} \right\} \right] \end{aligned} \quad (7.4)$$

where $n \geq 6$ represents a sum over all p states of the cesium atom, ω_1 and ω_2 are the frequencies of the first and second laser respectively, and ω_{nP_J} are the frequencies of the respective $6S_{1/2} \rightarrow nP_J$ transitions. e represents the usual elementary charge.

Similarly, when the lasers have orthogonal linear polarization (perpendicular), the two-photon signal strength for the $6S_{1/2} \text{ F}=4 \rightarrow 7S_{1/2} \text{ F}=4$ transition becomes

$$S_{\perp,4 \rightarrow 4} = \frac{2\pi}{\hbar^2} \frac{15}{64} |\tilde{\beta}|^2 E_1^2 E_2^2, \quad (7.5)$$

where the polarizability $\tilde{\beta}$ can be written as

$$\begin{aligned} \tilde{\beta} = & \frac{e^2}{6} \sum_n \left[\langle 7S_{1/2} || r || nP_{1/2} \rangle \langle nP_{1/2} || r || 6S_{1/2} \rangle \right. \\ & \times \left\{ \frac{1}{\omega_2 - \omega_{nP_{1/2}}} - \frac{1}{\omega_1 - \omega_{nP_{1/2}}} \right\} \\ & + \frac{1}{2} \langle 7S_{1/2} || r || nP_{3/2} \rangle \langle nP_{3/2} || r || 6S_{1/2} \rangle \\ & \left. \times \left\{ \frac{1}{\omega_2 - \omega_{nP_{3/2}}} - \frac{1}{\omega_1 - \omega_{nP_{3/2}}} \right\} \right]. \end{aligned} \quad (7.6)$$

Notice the change of signs between $\tilde{\alpha}$ and $\tilde{\beta}$, and the additional term of $\frac{1}{2}$ in the second term. The ratio of linestrengths for the $6S_{1/2} \text{ F}=4 \rightarrow 7S_{1/2} \text{ F}=4$ ($4 \rightarrow 4$) transition between parallel and perpendicular polarization is thus

$$\left(\frac{S_{\parallel}}{S_{\perp}} \right)_{4 \rightarrow 4} = \frac{12}{5} \frac{|\tilde{\alpha}|^2}{|\tilde{\beta}|^2}. \quad (7.7)$$

We can also work out the two-photon signal strengths for the $6S_{1/2} F=3 \rightarrow 7S_{1/2} F=3$ ($3 \rightarrow 3$) transition for parallel polarization

$$S_{\parallel,3 \rightarrow 3} = \frac{2\pi}{\hbar^2} \frac{7}{16} |\tilde{\alpha}|^2 E_1^2 E_2^2 \quad (7.8)$$

and for perpendicular polarization

$$S_{\perp,3 \rightarrow 3} = \frac{2\pi}{\hbar^2} \frac{7}{64} |\tilde{\beta}|^2 E_1^2 E_2^2. \quad (7.9)$$

This results in a ratio of linestrengths between parallel and perpendicular polarization of

$$\left(\frac{S_{\parallel}}{S_{\perp}} \right)_{3 \rightarrow 3} = 4 \frac{|\tilde{\alpha}|^2}{|\tilde{\beta}|^2} \quad (7.10)$$

for the $3 \rightarrow 3$ transition. In Figure 7.2, I have plotted Equations (7.7) and (7.10) for detuning $0 < \Delta < 550 \text{ cm}^{-1}$. Notice that the curve for the $3 \rightarrow 3$ transition has a much steeper slope than for the $4 \rightarrow 4$ transition.

To simplify our equations, we introduce the ratio of reduced dipole matrix elements R_{7S6P}

$$R_{7S6P} = \frac{\langle 7S_{1/2} || r || 6P_{3/2} \rangle}{\langle 7S_{1/2} || r || 6P_{1/2} \rangle} \quad (7.11)$$

which is the ratio we are measuring, and the ratio R_{6P6S}

$$R_{6P6S} = \frac{\langle 6P_{3/2} || r || 6S_{1/2} \rangle}{\langle 6P_{1/2} || r || 6S_{1/2} \rangle}. \quad (7.12)$$

$\langle 6P_{3/2} || r || 6S_{1/2} \rangle$ and $\langle 6P_{1/2} || r || 6S_{1/2} \rangle$ have been precisely measured multiple times, and their uncertainty from taking a weighted mean is $< 0.036\%$.

Inserting R_{7S6P} and R_{6P6S} into Equations (7.4) and (7.6), we re-write $\tilde{\alpha}$ in the following form

$$\tilde{\alpha} = K \left[\frac{R_{7S6P} (-R_{6P6S})}{\omega_1 - \omega_{6P_{3/2}}} + \frac{1}{\omega_1 - \omega_{6P_{1/2}}} + \frac{R_{7S6P} (-R_{6P6S})}{\omega_2 - \omega_{6P_{3/2}}} + \frac{1}{\omega_2 - \omega_{6P_{1/2}}} + P \right] \quad (7.13)$$

and $\tilde{\beta}$ in the following form

$$\tilde{\beta} = K \left[\frac{R_{7S6P} (-R_{6P6S}/2)}{\omega_1 - \omega_{6P_{3/2}}} - \frac{1}{\omega_1 - \omega_{6P_{1/2}}} - \frac{R_{7S6P} (-R_{6P6S}/2)}{\omega_2 - \omega_{6P_{3/2}}} + \frac{1}{\omega_2 - \omega_{6P_{1/2}}} + Q \right], \quad (7.14)$$

where

$$K = \frac{e^2}{6} \langle 7S_{1/2} || r || 6P_{1/2} \rangle \langle 6P_{1/2} || r || 6S_{1/2} \rangle.$$

We also introduce P and Q to wrap up the higher n terms ($n > 6$). P and Q contribute only slightly to the ratio compared to the $n = 6$ terms, but are important when making a $< 1\%$ measurement. The equations for P and Q are

$$P = \sum_{n>6, J, k} \frac{(-1)^{J-1/2} M_{nJ}}{\omega_k - \omega_{nP_J}}, \quad (7.15)$$

and

$$Q = \sum_{n>6, J, k} \frac{(-1)^k}{J + 1/2} \frac{M_{nJ}}{\omega_k - \omega_{nP_J}}. \quad (7.16)$$

where

$$M_{nJ} = \frac{\langle 7S_{1/2} || r || nP_J \rangle \langle nP_J || r || 6S_{1/2} \rangle}{\langle 7S_{1/2} || r || 6P_{1/2} \rangle \langle 6P_{1/2} || r || 6S_{1/2} \rangle}. \quad (7.17)$$

Here, $k = 1, 2$ for the two laser frequencies, and $J = 1/2, 3/2$ denotes the angular momentum of the nP_J state.

7.2.2 P_L ratio

In this section, we discuss what Ref. [117] calls the linear polarization degree (P_L), defined as

$$P_L = \frac{S_{\parallel} - S_{\perp}}{S_{\parallel} + S_{\perp}}. \quad (7.18)$$

The authors of [117] chose to fit their data to this linear polarization degree P_L . Using Equations (7.3), (7.5), (7.8) and (7.9), we can easily calculate P_L . In Figure 7.3, we plot P_L for both the $4 \rightarrow 4$ and $3 \rightarrow 3$ transitions for detuning $0 < \Delta < 550 \text{ cm}^{-1}$. Comparing this to the curves for S_{\parallel}/S_{\perp} in Figure 7.2, we see that the magnitude of P_L

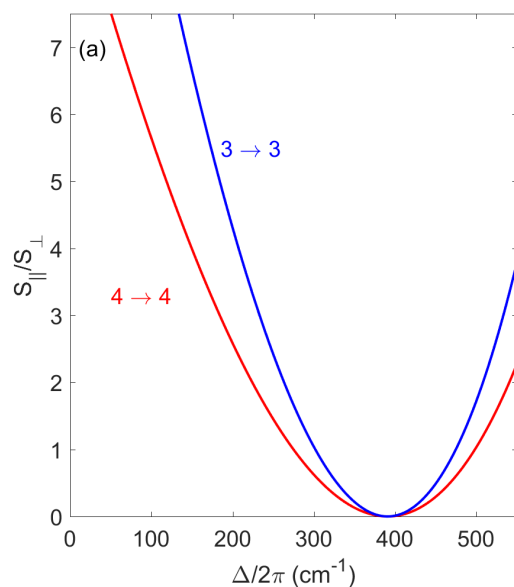


Fig. 7.2. S_{\parallel}/S_{\perp} theory curve for detuning $0 < \Delta < 550 \text{ cm}^{-1}$. The blue curve is for the $6S_{1/2} \text{ F}=3 \rightarrow 7S_{1/2} \text{ F}=3$ transition, while the red curve is for $4 \rightarrow 4$. This theory curve of S_{\parallel}/S_{\perp} was calculated using our final result of $R_{7S6P} = 1.5272$.

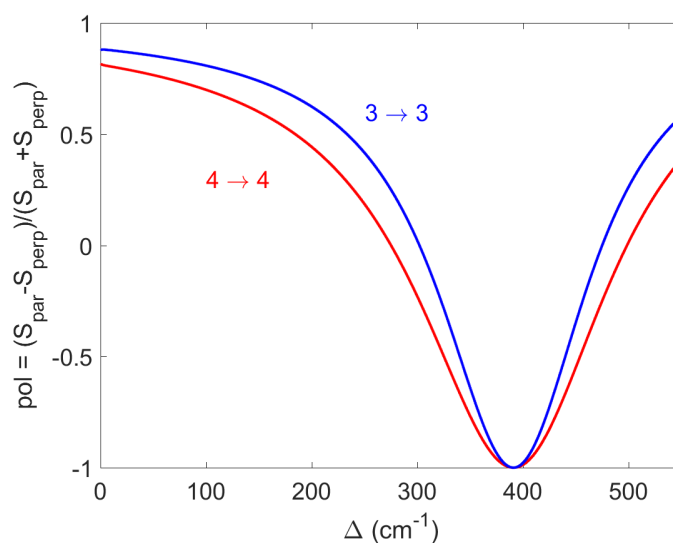


Fig. 7.3. P_L theory curve for detuning $0 < \Delta < 550 \text{ cm}^{-1}$. The blue curve is for the $6S_{1/2} \text{ F}=3 \rightarrow 7S_{1/2} \text{ F}=3$ transition, while the red curve is for $4 \rightarrow 4$. This theory curve of P_L was calculated using our final result of $R_{7S6P} = 1.5272$.

never exceeds 1, and has a zero-crossing where $S_{\parallel}/S_{\perp} = 1$. For our data analysis, we have chosen to report the result from fitting S_{\parallel}/S_{\perp} due to its simplicity. We believe that fitting to P_L weights the data points slightly differently, resulting in a marginally different final value R_{7S6P} .

7.3 Branching ratio experimental details

7.3.1 Earlier attempts (2015-2017)

We first began looking into a branching ratio measurement of the $7S_{1/2}$ state in late-2014. Initially, the plan was to conduct a new Hanle effect measurement (such as [59]) to determine the lifetime, and a branching ratio measurement similar to described in [117]. Eventually, we measured the lifetime of τ_{7S} using time-correlated single photon counting, as described earlier in Chapter 6. However, the scheme to measure the branching ratio remained the same.

The measurement scheme described in [117] requires two laser sources, one close to 852 nm, and one close to 1470 nm. Due to their rarity (and perhaps because of the atmospheric absorption line near that wavelength), laser diodes in the 1470 nm range are expensive to buy. We found a distributed feedback (DFB) laser diode at close to 1470 nm, with output power of several mW. DFB lasers have internal Bragg gratings which form the laser cavity, and have very stable single mode outputs. Because of this built-in stability, they do not tune very far in wavelength (only temperature tuning), and do not function well with optical feedback. We tried placing this diode into a Littrow cavity with no success. With $\sim 10^{\circ}\text{C}$ temperature tuning, I was only able to tune the center frequency by ~ 130 GHz, or ~ 4 cm^{-1} .

As a test, we re-purposed one of the 852 nm lasers from the PNC experimental setup to match frequencies and complete the two-photon transition from $6S_{1/2} \rightarrow 7S_{1/2}$. Matching frequencies was challenging, because we initially used the Coherent Wavemaster (estimated accuracy ~ 1 GHz) to measure the frequency of the 852 nm ECDL. We had to borrow the more accurate Bristol 671-NIR Laser Wavelength Meter

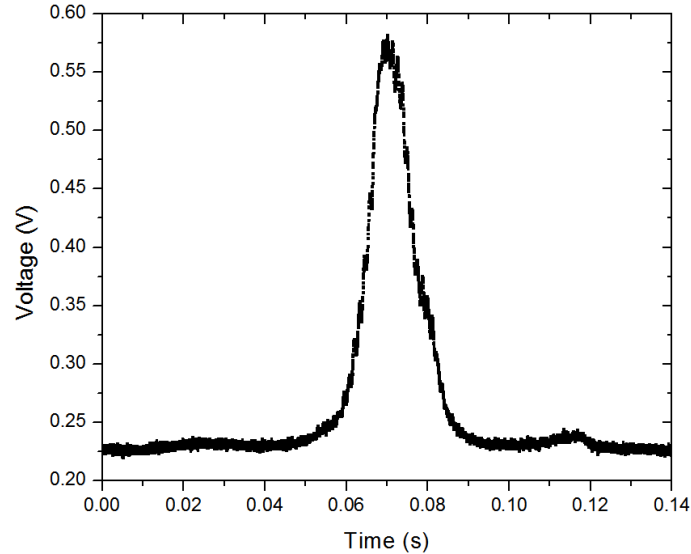


Fig. 7.4. Sample peak captured in 2015, with parallel laser polarizations in the vacuum chamber, with detuning $\Delta \approx 3 \text{ cm}^{-1}$.

from Professor Yong Chen’s group in order to monitor the 1470 nm laser wavelength. After matching frequencies to the two-photon transition, we then had to align both laser beams to coincide within the vacuum chamber, a distance of ~ 50 cm from the input windows.

Eventually, we were actually successful in obtaining two-photon excitation on the $6S_{1/2} F=4 \rightarrow 7S_{1/2} F=4$ transition. Figure 7.4 shows a $3 \rightarrow 3$ transition peak with parallel laser polarization, using the 852 nm ECDL and 1470 nm DFB laser diode, at a detuning of $\sim 3 \text{ cm}^{-1}$. However, due to the very limited detuning range ($2 < \Delta < 6 \text{ cm}^{-1}$), limited laser power, and poor quality of the recorded data, we put this measurement aside to work on other priorities.

7.3.2 Final experimental setup

In this section, I describe the experimental setup that we eventually used to make the measurement of R_{7S6P} , shown in Figure 7.5. We conducted tests using the larger vacuum chamber (the same one we use for PNC work), but were unable to obtain

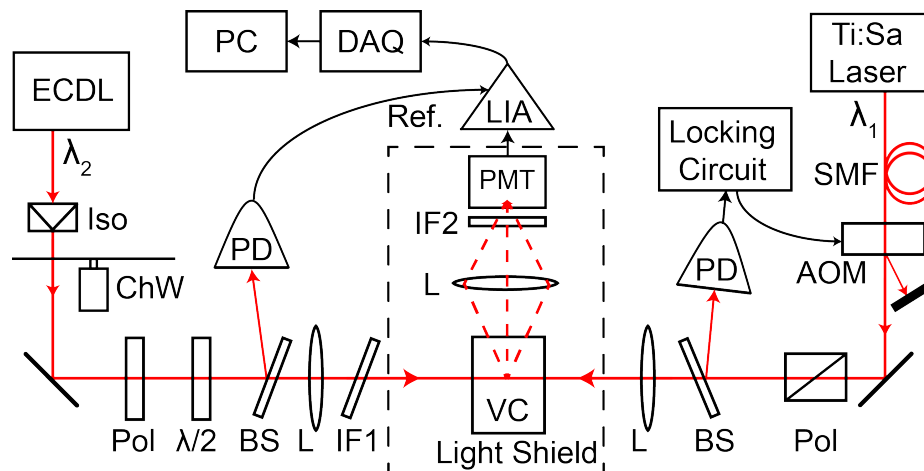


Fig. 7.5. Final experimental setup for the measurement of the relative peak amplitudes with perpendicular and parallel laser polarizations. We keep the polarization of the Ti:sapphire (Ti:Sa) laser beam constant and change the polarization of the external cavity diode laser (ECDL) beam. Other abbreviations in this figure are: (AOM) acousto-optic modulator; (BS) beam sampler; (ChW) beam chopper wheel; (DAQ) data acquisition system; (IF) interference filter; (Iso) optical isolator; (L) lens; (LIA) lock-in amplifier; (PC) personal computer; (PD) photodetector; (PMT) photomultiplier tube; (Pol) polarizer; (SMF) single-mode optical fiber; (VC) vapor cell; ($\lambda/2$) half-wave plate in a rotation stage.

sufficient atomic density to complete the measurement. We decided instead to conduct the experiment using a heated vapor cell, and detect decay fluorescence with a photomultiplier tube. The vapor cell offers much greater atomic density, while the smaller enclosure allows us to focus our laser beams more tightly, increasing our laser intensities.

As described earlier, the measurement scheme involves two lasers, one tuned close to the $6S_{1/2} \rightarrow 6P_{3/2}$ resonance (λ_1), and the second laser tuned close to the $6P_{3/2} \rightarrow 7S_{1/2}$ resonance (λ_2). We counter-propagate both laser beams through the vapor cell and record the atomic decay fluorescence peaks as we scan the frequency of one of the lasers. Then, we rotate the polarization of λ_2 and record more data. In this fashion

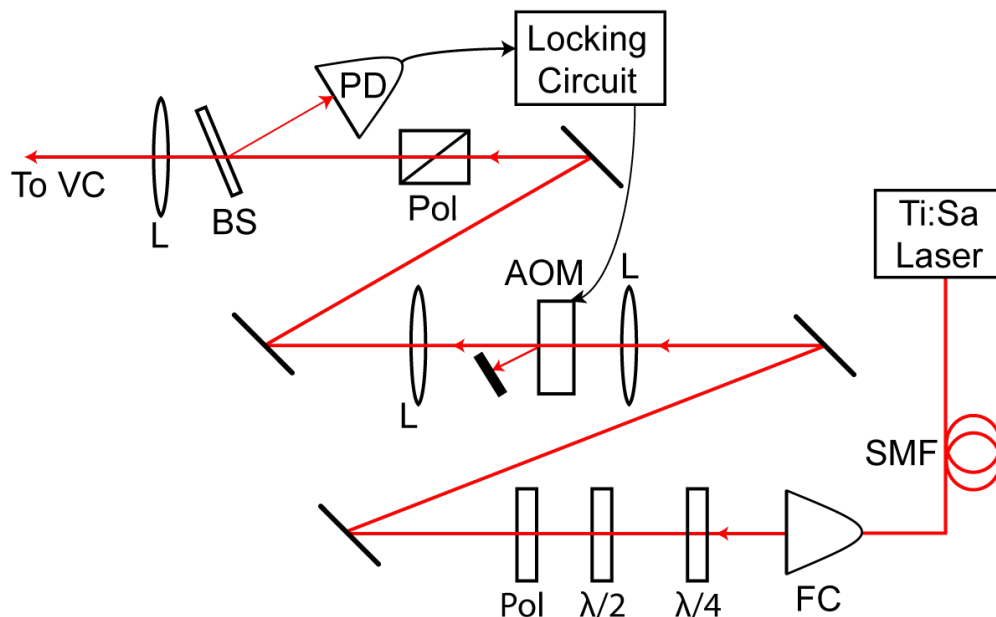


Fig. 7.6. Optical table setup for Ti:sapphire beam. The Ti:sapphire is located in SB50, and we send it through ~ 30 m of single mode fiber to the optical table in SB1. Abbreviations in this figure are: (AOM) acousto-optic modulator; (BS) beam sampler; (FC) fiber collimator; (L) lens; (PD) photodetector; (Pol) polarizer; (SMF) single-mode optical fiber; (VC) vapor cell; ($\lambda/2$) half-wave plate; ($\lambda/4$) quarter-wave plate.

of alternating the relative laser polarizations between parallel and perpendicular, we determine the ratio of absorption strengths

$$\frac{S_{\parallel}}{S_{\perp}} \quad (7.19)$$

at a particular detuning Δ . We can then use Equations (7.13) and (7.14) to determine R_{7S6P} .

To generate the light for λ_1 , we use a Ti:sapphire laser (Ti:Sa), tuned between 855 and 870 nm. The Ti:sapphire is located in room SB50, putting out 150 – 200 mW of laser power. We can usually couple about 100 – 120 mW into an optical fiber, and we pipe the light from room SB50 to the optical table in room SB1 using ~ 30 m of single mode fiber (HP780). Losses in the splices of the longer fiber mean that we

typically get 50 – 70 mW of laser output in SB1. We realized quickly that the output polarization from single mode fiber drifts by several degrees over timescales of minutes or longer. This leads to a change in the amount of λ_1 laser power going into the vapor cell for the experiment. In Figure 7.6 we show in more detail a diagram of the optics and components used to stabilize the power of the Ti:sapphire laser. We first pass the output beam from the fiber collimator through a zero-order quarter-wave plate (QWP) to linearize the polarization of λ_1 . We use an additional polarizer and laser power meter to confirm the linearity of laser polarization after passing through the quarter-wave plate. Following the quarter-wave plate, we pass the beam through a zero-order half-wave plate (HWP) to rotate the laser polarization to vertically aligned, then clean up the laser polarization with a linear polarizer. This beam is then focused through an acousto-optic modulator (AOM) with a pair of lenses ($f_1 = 15$ cm, $f_2 = 20$ cm). The AOM diffracts a fraction of the laser power into a beam block in order to keep the zeroth order beam power constant. Because stable laser power and polarization are extremely important, we then pass the beam through a high quality calcite polarizer, and use a beam sampler (Thorlabs BSF-10B) AR-coated on one side and uncoated on the other to pick off a small portion of the beam for monitoring with a photodetector. The output of this photodetector is fed into our locking electronics, which changes the rf power to the AOM to keep our laser beam power constant. We estimate a resultant λ_1 power stability of better than 0.1%. Finally, the λ_1 beam is focused into the vapor cell with a lens ($f = 15$ cm). Laser power into the vapor cell is typically ~ 20 mW.

For the second photon at 1415 to 1460 nm, we purchased an AR-coated 1450 nm laser diode (Toptica LD-1450-60-AR-2) and optical isolator from Toptica for more than \$5000. According to its specifications from Toptica, this laser diode would be able to put out 60 mW of laser power in a Littrow external cavity, when driven with ~ 250 mA of current. Because this ECDL would need to be tuned over a large wavelength range, we selected to set up the laser in a Littman configuration instead of the typical Littrow ECDL configuration. In the Littman configuration, the laser

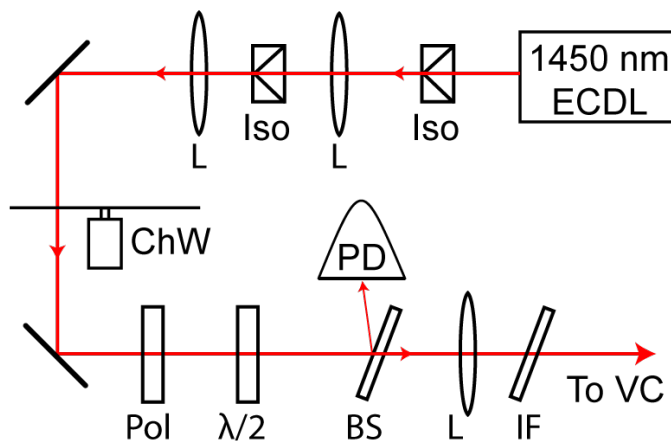


Fig. 7.7. Optics for polarization control of the 1450 nm ECDL. Abbreviations in this figure are: (BS) beam sampler; (ChW) beam chopper wheel; (IF) interference filter; (Iso) optical isolator; (L) lens; (PD) photodetector; (Pol) polarizer; (VC) vapor cell; ($\lambda/2$) half-wave plate in a rotation stage.

diode and grating are not moved, resulting in a fixed output beam direction. The first order diffraction from the grating is directed onto a high reflectivity mirror, which retro-reflects the light back to the grating and laser diode for feedback (see Figure 3.2(b)). Laser frequency is tuned by adjusting the angle of this reflector, instead of the grating in a Littrow ECDL, so the laser beam output angle does not change as we tune the laser frequency. We obtain ~ 25 mW of output laser power from the 1450 nm ECDL.

Polarization control of the 1450 nm ECDL is also extremely important, especially because we decided to rotate the polarization of this laser, while keeping the Ti:sapphire laser polarization fixed. We show in Figure 7.7 a more detailed diagram of the polarization optics for laser 2. Early tests of the Littman ECDL showed sensitivity to external feedback and back-reflections. We pass the beam through two optical isolators, one from Toptica, optimized for isolation at 1450 nm (> 35 dB isolation, aperture: 4.7 mm), and a tiny one from AC Photonics Inc (46 dB isolation at 1480 nm). Because the second isolator is so tiny (diameter: 3 mm, aperture: 0.8 mm), we have to focus and expand the beam going through it with a pair of

lenses ($f_1 = 6$ cm, $f_2 = 15$ cm). The output beam then passes through a chopper wheel (at ~ 266 Hz), and through two periscopes to send it across the optical table. We then pass the beam through a nanoparticle thin film linear polarizer (Thorlabs LPNIR050-MP2), with specified extinction ratio $> 10^6$ at 1450 nm. We follow the polarizer with a zero-order half-wave plate (HWP) optimized for 1480 nm. To rotate the laser polarization between vertically polarized (relative to the optical table), and horizontally polarized, we rotate this HWP between two pre-calibrated angles. We then pick off part of the beam with a wedged beam sampler, and focus the beam into the vapor cell with a $f = 15$ cm lens. Finally, before the beam enters the vapor cell, we pass it through a long-pass dichroic mirror at 1180 nm (Thorlabs DMLP1180). We found that the presence of the Ti:sapphire beam caused the output power of the 1450 nm ECDL to slowly drift by 1 – 2% over several minutes. The dichroic mirror blocks the Ti:sapphire beam and resolves this issue. The 1450 nm laser power going into the vapor cell is typically about 5 mW.

The vapor cell and photomultiplier setup we used, is the same one we normally use for locking the 1079 nm laser to the 2-photon $6S_{1/2} \rightarrow 7S_{1/2}$ transition (discussed earlier in Section 3.6.2), with several modifications. The PMT setup for 1079 nm laser locking contains a broadband 850 ± 20 nm interference filter, and a 1-in lens halfway between the 4 in distance from the imaging plane to the PMT. The first thing we did to improve our SNR was to replace the interference filter with a narrower bandwidth 850 ± 5 nm bandpass filter. This means that as we increase the detuning Δ , less laser light at ~ 860 nm will be scattered into the PMT, while fluorescence photons at 852 nm will be unaffected. We focus both beams into the vapor cell with a calculated width of ~ 80 μm . To reduce scattered light due to the lasers passing through the windows of the vapor cell, we want an imaging width of < 12 mm, the width of the vapor cell. With the 1:1 imaging system due to the 1-in lens, this means that we want to image a cross-section of $\sim 0.1 \times 6$ mm². The Hamamatsu R928 PMT we use is a side-on type photomultiplier tube, with a large active area of 8×24 mm². To reduce the amount of scattered laser light detected by the PMT, we place an aperture in

front of the PMT, of dimensions 2×6 mm. The 6 mm width spatially filters most of the photons scattered from the vapor cell windows, while the 2 mm height is more practical.

To calibrate the proper angles to rotate the HWP, we introduce an analyzing linear polarizer, which we insert into the beam path before the beam enters the vapor cell. We then monitor the laser power after the beam exits the vapor cell with a power meter. We first set the analyzing polarizer to pass only vertically polarized laser light, and rotate the HWP to find the angle which extinguishes the beam passing through the vapor cell. Then, we rotate the analyzing polarizer to pass only horizontally polarized light, and repeated the process with the HWP. As expected, the two optimum HWP angles were always 45° apart.

The laser polarization purity for this measurement is extremely important, and we made a number of different modifications to improve our extinction ratio. We initially tried having a linear polarizer after the HWP in the beam path, and rotated both the HWP and polarizer for each measurement. However, we found that rotating the polarizer caused the beam to move, so we removed this polarizer. Next, we note that clamping optics too tightly can cause strain birefringence, which worsens the laser polarization extinction ratio. We tested this out experimentally and found that replacing the metal O-rings for all optical components after the linear polarizers with plastic O-rings improved the laser extinction ratio (these O-rings are used to secure optics to the optical mounts). For example, applying this fix to the focusing lens led to a $10\times$ improvement in the laser extinction ratio for both the 1450 nm and Ti:sapphire laser beams. Ultimately, we improved the extinction ratio of the beams going into the vapor cell from 1,000:1 to $>10,000:1$.

Due to the poor 2-photon absorption strength and the large dc background caused by scattered Ti:sapphire laser light, the fluorescence signal was weak with poor signal-to-noise ratio. This made it difficult to obtain good fits to the Gaussian peaks. We decided to use phase sensitive detection to enhance our signal. We pass the 1450 nm beam through a chopper wheel at ~ 266 Hz. By detecting at this frequency, we

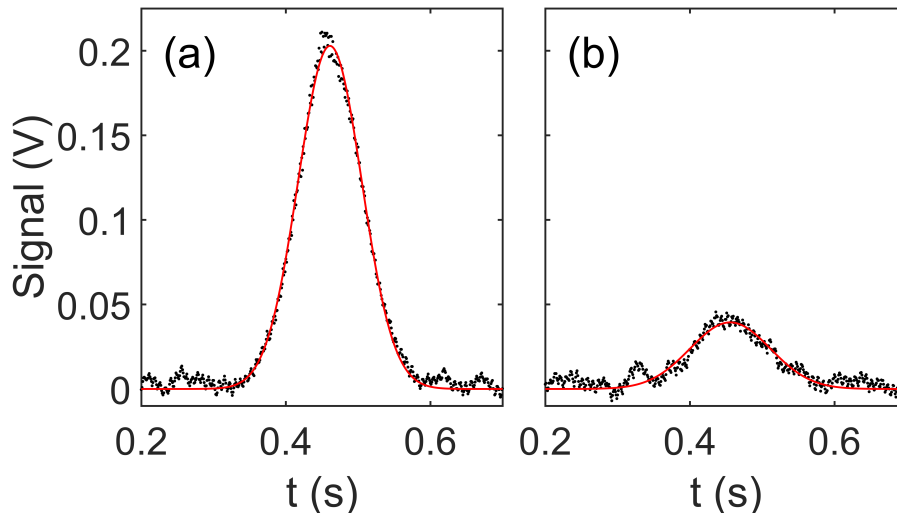


Fig. 7.8. Absorption spectra for (a) parallel polarization and (b) perpendicular polarization, at a detuning of $\Delta/2\pi = 107.5 \text{ cm}^{-1}$. The black dots are experimental data while the red curve is the least-squares Gaussian fit to the data. With a laser frequency scan rate of $\sim 2.0 \text{ GHz/sec}$, the total frequency width of these plots is $\sim 1.0 \text{ GHz}$. The ratio of peak heights at this detuning is $S_{\parallel}/S_{\perp} \approx 5.35$.

will not be sensitive to the scattered Ti:sapphire laser light which is not chopped. We send the PMT output and the square-wave output of the 1450 nm monitor PD to a Stanford Research Systems SR530 Lock-in amplifier. We set the output to give us $10\times$ gain, improving the signal-to-noise ratio and amplifying the peaks to a reasonable size for curve fitting. An example of our recorded data is shown in Figure 7.8. In our data, we noticed a high frequency sinusoidal oscillation at $\sim 120 \text{ Hz}$. We investigated and found this to be from the lock-in amplifier, but were unable to filter it out without ruining the Gaussian profiles. We found that the oscillations did not affect the Gaussian fits, so we proceeded with the measurement with the small oscillation present.

At the beginning of the day, there are a number of calibration procedures to take, which I outline in summary here. After turning on both lasers, we first tune the 1450 nm laser close to the detuning frequency where we want to make the measure-

ment. The 1450 nm Littman laser is tuned by turning a set-screw to adjust the reflector angle, which changes its output frequency. This is fairly coarse tuning (we can usually get the 1450 nm laser to within ~ 1 GHz of our target frequency), but with our accurate wavemeter (Burleigh) we can readout the frequency to 0.1 GHz. Following this, we calculate the corresponding laser frequency needed to complete the two-photon transition. We then tune the Ti:sapphire to the frequency needed ± 0.1 GHz. The Coherent wavemeter is only accurate to ~ 1 GHz, but we scan the Ti:sapphire laser frequency over a range of ~ 3 GHz. Making sure that the laser polarizations going into the vapor cell are parallel, we should now have detectable fluorescence signal from the PMT.

The next important thing to do is maximizing the Ti:sapphire laser power through the AOM, and stabilizing its power. We saw earlier in Figure 7.6 the QWP and HWP setup to linearly polarize the Ti:sapphire beam. The AOM power stabilization circuit is a home-made PCB designed by Ian C. Stevenson and takes a little finesse to get working. The capture range of the power stabilization circuit is small, but once the correct setpoint is found, the circuit keeps the output power stable unless there are huge fluctuations in the output power coming from the fiber.

After these steps, we then check on our two-photon signal size. Before the first measurement of the day, we always check the alignment of the two beams. We adjust the setscrews on the final mirrors of the Ti:sapphire beam and the 1450 nm beam to maximize the two-photon signal size. Usually, no adjustment is needed unless we had to tweak another optical component along the beam path. Finally, we record the extinction ratios of both lasers. For the Ti:sapphire laser beam, we check only the vertical polarization extinction ratio. For the 1450 nm laser beam, we record the extinction ratio for both vertical and horizontal laser polarization. With this daily set of calibrations out of the way, we are now ready to begin recording data.

7.3.3 Results and analysis

In Figure 7.8, I show an example of absorption spectra recorded at a detuning of $\Delta/2\pi = 107.5 \text{ cm}^{-1}$. In Figure 7.8(a), the laser polarizations are both vertically polarized (parallel polarization), while in Figure 7.8(b), the 1450 nm laser polarization is rotated by 90° (perpendicular polarization). We scan the frequency of the Ti:sapphire laser at $\sim 2.0 \text{ GHz/sec}$, for a total frequency width in these plots of $\sim 1.0 \text{ GHz}$. At this detuning, the ratio of peak heights $S_{\parallel}/S_{\perp} \approx 5.35$.

For each measurement at a particular detuning, we first begin with both lasers polarized parallel. We observe the absorption spectra on an oscilloscope, and capture some peaks with the National Instruments Data Acquisition System (DAQ). Before we start recording measurement data, we first measure and record the extinction ratios for both the 1450 nm laser and the Ti:sapphire laser. We make these measurements by inserting an analyzing polarizer immediately before the vapor cell, and a power meter immediately after the vapor cell. We can then measure the amount of laser power when the analyzer is parallel to the laser polarization, or crossed with the laser polarization. The Ti:sapphire laser polarization is never rotated, so we only record the vertically polarized extinction ratio (typically $> 10,000$). The 1450 nm laser is rotated between vertical and horizontal (relative to the optical table), so we record the extinction ratio at both polarizations. For vertical polarization (parallel), this ranges from $3,000 - 200$, while for horizontal polarization (perpendicular), the extinction ratio ranges from $20,000 - 5,000$. To correct for imperfect laser extinction ratio, we use the measured extinction ratios to calculate the corrections to apply the measured ratios.

Once we have recorded the laser extinction ratios and performed our standard system tests, we are then ready to make our measurements. We first record 30 absorption peaks with the parallel laser polarization. Labview is able to fit these curves to Gaussian peaks on-the-fly, and we monitor the amplitude, width, and standard deviation. Recording each set of 30 peaks takes approximately 2 minutes. After this

is complete, the peaks are saved, and we record the average fitted Gaussian amplitude and standard deviation of peak amplitude. At the same time, we rotate the 1450 nm HWP to the second calibrated angle, to rotate the laser polarization by 90° . We then repeat the 30-peak recording/fitting process, and extract the average values and standard deviation. At this point, we can roughly calculate an S_{\parallel}/S_{\perp} value to check if our results are in the right ballpark.

We continue taking data at the same detuning, going back-and-forth between parallel and perpendicular laser polarizations for at least 3 measurements of S_{\parallel} and S_{\perp} each. At low detunings Δ , the large ratio between the S_{\parallel} and S_{\perp} means that it is more challenging to make good measurements, so we always recorded more than 3 measurements of each. This is because we need to keep intensities low to avoid saturation for parallel polarizations, while ensuring sufficient signal-to-noise ratio for perpendicular polarizations. At larger Δ , the peak heights were more equal, and we increased the Ti:sapphire laser power from ~ 10 mW to ~ 30 mW to maximize the signal size. We make sure to record S_{\parallel} and S_{\perp} the same number of times. Once we have recorded sufficient data (typically 3 – 4 measurements at for each polarization), we change the detuning of the two lasers, and start the measurement process all over.

We recorded measurements over a detuning range of $60 < \Delta < 280 \text{ cm}^{-1}$. While we primarily recorded data for the $4 \rightarrow 4$ transition due to its smaller S_{\parallel}/S_{\perp} ratio, we also tuned our laser frequencies to be resonant with the $3 \rightarrow 3$ transition and recorded several datapoints. This serves as a check on our measurement technique and derived equations. We avoided small detunings for two reasons: scattered laser light through the PMT interference filter worsens the signal-to-noise ratio; the ratio S_{\parallel}/S_{\perp} is much larger at smaller detunings, making it difficult to obtain sufficient SNR with the smaller peak while avoiding saturation effects with the larger peak.

Before we can fit our data to Equations (7.13) and (7.14), there are several systematic effects we have to consider and apply corrections for. We show a summary of these corrections and their uncertainties in Table 7.1. We apply these corrections to and expand the error bars of the individual data points before curve fitting. For

Table 7.1

Sources of error and the correction applied to S_{\parallel}/S_{\perp} and uncertainty for each. We compute the uncertainty for each data point in Fig. 7.9 as the quadrature sum of these contributions. The final uncertainty is dominated by statistical uncertainty.

Error	% Correction	% Uncertainty
Statistical		0.26 – 1.17
Polarization purity	0.12 – 0.35	0.05
Beam power change	0.1 – 1	0.1 – 0.3
Magnetic field	-0.1	0.1
HWP rotation precision	0.05	0.05
Beam movement		0.01

some of these systematics, we list a range of values because the size of the correction and uncertainty is different for data points at different Δ .

The first error in Table 7.1 ‘Polarization purity’ refers to the fact that our two lasers have imperfect extinction ratio. I mentioned earlier that we recorded the laser extinction ratios at every Δ . From these measurements, we can work out the change in the measured ratio due to imperfect extinction ratio, and calculate corrections for each individual data point. As mentioned earlier, the extinction ratio changes with detuning Δ , so the magnitude of the correction varies from 0.12 – 0.35%. To determine the extinction ratio, we measure the laser power with a Thorlabs power meter with a reading uncertainty of ± 0.005 mW. This leads to a 0.05% uncertainty due to the correction for the extinction ratio. I have included more details in Section D.1 of the Appendices.

The next error of ‘Beam power change’ arises from the fact that we pick-off a portion of the 1450 nm beam with a Fresnel reflection from an uncoated surface of the beam sampler. This means that the reflected (and hence transmitted) laser power is slightly different for vertical and horizontal polarization. When measuring the

laser extinction ratio, we also measure the change in laser power with polarization, and can calculate the appropriate correction. This correction varies in magnitude from 0.1 – 1%. As with polarization purity, the uncertainty due to this correction (0.1 – 0.3%) comes from our measurement error of the transmitted laser power.

In the region where the vapor cell is located, we measure a ~ 0.5 G magnetic field due to the stainless steel optical table and Earth’s field. This field has no effect on the parallel polarization signal strength, but could slightly broaden the peak when we have perpendicular laser polarizations. We estimate that this increases our measured ratio by 0.1%, and we apply a correction in the opposite direction.

We manually rotate the 1450 nm laser half-wave plate 45° between measurements to rotate the 1450 nm laser polarization. While larger mis-rotations are easily identified and corrected, smaller errors are difficult to detect. We estimate that we can rotate the half-wave plate to the correct angle $\pm 0.25^\circ$. An error in the half-wave plate rotation angle always leads to a smaller measured S_{\parallel}/S_{\perp} ratio, because it leads to smaller S_{\parallel} or larger S_{\perp} . Therefore, some correction to the data is appropriate. We model the distribution of angles as a Gaussian distribution and convolve this with the extinction ratio due to mis-rotation. We estimate that this would require a correction of 0.05%, and we include an uncertainty of the same magnitude. I have included more details in Section D.2 of the Appendices.

Finally, we examined the effects beam movement due to rotation of the half-wave plate. We setup the 1450 nm ECDL, half-wave plate and focusing lens at a separate location and measured negligible movement of the beam at the focal point. Using the manufacturer’s specification of the waveplate, we estimate the beam displacement of $< 0.4 \mu\text{m}$. The resultant uncertainty on the ratio $S_{\parallel}/S_{\perp} = (\Delta x/w)^2$ is less than 0.01%. We find this to have minimal effect and include a 0.01% uncertainty due to beam movement.

For each individual data point, we add these errors in quadrature before curve fitting. We show our data including corrections and with expanded error bars in Figure 7.9(a). We have also plotted the best fit lines for both the $4 \rightarrow 4$ (in red) and

Table 7.2

State energies and electric dipole $E1$ transition moments $\langle 7S_{1/2} || r || nP_J \rangle$ and $\langle nP_J || r || 6S_{1/2} \rangle$ used to determine R . Transition moments are given in terms of a_0 . ^aState energies as found in NIST tables [118]. ^bWeighted average of several independent determinations from Refs. [66–68, 103–106, 108]. ^cRef. [64], including the Supplemental Information. ^dRef. [119]. ^eRef. [96].

n	E_{nP_J} (cm ⁻¹) ^a	$\langle 7S_{1/2} r nP_J \rangle$	$\langle nP_J r 6S_{1/2} \rangle$
$J = 1/2$			
6	11178.268	–	4.5057 (16) ^b
7	21765.348	10.31 (4) ^e	0.2781 (5) ^d
8	25708.835	0.914 (27) ^c	0.092 (10) ^c
9	27636.997	0.349 (10) ^c	0.043 (7) ^c
10	28726.812	0.191 (6) ^c	0.025 (5) ^c
11	29403.423	0.125 (4) ^c	0.016 (4) ^c
$J = 3/2$			
6	11732.307	–	–6.3398 (22) ^b
7	21946.397	14.32 (6) ^e	–0.5740 (7) ^d
8	25791.508	1.620 (35) ^c	–0.232 (14) ^c
9	27681.678	0.680 (14) ^c	–0.130 (10) ^c
10	28753.677	0.396 (9) ^c	–0.086 (7) ^c
11	29420.824	0.270 (7) ^c	–0.063 (6) ^c

$3 \rightarrow 3$ (in blue) transitions. In Figure 7.9(b) we show the residuals of the curve fits. We do a least squares fit to both curves using all our data at once, with R_{7S6P} the only adjustable parameter. To evaluate P and Q from Equations (7.15) and (7.16), we use a combination of experimental and theoretical values as listed in Table 7.2. Theoretical values are the recommended values from the Supplemental Information of [64].

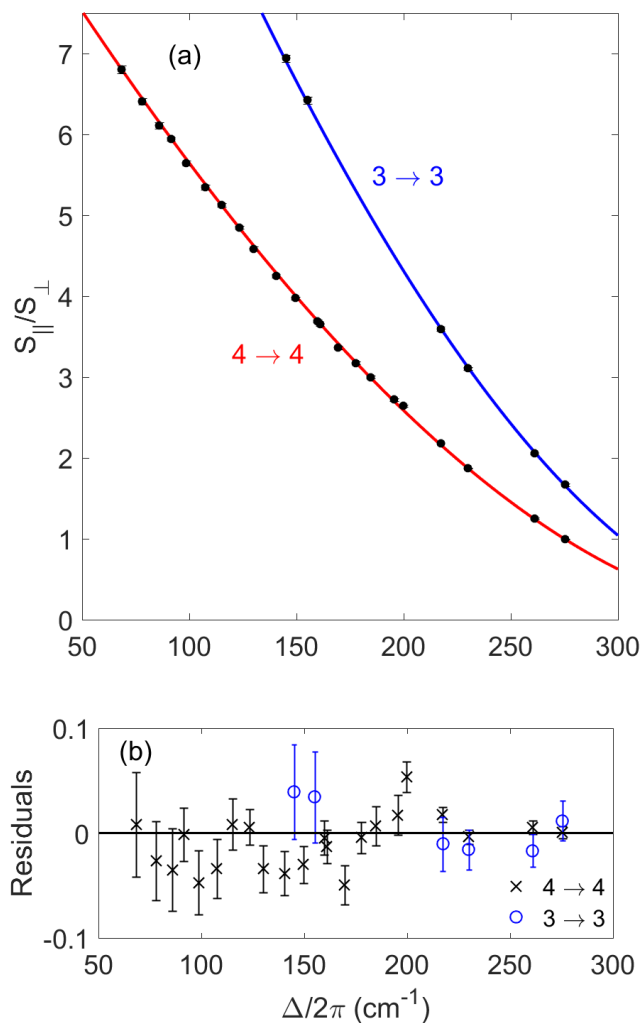


Fig. 7.9. (a) The ratio of peak heights S_{\parallel}/S_{\perp} as a function of detuning $\Delta/2\pi$. The lower (red) curve is for the $4 \rightarrow 4$ transition while the upper (blue) curve is for the $3 \rightarrow 3$ transition. The data points are the experimental data, with error bars showing 1σ uncertainties. (In many cases, the uncertainties are smaller than the data point size.) The smooth lines show the best fit plots of Equations (7.13)-(7.14), with $R = 1.5272$ the only adjustable parameter. (b) Residuals, showing the difference between data points and the fitted curve in (a). $4 \rightarrow 4$ residuals are shown with an \times , while $3 \rightarrow 3$ residuals are shown with an open circle (o). This figure is reproduced from [57].

Table 7.3

A list of the absolute values of the most recent precise measurements of the $\langle 6P_J || r || 6S_{1/2} \rangle$ matrix elements. For our calculations, we use the weighted average of these measurements, as listed in Table 7.2. ^aZhang reports slightly different lifetimes in the abstract from the text, I have used the number from the text to calculate these matrix elements.

Year	Ref	Authors	$6S_{1/2} - 6P_{1/2}$	$6S_{1/2} - 6P_{3/2}$
1992	[120]	Tanner <i>et al.</i>		6.3260(280)
1994	[103]	Young <i>et al.</i>	4.5097(45)	6.3403(104)
1999	[66]	Rafac <i>et al.</i>	4.4890(65)	6.3238(73)
2002	[104]	Derevianko <i>et al.</i>	4.5064(45)	6.3424(63)
2003	[105]	Amini <i>et al.</i>	4.5116(41)	6.3498(56)
2007	[106]	Bouloufa <i>et al.</i>	4.5051(233)	6.3404(313)
2013	[107]	Zhang ^a <i>et al.</i>	4.5058(45)	6.3404(63)
2015	[68]	Gregoire <i>et al.</i>	4.5080(40)	6.3450(50)
2015	[108]	Patterson <i>et al.</i>		6.3349(48)
This work		Weighted average	4.5057(16)	6.3398(22)

For $n \leq 7$, high precision experimental values are available. The $\langle 7S_{1/2} || r || 7P_J \rangle$ matrix elements can be extracted from the high precision Stark shift measurement by [96] and a theory calculation of the branching ratio [63]. In Chapter 8, we discuss a new determination of these matrix elements using the updated matrix elements determined in this chapter. There are many high precision measurements of the $\langle 6P_J || r || 6S_{1/2} \rangle$ matrix elements and I have listed the most recent in Table 7.3. We calculate the weighted average of these measurements and list the value we used in Table 7.2. Finally, we have recently made a re-newed measurement of the $\langle 7P_J || r || 6S_{1/2} \rangle$ reduced dipole matrix elements. The report will appear in Physical Review A, and we use these results for this calculation.

To evaluate our curve fit, we look at the residual sum of squares weighted by the uncertainty of each data point. The best fit value is $R_{7S6P} = 1.5272(16)$. Our fitted value of R_{7S6P} is also dependent on the theory and experimental values of the other matrix elements used (from Table 7.2), which each have some uncertainty. We individually vary the matrix elements used within their error bars, and find that within the error bars of the $\langle 6P_J || r || 6S_{1/2} \rangle$ matrix elements, R_{7S6P} changes by 0.04%, while the other terms had negligible effect. We add this error in quadrature with our statistical error and obtain our final result of $R_{7S6P} = 1.5272(17)$.

7.3.4 Comparison of result with theory

For this work, we collaborated with Prof. Marianna S. Safronova for assistance with the theoretical portions of the measurement. In addition to being able to calculate new reduced matrix elements for $\langle 7S_{1/2} || r || 6P_{1/2} \rangle$ and $\langle 7S_{1/2} || r || 6P_{3/2} \rangle$, she realized that our measurement could help theorists (such as herself) benchmark the accuracy of various calculation methods.

In Table 7.4, we list the calculated reduced dipole matrix elements $\langle 7S_{1/2} || r || 6P_{1/2} \rangle$, $\langle 7S_{1/2} || r || 6P_{3/2} \rangle$ and their ratio R_{7S6P} from Dirac-Hartree-Fock (DHF) and several linearized coupled-cluster (LCC) calculations from [57, 64]. The lowest-order DHF values shown are listed only to show the effect of electronic correlations. The *ab initio* LCC results labelled ‘SD’ are obtained by considering single and double (SD) excitations of the lowest-order wave function. The results labelled ‘SDpT’ include the effects of partial triple excitations. Finally, the scaled SD and SDpT values are also listed with subscript ‘sc’. There is some debate about how scaling affects the ratio precision. Comparing our measured ratio R_{7S6P} with the various approximations, it appears that the inclusion of partial triple contributions or scaling improves agreement of theory with experiment.

We show in Table 7.5 a comparison of our results with various theoretical determinations. As far as we know, our report is the first measurement of the branching

Table 7.4

Absolute values of the $7S_{1/2} - 6P_J$ reduced dipole matrix elements (in a_0) and their ratio calculated in different approximations (see text for more details). This data is from references [64] and [57].

	DHF	SD	SD _{sc}	SDpT	SDpT _{sc}	Experiment
$7s - 6p_{1/2}$	4.4177	4.2006	4.2434	4.2325	4.2313	4.249(4)
$7s - 6p_{3/2}$	6.6729	6.4258	6.4795	6.4608	6.4658	6.489(5)
R_{7S6P}	1.5105	1.5297	1.5270	1.5265	1.5281	1.5272(17)

ratio of the cesium $7S_{1/2}$ state. Our reported value of the ratio is in good agreement with various theoretical determinations over the past 30 years.

7.4 Calculation of matrix elements

From Equation (6.5), we derived the following equations:

$$\langle 7S || r || 6P_{1/2} \rangle = \frac{3}{2} \frac{c^2}{\alpha \omega_{1/2}^3} \frac{(1 + R_{7S6P})}{\tau_{7S}} \quad (7.20)$$

$$\langle 7S || r || 6P_{3/2} \rangle = R_{7S6P} \times \langle 7S || r || 6P_{1/2} \rangle \quad (7.21)$$

With our measurement of

$$\tau_{7S} = 48.28(7) \text{ ns}$$

and our determination of

$$R_{7S6P} = 1.5272(17),$$

we can now calculate the two reduced dipole matrix elements

$$\langle 7S_{1/2} || r || 6P_{1/2} \rangle = -4.249(4) a_0$$

and

$$\langle 7S_{1/2} || r || 6P_{3/2} \rangle = -6.489(5) a_0.$$

Table 7.5

Experimental and theoretical results for the ratio and absolute values of reduced dipole matrix elements for the cesium $6p\ ^2P_J \rightarrow 7s\ ^2S_{1/2}$ transitions. We compute the ratio R_{7S6P} from the values of $\langle 7s_{1/2} || r || 6p_{1/2} \rangle$ and $\langle 7s_{1/2} || r || 6p_{3/2} \rangle$ reported in Refs. [21, 63, 64, 71, 115, 121].

Group	Ratio $ R_{7S6P} $	$ \langle 7s_{1/2} r 6p_{1/2} \rangle $	$ \langle 7s_{1/2} r 6p_{3/2} \rangle $
<i>Experimental</i>			
This work	1.5272 (17)	4.249 (4)	6.489 (5)
<i>Theoretical</i>			
Dzuba <i>et al.</i> , 1989 [115]	1.530	4.253	6.507
Blundell <i>et al.</i> , 1991 [121]	1.526	4.228	6.451
Blundell <i>et al.</i> , 1992 [21]	1.527	4.236	6.470
Safronova <i>et al.</i> , 1999 [63]	1.527	4.243	6.479
Dzuba <i>et al.</i> , 2001 [71]	1.526	4.255	6.495
Porsev <i>et al.</i> , 2010 [14]	–	4.245	–
Safronova <i>et al.</i> , 2016 [64]	1.5270 (27)	4.243 (11)	6.480 (19)

We determine the error bars for the matrix elements by varying τ_{7S} and R_{7S6P} by their uncertainties and calculating the range of matrix elements obtained. We rely on lowest order DHF calculations from Prof. Safronova to determine the correct signs of these two matrix elements (or see Section 2.2). We have listed our new results in Table 7.5 together with past theoretical determinations. Our reported values for the two reduced dipole matrix elements $\langle 7S_{1/2} || r || 6P_J \rangle$ are in-line with the many theoretical calculations of the matrix elements.

High precision measurements such as those reported here provide a benchmark for future atomic theory calculations, which are necessary for new parity violation measurements. In the following chapter, we discuss the immediate impact these measurements have on determinations of Q_{weak} in cesium.

8. NEW DETERMINATION OF CS $6S \rightarrow 7S$ VECTOR POLARIZABILITY β

In this chapter, we begin with a review of our more precise determinations of matrix elements between various Cs states. Using these new matrix elements, we are then able to calculate new values for α , β and determine a new value of Q_w .

8.1 Summary of 6S-7P measurement

In 2013, our group made a measurement of the $\langle 7P_{1/2} || r || 6S_{1/2} \rangle$ and $\langle 7P_{3/2} || r || 6S_{1/2} \rangle$ matrix elements [54]. In that measurement, during which I was around to observe, we measured the absorption depth of a laser beam through a vapor cell containing cesium atoms. A laser, tunable between 456 – 459 nm, was tuned to one of the $6S \rightarrow 7P_J$ resonances and its absorption compared against that of an 894 nm laser tuned to the $6S \rightarrow 6P_{1/2}$ resonance. By carefully overlapping both laser beams so that they have the same path length through the vapor cell, we can determine the ratio of matrix elements between $\langle 7P_J || r || 6S_{1/2} \rangle$ and the precisely known (0.04%) $\langle 6P_{1/2} || r || 6S_{1/2} \rangle$. The reported results were

$$\langle 7P_{1/2} || r || 6S_{1/2} \rangle = 0.2789(16) \text{ a}_0$$

and

$$\langle 7P_{3/2} || r || 6S_{1/2} \rangle = 0.5780(7) \text{ a}_0,$$

with fractional uncertainties of 0.6% and 0.12% respectively. The reason for the large uncertainty in $\langle 7P_{1/2} || r || 6S_{1/2} \rangle$ is that the absorption depth of the 459 nm laser was too shallow, due to having to limit the 894 nm laser beam absorption. It was more difficult to get a good Gaussian fit to the shallow data, resulting in larger statistical uncertainty and a less precise measurement.

Due to the 0.6% uncertainty in $\langle 7P_{1/2} || r || 6S_{1/2} \rangle$, we began in 2018 to look at a new measurement of this matrix element. Led by Amy Damitz, and assisted by an REU undergrad Eric Putney, we assembled a new ECDL at 456 nm. Unlike the tunable 456 – 459 nm AR-coated laser diode previously assembled, this new laser would not tune up to 459 nm. With a pair of blue lasers, each tuned to $6S \rightarrow 7P_J$ absorption resonances of different J , we can now make a direct measurement of the ratio between the two matrix elements

$$R_{7P7P} = \frac{\langle 6S_{1/2} || r || 7P_{3/2} \rangle}{\langle 6S_{1/2} || r || 7P_{1/2} \rangle}. \quad (8.1)$$

In making a new measurement of R_{7P7P} , we also decided to fit the curves to the Voigt function, a convolution of a Gaussian and Lorentzian function. We found a significant difference (at the $< 1\%$ level) to the fitted absorption amplitudes between Gaussian and Voigt fits. We re-examined the 2013 data and discovered the same thing with that data. Because of this, we also decided to re-measure the ratio

$$R_{7P6P} = \frac{\langle 6S_{1/2} || r || 7P_{3/2} \rangle}{\langle 6S_{1/2} || r || 6P_{1/2} \rangle}. \quad (8.2)$$

We found a difference of $\sim 0.3\%$ in the ratio R_{7P6P} measured in 2019 compared to our earlier 2013 measurement.

Our final reported results are

$$R_{7P6P} = 7.8474(72)$$

$$R_{7P7P} = 2.0646(26)$$

which have uncertainties of approximately 0.09% and 0.13%. We use $\langle 6S_{1/2} || r || 6P_{1/2} \rangle = 4.5057(16) a_0$ as derived earlier from a weighted mean of 10 different measurements, we obtain

$$\langle 6S_{1/2} || r || 7P_{3/2} \rangle = 0.57417(57) a_0,$$

$$\langle 6S_{1/2} || r || 7P_{1/2} \rangle = 0.27810(45) a_0.$$

These matrix elements have uncertainties of 0.1% and 0.16% respectively, an improvement over the 2013 measurement which reported uncertainties of 0.12% and 0.6%. The work described in this section was published in Physical Review A [119].

8.2 Revisiting the 7S-7P matrix elements

The most precise result of the reduced dipole matrix elements $\langle 7S_{1/2} || r || 7P_{3/2} \rangle$ and $\langle 7S_{1/2} || r || 7P_{1/2} \rangle$ is derived from a dc Stark shift measurement of the $6S \rightarrow 7S$ transition by Bennett, Roberts and Wieman in 1998 [96]. The authors applied a strong dc electric field (up to 10 kV/cm) to an atomic beam of cesium atoms and measured the shift in frequency of the resonance peak to determine the Stark polarizability

$$\frac{1}{2}\alpha_{7S-6S} = 0.7262(8) \text{ Hz(V/cm)}^{-2}.$$

In atomic units, this converts ($\times 4018.7782^1$) to

$$\alpha_{7S-6S} = \alpha_{7S} - \alpha_{6S} = 5836.9(64) \text{ a}_0^3$$

where α_{7S} (α_{6S}) is the Stark polarizability of the 7S (6S) state.

This experimental value of α_{7S-6S} can be used to derive accurate values for $\langle 7S_{1/2} || r || 7P_{3/2} \rangle$ and $\langle 7S_{1/2} || r || 7P_{1/2} \rangle$ because α_{7S} depends almost entirely on these two matrix elements [63]. This was first presented by Safronova, Johnson and Derevianko in 1999, who combined $\alpha_{7S-6S} = 5837(6) \text{ a}_0^3$ with $\alpha_{6S} = 399.9(1.9) \text{ a}_0^3$ to obtain α_{7S} , which can be calculated from the sum of $\langle 7S_{1/2} || r || nP_J \rangle$ matrix elements

$$\alpha_{7S} = \frac{1}{3} \sum_n \left[\frac{|\langle 7S_{1/2} || r || nP_{1/2} \rangle|^2}{E_{nP_{1/2}} - E_{7S}} + \frac{|\langle 7S_{1/2} || r || nP_{3/2} \rangle|^2}{E_{nP_{3/2}} - E_{7S}} \right]. \quad (8.3)$$

The $7S - 7P_J$ terms contribute 10 times as much as $7S - 6P_J$ terms, while all other terms ($n > 7$) contribute only 0.5% to α_{7S} . The authors of [63] used a combination of experimental matrix element values ($6P_J \rightarrow 7S$), theoretical values ($7S \rightarrow nP_J$, for $n > 7$) and precise calculations of the ratio

$$R_{7S7P} = \frac{\langle 7S_{1/2} || r || 7P_{3/2} \rangle}{\langle 7S_{1/2} || r || 7P_{1/2} \rangle} \quad (8.4)$$

where $R_{7S7P} = 1.3892(3)$ to derive

$$\langle 7S_{1/2} || r || 7P_{1/2} \rangle = 10.308(15) \text{ a}_0$$

¹For the full conversion, see Appendix B.

and

$$\langle 7S_{1/2} || r || 7P_{3/2} \rangle = 14.320(20) a_0,$$

with uncertainties of 0.15% and 0.14%, respectively. Here, the 0.5% uncertainty in the values of the $\langle 7S_{1/2} || r || 6P_{3/2} \rangle$ and $\langle 7S_{1/2} || r || 6P_{1/2} \rangle$ matrix elements contributed significantly to the uncertainties of the derived matrix elements.

The results reported in [63] were the most precise determinations of $\langle 7S_{1/2} || r || 7P_{3/2} \rangle$ and $\langle 7S_{1/2} || r || 7P_{1/2} \rangle$ until more recently, when Table I of reference [64] listed the following values for these two reduced dipole matrix elements: $\langle 7S_{1/2} || r || 7P_{1/2} \rangle = 10.31(4) a_0$, and $\langle 7S_{1/2} || r || 7P_{3/2} \rangle = 14.32(6) a_0$. The matrix element values are the same, but these uncertainties are three times as large as the ones reported in 1999 [63].

As discussed in the earlier chapter, we have new measurements of $\langle 7S_{1/2} || r || 6P_{1/2} \rangle$ and $\langle 7S_{1/2} || r || 6P_{3/2} \rangle$, which were one of the major contributors to the uncertainty in $\langle 7S_{1/2} || r || 7P_{1/2} \rangle$ and $\langle 7S_{1/2} || r || 7P_{3/2} \rangle$. Using Equation 8.3 and the Stark shift measurement by [96], we can derive new values for the $7S - 7P_J$ matrix elements.

The Stark shift measurement by [96] reported the $\alpha_{7S-6S} = 5836.9(64) a_0^3$, so we need to add to it the scalar Stark polarizability of the cesium $6S_{1/2}$ ground state α_{6S} . To determine α_{6S} , we take the average of $\alpha_{6S} = 401.0(6) a_0^3$ from reference [105] and $\alpha_{6S} = 401.2(7) a_0^3$ from reference [68] to obtain the weighted average $\alpha_{6S} = 401.1(5) a_0^3$. The sum of these two Stark polarizabilities is

$$\alpha_{7S} = 6238.0(64) a_0^3.$$

We show in Table 8.1 the value of α_{7S} and the contributions from the $\langle 7S_{1/2} || r || nP_J \rangle$ matrix elements for $n = 6, 8 - 12$, as calculated using (Equation 8.3). For the tail contributions ($n > 12$), we extrapolate the contributions from $n = 10 - 12$ to get $0.3(1) a_0^3$ from $nP_{3/2}$ and $0.04 a_0^3$ from $nP_{1/2}$. We deduct these contributions from α_{7S} to extract the combined contributions due to the $\langle 7S_{1/2} || r || 7P_{1/2} \rangle$ and $\langle 7S_{1/2} || r || 7P_{3/2} \rangle$ matrix elements. Using the theoretically calculated value of $R_{7S7P} = 1.3892(3)$ and Equation 8.3, we now have

$$\frac{1}{3} |\langle 7S_{1/2} || r || 7P_{1/2} \rangle|^2 \left[\frac{1}{E_{nP_{1/2}} - E_{7S}} + \frac{R_{7S7P}^2}{E_{nP_{3/2}} - E_{7S}} \right] = 6828.3(66) a_0^3 \quad (8.5)$$

Table 8.1

We show in this table the calculated contributions to α_{7S} from the $\langle 7S_{1/2}||r||nP_J\rangle$ matrix elements for $n = 6, 8 - 12$ using Equation (8.3). We deduct from α_{7S} the other contributions listed, to calculate the contributions from the $\langle 7S_{1/2}||r||7P_J\rangle$ matrix elements.

Contributing Term	$d(a_0^3)$	$\delta d(\%)$	$E_{nP_J}(\text{cm}^{-1})$	Polarizability (a_0^3)
α_{7S}				6238.0(64)
				-
$\langle 7S_{1/2} r 6P_{1/2}\rangle$	-4.249	0.094	11178.27	-179.52(34)
$\langle 7S_{1/2} r 8P_{1/2}\rangle$	0.914	2.9	25708.84	8.52(50)
$\langle 7S_{1/2} r 9P_{1/2}\rangle$	0.349	2.9	27637.00	0.98(6)
$\langle 7S_{1/2} r 10P_{1/2}\rangle$	0.191	3.1	28726.81	0.26
$\langle 7S_{1/2} r 11P_{1/2}\rangle$	0.125	3.5	29403.42	0.11
$\langle 7S_{1/2} r 12P_{1/2}\rangle$	0.090	3.9	29852.68	0.05
$\langle 7S_{1/2} r 6P_{3/2}\rangle$	-6.489	0.077	11732.31	-452.8(7)
$\langle 7S_{1/2} r 8P_{3/2}\rangle$	1.620	2.2	25791.51	26.46(115)
$\langle 7S_{1/2} r 9P_{3/2}\rangle$	0.680	2.1	27681.68	3.70(15)
$\langle 7S_{1/2} r 10P_{3/2}\rangle$	0.396	2.2	28753.68	1.12
$\langle 7S_{1/2} r 11P_{3/2}\rangle$	0.270	2.4	29420.82	0.49
$\langle 7S_{1/2} r 12P_{3/2}\rangle$	0.201	3.7	29864.54	0.26
Tail ($n > 12$)				0.34(10)
$\langle 7S_{1/2} r 7P_{1/2}\rangle$				=
$+\langle 7S_{1/2} r 7P_{3/2}\rangle$				6828.3 (66)

where we derive

$$\langle 7S_{1/2} || r || 7P_{1/2} \rangle = 10.325(5) a_0$$

and

$$\langle 7S_{1/2} || r || 7P_{3/2} \rangle = 14.344(7) a_0.$$

These newly calculated reduced dipole matrix elements have an uncertainty of $\sim 0.05\%$, a $3\times$ improvement over the previous uncertainties of 0.15% . With these new values for the $\langle 7S_{1/2} || r || 7P_J \rangle$ matrix elements, all the most important matrix elements for calculation of the cesium $6S_{1/2} \rightarrow 7S_{1/2}$ scalar transition polarizability have uncertainties of $< 0.2\%$. We review the values and uncertainties of all eight reduced dipole matrix elements in the next section.

8.3 Review of E1 matrix elements

In this section, we review the 8 key $mS - nP_J$ matrix elements for $6 \leq m, n \leq 7$ and $J = 1/2, 3/2$ as discussed earlier in Section 2.4. Figure 8.1 shows a simplified energy level diagram listing the uncertainties of these matrix elements. We show in Table 8.2 a list of our recommended matrix element values, and their most precise previous values.

6S – 6P_J There have been many precise measurements of the $6S - 6P_J$ reduced dipole matrix elements. A variety of experimental techniques have been used, including time-resolved fluorescence [103, 108, 120, 122], absorption [66], polarizability measurements [105], atom interferometry [68], and photoassociation spectroscopy [67, 104, 106]. There is good agreement between these multiple independent measurements, and we have tabulated the results from these 10 measurements in Table 7.2. Our recommended values for these matrix elements are the weighted average: $\langle 6S_{1/2} || r || 6P_{1/2} \rangle = 4.5057(16) a_0$ and $\langle 6S_{1/2} || r || 6P_{3/2} \rangle = 6.3398(22) a_0$, precisions of $\sim 0.036\%$.

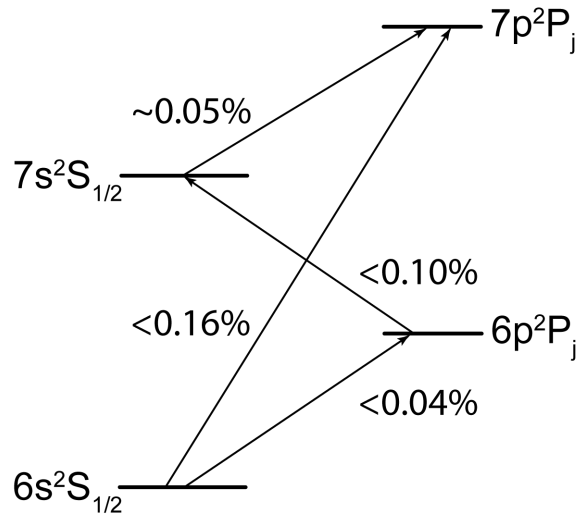


Fig. 8.1. Figure summarizing the uncertainties in the reduced dipole matrix elements between the lowest four cesium states. With our recent efforts measuring the $6S_{1/2} \rightarrow 6P_J$ and $6P_J \rightarrow 7S_{1/2}$ matrix elements, all uncertainties have been reduced under 0.2%. Combined, these matrix elements comprise 98.5% of the sum over states contributions to α .

$7S - 6P_J$ I have covered in great detail our measurements of the $7S - 6P_J$ reduced matrix elements in Chapters 6 and 7. The final result from those measurements was $\langle 7S_{1/2} || r || 6P_{1/2} \rangle = -4.249(4) a_0$ and $\langle 7S_{1/2} || r || 6P_{3/2} \rangle = -6.489(5) a_0$, precisions of $< 0.1\%$.

$6S - 7P_J$ We described our group's new measurements of the $6S - 7P_J$ reduced matrix elements in Section 8.1. The results were $\langle 6S_{1/2} || r || 7P_{1/2} \rangle = 0.27810(45) a_0$ and $\langle 6S_{1/2} || r || 7P_{3/2} \rangle = 0.57417(57) a_0$. These matrix elements now have precision better than 0.16%.

$7S - 7P_J$ In Section 8.2, we used the Stark shift measurement of Ref. [96] and our new $7S - 6P_J$ matrix elements to determine new values for the $7S - 7P_J$ matrix elements. Since the $7S - 6P_J$ matrix elements were the largest contribution to the error, the uncertainty has been improved from 0.15% to $\sim 0.05\%$. Our recommended values

Table 8.2

This table lists the newest values of matrix elements for the lowest cesium transitions and their present uncertainties. See text for more information. ^aWeighted mean of multiple measurements, see Table 7.3. ^bMost recent theory determination from [64]. ^cRef. [123]. ^dRef. [63].

Matrix Element	Old Value (a_0)	Recommended (a_0)	Error (%)
$\langle 6S_{1/2} r 6P_{1/2} \rangle$	-	4.5057(16) ^a	0.036
$\langle 6S_{1/2} r 6P_{3/2} \rangle$	-	6.3398(22) ^a	0.035
$\langle 7S_{1/2} r 6P_{1/2} \rangle$	4.243 ^b	-4.249(4)	0.094
$\langle 7S_{1/2} r 6P_{3/2} \rangle$	6.480 ^b	-6.489(5)	0.077
$\langle 6S_{1/2} r 7P_{1/2} \rangle$	0.2790(16) ^c	0.27810(45)	0.16
$\langle 6S_{1/2} r 7P_{3/2} \rangle$	0.5780(7) ^c	0.57417(57)	0.10
$\langle 7S_{1/2} r 7P_{1/2} \rangle$	10.308(15) ^d	10.325(5)	0.05
$\langle 7S_{1/2} r 7P_{3/2} \rangle$	14.320(20) ^d	14.344(7)	0.05

for the matrix elements are $\langle 7S_{1/2} || r || 7P_{1/2} \rangle = 10.325(5) a_0$ and $\langle 7S_{1/2} || r || 7P_{3/2} \rangle = 14.344(7) a_0$.

8.4 Determination of α and β by sum over states

With all the details included previously, we are now ready to calculate a new value for the scalar (α) and vector (β) transition polarizabilities of the cesium $6S_{1/2} \rightarrow 7S_{1/2}$ transition.

We reviewed earlier in Section 2.4 the theory behind α and β . They are important because E_{PNC} was measured by the Wieman group as ratio of β , and our technique will measure it relative to α . Hence, precise determinations of α and β are necessary to extract a precise value of the weak charge Q_{weak} .

The scalar transition polarizability α can be calculated with the following equation, reproduced from Section 2.4, Equation (2.16)

$$\alpha = -\frac{1}{6} \sum_n \left[\langle 7S_{1/2} || r || nP_{1/2} \rangle \langle nP_{1/2} || r || 6S_{1/2} \rangle \left(\frac{1}{E_{nP_{1/2}} - E_{7S}} + \frac{1}{E_{nP_{1/2}} - E_{6S}} \right) - \langle 7S_{1/2} || r || nP_{3/2} \rangle \langle nP_{3/2} || r || 6S_{1/2} \rangle \left(\frac{1}{E_{nP_{3/2}} - E_{7S}} + \frac{1}{E_{nP_{3/2}} - E_{6S}} \right) \right]. \quad (8.6)$$

Similarly, we can also calculate β using Equation (2.18), reproduced here

$$\beta = -\frac{1}{6} \sum_n \left[\langle 7S_{1/2} || r || nP_{1/2} \rangle \langle nP_{1/2} || r || 6S_{1/2} \rangle \left(\frac{1}{E_{nP_{1/2}} - E_{7S}} - \frac{1}{E_{nP_{1/2}} - E_{6S}} \right) + \frac{1}{2} \langle 7S_{1/2} || r || nP_{3/2} \rangle \langle nP_{3/2} || r || 6S_{1/2} \rangle \left(\frac{1}{E_{nP_{3/2}} - E_{7S}} - \frac{1}{E_{nP_{3/2}} - E_{6S}} \right) \right]. \quad (8.7)$$

For calculating α , once we take into account the signs of the matrix elements as listed in Tables 8.2 and 7.2, all the contributing terms have the same sign. The major contributing terms to Equations (8.6) and (8.7) are the eight matrix elements $6S - 6P_{1/2}$, $6S - 6P_{3/2}$, $6S - 7P_{1/2}$, $6S - 7P_{3/2}$, $7S - 6P_{1/2}$, $7S - 6P_{3/2}$, $7S - 7P_{1/2}$ and $7S - 7P_{3/2}$. These eight reduced matrix elements contribute 98.5% of the sum towards α . For β , due to the change in signs in Equation (8.7), there is a huge amount of cancellation. This means that a precise calculation of β is much more difficult.

We show in Table 8.3 a breakdown of our calculations for α . In columns 2 and 5, we list the values of reduced dipole matrix elements used for $\langle 7S_{1/2} || r || nP_J \rangle$ and $\langle nP_J || r || 6S_{1/2} \rangle$ respectively. We list the principal quantum number n of the nP_J state in the first column. In the upper half, $J = 1/2$, while $J = 3/2$ in the lower half of the table. Columns 3 and 6, labelled $\delta d(\%)$, list the fractional error of the listed matrix elements. In column 8, labelled $E_{nP_{1/2}}$, we list the energy levels of the various nP_J states used for the calculation.

Following Equation 8.6, we list in column 9 the contribution to α for each n term where $6 \leq n \leq 12$. The error for each contribution to α is listed in column 10, and is calculated by adding the errors listed in columns 4 and 7 in quadrature. Finally there are two other terms contributing to α , $\alpha_{n>12}$ and α_{vc} . $\alpha_{n>12}$ denotes

the contributions from the higher nP_J states for $n > 12$. To determine $\alpha_{n>12}$, Prof. Walter Johnson calculated the contributions from Hartree-Fock (HF) bound state wavefunctions for bound ($n > 12$) and continuum using a B-spline basis set. He obtained a value of $-0.45 a_0^3$. Noting that the HF values for contributions to α for $n = 6 - 12$ are $\sim 30\%$ too high, he scaled the value to obtain $\alpha_{n>12} = -0.30(15) a_0^3$. α_{vc} is a contribution due to excitations from the nucleus core to the valence shell, we determine $\alpha_{vc} = +0.2(0.1) a_0^3$, in agreement with [63, 124].

Finally, by summing the terms in column 9 of Table 8.3, we list in the last row the value of our new determination of

$$\alpha = -268.82(30) a_0^3. \quad (8.8)$$

The uncertainty of α is calculated by adding all the errors in column 10 in quadrature, for a precision of 0.11%. The most recent calculation of α in 2002 by [72] using the same sum over states technique determines the value $\alpha = -268.9(11) a_0^3$, with uncertainties four times as large as our determination. From Table 8.3, we notice in column 10 that the largest contribution to the uncertainty in α is due to the $7S - 8P_{3/2}$ and $8P_{3/2} - 6S$ term. Specifically, the $8P_{3/2} - 6S$ reduced matrix element with a theoretical uncertainty of 6%. A future measurement to improve the uncertainty of the $8P_{3/2} - 6S$ matrix element would improve the precision of α .

Using our value of α , we can calculate a new value of β . We combine our result of $\alpha = -268.82(30) a_0^3$ with the same high precision determination of $\alpha/\beta = 9.905(11)$ by [77] to obtain

$$\beta = 27.139(42) a_0^3, \quad (8.9)$$

where the uncertainty of 0.15% was found by adding the fractional uncertainties of α and α/β in quadrature. We show in Table 8.4 our current results and past determinations of α and β . Compared with the determination of $\beta = 26.957(51) a_0^3$ through M_{hf}/β by [73, 76], our determination of β is of higher precision but the two values do not agree. The difference of $0.182 a_0^3$ (0.67%) is larger than the sum of uncertainties $0.093 a_0^3$ (0.34%).

Table 8.3
 E1 dipole moments, eigenstate energies, and contributions to the scalar polarizability α . See text for a full description. $n = 6, 7$ matrix elements as discussed earlier, theory values from Ref. [64].

n	$d(ea_0)$	$\delta d(\%)$	$\delta\alpha(a_0^3)$	$d(ea_0)$	$\delta d(\%)$	$\delta\alpha(a_0^3)$	$E_{np_{1/2}}$ (cm $^{-1}$)	$\alpha(a_0^3)$	$\delta\alpha(a_0^3)$	$\beta(a_0^3)$	$\delta\beta(a_0^3)$
	$\langle 7S_{1/2} r np_{1/2} \rangle$			$\langle np_{1/2} r 6S_{1/2} \rangle$							
6	-4.249	0.094	0.031	4.5057	0.035	0.011	11178.27	-32.54	0.03	-157.83	0.16
7	10.325	0.05	0.019	0.2781	0.16	0.060	21765.35	-37.35	0.06	-27.70	0.05
8	0.914	2.9	0.016	0.092	11	0.061	25708.84	-0.55	0.06	-0.309	0.04
9	0.349	2.9	0.002	0.043	16	0.013	27637.00	-0.08	0.01	-0.04	0.01
10	0.191	3.1	0.001	0.025	20	0.005	28726.81	-0.02	0.00	-0.011	0.00
11	0.125	3.5	0.000	0.016	27	0.002	29403.42	-0.01	0.00	-0.004	0.00
12	0.09	3.9	0.000	0.012	28	0.001	29852.68	-0.00	0.00	-0.002	0.00
	$\langle 7S_{1/2} r np_{3/2} \rangle$			$\langle np_{3/2} r 6S_{1/2} \rangle$							
6	-6.489	0.077	0.072	-6.3398	0.035	0.033	11732.31	-92.93	0.08	174.73	0.15
7	14.344	0.05	0.051	-0.5742	0.1	0.101	21946.39	-102.05	0.12	37.30	0.04
8	1.62	2.2	0.053	-0.232	6.2	0.151	25791.51	-2.43	0.16	0.68	0.04
9	0.68	2.1	0.010	-0.130	7.4	0.035	27681.68	-0.47	0.04	0.12	0.01
10	0.396	2.2	0.004	-0.086	8.3	0.014	28753.68	-0.17	0.01	0.04	0.00
11	0.270	2.4	0.002	-0.063	8.9	0.007	29420.82	-0.08	0.01	0.02	0.00
12	0.201	3.7	0.002	-0.049	9.5	0.004	29864.54	-0.04	0.00	0.01	0.00
							$\alpha_{n>12} =$	-0.30	0.15	0.01	0.01
							$\alpha_{vc} =$	<u>+0.20</u>	0.10		
							$\alpha =$	-268.82	0.30	27.01	0.23

Table 8.4

This table lists several determinations of α and β since 1992. We have listed our direct calculations of both α and β through sum over states, but the sum for beta has large uncertainty due to cancellation of terms. The determinations labeled "Sum over states (α)" combine a calculation of α and the high precision measurement of α/β by [77] to determine β . β with the best precision (before this work) combines the measurement in 1999 by [73] of M_{hf}/β and the calculation in 2000 of M_{hf} [76]. I have bolded the two highest precision determinations of β in the Table.

Year	Reference	Remarks	$ \alpha (a_0^3)$	$ \beta (a_0^3)$
2019	This work	Sum over states (α)	268.82 (30)	27.139 (42)
2019	This work	Sum over states (β)		27.01 (23)
2002	Dzuba [72]	Sum over states (α)		27.15 (11)
2002	Vasilyev [124]	Sum over states (α)	269.7 (11)	27.22 (11)
2000	Dzuba [76]	M_{hf} calculation		26.957 (51)
1999	Bennett [73]	M_{hf}/β		27.024 (80)
1999	Safronova [63]	Sum over states (α)	268.6 (22)	27.11 (22)
1999	Safronova [63]	Sum over states (β)		27.16
1997	Dzuba [70]	Sum over states (α)	269.0 (13)	27.15 (13)
1992	Blundell [21]	Sum over states (α)	268 (3)	27.00

In Table 8.4, we have also listed β when calculated through sum over states (Equation (8.7)), which has the value

$$\beta_{\Sigma} = 27.01(23) a_0^3, \quad (8.10)$$

an uncertainty of 0.85%. The much larger uncertainty compared to Equation 8.9 is due to the difference in signs of the various contributing terms in Equation 8.7. The different signs lead to cancellations when adding them up, while the uncertainties add in quadrature. Because of the large uncertainty, this method of obtaining β is not very useful, except to serve as a check on our calculations.

Comparing our results with the past nearly 30 years of determinations of β , we find fairly good agreement between our results and other determinations of β through sum over states of α . 98.5% of the contributions to α come from matrix elements discussed earlier, where we have either directly or indirectly determined more precise values for. It is thus slightly surprising that our determination of α still agrees so well with earlier sum over states determinations of α . The previously highest precision determinations by [73,76] are fairly low when compared to all other values. This might suggest that there are additional corrections to α and β that need to be included or considered for one or both methods.

In the following section, we use our new determination of the vector transition polarizability β to calculate new values of Q_w , the weak charge of the Cs nucleus.

8.5 A new determination of Q_w

With a new determination of α and β , we are now ready to discuss atomic parity violation. In a future two-color two-photon measurement, we will be measuring E_{PNC}/α , and that is where our new determination of α will come in useful. In the mean time, we use β and past measurements of E_{PNC}/β to find a new value of Q_w , the weak charge of the cesium nucleus.

The best experimental measurement of E_{PNC} by the Wieman group [28, 29] is a 0.35% measurement of

$$\frac{\text{Im}E_{PNC}}{\beta} = 1.5935(56) \text{ mV/cm}.$$

We note that there is a more recent determination of $\text{Im}E_{PNC}/\beta = 1.538(40) \text{ mV/cm}$ by [125] which we have chosen not to include because of the large uncertainties.

For convenience, we defined earlier on in Section 1.3, Equation (1.2)

$$E_{PNC} = k_{PNC} \cdot Q_w.$$

Here, k_{PNC} refers to the proportionality factor determined from atomic theory calculations. To determine Q_w , we combine the experimental measurement E_{PNC}/β

from [28] with our new determination of $\beta = 27.139(42) a_0^3$ and many-body calculations done by Porsev et. al. [13,14] which find $k_{PNC} = 0.8906(24) \times 10^{-11} i|e|a_0/N$ to determine a new value of Q_w . The calculated value is

$$Q_w = 73.66(28)_e(20)_t, \quad (8.11)$$

which disagrees slightly with the Standard Model (SM) prediction of

$$Q_{SM}^{2018} = 73.21(1) \quad (8.12)$$

from *The 2018 Review of Particle Physics* [126].

However, atomic theory is not settled on the value of k_{PNC} . In 2012, Dzuba et. al. [15, 127] published a paper pointing out some errors with the analysis done by [13,14]. In summary, they keep the main calculations from [13,14], but re-calculate the tail and correction terms to determine $k_{PNC} = 0.8977(40) \times 10^{-11} i|e|a_0/N$. This brings the value of k_{PNC} back into good agreement with their earlier 2002 result of $k_{PNC} = 0.898(4) \times 10^{-11} i|e|a_0/N$ [72, 128]. Combined with our recommended value of $\beta = 27.139(42) a_0^3$ would result in

$$Q_w = 73.07(28)_e(33)_t. \quad (8.13)$$

This determination of Q_w has larger uncertainty, but agrees well with the SM prediction within $1\text{-}\sigma$. We show our two determinations of Q_w and various determinations over the past 30 years in Table 8.5.

The disagreement between our two calculated values of Q_w , with Q_{SM}^{2018} somewhere in between the two, suggests the need for new atomic theory calculations in cesium. We have had private communications with Andrei Derevianko, who informed us of his intention to make a re-newed effort to calculate k_{PNC} . This will be necessary before any new cesium E_{PNC} measurements are meaningful.

Table 8.5

This table lists the various determinations of Q_w for cesium since 1992. I have listed our determinations using both theory values of k_{PNC} . Where publications list multiple values, I have included the ‘recommended’ values. Some papers report separate experimental and theoretical uncertainties, I have added them in quadrature.

Year	Reference	New value	$ k_{PNC} $ ($\times 10^{-11}i e a_0/N$)	$ Q_w $
2019	This work	β	0.8906 (24)	73.59 (34)
2019	This work	β	0.8977 (40)	73.01 (43)
2018	2018 Q_{SM}			73.21
2012	Roberts [15,127]	k_{PNC}	0.8977 (40)	72.58 (43)
2009	Porsev [13,14]	k_{PNC}	0.8906 (24)	73.16 (35)
2005	Flambaum [128]	k_{PNC}	0.898 (4)	72.66 (46)
2002	Dzuba [72]	β, k_{PNC}	0.904 (5)	72.59 (53)
2002	Vasilyev [124]	β	0.9057 (37)	72.65 (49)
2001	Johnson [129]	k_{PNC}	0.9057 (37)	72.12 (44)
2001	Kozlov [130]	k_{PNC}	0.901	72.5 (7)
2001	Dzuba [131]	k_{PNC}	0.902	72.42 (79)
2000	Derevianko [75]	k_{PNC}	0.8991 (36)	72.65 (44)
2000	Dzuba [76]	M_{hf} calc	0.9065 (36)	71.88 (40)
1999	Bennett [73]	M_{hf}/β	0.9065 (36)	72.06 (44)
1997	Dzuba [70]	β	0.9065 (10)	72.41 (84)
1997	Wood [28]	E_{PNC}/β		72.11 (93)
1992	Blundell [21]	β, k_{PNC}	0.905 (9)	71.04 (181)

9. CONCLUSION

This dissertation is a compilation of my contributions towards a better atomic parity violation (APV) measurement in cesium. Yet, there is still much that needs to be done. In this concluding chapter I summarize my contributions, and list some of the many things that still have to be done for a new parity non-conservation (PNC) measurement in Cs to be completed.

My contributions can be broadly split into three categories: (a) Improvements to the PNC experimental setup towards a new two-photon two-color measurement of E_{PNC}/α ; (b) More precise determinations of reduced dipole matrix elements in Cs; (c) New calculations of the transition polarizabilities α and β which are necessary for PNC measurements.

9.1 Contributions towards atomic parity violation

I assembled a test power build-up cavity using old mirrors from Carl Wieman's group at Colorado, and learned what is needed to couple light into an optical cavity. To lock the 1079 nm laser to the PBC, I designed and tested a customizable locking circuit design that will allow us to achieve high servo loop bandwidth. Using one of these locking boxes, I have been successful in locking the 1079 nm laser to a stable invar cavity using the Pound-Drever-Hall locking technique.

We determined new values for some of the most critical cesium reduced dipole matrix elements through a combination of experimental measurements and calculations. We performed a lifetime measurement of the $7S_{1/2}$ state, and subsequently measured its branching ratio, in order to determine the $7S - 6P_J$ matrix elements to $< 0.1\%$ uncertainty. Using these matrix elements and a Stark shift measurement of the $7S$ state, we were able to calculate new values for the $7S - 7P_J$ matrix elements,

with uncertainty $\sim 0.05\%$. I helped Amy with a new measurement of the $6S - 7P_J$ matrix elements, measuring them to a precision of better than 0.15% . Finally, we reviewed the literature for $6S - 6P_J$ measurements, and calculate new values for them using a weighted average of 10 different high precision measurements conducted from 1992 – 2005. These matrix elements have an uncertainty of $\sim 0.035\%$.

With our precise determinations of matrix elements, we calculated new precise values for α and β the scalar and vector transition polarizabilities. These parameters have a direct impact on cesium APV determinations of the weak charge and the weak mixing angle. We use our value of β and Wieman's measurement of E_{PNC}/β to determine new values of the weak charge in cesium Q_w .

9.2 Future work

The PNC amplitude is about $20,000\times$ smaller than the M1 transition amplitude. To amplify the signal, a high finesse optical cavity will need to be constructed and placed within the vacuum chamber to increase the intensity of the 540 nm laser. The mirrors will also be highly reflective at 1079 nm because we want counter-propagating beams to setup a standing wave pattern within the cavity. The custom-coated mirrors for the PBC have already been fabricated for this two-color cavity. A multi-stage lock will need to be implemented to keep the laser locked to this power build-up cavity, and to the peak of the $6S \rightarrow 7S$ transition resonance. In addition, coupling both laser beams into the high finesse cavity at once will be a challenge.

Electric field plates will need to be fabricated to apply an extremely weak (mV/cm) electric field. The field plates will be mounted on the same structure as the PBC, and will need to be precisely positioned. New instrumentation to source and measure a mV scale voltage will be needed. Stray electric fields result in systematic measurement error so it will be necessary to develop procedures to measure and eliminate these stray fields.

LIST OF REFERENCES

LIST OF REFERENCES

- [1] T. D. Lee and C. N. Yang, “Question of Parity Conservation in Weak Interactions,” *Physical Review*, vol. 104, pp. 254–258, Oct. 1956.
- [2] C. S. Wu, E. Ambler, R. W. Hayward, D. D. Hoppes, and R. P. Hudson, “Experimental Test of Parity Conservation in Beta Decay,” *Physical Review*, vol. 105, pp. 1413–1415, Feb. 1957.
- [3] W. C. Haxton and C. E. Wieman, “Atomic Parity Nonconservation and Nuclear Anapole Moments,” *Annual Review of Nuclear and Particle Science*, vol. 51, no. 1, pp. 261–293, 2001.
- [4] J. Ginges and V. V. Flambaum, “Violations of fundamental symmetries in atoms and tests of unification theories of elementary particles,” *Physics Reports*, vol. 397, no. 2, pp. 63–154, 2004.
- [5] B. Roberts, V. Dzuba, and V. Flambaum, “Parity and time-reversal violation in atomic systems,” *Annual Review of Nuclear and Particle Science*, vol. 65, pp. 63–86, 2015.
- [6] M. S. Safronova, D. Budker, D. DeMille, D. F. J. Kimball, A. Derevianko, and C. W. Clark, “Search for new physics with atoms and molecules,” *Rev. Mod. Phys.*, vol. 90, p. 025008, Jun 2018.
- [7] C. Chen, Y.-Y. Yin, and D. S. Elliott, “Interference between optical transitions,” *Physical Review Letters*, vol. 64, pp. 507–510, Jan. 1990.
- [8] C. Chen and D. S. Elliott, “Measurements of optical phase variations using interfering multiphoton ionization processes,” *Physical Review Letters*, vol. 65, pp. 1737–1740, Oct. 1990.
- [9] Y.-Y. Yin, C. Chen, D. S. Elliott, and A. V. Smith, “Asymmetric photoelectron angular distributions from interfering photoionization processes,” *Physical Review Letters*, vol. 69, pp. 2353–2356, Oct. 1992.
- [10] M. Gunawardena and D. S. Elliott, “Atomic Homodyne Detection of Weak Atomic Transitions,” *Physical Review Letters*, vol. 98, p. 043001, Jan. 2007.
- [11] M. Gunawardena and D. S. Elliott, “Weak signal detection using coherent control,” *Physical Review A*, vol. 76, p. 033412, Sept. 2007.
- [12] J. Erler and P. Langacker, “Indications for an Extra Neutral Gauge Boson in Electroweak Precision Data,” *Physical Review Letters*, vol. 84, pp. 212–215, Jan. 2000.

- [13] S. G. Porsev, K. Beloy, and A. Derevianko, “Precision determination of electroweak coupling from atomic parity violation and implications for particle physics,” *Phys. Rev. Lett.*, vol. 102, p. 181601, May 2009.
- [14] S. G. Porsev, K. Beloy, and A. Derevianko, “Precision determination of weak charge of ^{133}Cs from atomic parity violation,” *Phys. Rev. D*, vol. 82, p. 036008, Aug 2010.
- [15] V. A. Dzuba, J. C. Berengut, V. V. Flambaum, and B. Roberts, “Revisiting parity nonconservation in cesium,” *Phys. Rev. Lett.*, vol. 109, p. 203003, Nov 2012.
- [16] R. Diener, S. Godfrey, and I. Turan, “Constraining extra neutral gauge bosons with atomic parity violation measurements,” *Physical Review D*, vol. 86, p. 115017, Dec. 2012.
- [17] C. Boehm and P. Fayet, “Scalar Dark Matter candidates,” *Nuclear Physics B*, vol. 683, pp. 219–263, 2004. 56 pages, with a new section on theories with an extra $U(1)$ gauge symmetry.
- [18] C. Bouchiat and P. Fayet, “Constraints on the parity-violating couplings of a new gauge boson,” *Physics Letters B*, vol. 608, pp. 87–94, Feb. 2005.
- [19] H. Davoudiasl, H.-S. Lee, and W. J. Marciano, “Muon Anomaly and Dark Parity Violation,” *Physical Review Letters*, vol. 109, p. 031802, July 2012.
- [20] H. Davoudiasl and I. M. Lewis, “Dark matter from hidden forces,” *Physical Review D*, vol. 89, p. 055026, Mar. 2014.
- [21] S. A. Blundell, J. Sapirstein, and W. R. Johnson, “High-accuracy calculation of parity nonconservation in cesium and implications for particle physics,” *Phys. Rev. D*, vol. 45, pp. 1602–1623, Mar 1992.
- [22] H. Davoudiasl, H.-S. Lee, and W. J. Marciano, “Dark Z implications for parity violation, rare meson decays, and Higgs physics,” *Physical Review D*, vol. 85, p. 115019, June 2012.
- [23] M. A. Bouchiat and C. Bouchiat, “I. Parity violation induced by weak neutral currents in atomic physics,” *Journal de Physique*, vol. 35, pp. 899–927, Dec. 1974.
- [24] M. A. Bouchiat and C. Bouchiat, “Parity violation induced by weak neutral currents in atomic physics. part II,” *Journal de Physique*, vol. 36, no. 6, pp. 493–509, 1975.
- [25] S. L. Gilbert, M. C. Noecker, R. N. Watts, and C. E. Wieman, “Measurement of Parity Nonconservation in Atomic Cesium,” *Physical Review Letters*, vol. 55, no. 24, pp. 2680–2683, 1985.
- [26] S. L. Gilbert and C. E. Wieman, “Atomic-beam measurement of parity nonconservation in cesium,” *Physical Review A*, vol. 34, no. 2, pp. 792–803, 1986.
- [27] M. C. Noecker, B. P. Masterson, and C. E. Wieman, “Precision Measurement of Parity Nonconservation in Atomic Cesium: A Low-Energy Test of the Electroweak Theory,” *Physical Review Letters*, vol. 61, pp. 310–313, July 1988.

- [28] C. S. Wood, S. C. Bennett, D. Cho, B. P. Masterson, J. L. Roberts, C. E. Tanner, and C. E. Wieman, “Measurement of parity nonconservation and an anapole moment in cesium,” *Science*, vol. 275, no. 5307, pp. 1759–1763, 1997.
- [29] C. S. Wood, S. C. Bennett, J. L. Roberts, D. Cho, and C. E. Wieman, “Precision measurement of parity nonconservation in cesium,” *Canadian Journal of Physics*, vol. 77, pp. 7–75, May 1999.
- [30] M. J. D. Macpherson, K. P. Zetie, R. B. Warrington, D. N. Stacey, and J. P. Hoare, “Precise measurement of parity nonconserving optical rotation at 876 nm in atomic bismuth,” *Physical Review Letters*, vol. 67, pp. 2784–2787, Nov. 1991.
- [31] D. M. Meekhof, P. A. Vetter, P. K. Majumder, S. K. Lamoreaux, and E. N. Fortson, “Optical-rotation technique used for a high-precision measurement of parity nonconservation in atomic lead,” *Physical Review A*, vol. 52, pp. 1895–1908, Sept. 1995.
- [32] S. J. Phipp, N. H. Edwards, P. E. G. Baird, and S. Nakayama, “A measurement of parity non-conserving optical rotation in atomic lead,” *Journal of Physics B Atomic Molecular Physics*, vol. 29, pp. 1861–1869, May 1996.
- [33] P. S. Drell and E. D. Commins, “Parity nonconservation in atomic thallium,” *Physical Review A*, vol. 32, pp. 2196–2210, Oct. 1985.
- [34] N. H. Edwards, S. J. Phipp, P. E. G. Baird, and S. Nakayama, “Precise Measurement of Parity Nonconserving Optical Rotation in Atomic Thallium,” *Physical Review Letters*, vol. 74, pp. 2654–2657, Apr. 1995.
- [35] D. DeMille, “Parity Nonconservation in the $6s\ ^2S_0 \rightarrow 6s5d\ ^3D_1$ Transition in Atomic Ytterbium,” *Physical Review Letters*, vol. 74, pp. 4165–4168, May 1995.
- [36] D. F. Kimball, “Parity-nonconserving optical rotation on the $6s6p\ ^3P_0$ to $6s6p\ ^1P_1$ transition in atomic ytterbium,” *Physical Review A*, vol. 63, p. 052113, Apr. 2001.
- [37] K. Tsigutkin, D. Dounas-Frazer, A. Family, J. E. Stalnaker, V. V. Yashchuk, and D. Budker, “Observation of a Large Atomic Parity Violation Effect in Ytterbium,” *Physical Review Letters*, vol. 103, p. 071601, Aug. 2009.
- [38] K. Tsigutkin, D. Dounas-Frazer, A. Family, J. E. Stalnaker, V. V. Yashchuk, and D. Budker, “Parity violation in atomic ytterbium: Experimental sensitivity and systematics,” *Physical Review A*, vol. 81, p. 032114, Mar. 2010.
- [39] D. Antypas, A. Fabricant, L. Bougas, K. Tsigutkin, and D. Budker, “Towards improved measurements of parity violation in atomic ytterbium,” *Hyperfine Interactions*, vol. 238, p. 21, Nov. 2017.
- [40] D. Antypas, A. Fabricant, J. Stalnaker, K. Tsigutkin, V. Flambaum, and D. Budker, “Isotopic variation of parity violation in atomic ytterbium,” *Nature Physics*, vol. 15, no. 2, p. 120, 2019.
- [41] E. Gomez, S. Aubin, G. D. Sprouse, L. A. Orozco, and D. P. DeMille, “Measurement method for the nuclear anapole moment of laser-trapped alkali-metal atoms,” *Physical Review A*, vol. 75, p. 033418, Mar. 2007.

- [42] N. Leefler, L. Bougas, D. Antypas, and D. Budker, “Towards a new measurement of parity violation in dysprosium,” *arXiv:1412.1245 [physics]*, Dec. 2014. arXiv: 1412.1245.
- [43] T. W. Koerber, M. Schacht, W. Nagourney, and E. N. Fortson, “Radio frequency spectroscopy with a trapped Ba+ ion: recent progress and prospects for measuring parity violation,” *Journal of Physics B: Atomic, Molecular and Optical Physics*, vol. 36, no. 3, p. 637, 2003.
- [44] A. Kleczewski, M. R. Hoffman, J. A. Sherman, E. Magnuson, B. B. Blinov, and E. N. Fortson, “Coherent excitation of the $6s_{1/2}$ to $5d_{3/2}$ electric-quadrupole transition in $^{138}\text{Ba}^+$,” *Physical Review A*, vol. 85, p. 043418, Apr. 2012.
- [45] S. R. Williams, A. Jayakumar, M. R. Hoffman, B. B. Blinov, and E. N. Fortson, “Method for measuring the $6s_{1/2}$ to $5d_{3/2}$ magnetic-dipole-transition moment in Ba+,” *Physical Review A*, vol. 88, p. 012515, July 2013.
- [46] O. O. Versolato, L. W. Wansbeek, G. S. Giri, J. E. v. d. Berg, D. J. v. d. Hoek, K. Jungmann, W. L. Kruithof, C. J. G. Onderwater, B. K. Sahoo, B. Santra, P. D. Shidling, R. G. E. Timmermans, L. Willmann, and H. W. Wilschut, “Atomic parity violation in a single trapped radium ion,” *Hyperfine Interactions*, vol. 199, p. 9, July 2011.
- [47] M. N. Portela, E. A. Dijck, A. Mohanty, H. Bekker, J. E. v. d. Berg, G. S. Giri, S. Hoekstra, C. J. G. Onderwater, S. Schlessler, R. G. E. Timmermans, O. O. Versolato, L. Willmann, H. W. Wilschut, and K. Jungmann, “Ra+ ion trapping: toward an atomic parity violation measurement and an optical clock,” *Applied Physics B*, vol. 114, pp. 173–182, Jan. 2014.
- [48] S. Rahaman, J. Danielson, M. Schacht, M. Schauer, J. Zhang, and J. Torgerson, “MW-Optical Double Resonance in $^{171}\text{Yb}^+$ Trapped Single Ion and its Application for Precision Experiments,” *arXiv:1304.5732 [physics]*, Apr. 2013. arXiv: 1304.5732.
- [49] V. V. Flambaum and D. W. Murray, “Anapole moment and nucleon weak interactions,” *Physical Review C*, vol. 56, pp. 1641–1644, Sept. 1997.
- [50] W. R. Johnson, M. S. Safronova, and U. I. Safronova, “Combined effect of coherent Z exchange and the hyperfine interaction in the atomic parity-nonconserving interaction,” *Physical Review A*, vol. 67, p. 062106, June 2003.
- [51] M. S. Safronova, R. Pal, D. Jiang, M. G. Kozlov, W. R. Johnson, and U. I. Safronova, “New directions in atomic PNC,” *Nuclear Physics A*, vol. 827, pp. 411c–413c, Aug. 2009.
- [52] C. S. Wood, *High precision atomic parity non-conservation measurement using a spin polarized cesium beam and the nuclear anapole moment of Cs*. PhD thesis, University of Colorado, Jan. 1997.
- [53] D. Antypas, *Measure of a weak transition moment using coherent control*. PhD thesis, Purdue University, Dec. 2013.
- [54] D. Antypas and D. S. Elliott, “Measurement of a weak transition moment using two-pathway coherent control,” *Physical Review A*, vol. 87, p. 042505, Apr. 2013.

- [55] D. Antypas and D. S. Elliott, “Measurement of weak optical transition moments through two-pathway coherent control,” *Canadian Journal of Chemistry*, 2014.
- [56] G. Toh, J. A. Jaramillo-Villegas, N. Glotzbach, J. Quirk, I. C. Stevenson, J. Choi, A. M. Weiner, and D. S. Elliott, “Measurement of the lifetime of the $7s^2S_{1/2}$ state in atomic cesium using asynchronous gated detection,” *Phys. Rev. A*, vol. 97, p. 052507, May 2018.
- [57] G. Toh, A. Damitz, N. Glotzbach, J. Quirk, I. C. Stevenson, J. Choi, M. S. Safronova, and D. S. Elliott, “Electric dipole matrix elements for the $6p^2P_J \rightarrow 7s^2S_{1/2}$ transition in atomic cesium,” *Phys. Rev. A*, vol. 99, p. 032504, Mar 2019.
- [58] G. Toh, D. Antypas, and D. S. Elliott, “Measurement of the Stark shift of the $6s^2S_{1/2} \rightarrow 7p^2P_J$ transitions in atomic cesium,” *Phys. Rev. A*, vol. 89, p. 042512, Apr 2014.
- [59] M. A. Bouchiat, J. Guena, and L. Pottier, “Absolute polarization measurements and natural lifetime in the $7S_{1/2}$ state of Cs,” *Journal de Physique Lettres*, vol. 45, pp. 523–532, June 1984.
- [60] G. Yang, J. Wang, B. Yang, and J. Wang, “Determination of the hyperfine coupling constant of the cesium $7s_{1/2}$ state,” *Laser Physics Letters*, vol. 13, no. 8, p. 085702, 2016.
- [61] D. A. Steck, “Cesium D line data,” Dec. 2010.
- [62] E. Iskrenova-Tchoukova, M. S. Safronova, and U. I. Safronova, “High-precision study of cs polarizabilities,” *J. Comp. Methods in Sci. and Eng.*, vol. 7, pp. 521–540, Sept. 2007.
- [63] M. S. Safronova, W. R. Johnson, and A. Derevianko, “Relativistic many-body calculations of energy levels, hyperfine constants, electric-dipole matrix elements, and static polarizabilities for alkali-metal atoms,” *Phys. Rev. A*, vol. 60, pp. 4476–4487, Dec 1999.
- [64] M. S. Safronova, U. I. Safronova, and C. W. Clark, “Magic wavelengths, matrix elements, polarizabilities, and lifetimes of Cs,” *Phys. Rev. A*, vol. 94, p. 012505, Jul 2016.
- [65] C. E. Tanner, “Precision measurements of atomic lifetimes,” in *AIP Conference Proceedings*, vol. 323, pp. 130–145, AIP, 1994.
- [66] R. J. Rafac, C. E. Tanner, A. E. Livingston, and H. G. Berry, “Fast-beam laser lifetime measurements of the cesium $6p^2P_{1/2,3/2}$ states,” *Phys. Rev. A*, vol. 60, pp. 3648–3662, Nov 1999.
- [67] Y. Zhang, J. Ma, J. Wu, L. Wang, L. Xiao, and S. Jia, “Experimental observation of the lowest levels in the photoassociation spectroscopy of the 0_g^- purely-long-range state of Cs_2 ,” *Phys. Rev. A*, vol. 87, p. 030503, Mar 2013.
- [68] M. D. Gregoire, I. Hromada, W. F. Holmgren, R. Trubko, and A. D. Cronin, “Measurements of the ground-state polarizabilities of Cs, Rb, and K using atom interferometry,” *Phys. Rev. A*, vol. 92, p. 052513, Nov 2015.

- [69] V. Dzuba, V. Flambaum, and O. Sushkov, “Summation of the high orders of perturbation theory for the parity nonconserving E1-amplitude of the $6s \rightarrow 7s$ transition in the caesium atom,” *Physics Letters A*, vol. 141, no. 3, pp. 147 – 153, 1989.
- [70] V. A. Dzuba, V. V. Flambaum, and O. P. Sushkov, “Polarizabilities and parity nonconservation in the Cs atom and limits on the deviation from the standard electroweak model,” *Phys. Rev. A*, vol. 56, pp. R4357–R4360, Dec 1997.
- [71] V. A. Dzuba, V. V. Flambaum, and J. S. M. Ginges, “Calculations of parity-nonconserving $s-d$ amplitudes in Cs, Fr, Ba+, and Ra+,” *Phys. Rev. A*, vol. 63, p. 062101, May 2001.
- [72] V. A. Dzuba, V. V. Flambaum, and J. S. M. Ginges, “High-precision calculation of parity nonconservation in cesium and test of the standard model,” *Phys. Rev. D*, vol. 66, p. 076013, Oct 2002.
- [73] S. C. Bennett and C. E. Wieman, “Measurement of the $6s \rightarrow 7s$ Transition Polarizability in Atomic Cesium and an Improved Test of the Standard Model,” *Physical Review Letters*, vol. 82, pp. 2484–2487, Mar. 1999.
- [74] S. C. Bennett, *High-precision measurements in atomic cesium supporting a low-energy test of the standard model*. PhD thesis, University of Colorado, 1998.
- [75] A. Derevianko, “Reconciliation of the measurement of parity nonconservation in Cs with the standard model,” *Phys. Rev. Lett.*, vol. 85, pp. 1618–1621, Aug 2000.
- [76] V. A. Dzuba and V. V. Flambaum, “Off-diagonal hyperfine interaction and parity nonconservation in cesium,” *Phys. Rev. A*, vol. 62, p. 052101, Oct 2000.
- [77] D. Cho, C. S. Wood, S. C. Bennett, J. L. Roberts, and C. E. Wieman, “Precision measurement of the ratio of scalar to tensor transition polarizabilities for the cesium 6s-7s transition,” *Physical Review A*, vol. 55, pp. 1007–1011, Feb. 1997.
- [78] “External-cavity diode lasers,” *Encyclopedia of Laser Physics and Technology*.
- [79] D. W. Preston, “Doppler-free saturated absorption: Laser spectroscopy,” *American Journal of Physics*, vol. 64, pp. 1432–1436, Nov. 1996.
- [80] R. W. Fox, C. W. Oates, and L. W. Hollberg, “1. Stabilizing diode lasers to high-finesse cavities,” in *Experimental Methods in the Physical Sciences* (R. D. v. Z. a. J. P. Looney, ed.), vol. 40 of *Cavity-Enhanced Spectroscopies*, pp. 1–46, Academic Press, 2003.
- [81] T. Okoshi, K. Kikuchi, and A. Nakayama, “Novel method for high resolution measurement of laser output spectrum,” *Electronics Letters*, vol. 16, pp. 630–631, July 1980.
- [82] X. Baillard, A. Gauguet, S. Bize, P. Lemonde, P. Laurent, A. Clairon, and P. Rosenbusch, “Interference-filter-stabilized external-cavity diode lasers,” *Optics Communications*, vol. 266, no. 2, pp. 609 – 613, 2006.
- [83] V. Gerginov and C. E. Tanner, “Fluorescence of a highly collimated atomic cesium beam: theory and experiment,” *Optics Communications*, vol. 222, pp. 17–28, July 2003.

- [84] Y. N. Zhao, J. Zhang, J. Stuhler, G. Schuricht, F. Lison, Z. H. Lu, and L. J. Wang, “Sub-Hertz frequency stabilization of a commercial diode laser,” *Optics Communications*, vol. 283, pp. 4696–4700, Dec. 2010.
- [85] K. G. Libbrecht and J. L. Hall, “A low-noise high-speed diode laser current controller,” *Review of Scientific Instruments*, vol. 64, pp. 2133–2135, Aug. 1993.
- [86] C. M. Seck, P. J. Martin, E. C. Cook, B. C. Odom, and D. A. Steck, “Noise reduction of a Libbrecht-Hall style current driver,” *Review of Scientific Instruments*, vol. 87, p. 064703, June 2016.
- [87] C. J. Erickson, M. V. Zijil, G. Doermann, and D. S. Durfee, “An ultrahigh stability, low-noise laser current driver with digital control,” *Review of Scientific Instruments*, vol. 79, p. 073107, July 2008.
- [88] D. L. Troxel, C. J. Erickson, and D. S. Durfee, “Note: Updates to an ultra-low noise laser current driver,” *Review of Scientific Instruments*, vol. 82, p. 096101, Sept. 2011.
- [89] Texas Instruments, *Low-Noise, High-Precision, JFET-Input Operational Amplifier*, Jul. 2016. Rev. I.
- [90] R. V. Pound, “Electronic Frequency Stabilization of Microwave Oscillators,” *Review of Scientific Instruments*, vol. 17, pp. 490–505, Nov. 1946.
- [91] R. W. P. Drever, J. L. Hall, F. V. Kowalski, J. Hough, G. M. Ford, A. J. Munley, and H. Ward, “Laser phase and frequency stabilization using an optical resonator,” *Applied Physics B*, vol. 31, pp. 97–105, June 1983.
- [92] E. D. Black, “An introduction to Pound-Drever-Hall laser frequency stabilization,” *American Journal of Physics*, vol. 69, pp. 79–87, Dec. 2000.
- [93] C. Tresp, “A setup for highly precise excitation and detection of Rydberg atoms,” Master’s thesis, Universitat Stuttgart, Oct. 2012.
- [94] P. Eich, “Frequency and phase stabilization of diode lasers using a femtosecond frequency comb,” Master’s thesis, Universitat Des Saarlandes, July 2012.
- [95] M. Zhu and J. L. Hall, “Stabilization of optical phase/frequency of a laser system: application to a commercial dye laser with an external stabilizer,” *JOSA B*, vol. 10, pp. 802–816, May 1993.
- [96] S. C. Bennett, J. L. Roberts, and C. E. Wieman, “Measurement of the dc stark shift of the $6S \rightarrow 7S$ transition in atomic cesium,” *Phys. Rev. A*, vol. 59, pp. R16–R18, Jan 1999.
- [97] C. C. Speake, “Forces and force gradients due to patch fields and contact-potential differences,” *Classical and Quantum Gravity*, vol. 13, no. 11A, p. A291, 1996.
- [98] D. A. Hite, Y. Colombe, A. C. Wilson, K. R. Brown, U. Warring, R. Jrdens, J. D. Jost, K. S. McKay, D. P. Pappas, D. Leibfried, and D. J. Wineland, “100-Fold Reduction of Electric-Field Noise in an Ion Trap Cleaned with In Situ Argon-Ion-Beam Bombardment,” *Physical Review Letters*, vol. 109, p. 103001, Sept. 2012.

- [99] E. Gomez, F. Baumer, A. D. Lange, G. D. Sprouse, and L. A. Orozco, “Lifetime measurement of the $6s$ level of rubidium,” *Phys. Rev. A*, vol. 72, p. 012502, Jul 2005.
- [100] E. Gomez, L. A. Orozco, A. Perez Galvan, and G. D. Sprouse, “Lifetime measurement of the $8s$ level in francium,” *Phys. Rev. A*, vol. 71, p. 062504, Jun 2005.
- [101] B. Hoeling, J. R. Yeh, T. Takekoshi, and R. J. Knize, “Measurement of the lifetime of the atomic cesium $5^2D_{5/2}$ state with diode-laser excitation,” *Opt. Lett.*, vol. 21, pp. 74–76, Jan 1996.
- [102] D. Sheng, A. Pérez Galván, and L. A. Orozco, “Lifetime measurements of the $5d$ states of rubidium,” *Phys. Rev. A*, vol. 78, p. 062506, Dec 2008.
- [103] L. Young, W. T. Hill, S. J. Sibener, S. D. Price, C. E. Tanner, C. E. Wieman, and S. R. Leone, “Precision lifetime measurements of Cs $6p\ ^2P_{1/2}$ and $6p\ ^2P_{3/2}$ levels by single-photon counting,” *Phys. Rev. A*, vol. 50, pp. 2174–2181, Sep 1994.
- [104] A. Derevianko and S. G. Porsev, “Determination of lifetimes of $6P_J$ levels and ground-state polarizability of Cs from the van der Waals coefficient C_6 ,” *Phys. Rev. A*, vol. 65, p. 053403, Apr 2002.
- [105] J. M. Amini and H. Gould, “High precision measurement of the static dipole polarizability of cesium,” *Phys. Rev. Lett.*, vol. 91, p. 153001, Oct 2003.
- [106] N. Bouloufa, A. Crubellier, and O. Dulieu, “Reexamination of the 0_g^- pure long-range state of Cs_2 : Prediction of missing levels in the photoassociation spectrum,” *Phys. Rev. A*, vol. 75, p. 052501, May 2007.
- [107] Y. Zhang, S. Miyakawa, K. Kasai, Y. Okada-Shudo, and M. Watanabe, “Efficient phase noise suppression of an external-cavity diode-laser by optical filtering and resonant optical feedback,” *Applied Physics B*, vol. 108, pp. 39–42, July 2012.
- [108] B. M. Patterson, J. F. Sell, T. Ehrenreich, M. A. Gearba, G. M. Brooke, J. Scoville, and R. J. Knize, “Lifetime measurement of the cesium $6P_{3/2}$ level using ultrafast pump-probe laser pulses,” *Phys. Rev. A*, vol. 91, p. 012506, Jan 2015.
- [109] D. DiBerardino, C. E. Tanner, and A. Sieradzian, “Lifetime measurements of cesium $5d^2D_{5/2,3/2}$ and $11s^2S_{1/2}$ states using pulsed-laser excitation,” *Phys. Rev. A*, vol. 57, pp. 4204–4211, Jun 1998.
- [110] W. Z. Zhao, J. E. Simsarian, L. A. Orozco, W. Shi, and G. D. Sprouse, “Measurement of the $7p^2P_{3/2}$ level lifetime in atomic francium,” *Phys. Rev. Lett.*, vol. 78, pp. 4169–4172, Jun 1997.
- [111] J. E. Simsarian, L. A. Orozco, G. D. Sprouse, and W. Z. Zhao, “Lifetime measurements of the $7p$ levels of atomic francium,” *Phys. Rev. A*, vol. 57, pp. 2448–2458, Apr 1998.

- [112] A. Tosi, C. Scarcella, G. Boso, and F. Acerbi, “Gate-free InGaAs/InP single-photon detector working at up to 100 Mcount/s,” *IEEE Photonics Journal*, vol. 5, pp. 6801308–6801308, 08 2013.
- [113] J. Hoffnagle, V. Telegdi, and A. Weis, “Empirical determination of the scalar polarizability α in the $6s \rightarrow 7s$ transition in cesium,” *Physics Letters A*, vol. 86, no. 9, pp. 457 – 460, 1981.
- [114] J. Marek, “Study of the time-resolved fluorescence of the Cs-Xe molecular bands,” *Journal of Physics B: Atomic and Molecular Physics*, vol. 10, no. 9, p. L325, 1977.
- [115] V. Dzuba, V. Flambaum, A. Krafmakher, and O. Sushkov, “Summation of the high orders of perturbation theory in the correlation correction to the hyperfine structure and to the amplitudes of e1-transitions in the caesium atom,” *Physics Letters A*, vol. 142, no. 6, pp. 373 – 377, 1989.
- [116] C. Bouchiat, C. Piketty, and D. Pignon, “A theoretical analysis of parity violation induced by neutral currents in atomic cesium,” *Nuclear Physics B*, vol. 221, no. 1, pp. 68 – 108, 1983.
- [117] A. Sieradzan, M. D. Havey, and M. S. Safronova, “Combined experimental and theoretical study of the $6p^2P_j \rightarrow 8s^2S_{1/2}$ relative transition matrix elements in atomic cs,” *Phys. Rev. A*, vol. 69, p. 022502, Feb 2004.
- [118] A. Kramida, Yu. Ralchenko, J. Reader, and NIST ASD Team. NIST Atomic Spectra Database (ver. 5.6.1), [Online]. Available: <https://physics.nist.gov/asd> [2018, December 7]. National Institute of Standards and Technology, Gaithersburg, MD., 2018.
- [119] A. Damitz, G. Toh, E. Putney, C. E. Tanner, and D. S. Elliott, “Measurement of the radial matrix elements for the $6s^2S_{1/2} \rightarrow 7p^2P_J$ transitions in cesium,” *Phys. Rev. A*, vol. 99, p. 062510, Jun 2019.
- [120] C. E. Tanner, A. E. Livingston, R. J. Rafac, F. G. Serpa, K. W. Kukla, H. G. Berry, L. Young, and C. A. Kurtz, “Measurement of the $6p^2 P_{3/2}$ state lifetime in atomic cesium,” *Phys. Rev. Lett.*, vol. 69, pp. 2765–2767, Nov 1992.
- [121] S. A. Blundell, W. R. Johnson, and J. Sapirstein, “Relativistic all-order calculations of energies and matrix elements in cesium,” *Phys. Rev. A*, vol. 43, pp. 3407–3418, Apr 1991.
- [122] R. J. Rafac, C. E. Tanner, A. E. Livingston, K. W. Kukla, H. G. Berry, and C. A. Kurtz, “Precision lifetime measurements of the $6p^2 P_{1/2,3/2}$ states in atomic cesium,” *Phys. Rev. A*, vol. 50, pp. R1976–R1979, Sep 1994.
- [123] D. Antypas and D. S. Elliott, “Measurement of the radial matrix elements of the $6s^2S_{1/2} \rightarrow 7p^2P_J$ transitions in atomic cesium,” *Phys. Rev. A*, vol. 88, p. 052516, Nov 2013.
- [124] A. A. Vasilyev, I. M. Savukov, M. S. Safronova, and H. G. Berry, “Measurement of the $6s - 7p$ transition probabilities in atomic cesium and a revised value for the weak charge Q_W ,” *Phys. Rev. A*, vol. 66, p. 020101, Aug 2002.

- [125] J. Guena, M. Lintz, and M. A. Bouchiat, “Measurement of the parity violating 6s-7s transition amplitude in cesium achieved within 2×10^{-13} atomic-unit accuracy by stimulated-emission detection,” *Physical Review A*, vol. 71, p. 042108, Apr. 2005.
- [126] M. Tanabashi et. al., “Review of particle physics,” *Phys. Rev. D*, vol. 98, p. 030001, Aug 2018.
- [127] B. M. Roberts, V. A. Dzuba, and V. V. Flambaum, “Quantum electrodynamics corrections to energies, transition amplitudes, and parity nonconservation in Rb, Cs, Ba⁺, Tl, Fr, and Ra⁺,” *Phys. Rev. A*, vol. 87, p. 054502, May 2013.
- [128] V. V. Flambaum and J. S. M. Ginges, “Radiative potential and calculations of qed radiative corrections to energy levels and electromagnetic amplitudes in many-electron atoms,” *Phys. Rev. A*, vol. 72, p. 052115, Nov 2005.
- [129] W. R. Johnson, I. Bednyakov, and G. Soff, “Vacuum-polarization corrections to the parity-nonconserving 6s – 7s transition amplitude in ¹³³Cs,” *Phys. Rev. Lett.*, vol. 87, p. 233001, Nov 2001.
- [130] M. G. Kozlov, S. G. Porsev, and I. I. Tupitsyn, “High-accuracy calculation of 6s → 7s parity-nonconserving amplitude in Cs,” *Phys. Rev. Lett.*, vol. 86, pp. 3260–3263, Apr 2001.
- [131] V. A. Dzuba, C. Harabati, W. R. Johnson, and M. S. Safronova, “Breit correction to the parity-nonconservation amplitude in cesium,” *Phys. Rev. A*, vol. 63, p. 044103, Mar 2001.
- [132] J. E. Sansonetti, “Wavelengths, transition probabilities, and energy levels for the spectra of cesium (CsI-CsLV),” *Journal of Physical and Chemical Reference Data*, vol. 38, no. 4, pp. 761–923, 2009.

APPENDICES

A. $6S \rightarrow 7S$ ENERGY LEVEL DIAGRAM

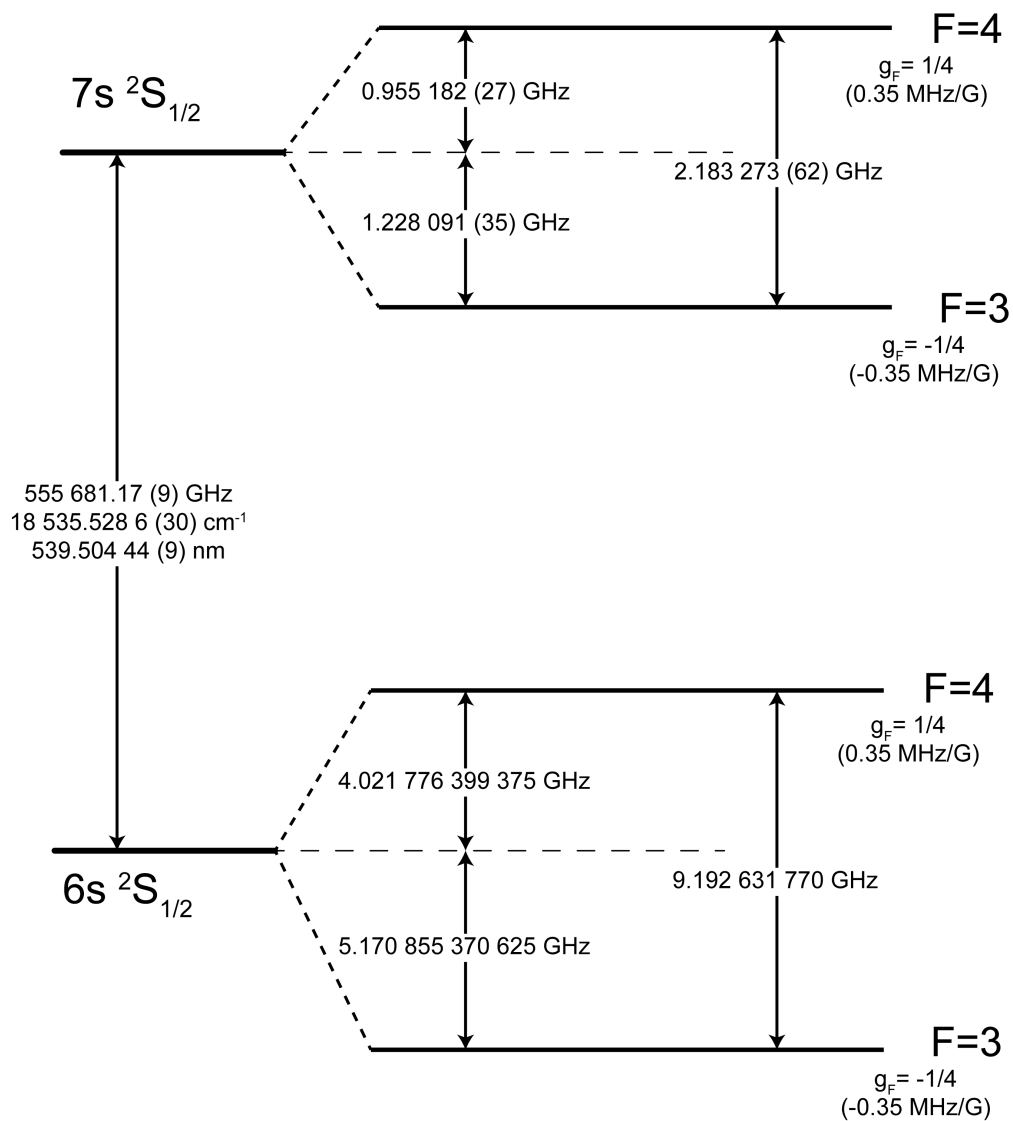


Fig. A.1. This figure shows the $6S \rightarrow 7S$ energy levels. The $6S$ hyperfine splitting is exact, $7S$ hyperfine splitting is from [60], while the energy level difference is from [132].

B. IMPORTANT CESIUM FACTS

In this Appendix, we list some important quantities of the Cesium atom and the 6S \rightarrow 7S transition.

To convert from units of μ_B to SI units, we multiply by

$$\mu_B = 9.27401 \cdot 10^{-24} J/T$$

$$\mu_B = 3.093478 \cdot 10^{-32} C \cdot m$$

$$\mu_B = 3.093478 \cdot 10^{-30} C \cdot cm$$

Polarizabilities (e.g. α) are commonly reported in either units of $\text{Hz}(\text{V}/\text{cm})^{-2}$ or a_0^3 . To convert from units of $\text{Hz}(\text{V}/\text{cm})^{-2}$ to a_0^3 , we multiply by

$$\frac{h}{4\pi\epsilon_0 a_0^3} = \frac{6.62607015 \times 10^{-34} J_s}{4\pi \times 8.85418782 \times 10^{-12} F/m \times (5.2917721 \times 10^{-11} m)^3}$$

$$\frac{h}{4\pi\epsilon_0 a_0^3} = 4018.7782 \frac{(V/cm)^2}{Hz}$$

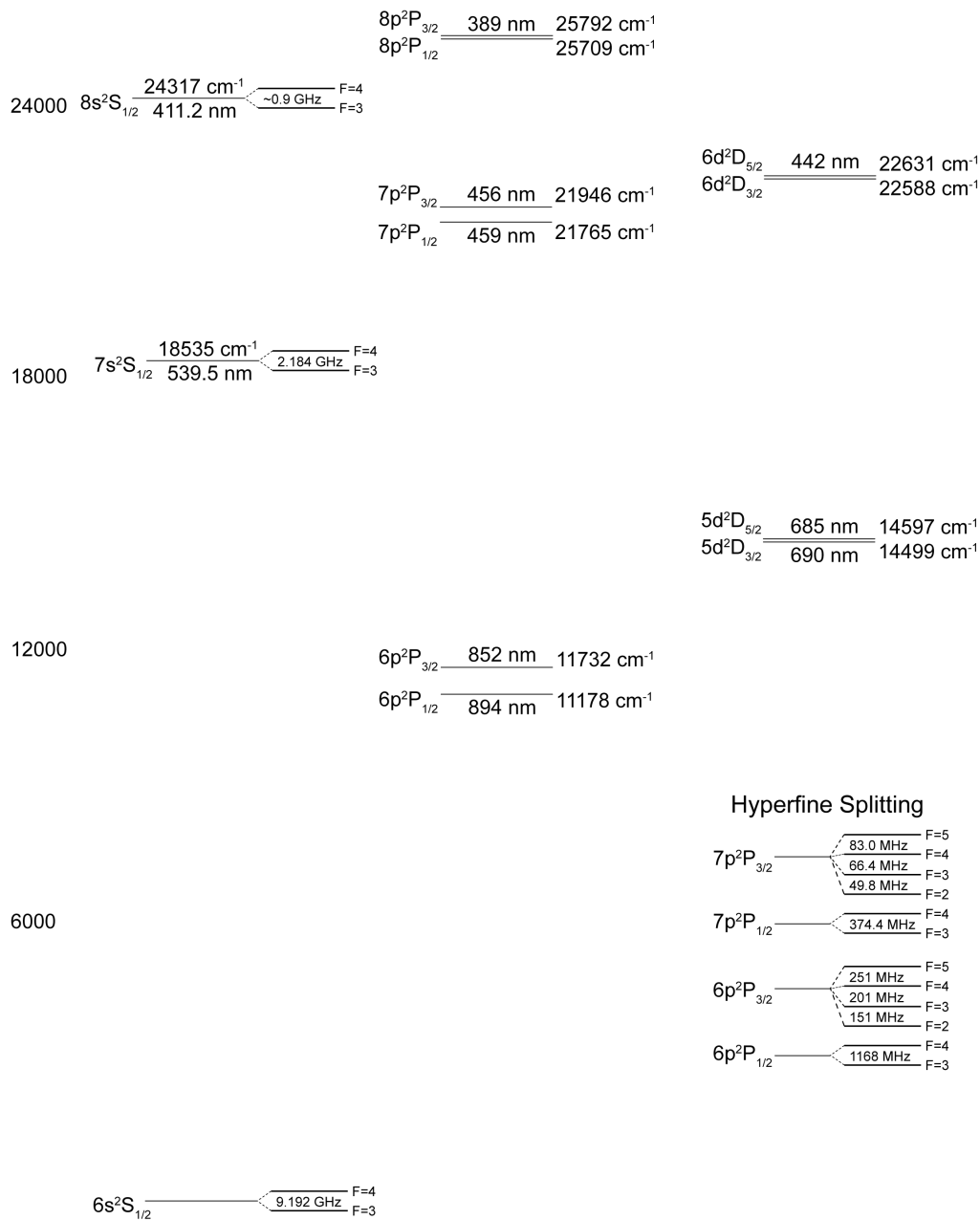


Fig. B.1. This diagram shows the lowest energy levels (for S, P and D orbitals) of Cs-133. Data for the energy levels is from the NIST database, while hyperfine splitting data is from a variety of sources. I have listed the hyperfine splitting of the $6P_j$ and $7P_j$ states are in the lower right corner.

C. $C_{FM}^{F'M'}$ COEFFICIENTS

This is a list of Clebsch Gordon coefficients, from [26]

$$\begin{aligned}
 C_{4,m}^{4,m} &= +\frac{m}{4} \\
 C_{4,m-1}^{4,m} &= -\frac{1}{8}[(5-m)(4+m)]^{1/2} \\
 C_{4,m+1}^{4,m} &= +\frac{1}{8}[(5+m)(4-m)]^{1/2} \\
 C_{4,m}^{3,m} &= +\frac{(16-m^2)^{1/2}}{4} \\
 C_{4,m-1}^{3,m} &= -\frac{1}{8}[(5-m)(4-m)]^{1/2} \\
 C_{4,m+1}^{3,m} &= -\frac{1}{8}[(5+m)(4+m)]^{1/2} \\
 C_{3,m}^{4,m} &= +\frac{(16-m^2)^{1/2}}{4} \\
 C_{3,m-1}^{4,m} &= +\frac{1}{8}[(3+m)(4+m)]^{1/2} \\
 C_{3,m+1}^{4,m} &= +\frac{1}{8}[(3-m)(4-m)]^{1/2} \\
 C_{3,m}^{3,m} &= -\frac{m}{4} \\
 C_{3,m-1}^{3,m} &= +\frac{1}{8}[(3+m)(4-m)]^{1/2} \\
 C_{3,m+1}^{3,m} &= -\frac{1}{8}[(3-m)(4+m)]^{1/2}
 \end{aligned}$$

D. CORRECTIONS TO DATA FOR BRANCHING RATIO MEASUREMENT

In this Appendix, we detail the calculations for corrections to the branching ratio measurement due to imperfect extinction ratio and manual rotation of the half-wave plate (HWP).

D.1 Imperfect extinction ratio

Recall that S_{\parallel} is the signal with parallel laser polarizations, while S_{\perp} is the signal with perpendicular laser polarizations. We denote with tilde the measured signals \tilde{S}_{\parallel} and \tilde{S}_{\perp} . Now, let \tilde{x} be the measured ratio of linestrengths

$$\tilde{x} = \frac{\tilde{S}_{\parallel}}{\tilde{S}_{\perp}} \tag{D.1}$$

and x be the actual ratio of linestrengths

$$x = \frac{S_{\parallel}}{S_{\perp}}. \tag{D.2}$$

If the extinction ratio is $1 : y$ when laser polarizations are parallel, and we denote the laser intensity with I , then

$$I_{\parallel} = \frac{y}{1+y} I_0 \tag{D.3}$$

$$I_{\perp} = \frac{1}{1+y} I_0 \tag{D.4}$$

If the extinction ratio is $1 : z$ when laser polarizations are perpendicular, then

$$I_{\parallel} = \frac{z}{1+z} I_0 \tag{D.5}$$

$$I_{\perp} = \frac{1}{1+z} I_0 \tag{D.6}$$

We can now write the measured ratio of linestrengths as a function of the extinction ratios y and z

$$\begin{aligned}
\tilde{x} &= \frac{\frac{y}{1+y}S_{\parallel} + \frac{1}{1+y}S_{\perp}}{\frac{1}{1+z}S_{\parallel} + \frac{z}{1+z}S_{\perp}} \\
&= \left(\frac{y}{1+y}\right)\left(\frac{z+1}{z}\right)\left(\frac{S_{\parallel} + \frac{1}{y}S_{\perp}}{\frac{1}{z}S_{\parallel} + S_{\perp}}\right) \\
&= \left(\frac{y}{1+y}\right)\left(\frac{z+1}{z}\right)\left(\frac{x + 1/y}{1 + x/z}\right) \\
&= \left(\frac{y}{1+y}\right)\left(\frac{z+1}{z}\right)x\left(\frac{1 + \frac{1}{xy}}{1 + \frac{x}{z}}\right) \\
\tilde{x} &= x\left(\frac{y}{1+y}\right)\left(\frac{z+1}{z}\right)\left(1 + \frac{1}{xy} - \frac{x}{z} + \dots\right)
\end{aligned} \tag{D.7}$$

Shifting all the terms to the other side, we obtain

$$x = \tilde{x} \left[\frac{\left(\frac{1+y}{y}\right)\left(\frac{z}{1+z}\right)}{1 + 1/(xy) - x/z} \right]. \tag{D.8}$$

In the denominator of the right hand side, x and \tilde{x} are close enough that we can substitute $x = \tilde{x}$ to simplify the calculation of the correction. Finally, we use the following equation

$$x = \tilde{x} \left[\frac{\left(\frac{1+y}{y}\right)\left(\frac{z}{1+z}\right)}{1 + 1/(\tilde{x}y) - \tilde{x}/z} \right] \tag{D.9}$$

to calculate the proper correction for our measured \tilde{x} .

D.2 Manual rotation of half-wave plate

For the branching ratio measurement described in Chapter 7, we manually rotate the half-wave plate (HWP) to change the laser polarization of the 1470 nm laser. Let θ be the rotation angle of the half-wave plate. We define the intensity of the parallel component to be $I_{\parallel}(\theta)$, and a function describing the manual mis-rotation as $f(\theta)$. The laser intensity in the other polarization is then

$$\bar{I} = \int_{-\infty}^{\infty} I_{\parallel}(\theta)f(\theta)d\theta \tag{D.10}$$

If θ is small (and in radians), we can re-write $I_{\parallel}(\theta)$ as

$$I_{\parallel}(\theta) = I_0 \sin^2(2\theta) \approx 4 I_0 \theta^2 \quad (\text{D.11})$$

We approximate the mis-rotation probability as a Gaussian distribution of amplitude A

$$f(\theta) d\theta = A \exp(-a^2\theta^2) d\theta. \quad (\text{D.12})$$

The normalization condition for $f(\theta)$ is

$$\begin{aligned} \int_{-\infty}^{\infty} f(\theta) d\theta = 1 &= A \frac{1}{a} \sqrt{\pi} \\ A &= \frac{a}{\sqrt{\pi}}. \end{aligned} \quad (\text{D.13})$$

Substituting this into Equation (D.12), we get

$$f(\theta) d\theta = \frac{a}{\sqrt{\pi}} \exp(-a^2\theta^2) d\theta \quad (\text{D.14})$$

If we estimate our manual rotation uncertainty (θ_0) to have a half-width at half maximum (HWHM) at $\theta_0 = 0.25^\circ$ (4.4 mrad),

$$\begin{aligned} \exp(-a^2\theta_0^2) &= \frac{1}{2} \\ -a^2\theta_0^2 &= \ln \frac{1}{2} = -\ln 2 \\ a &= \frac{\sqrt{\ln 2}}{\theta_0} \\ a &= \frac{\sqrt{\ln 2}}{4.4 \times 10^{-3}} = 190 \end{aligned} \quad (\text{D.15})$$

Therefore, for $\theta_0 = 0.25^\circ = 4.4$ mrad,

$$\begin{aligned} \bar{I} &= \int_{-\infty}^{\infty} 4 I_0 \theta^2 \frac{a}{\sqrt{\pi}} \exp(-a^2\theta^2) d\theta \\ &= \frac{4 I_0 a}{\sqrt{\pi}} \int_{-\infty}^{\infty} \theta^2 \exp(-a^2\theta^2) d\theta \\ &= \frac{2 I_0}{a^2} = \frac{2 I_0}{(190)^2} = 6 \times 10^{-5} I_0 \end{aligned} \quad (\text{D.16})$$

This is equivalent to an extinction ratio of 1:16000 due to rotation angle error.